University of Southampton Research Repository

Copyright © and Moral Rights for this thesis and, where applicable, any accompanying data are retained by the author and/or other copyright owners. A copy can be downloaded for personal non-commercial research or study, without prior permission or charge. This thesis and the accompanying data cannot be reproduced or quoted extensively from without first obtaining permission in writing from the copyright holder/s. The content of the thesis and accompanying research data (where applicable) must not be changed in any way or sold commercially in any format or medium without the formal permission of the copyright holder/s.

When referring to this thesis and any accompanying data, full bibliographic details must be given, e.g.

Thesis: Author (Year of Submission) "Full thesis title", University of Southampton, name of the University Faculty or School or Department, PhD Thesis, pagination.

Data: Author (Year) Title. URI [dataset]

**UNIVERSITY OF SOUTHAMPTON**

Faculty of Engineering and Physical Science

# Smart Composite Magnetorheological Elastomer Materials under Coupled Effects of Temperature and Magnetic Field for Vibration Control

By

**Yanxiang WAN**

Supervisor: Dr. Yeping Xiong
Dr. Shengming Zhang

Thesis for the degree of Doctor of Philosophy

June 18th, 2019

# Abstract

Magnetorheological Elastomers (MREs) are a class of smart materials composed of an elastomer matrix and micron-sized magnetic particles. Their unique elastic and rheological properties can be changed continuously, rapidly and reversibly responding to the applied magnetic field. MRE's real-time controllable stiffness and damping properties have many advantages and offer wide applications to vibration control in various engineering fields. In order to expand the application of MREs in ship vibration control, a better understanding of MRE dynamic properties is essential. Previous studies about MREs were mainly focused on the influences of external magnetic field, strain amplitude and frequency on the dynamic properties. However, the temperature effect was rarely reported. This thesis is mainly focus on the temperature effect and the coupling effects with other impact factors on the compressive dynamic properties of MREs. The MRE samples used in this project are fabricated with silicone rubber and iron particles. The experimental investigation on the mechanical properties of MREs is carried out with dynamic mechanical analysis (DMA) tests. The influence of excitation frequency, strain amplitude, pre-strain, external magnetic field and environment temperature along with their coupling effects on the dynamic properties of MREs are investigated. The static test and the differential scanning calorimetry (DSC) test are performed as well. A new mathematical model is developed to describe these influence factors. The excellent correlation between the experimental data and modelling results is confirmed by the goodness-of-fit statistical analysis. The generalized dynamic modulus master curve of MREs is constructed for the first time by the horizontal and vertical shift factors. The constructed master curve and shift factors can be used to predict the viscoelastic properties of the MREs beyond the DMA experiment range of magnetic fields, temperatures, strain amplitudes and frequencies. In addition, a prototype of MRE based mount system along with the control strategy is designed, manufactured and tested. The natural frequency shift ability and the performance of the force transmissibility of the designed system under different test conditions are evaluated by experimental and numerical investigations. A series of case studies are carried out to perform the designed device under the different external magnetic fields and the environment temperatures. The results indicate the MRE based device is capable of solving the vibration control problems in marine engineering.



**Keywords:** magnetorheological elastomers, dynamic mechanical analysis, temperature effect, generalized mathematical model, MRE vibration control device

# Table of contents

**Abstract** ..... 2

**Table of contents** ..... 3

**List of figure** ..... 7

**List of table** ..... 19

Research Thesis: Declaration of Authorship ..... 21

**Acknowledgements** ..... 22

**Nomenclature** ..... 23

**1 Introduction** ..... 25

**1.1 Background** ..... 25

**1.2 Research novelties** ..... 26

**1.3 Aims and objectives** ..... 27

**1.3.1 Aims** ..... 27

**1.3.2 Objectives** ..... 27

**1.4 Thesis structure** ..... 27

**2 Literature review** ..... 29

**2.1 Introduction** ..... 29

**2.2 MRE fabrication** ..... 30

**2.2.1 Matrix material** ..... 30

**2.2.2 Magnetic particle** ..... 32

**2.2.3 Additive** ..... 35

**2.2.4 Microstructure** ..... 36

**2.3 Physical phenomena of MRE** ..... 37

**2.3.1 MR effect** ..... 37

**2.3.2 Mullins effect** ..... 39

**2.3.3 Payne effect** ..... 41

**2.4 Dependent properties of MREs** ..... 42

**2.4.1 Magnetic field dependence** ..... 42

**2.4.2 Strain amplitude and frequency dependence** ..... 44

**2.4.3 Temperature dependence** ..... 44

**2.5 Modelling of MRE** ..... 46
**2.5.1 Phenomenological models** ..... 46
**2.5.2 Micromechanical models** ..... 49
**2.6 Applications of MRE** ..... 54
**2.6.1 MRE absorbers** ..... 55
**2.6.2 MRE isolators** ..... 57
**2.6.3 Vibration control structures** ..... 61
**2.6.4 Other applications** ..... 63
**2.7 Research gaps** ..... 64
**3 Methodology** ..... 66
**3.1 Experimental investigation on the mechanical properties of MREs** ..... 66
**3.2 Mathematical modelling of MRE materials** ..... 68
**3.3 Design of MRE based devices for semi-active vibration control** ..... 70
**4 Experimental investigation on MRE** ..... 72
**4.1 Introduction** ..... 72
**4.2 Experimental setup** ..... 73
**4.2.1 MRE sample manufacture** ..... 73
**4.2.2 Experiment design for mechanical characterization of MREs** ..... 76
**4.2.3 Oven design** ..... 78
**4.2.4 Experiment test machine** ..... 79
**4.2.5 Experimental data processing** ..... 80
**4.3 Dynamic mechanical analysis measurement result** ..... 81
**4.3.1 Hysteresis loop** ..... 84
**4.3.2 Dynamic mechanical properties** ..... 91
**4.3.3 Temperature effect** ..... 104
**4.4 Static mechanical test** ..... 113
**4.5 Differential scanning calorimetry test** ..... 114
**4.6 Summary** ..... 116
**5 Mathematical modelling of MREs** ..... 118
**5.1 Introduction** ..... 118
**5.2 Linear viscoelastic model** ..... 119

**5.2.1 Viscoelastic models in literature** ..... 119
**5.2.2 The proposed model for viscoelastic properties of MREs** ..... 122
**5.2.3 Fitting procedure and goodness-of-fit statistics** ..... 123
**5.2.4 Comparative analysis of viscoelastic models** ..... 125
**5.3 Temperature effect** ..... 131
**5.3.1 Shift factor equations** ..... 132
**5.3.2 Applicability of the time-temperature superposition principle** ..... 134
**5.3.3 Master curves construction** ..... 138
**5.3.4 Goodness-of-fit statistics of shift factors** ..... 143
**5.4 Dependence of magnetic field** ..... 145
**5.4.1 Basic equation** ..... 145
**5.4.2 The magnetic field induced modulus** ..... 146
**5.4.3 Magnetic field dependent dynamic properties** ..... 151
**5.5 Dependence of strain amplitude** ..... 154
**5.5.1 Linear viscoelastic limit** ..... 154
**5.5.2 The Kraus model** ..... 156
**5.5.3 Strain amplitude dependent dynamic properties** ..... 161
**5.6 Generalized mathematical model for dynamic properties of MREs** ..... 167
**5.6.1 State of the art** ..... 167
**5.6.2 Description of the model** ..... 169
**5.6.3 Parameter identification** ..... 170
**5.7 Summary** ..... 172
**6 Characterization of MRE based mount** ..... 174
**6.1 Introduction** ..... 174
**6.2 Design of semi-active MRE mount** ..... 175
**6.2.1 Design and assembly of MRE mount** ..... 175
**6.2.2 Manufacture and test of the MRE core** ..... 179
**6.3 Experiment on efficiency of the MRE mount** ..... 181
**6.3.1 Transmissibility and frequency shift of the MRE mount** ..... 181
**6.3.2 Dynamic properties of the designed MRE mount** ..... 184
**6.4 Modelling and simulation of MRE mount** ..... 185

**6.4.1 Dynamic modelling of the MRE mount** ..... 185
**6.4.2 Results and discussion** ..... 188
**6.5 Experimental case studies on the MRE mount** ..... 191
**6.5.1 On-off control of single mount at system resonance frequency** ..... 191
**6.6.2 Real-time control of single mount with varying frequency** ..... 193
**6.6 Summary** ..... 199
**7 Conclusion** ..... 201
**7.1 Contribution of the work** ..... 201
**7.2 Recommendations for future work** ..... 202
**Reference** ..... 204
**Appendix A List of publication** ..... 218
**Appendix B Additional DMA experiment results** ..... 221
**Appendix C Design calculation of oven** ..... 238
**C.1 Introduction** ..... 238
**C.2 Heat transfer** ..... 238
**C.3 Summary** ..... 240
**Appendix D Numerical results of particle filled elastomer** ..... 241
**D.1 Introduction** ..... 241
**D.2 FEA of hyper-elastic behaviour** ..... 241
**D.3 FEA of MRE in the absence of an external magnetic field** ..... 244
**D.4 Summary** ..... 249

# List of figure

Figure 2. 1 Damping ratio of MREs based on different types of matrix. [Chen et al. (2008)]..... 31

Figure 2. 2 The MR effect of Perbunan 3445 with ASC300 and carbonyl iron (CI), displayed in left as the absolute increase in shear modulus (in MPa), and in right as the relative increase in shear modulus (in %). [Lokander and Stenberg (2003)] ..... 33

Figure 2. 3 The storage modulus of different diametric MRE samples. [Yang et al. (2013)]..... 34

Figure 2. 4 SEM images of (a) isotropic MREs and (b) anisotropic MREs. [Wu et al. (2012)]... 36

Figure 2. 5 Loss factors of MRE samples under different temperatures. [Gong et al. (2012)] .... 37

Figure 2. 6 Loss factors of MRE samples under different magnetic field strengths: (a) testing at 25 °C; (b) testing at 60 °C. [Gong et al. (2012)] ..... 37

Figure 2. 7 Stress–strain relationships with various magnetic fields. [Li et al. (2010)] ..... 38

Figure 2. 8 Comparison of relative MR response for all deformation modes, and all types of MREs with particle concentrations from 10% to 30%. [Schubert and Harrison (2015)]..... 39

Figure 2. 9 Hysteresis loops of (a) isotropic and (b) anisotropic samples for various magnetic field strength values. Minimum strain amplitude $\gamma a = 6.25 \times 10^{-3}$. [Kaleta et al. (2011)]... 39

Figure 2. 10 Schematic representation of the Mullins effect: (a) loading-unloading curves in simple tension ($\lambda$ is stretch) [Ogden and Roxburgh (1999)]; and (b) stress-stretch response of a filled rubber under cyclic uniaxial conditions. [Merckel et al. (2012)] ..... 40

Figure 2. 11 Storage modulus (a) and loss modulus (b) versus increasing–decreasing strain amplitude in a maximum magnetic field of 600 mT. Initial curves are indicated by arrows. [Sorokin et al. (2017)] ..... 42

Figure 2. 12 Dependence of storage modulus (left) and loss modulus (right) of isotropic MRE with different concentrations of small iron particles (in vol.%) in silicone on the magnetic flux density. [Böse and Röder (2009)] ..... 43

Figure 2. 13 Storage modulus and loss modulus as a function of amplitude and frequency. [Li and Su (2011)] ..... 44

Figure 2. 14 Temperature-dependent storage modulus of samples with different ratios of cis-polybutadiene rubber and natural rubber at 800 mT: (a) 100:0, (b) 80:20, (c) 60:40, (d) 40:60, (e) 20:80, and (f) 0:100. [Zhang et al. (2011)] ..... 45

Figure 2. 15 Kelvin-Voigt model for MRE ($\gamma^*$ is input strain and $\tau^*$ is response stress)..... 47

Figure 2. 16 A rheological model for examining dynamic properties of MREs comprising three components to simulate (a) the viscoelasticity of the polymer composite, (b) the magnetic-field-induced mechanical properties, and (c) interfacial slippage between the matrix and the particles. [Chen and Jerrams (2011)] ..... 48

Figure 2. 17 Schematic diagram of the MRE model. [Yang et al. (2013)] ..... 48

Figure 2. 18 Calculation principles. [Daniel et al. (2014)]..... 49

Figure 2. 19 Layer-like unit cell. [Li et al. (2015)] ..... 49

Figure 2. 20 Multiscale approach—principle. [Daniel et al. (2008)] ..... 51

Figure 2. 21 The single-chain model of two adjacent magnetic particles. [Jolly et al. (1996)] .... 52

Figure 2. 22 The multi-chain model of the magnetic particles. [Zhu et al. (2006)] ..... 53

Figure 2. 23 The schematic diagram of the ATVA: 1. cover; 2. guide rod; 3. linear bearing; 4. magnetic conductor; 5. shear plate; 6.MREs; 7. base; 8. electromagnet; 9. mounting shell. [Deng and Gong (2008)]..... 56

Figure 2. 24 The MRE AATVA (a) schematic diagram and (b) photograph: (1) mounting shell; (2) MRE; (3) helical spring; (4) shear block; (5) magnetic conductor; (6) guide rod; (7) connector of the voice coil motor and the shell; (8) voice coil motor; (9) flange; (10) base. [Liao et al. (2011)] ..... 56

Figure 2. 25 The structure and prototyping of laminated MRE absorber. [Sun et al. (2015)] ..... 57

Figure 2. 26 Shake table vibration experiment setup. [Behrooz et al. (2014)] ..... 58

Figure 2. 27 Cross section of the MRE base isolator. [Li and Li (2015)]..... 59

Figure 2. 28 Schematic configuration of MRE buffer: 1-Outer cylinder; 2-Coil; 3-Piston; 4-Primary flux; path 5-MRE). [Fu et al. (2013)] ..... 59

Figure 2. 29 (a) MRE device and (b) device structure [Zhu and Rui (2014)] ..... 60

Figure 2. 30 Three-layered adaptive beam with MR material situated in the middle layer. [Yalcintas et al. (2004)]..... 62

Figure 2. 31 MRE-based composite floor supporting equipment (a) and MRE-based composite wall supporting equipment (b). [Ni et al. (2010)]..... 62

Figure 2. 32 MRE embedded viscoelastic cored sandwich beam subjected to periodic magnetic field and axial load. [Nayak et al. (2012)] ..... 63

Figure 2. 33 MRE micro actuator. [Tang et al. (2018)]..... 64

Figure 2. 34 MRE sensor. [Kawasetsu et al (2018)] ..... 64

Figure 3. 1 Flow chart of the project ..... 66

Figure 3. 2 Flow chart of Part I: DMA experiment..... 68

Figure 3. 3 Flow chart of Part II: Mathematical modelling..... 70

Figure 3. 4 Flow chart of Part III: Design of MRE based mount..... 71

Figure 4. 1 Silicone rubber A and B ..... 74

Figure 4. 2 ALDRICH iron particles ..... 74

Figure 4. 3 Vacuum chamber and vacuum pump ..... 74

Figure 4. 4 Aluminium moulds ..... 75

Figure 4. 5 MRE mixture ..... 75

Figure 4. 6 Anisotropic MRE sample curing..... 75

Figure 4. 7 One pair of N42 ..... 75

Figure 4. 8 Two pairs of N42 ..... 75

Figure 4. 9 MRE sample according to the BS ISO standard ..... 77

Figure 4. 10 The complex modulus of different excitation frequencies and loading cycles ..... 77

Figure 4. 11 The high temperature glass ..... 78

Figure 4. 12 Heating wire ..... 78

Figure 4. 13 MRE sample with two permanent magnets ..... 79

Figure 4. 14 Experimental setup for uniaxial harmonic compression test ..... 80

Figure 4. 15 Results comparison and error analysis for static compression test ..... 82

Figure 4. 16 Results comparison and error analysis of dynamic compression test. (a) storage modulus and (b) loss modulus ..... 83

Figure 4. 17 Hysteresis loop of MRE samples under uniaxial compression with pre-strain of 5%, test frequency of 10 Hz, strain amplitude of 1.5 %, and external magnetic field varying from 0 to 465 mT in room temperature ..... 85

Figure 4. 18 Hysteresis loops of MRE samples under uniaxial compression with pre-strain of 5%, strain amplitude of 1.5%, non-magnetic field, and different vibration frequencies from 10 Hz to 60Hz in room temperature ..... 86

Figure 4. 19 Hysteresis loops of MRE samples under uniaxial compression with pre-strain of 5%, strain amplitude of 1.5%, external magnetic field of 265 mT, and different vibration frequencies from 10 Hz to 60Hz in room temperature ..... 86

Figure 4. 20 Hysteresis loops of MRE samples under uniaxial compression with vibration frequency of 10 Hz, non-magnetic field, pre-strain of 5%, and different strain amplitudes from 0.25% to 1.5% in test temperature of 30 ℃ ..... 88

Figure 4. 21 Hysteresis loops of MRE samples under uniaxial compression with vibration frequency of 10 Hz, external magnetic field of 265 mT, pre-strain of 5%, and different strain amplitudes from 0.25% to 1.5% in test temperature of 30 ℃ ..... 88

Figure 4. 22 Hysteresis loops of MRE sample under uniaxial compression with vibration frequency of 60 Hz, non- magnetic field, pre-strain of 5%, and different strain amplitudes from 0.25% to 1.5% in test temperature of 30 ℃ ..... 89

Figure 4. 23 Hysteresis loops of MRE sample under uniaxial compression with vibration frequency of 60 Hz, external magnetic field of 265 mT, pre-strain of 5%, and different strain amplitudes from 0.25% to 1.5% in test temperature of 30 ℃ ..... 90

Figure 4. 24 Hysteresis loops of MRE sample under uniaxial compression with pre-strain of 5%, strain amplitude of 1.5%, vibration frequency of 60 Hz, and external magnetic field of 265 mT in different test temperatures ..... 91

Figure 4. 25 Dependence of storage modulus on strain amplitude at room temperature, pre-strain of 5%, magnetic field of 0 mT ..... 92

Figure 4. 26 Dependence of loss modulus on strain amplitude at room temperature, pre-strain of 5%, magnetic field of 0 mT ..... 92

Figure 4. 27 Dependence of tan delta on strain amplitude at room temperature, pre-strain of 5%, magnetic field of 0 mT ..... 93

Figure 4. 28 Dependence of storage modulus on strain amplitude at room temperature, pre-strain of 5%, magnetic field of 265 mT ..... 94

Figure 4. 29 Dependence of loss modulus on strain amplitude at room temperature, pre-strain of 5%, magnetic field of 265 mT ..... 94

Figure 4. 30 Dependence of tan delta on strain amplitude at room temperature, pre-strain of 5%, magnetic field of 265 mT ..... 95

Figure 4. 31 Dependence of storage modulus on strain amplitude and pre-strain at room temperature, excitation frequency of 60 Hz with (a) 0 mT, (b) 265 mT magnetic field ..... 96

Figure 4. 32 Dependence of loss modulus on strain amplitude and pre-strain at room temperature, excitation frequency of 60 Hz with (a) 0 mT, (b) 265 mT magnetic field ..... 97

Figure 4. 33 Dependence of tangent delta on strain amplitude and pre-strain at room temperature, excitation frequency of 60 Hz with (a) 0 mT, (b) 265 mT magnetic field ..... 97

Figure 4. 34 Dependence of storage modulus on external magnetic field and frequency at room temperature, pre-strain of 5%, and strain amplitude of 1.5% ..... 98

Figure 4. 35 Dependence of loss modulus on external magnetic field and frequency at room temperature, pre-strain of 5%, and strain amplitude of 1.5% ..... 98

Figure 4. 36 Dependence of tan delta on external magnetic field and frequency at room temperature, pre-strain of 5%, and strain amplitude of 1.5% ..... 99

Figure 4. 37 Dependence of storage modulus on external magnetic field and frequency at room temperature, pre-strain of 5%, and the strain amplitude is 1.5% ..... 100

Figure 4. 38 Dependence of loss modulus on external magnetic field and frequency at room temperature, pre-strain of 5%, and the strain amplitude is 1.5% ..... 100

Figure 4. 39 Dependence of tangent delta on external magnetic field and frequency at room temperature, pre-strain of 5%, and the strain amplitude is 1.5% ..... 101

Figure 4. 40 Dependence of storage modulus on external magnetic field and strain amplitude at room temperature, pre-strain of 5%, and the test frequency is 10 Hz and 60 Hz ..... 102

Figure 4. 41 Dependence of loss modulus on external magnetic field and strain amplitude at room temperature, pre-strain of 5%, and the test frequency is 10 Hz and 60 Hz ..... 102

Figure 4. 42 Dependence of tangent delta on external magnetic field and strain amplitude at room temperature, pre-strain of 5%, and the test frequency is 10 Hz and 60 Hz ..... 103

Figure 4. 43 Dependence of storage modulus on temperature and frequency at pre-strain of 5%, strain amplitude of 1%, and magnetic field of 0 mT ..... 104

Figure 4. 44 Dependence of loss modulus on temperature and frequency at pre-strain of 5%, strain amplitude of 1%, and magnetic field of 0 mT ..... 104

Figure 4. 45 Dependence of tan delta on temperature and frequency at pre-strain of 5%, strain amplitude of 1%, and magnetic field of 0 mT .....105

Figure 4. 46 Dependence of storage modulus on temperature and frequency at pre-strain of 5%, strain amplitude of 1%, and magnetic field of 265 mT .....106

Figure 4. 47 Dependence of loss modulus on temperature and frequency at pre-strain of 5%, strain amplitude of 1%, and magnetic field of 265 mT .....106

Figure 4. 48 Dependence of tan delta on temperature and frequency at pre-strain of 5%, strain amplitude of 1%, and magnetic field of 265 mT .....107

Figure 4. 49 Dependence of storage modulus on temperature and frequency at pre-strain of 5%, strain amplitude of 1%, and magnetic field of 465 mT .....108

Figure 4. 50 Dependence of loss modulus on temperature and frequency at pre-strain of 5%, strain amplitude of 1%, and magnetic field of 465 mT .....108

Figure 4. 51 Dependence of tan delta on temperature and frequency at pre-strain of 5%, strain amplitude of 1%, and magnetic field of 465 mT .....109

Figure 4. 52 Dependence of storage modulus on strain amplitude and pre-strain at 40 ℃, 60 Hz excitation frequency and in absence of external magnetic field.....110

Figure 4. 53 Dependence of loss modulus on strain amplitude and pre-strain at 40 ℃, 60 Hz excitation frequency and in absence of external magnetic field.....111

Figure 4. 54 Dependence of tan delta on strain amplitude and pre-strain at 40 ℃, 60 Hz excitation frequency and in absence of external magnetic field.....111

Figure 4. 55 Dependence of storage modulus on strain amplitude and pre-strain at 50 ℃, 60 Hz excitation frequency and in absence of external magnetic field.....112

Figure 4. 56 Dependence of loss modulus on strain amplitude and pre-strain at 50 ℃, 60 Hz excitation frequency and in absence of external magnetic field.....112

Figure 4. 57 Dependence of tan delta on strain amplitude and pre-strain at 50 ℃, 60 Hz excitation frequency and in absence of external magnetic field.....113

Figure 4. 58 The static stress-strain curve of MRE.....114

Figure 4. 59 Differential scanning calorimetry (DSC) test result of the MRE sample .....115

Figure 5. 1 Diagram of linear viscoelastic models: (a) the Maxwell model, (b) the fractional Maxwell model, (c) The Zener model, and (d) the fractional Zener model.....120

Figure 5. 2 Diagram of the proposed viscoelastic model. .....122

Figure 5. 3 Comparison fitting capability between our proposed model and the fractional Zener model and the CAM model for the MRE sample: (a) storage modulus, and (b) loss modulus of the MRE sample subjected to uniaxial harmonic compression with 1% strain amplitude in the temperature of 35℃ and non-magnetic field. .....126

Figure 5. 4 Comparison fitting capability between our proposed model and the fractional Zener model and the CAM model for the MRE sample: (a) storage modulus, and (b) loss modulus of the MRE sample under uniaxial harmonic compression with 0.25% strain amplitude, the temperature of 25℃ and the magnetic field of 300 mT. .....127

Figure 5. 5 Comparison fitting capability between our proposed model and the fractional Zener model and the CAM model for the MRE sample: (a) storage modulus, and (b) loss modulus of the MRE sample under uniaxial harmonic compression with 0.25% strain amplitude, the temperature of 60℃ and the magnetic field of 300 mT. .....128

Figure 5. 6 Comparison fitting capability between our proposed model and the fractional Zener model and the CAM model for the MRE sample: (a) storage modulus, and (b) loss modulus of the MRE sample under uniaxial harmonic compression with 1% strain amplitude, the temperature of 60℃ and the magnetic field of 500 mT. .....129

Figure 5. 7 (a) The Cole-Cole plot, and (b) the Black diagrams of the MRE samples under 0.25% uniaxial harmonic compression and 300 mT magnetic field. .....135

Figure 5. 8 (a) The Cole-Cole plot, and (b) the Black diagrams of the MRE samples under 1% uniaxial harmonic compression and non-magnetic field. .....136

Figure 5. 9 The wicket plot calculated by applying the vertical shift factor to: (a) Cole-Cole plot, and (b) the Black diagrams of the MRE samples under 0.25% uniaxial harmonic compression and 300 mT magnetic field. .....137

Figure 5. 10 The wicket plot calculated by applying the vertical shift factor to: (a) Cole-Cole plot, and (b) the Black diagrams of the MRE samples under 1% uniaxial harmonic compression and non-magnetic field. .....138

Figure 5. 11 Comparison between experimental and predicted data of: (a) storage modulus, and (b) loss modulus of the MRE samples under 0.25% strain amplitude and 300 mT magnetic field. .....140

Figure 5. 12 Dynamic modulus master curve of the MRE samples under 0.25% strain amplitude and 300 mT magnetic field, (a) storage modulus, and (b) loss modulus. .....140

Figure 5. 13 Comparison between experimental and predicted data of: (a) storage modulus, and (b) loss modulus of the MRE samples under 1% strain amplitude and non-magnetic field. .....141

Figure 5. 14 The frequency and temperature dependent (a) storage modulus and (b) loss modulus of the MRE samples under 1% strain amplitude and non-magnetic field. .....142

Figure 5. 15 Comparison between numerical and functional shift factors: (a) horizontal shift factor and vertical shift factor of the MRE samples under 0.25% strain amplitude and 300 mT magnetic field. .....144

Figure 5. 16 Comparison between numerical and functional shift factors: (a) horizontal shift factor and vertical shift factor of the MRE samples under 1% strain amplitude and non-magnetic field. .....144

Figure 5. 17 The Comparison of magnetic field dependent: (a) storage modulus and (b) loss modulus between experimental data and fitting results of the MRE sample under uniaxial compression with 5% pre-strain, 1% strain amplitude, and 10 Hz excitation frequency in room temperature.....149

Figure 5. 18 The Comparison of magnetic field dependent: (a) storage modulus and (b) loss modulus between experimental data and fitting results of the MRE sample under uniaxial compression with 5% pre-strain, 1% strain amplitude, and 30 Hz excitation frequency in room temperature.....150

Figure 5. 19 The Comparison of magnetic field dependent: (a) storage modulus and (b) loss modulus between experimental data and fitting results of the MRE sample under uniaxial compression with 5% pre-strain, 1% strain amplitude, and 50 Hz excitation frequency in room temperature.....151

Figure 5. 20 Measured data of magnetic field dependent: (a) storage modulus, and (b) loss modulus of the MRE sample under uniaxial compression with 5% pre-strain and 1% strain amplitude in room temperature .....152

Figure 5. 21 Predicted results by using the proposed model for magnetic field dependent: (a) storage modulus, and (b) loss modulus of the MRE sample under uniaxial compression with 5% pre-strain and 1% strain amplitude in room temperature.....153

Figure 5. 22 Comparison of predicted results and measured data of strain amplitude dependent: (a) storage modulus, and (b) loss modulus of the MRE sample under uniaxial compression with 3% pre-strain, in non-magnetic field and room temperature. .....158

Figure 5. 23 Comparison of predicted results and measured data of strain amplitude dependent: (a) storage modulus, and (b) loss modulus of the MRE sample under uniaxial compression with 3% pre-strain, in non-magnetic field and temperature of 50 °C.....159

Figure 5. 24 Comparison of predicted results and measured data of strain amplitude dependent: (a) storage modulus, and (b) loss modulus of the MRE sample under uniaxial compression with 3% pre-strain, in magnetic field of 300 mT and temperature of 30 °C.....160

Figure 5. 25 Comparison of predicted results and measured data of strain amplitude dependent: (a) storage modulus, and (b) loss modulus of the MRE sample under uniaxial compression with 3% pre-strain, in magnetic field of 300 mT and temperature of 40 °C.....161

Figure 5. 26 Measured data of strain amplitude dependent: (a) storage modulus, and (b) loss modulus of the MRE sample under uniaxial compression with 3% pre-strain in non-magnetic field and room temperature .....164

Figure 5. 27 Predicted results by using the Kraus model for strain amplitude dependent: (a) storage modulus, and (b) loss modulus of the MRE sample under uniaxial compression with 3% pre-strain in non-magnetic field and room temperature. .....165

Figure 5. 28 Measured data of strain amplitude dependent: (a) storage modulus, and (b) loss modulus of the MRE sample under uniaxial compression with 3% pre-strain in magnetic field of 300 mT and temperature of 40 °C. .....166

Figure 5. 29 Predicted results by using the Kraus model for strain amplitude dependent: (a) storage modulus, and (b) loss modulus of the MRE sample under uniaxial compression with 3% pre-strain in magnetic field of 300 mT and temperature of 40 °C.....167

Figure 5. 30 Comparison of predicted results and measured data of strain amplitude dependent: (a) storage modulus, and (b) loss modulus of the MRE sample under uniaxial compression with 3% pre-strain, in magnetic field of 0 to 500 mT, strain amplitude of 0.1% to 1,5%, and temperature of 22 °C to 60 °C. .....171

Figure 6. 1 The control circuit diagram of the designed MRE mount system.....175

Figure 6. 2 Sorensen DLM 60-10 Power Supply.....176

Figure 6. 3 Electromagnet.....178

Figure 6. 4 AltIMU-10 v5 Gyro.....178

Figure 6. 5 Thermometer Evaluation Board - MLX90614 .....178

Figure 6. 6 Arduino uno rev3 .....178

Figure 6. 7 MRE based mount.....180

Figure 6. 8 Rubber naval mount.....180

Figure 6. 9 Vibration control system.....180

Figure 6. 10 One large cylinder MRE.....180

Figure 6. 11 Three-cylinder MRE.....180

Figure 6. 12 Transmissibility of (a) one large cylinder, and (b) three-cylinder MRE device under vibration frequency.....181

Figure 6. 13 force transmissibility of MRE mount under different magnetic field and vibration frequency.....182

Figure 6. 14 Transmissibility of MRE mount under different working state (a) 0 mT, and (b) 210 mT external magnetic field .....183

Figure 6. 15 Storage modulus of MRE mount under different working states: (a) 0 mT, and (b) 210 mT external magnetic field.....184

Figure 6. 16 Loss modulus of MRE mount under different working states: (a) 0 mT, and (b) 210 mT external magnetic field .....185

Figure 6. 17 The dynamic model of: (a) a six-DOF system, and (b) a single-DOF system.....186

Figure 6. 18 The comparison of the experiment data and numerical results of the force transmissibility of the MRE mount under various magnetic fields in room temperature....189

Figure 6. 19 The comparison of the experiment data and numerical results of the force transmissibility of the MRE mount under various temperatures in absence of external magnetic field. .....189

Figure 6. 20 The comparison of the experiment data and numerical results of the force transmissibility of the MRE mount under various temperatures in magnetic field of 210 mT. .....190

Figure 6. 21 (a)Load and (b)dynamic position time sequences of MRE mount under 250 pre-load and 50 N dynamic load with 30 Hz excitation frequency. .....192

Figure 6. 22 (a) Vibration displacement and (b) force transmissibility time sequences of MRE mount under 50 N dynamic load and 30 Hz frequency. .....192

Figure 6. 23 Experiment setup of the semi-active MRE mount test.....194

Figure 6. 24 Labview VI: (a) front panel, and (b) block diagram for self-control MRE mount..195

Figure 6. 25 Comparison of the displacement of MRE mount upper deck under different working states at room temperature (20 °C). ....195

Figure 6. 26 Comparison of the force transmissibility of MRE mount upper deck under different working states at room temperature (20 °C). ....196

Figure 6. 27 Comparison of the displacement of MRE mount upper deck under different working states at 50 °C. ....197

Figure 6. 28 Comparison of the force transmissibility of MRE mount upper deck under different working states at 50 °C. ....197

Figure 6. 29 Comparison of the displacement of MRE mount upper deck with large deformation at 20 ℃ ....197

Figure 6. 30 Comparison of the force transmissibility of MRE mount upper deck with large deformation at 20 ℃ ....198

Figure 6. 31 Comparison of the displacement of MRE mount upper deck with large deformation at 50 ℃ ....198

Figure 6. 32 Comparison of the force transmissibility of MRE mount upper deck with large deformation at 50 ℃ ....199

Figure B. 1 Dependence of loss factor on strain amplitude at room temperature, pre-strain of 5%, magnetic field of 0 mT, and vibration frequency from 10 Hz to 60 Hz....221

Figure B. 2 Dependence of transmissibility on strain amplitude at room temperature, pre-strain of 5%, magnetic field of 0 mT, and vibration frequency from 10 Hz to 60 Hz ....221

Figure B. 3 Dependence of loss factor on frequency at room temperature, pre-strain of 5%, magnetic field of 300 mT, and strain amplitudes from 0.25% to 1.5% ....221

Figure B. 4 Dependence of transmissibility on frequency at room temperature, pre-strain of 5%, magnetic field of 300 mT, and strain amplitudes from 0.25% to 1.5% ....222

Figure B. 5 Dependence of loss factor on external magnetic field and frequency at room temperature, pre-strain of 5%, and strain amplitude of 1.5% ....222

Figure B. 6 Dependence of loss factor on external magnetic field and strain amplitude at room temperature, pre-strain of 5%, and the test frequency is 10 Hz and 60 Hz ....222

Figure B. 7 Dependence of transmissibility on external magnetic field and strain amplitude at room temperature, pre-strain of 5%, and the test frequency is 10 Hz and 60 Hz....223

Figure B. 8 Dependence of storage modulus on temperature and frequency at pre-strain of 5%, strain amplitude of 1%, and non-magnetic field....223

Figure B. 9 Dependence of storage modulus on temperature and strain amplitude at pre-strain of 5%, vibration frequency of 10 Hz, and non-magnetic field....223

Figure B. 10 Dependence of storage modulus on temperature and strain amplitude at pre-strain of 5%, vibration frequency of 60 Hz and non-magnetic field....224

Figure B. 11 Dependence of loss modulus on temperature and frequency at pre-strain of 5%, strain amplitude of 1%, and non-magnetic field.....224

Figure B. 12 Dependence of loss modulus on temperature and strain amplitude at pre-strain of 5%, vibration frequency of 10 Hz, and non-magnetic field.....224

Figure B. 13 Dependence of loss modulus on temperature and strain amplitude at pre-strain of 5%, vibration frequency of 60 Hz, and non-magnetic field.....225

Figure B. 14 Dependence of loss factor on temperature and frequency at pre-strain of 5%, strain amplitude of 1%, and non-magnetic field.....225

Figure B. 15 Dependence of loss factor on temperature and frequency at pre-strain of 5%, strain amplitude of 1%, and non-magnetic field.....225

Figure B. 16 Dependence of loss factor on temperature and strain amplitude at pre-strain of 5%, vibration frequency of 10 Hz, and non-magnetic field .....226

Figure B. 17 Dependence of loss factor on temperature and strain amplitude at pre-strain of 5%, vibration frequency of 60 Hz and non-magnetic field .....226

Figure B. 18 Dependence of transmissibility on temperature and frequency at pre-strain of 5%, strain amplitude of 1%, and non-magnetic field.....226

Figure B. 19 Dependence of transmissibility on temperature and frequency at pre-strain of 5%, strain amplitude of 1%, and non-magnetic field.....227

Figure B. 20 Dependence of transmissibility on temperature and strain amplitude at pre-strain of 5%, vibration frequency of 10 Hz, and non-magnetic field.....227

Figure B. 21 Dependence of transmissibility on temperature and strain amplitude at pre-strain of 5%, vibration frequency of 60 Hz and non-magnetic field.....227

Figure B. 22 Dependence of storage modulus on temperature and frequency at pre-strain of 5%, strain amplitude of 1%, and magnetic field of 300 mT .....228

Figure B. 23 Dependence of storage modulus on temperature and frequency at pre-strain of 5%, strain amplitude of 1%, and magnetic field of 300 mT .....228

Figure B. 24 Dependence of storage modulus on temperature and strain amplitude at pre-strain of 5%, vibration frequency of 10 Hz, and magnetic field of 300 mT .....228

Figure B. 25 Dependence of storage modulus on temperature and strain amplitude at pre-strain of 5%, vibration frequency of 60 Hz, and magnetic field of 300 mT .....229

Figure B. 26 Dependence of loss modulus on temperature and frequency at pre-strain of 5%, strain amplitude of 1%, and magnetic field of 300 mT .....229

Figure B. 27 Dependence of loss modulus on temperature and frequency at pre-strain of 5%, strain amplitude of 1%, and magnetic field of 300 mT .....229

Figure B. 28 Dependence of loss modulus on temperature and strain amplitude at pre-strain of 5%, vibration frequency of 10 Hz, and magnetic field of 300 mT .....230

Figure B. 29 Dependence of loss modulus on temperature and strain amplitude at pre-strain of 5%, vibration frequency of 60 Hz, and magnetic field of 300 mT .....230

Figure B. 30 Dependence of loss factor on temperature and frequency at pre-strain of 5%, strain amplitude of 1%, and magnetic field of 300 mT .....230

Figure B. 31 Dependence of loss factor on temperature and frequency at pre-strain of 5%, strain amplitude of 1%, and magnetic field of 300 mT .....231

Figure B. 32 Dependence of loss factor on temperature and strain amplitude at pre-strain of 5%, vibration frequency of 10 Hz, and 300 mT .....231

Figure B. 33 Dependence of loss factor on temperature and strain amplitude at pre-strain of 5%, vibration frequency of 60 Hz, and magnetic field of 300 mT .....231

Figure B. 34 Dependence of transmissibility on temperature and frequency at pre-strain of 5%, strain amplitude of 1%, and magnetic field of 300 mT .....232

Figure B. 35 Dependence of transmissibility on temperature and frequency at pre-strain of 5%, strain amplitude of 1%, and magnetic field of 300 mT .....232

Figure B. 36 Dependence of transmissibility on temperature and strain amplitude at pre-strain of 5%, vibration frequency of 10 Hz, and 300 mT .....232

Figure B. 37 Dependence of transmissibility on temperature and strain amplitude at pre-strain of 5%, vibration frequency of 60 Hz, and 300 mT .....233

Figure B. 38 Dependence of storage modulus on temperature and frequency at pre-strain of 5%, strain amplitude of 1%, and magnetic field of 500 mT .....233

Figure B. 39 Dependence of storage modulus on temperature and strain amplitude at pre-strain of 5%, vibration frequency of 10 Hz, and magnetic field of 500 mT .....233

Figure B. 40 Dependence of storage modulus on temperature and strain amplitude at pre-strain of 5%, vibration frequency of 60 Hz, and magnetic field of 500 mT .....234

Figure B. 41 Dependence of loss modulus on temperature and frequency at pre-strain of 5%, strain amplitude of 1%, and magnetic field of 500 mT .....234

Figure B. 42 Dependence of loss modulus on temperature and strain amplitude at pre-strain of 5%, vibration frequency of 10 Hz, and magnetic field of 500 mT .....234

Figure B. 43 Dependence of loss modulus on temperature and strain amplitude at pre-strain of 5%, vibration frequency of 60 Hz, and magnetic field of 500 mT .....235

Figure B. 44 Dependence of loss factor on temperature and frequency at pre-strain of 5%, strain amplitude of 1%, and magnetic field of 500 mT .....235

Figure B. 45 Dependence of loss factor on temperature and frequency at pre-strain of 5%, strain amplitude of 1%, and magnetic field of 500 mT .....235

Figure B. 46 Dependence of loss factor on temperature and strain amplitude at pre-strain of 5%, vibration frequency of 10 Hz, and magnetic field of 500 mT .....236

Figure B. 47 Dependence of loss factor on temperature and strain amplitude at pre-strain of 5%, vibration frequency of 60 Hz, and magnetic field of 500 mT .....236

Figure B. 48 Dependence of transmissibility on temperature and frequency at pre-strain of 5%, strain amplitude of 1%, and magnetic field of 500 mT .....236

Figure B. 49 Dependence of transmissibility on temperature and frequency at pre-strain of 5%, strain amplitude of 1%, and magnetic field of 500 mT .....237

Figure B. 50 Dependence of transmissibility on temperature and strain amplitude at pre-strain of 5%, vibration frequency of 10 Hz, and magnetic field of 500 mT .....237

Figure B. 51 Dependence of transmissibility on temperature and strain amplitude at pre-strain of 5%, vibration frequency of 60 Hz, and magnetic field of 500 mT .....237

Figure C. 1 The diagram of cubic box .....239

Figure C. 2 The rate of heat loss vary with test temperature when the room temperature is 20 °C .....240

Figure D. 1 Hyper-elastic behaviour of PP rubber under: (a) uniaxial tension, (b) equibiaxial tension, and (c) pure shear based on the Mooney-Rivlin .....243

Figure D. 2 Hyper-elastic behaviour of PP rubber under: (a) uniaxial tension, (b) equibiaxial tension, and (c) pure shear based on the Ogden model.....244

Figure D. 3 Comparison of FEA and various theoretical models for predicting the effect of iron particles embedded in PP rubbery matrix on the elastic modulus of MREs.....247

Figure D. 4 The uniaxial tension stress-stretch behaviour of PP rubber filled with different volume fractions of iron particles. .....248

Figure D. 5 The equibiaxial tension stress-stretch behaviour of PP rubber filled with different volume fractions of iron particles. .....248

Figure D. 6 The pure shear stress-stretch behaviour of PP rubber filled with different volume fractions of iron particles. .....248

# List of table

Table 2. 1 Summary of the matrix material selected for MRE in previous researches ..... 31

Table 2. 2 Summary of the filler particles selected for MRE in previous researches..... 34

Table 4. 1 Test specimen dimension and the test conditions for MRE samples ..... 76

Table 4. 2 Test loading cycles with excitation frequency ..... 77

Table 4. 3 Test plan for 10 Hz compression test..... 87

Table 4. 4 Test plan for 60 Hz compression test..... 87

Table 5. 1 The criteria for statistical analysis [Yusoff et al. (2011)]. .....124

Table 5. 2 Goodness-fit-statistics of the proposed model, the fractional Zener model, and the CAM model for storage modulus of the MRE sample under uniaxial harmonic compression with different magnetic fields, test temperatures, and strain amplitudes. .....130

Table 5. 3 Goodness-fit-statistics of the proposed model, the fractional Zener model, and the CAM model for loss modulus of the MRE sample under uniaxial harmonic compression with different magnetic fields, test temperatures, and strain amplitudes. .....130

Table 5. 4 The maximum geometrical deviation (MGD) and average geometrical deviation (AGD) of the predictive models for storage modulus. .....131

Table 5. 5 The maximum geometrical deviation (MGD) and average geometrical deviation (AGD) of the predictive models for loss modulus. .....131

Table 5. 6 Goodness-of-fit analysis of the master curve and the proposed model for the MRE sample under uniaxial compression with 0.25% strain amplitude in the magnetic field of 300mT. .....142

Table 5. 7 Goodness-of-fit analysis of the master curve and the proposed model for the MRE sample under uniaxial compression with 1% strain amplitude in absence of magnetic field. .....143

Table 5. 8 Goodness-of-fit statistical analysis of the dynamic modulus master curve constructed by different horizontal shift factors. .....144

Table 5. 9 Statistical analysis results of Goodness-of-fit for magnetic field dependent storage modulus and loss modulus of MREs under uniaxial harmonic compression with 5% pre-strain and 1% strain amplitude in room temperature. .....151

Table 5. 10 Goodness-of-fit statistical analysis of different expressions for the asymptotic values of storage modulus and loss modulus at large strain amplitude under prestrain of 3% prestrain, magnetic field of 0 mT, and temperature of 20°C .....162

Table 5. 11 Goodness-of-fit statistical analysis of different expressions for the asymptotic values of storage modulus and loss modulus at large strain amplitude under prestrain of 3% prestrain, magnetic field of 300 mT, and temperature of 20°C ..... 163

Table 5. 12 Goodness-of-fit statistical analysis of different storage modulus master curves ..... 172

Table 5. 13 Goodness-of-fit statistical analysis of different loss modulus master curves ..... 172

Table 6. 1 Magnetic field generated by the power supply ..... 177

Table 6. 2 The resonance frequency of the MRE mount in different temperatures and external magnetic fields. ..... 190

# Research Thesis: Declaration of Authorship

| | |
|---|---|
| Print name: | Yanxiang Wan |

| | |
|---|---|
| Title of thesis: | Smart Composite Magnetorheological Elastomer Materials under Coupled Effects of Temperature and Magnetic Field for Vibration Control |

I declare that this thesis and the work presented in it are my own and has been generated by me as the result of my own original research.

I confirm that:

1. This work was done wholly or mainly while in candidature for a research degree at this University;
2. Where any part of this thesis has previously been submitted for a degree or any other qualification at this University or any other institution, this has been clearly stated;
3. Where I have consulted the published work of others, this is always clearly attributed;
4. Where I have quoted from the work of others, the source is always given. With the exception of such quotations, this thesis is entirely my own work;
5. I have acknowledged all main sources of help;
6. Where the thesis is based on work done by myself jointly with others, I have made clear exactly what was done by others and what I have contributed myself;
7. Parts of this work have been published as:

Wan Y, Xiong Y, & Zhang S. (2017). Temperature effect on dynamic properties of magnetorheological elastomers. Advances in Engineering Research, 110, 415-420.

Wan Y, Xiong Y, & Zhang S. (2018). Temperature dependent dynamic mechanical properties of Magnetorheological elastomers: Experiment and modeling. Composite Structures, 202, 768-773.

Wan Y, Xiong Y, & Zhang S. (2019). Temperature effect on viscoelastic properties of anisotropic magnetorheological elastomers under compression. Smart Materials and Structures, 28(1), 015005.

| | | | |
|---|---|---|---|
| Signature: | | Date: | |

## Acknowledgements

The author would like to thank supervisor Associate Prof. Yeping Xiong. Without her advice, encouragement and support, this thesis would not have been possible. The author would also like thank to Dr. Shengming Zhang for generously providing useful advice and help for this research. Thanks also go to Prof. Ajit Shenoi and Prof. Atul Bhaskar for their comments and advice at the transfer viva.

The author would like to thank Dr. Guanghong Zhu, Dr. Kyriaki Sapouna, Dr. Andy Robinson and Mr. Marcos Benega for their suggestion, training and helping with the experimental work.

The author would also like to thank Dr. Wei Wang, Dr. Yuming Cai, Mr. Yu Cao, Dr. Caoyang Yu, Mr. Zhengzhou Wang, Dr. Trewut Anurakpandit, Mr. Mehment Cihan and Miss. Qiu Jing for their encouragements and friendships.

The author would like to thank his parents for their selfless love. Thanks for them being financially and mentally supportive during the research life.

Last but not least, the author would like to thank the Lloyd's Register for the sponsorship.

# Nomenclature

| Term | Definition |
|---|---|
| $A$ | Coefficient of frequency dependent stiffness |
| $B$ | Magnetic flux intensity |
| $C$ | Viscosity coefficient of dashpot |
| $D$ | Damping |
| $E_0$ | Relaxed modulus |
| $E_\infty$ | Instantaneous modulus |
| $E_e$ | Equilibrium modulus |
| $E_g$ | Glassy modulus |
| $E_s$ | Static stiffness |
| $E'$ | Storage Young's modulus |
| $E''$ | Loss modulus |
| $E^*$ | Complex modulus |
| $\lvert E^* \rvert$ | Absolute Complex modulus |
| $F_{ex}$ | Excitation force |
| $K$ | Stiffness |
| $M$ | Mass |
| $R^2$ | Coefficient of determination |
| $S_e/S_y$ | Standard error ratio |
| $T_r$ | Reference temperature |
| $X$ | Displacement |
| $\dot{X}$ | Velocity |
| $\ddot{X}$ | Acceleration |
| $a_T$ | Horizontal shift factor |
| $b'_K$ | Shift factor for strain amplitude dependent storage modulus |

| | |
|---|---|
| $b_K''$ | Shift factor for strain amplitude dependent loss modulus |
| $b_M'$ | Shift factor for magnetic field dependent storage modulus |
| $b_M''$ | Shift factor for magnetic field dependent loss modulus |
| $b_T$ | Vertical shift factor |
| $c_{MR}'$ | MR effect on storage modulus |
| $c_{MR}''$ | MR effect on loss modulus |
| $\alpha$ | Fractional derivative |
| $\beta$ | Shape parameter |
| $tan\,\delta$ | Tangent of the loss angle |
| $\varepsilon$ | Strain |
| $\rho$ | Density |
| $\sigma$ | Stress |
| $\tau$ | Relaxation time |
| $\omega$ | Excitation frequency |
| $\omega_c$ | Crossover frequency |
| $\omega_s$ | Scalar parameter |

# 1 Introduction

## 1.1 Background

Ship structures experience various time-varying dynamic loadings and the induced vibrations not only cause fatigue damage of ship, affect the health of crew onboard, cause damage to the cargos, but more importantly raise great environmental concerns because of structure-borne, water-borne and air-borne noise. Recently, the stricter requirements for the noise levels onboard have been adopted by the International Maritime Organization (IMO) Maritime Safety Committee (MSC) to limit noise levels and to reduce seafarers' exposure to noise [Resolution MSC. 337(91)], in which the noise level limits for accommodation spaces are reduced by 5 dB compared with IMO A468 (XII) when ship size is greater than 10,000 GT. There is an increasing demand in marine industry for low vibration, low noise products to meet performance standards and to reduce environmental noise pollution.

It is well known that the better way to reduce harmful noise is to control the vibration. The theory and methodology of vibration control have been developed to avoid or reduce the harmful vibrations. Among these vibration control methods, the semi-active vibration control method based on the adjustable parameter characteristics of smart materials (i.e. stiffness, damping) has received considerable attention because it takes advantages of both the passive and active vibration control methods. Smart material based semi-active vibration control system can adapt to the changes in external excitations without high-energy consumption when compared to active vibration control system and provide more effective performance in a wide range of frequencies than passive vibration control system.

Magnetorheological elastomer (MRE) is a promising smart material due to its unique elastic and rheological properties that can be changed continuously, rapidly and reversibly responding to the applied magnetic field. MRE's real-time controllable stiffness and damping properties have many advantages and offer wide applications to vibration control in various engineering fields, hence attracted much attention in recent years. Many researchers have focused on the development of MRE based semi-active vibration control system and conducted experimental studies on the influence of amplitude, frequency and magnetic field on the mechanical characteristics of MREs. However, there are a few published studies investigating the temperature dependent magneto-mechanical properties of MREs.

Most of previous MRE models are normally consider only one or two impact factors, such as magnetic field and load amplitude, on the dynamic mechanical properties. A generalized

mathematical model for MREs is lacking due to the difficulties in modelling their complex anisotropic and nonlinear dynamic behaviours mathematically, as well as the complex interactions between magnetic field and MRE composites. Moreover, the challenge also lies in how to experimentally investigate the coupling mechanism, design adaptive control system, compact magnetic device incorporating required dynamic properties of MRE materials and their integrated structures for practical applications in the changing operational environment. Comparing to the extensive studies on the magneto-mechanical properties of MREs by experiments, there are few published studies on numerical modelling the material properties of MREs under magnetic, thermal, mechanical, and their combination loads.

The project aims to investigate the nonlinear dynamic behaviour of MREs under the combined magnetic-thermal-mechanical load and to develop a prototype of MRE based semi-active vibration control device. A generalized mathematical model is proposed to describe the dynamic properties of MREs under combined magnetic-thermal-mechanical loads. A generalized master curve is constructed for dynamic modulus of MREs capable of taking into account magnetic field, temperature, strain amplitude, and excitation frequency. The numerical and experimental examples are presented to demonstrate the capabilities and performances of MRE based semi-active vibration control system for vibration control in marine engineering.

## 1.2 Research novelties

Experimental:

1. Achieve the temperature dependent compressive dynamic mechanical properties of MREs based on silicone rubber and iron particles.

2. Design and manufacture a new heating oven to control the environment temperature of the MRE samples instead of using traditional water-based system.

3. Achieve the coupling effects of strain amplitude, frequency, external magnetic field and environment temperature on the dynamic mechanical properties of MRE samples under uniaxial compression load.

4. Develop a porotype of semi-active vibration control device based on anisotropic MRE material and test under different magnetic field and temperature conditions.

Modelling:

1. Develop a new approach for modelling the viscoelastic behaviour of MREs under uniaxial harmonic compression.

2. Construct the dynamic modulus master curve of the MREs by using the horizontal shift factor and the vertical shift factor.

3. Propose new fractional functions to fit the magnetic field induced storage modulus and loss modulus of MREs under uniaxial harmonic compression.

4. Apply the Kraus model to predict the strain amplitude effect on the dynamic moduli of MREs within medium strain range.

5. Propose a generalized mathematical model for describing the magnetic field, temperature, strain amplitude and frequency dependent dynamic moduli of MREs under uniaxial harmonic compression.

## 1.3 Aims and objectives

### 1.3.1 Aims

The project aim to achieve a good understanding on the nonlinear dynamic behaviour of MREs under the combined magnetic-thermal-mechanical load, and to develop a prototype of MRE based semi-active vibration control device.

### 1.3.2 Objectives

(1) Achieve the dependent mechanical properties of MREs under uniaxial harmonic compression through the dynamic mechanical analysis (DMA) tests.
(2) Develop a generalized mathematical model to describe the dynamic mechanical properties of MREs dependence on magnetic field, temperature, strain amplitude and excitation frequency.
(3) Design a prototype semi-active vibration control device based on MRE material.
(4) Perform the case studies to demonstrate the capability and effectiveness of the prototype of MRE based device in different load conditions and environment temperatures.

## 1.4 Thesis structure

Chapter 2 gives a review of the current research on MRE materials. The review contains MRE fabrication methods, physical phenomena and mechanical properties of MRE, MRE modelling

and applications. The summary of the current literatures and research gaps are given at the end of this chapter.

Chapter 3 states the methodology to characterise the material properties of MRE through the experimental study and modelling.

Chapter 4 performs the experimental investigation on the mechanical properties of MRE material. The dependences of pre-strain, frequency, strain amplitude, magnetic field and environment temperature are considered. Coupling effects between these influences are also compared and discussed.

Chapter 5 develops a mathematical model for describing the elastic and rheological properties of MREs. A generalized master curve is constructed for dynamic modulus of MREs considering the magnetic field, temperature, strain amplitude, and excitation frequency.

Chapter 6 demonstrates a compression based MRE mount. This chapter includes design, manufacture and assemble the designed MRE mount. The efficiency of the design device is evaluated with several case studies.

Chapter 7 discusses the contributions of this project and the recommendations for the future studies on MRE material and its applications.

# 2 Literature review

## 2.1 Introduction

Magnetorheological (MR) materials are a new type of smart materials whose mechanical properties can be changed continuously, rapidly and reversibly by the application of the external magnetic field. MR materials can be broadly classified into MR fluids (MRFs), MR elastomers (MREs), and MR foams [Carlson and Jolly (2000), Skalski and Kalita (2017)]. Their controllable mechanical properties have many advantages and offer wide potential applications to vibration control in various engineering fields and therefore attracted much more attention in recent years. The most common MR materials are MRFs comprising the magnetic particles suspended in a liquid-state carrier material. In the presence of an external magnetic field, MRFs can reversibly change their states between free-flowing, linear viscous liquids, and semi-solids having controllable yield strength when the magnetic field is turned on and off [Vicente et al. (2011), Baranwal and Deshmukh (2012), Sariman et al. (2015)]. MREs are the solid-state analogue of MRFs and they consist of magnetic particle filler and a non-magnetic matrix, and some additives. The stiffness and rheological properties of MREs can be changed rapidly and reversibly responding to the applied magnetic field. MREs have a magnetic field dependent stiffness while MRFs have a magnetic field dependent yield strength [Li et al. (2014), Ubaidillah et al. (2015), Ying and Ni (2017)]. This makes the two kinds of MR materials complementary rather than competitive to each other.

The aims of this project are to investigate the nonlinear dynamic behaviour of MREs under the combined magnetic-thermal-mechanical load and develop a prototype MRE based semi-active vibration control system. Therefore, the literature review in this chapter focuses on the recent research and development of MRE materials and MRE-based applications. Section 2.2 reviews the recent research on the influence of fabrication process (e.g. matrix material, particle filler, and additives) to the mechanical properties of MREs. Section 2.3 presents the physical phenomena of MREs including MR effect, the Mullins effect, and the Payne effect. Section 2.4 reviews the recent studies on dependent mechanical properties of MREs in various working conditions such as magnetic field dependence, strain amplitude and frequency dependence, and temperature dependence. Section 2.5 reviews the recent development of mathematical models for describing the nonlinear dynamic mechanical behaviour of MREs. Section 2.6 reviews the recent development in design applications of MRE based devices (e.g. MRE absorber, MRE isolator, and MRE composite structure) in vibration control. The other new applications of

MRE material are discussed in this section as well. Finally, the research gaps are presented in Section 2.7 after the comprehensive reviews.

## 2.2 MRE fabrication

### 2.2.1 Matrix material

Rubber and rubber-like material are usually used for the matrix in MRE materials fabrication process, and the most frequently used ones are natural rubber, silicone rubber, chloroprene rubber, synthetic rubber etc. The rubber selection for MRE fabrication is normally according to its particular application. As shown in Table 2.1 the silicon rubber and natural rubber are the most popular materials for MRE matrices.

In order to achieve high MR effects, silicone rubber (SiR) is usually selected as the matrix to fabricate the MREs [Zhu et al. (2013)]. The main reason making this rubber so popular applied in MRE fabrication is it can be cured in room temperature which is much easier than other materials. This rubber also offers highly resistance to extreme temperatures (normally from −100 °C to 300 °C) and good chemical stability. The disadvantage of this soft matrix is its unsatisfactory load carrying capacity such as stiffness may not suitable for some specific applications. Natural rubber has higher stiffness, better processing properties and flexibility than silicone rubber which are suitable for most common applications [Chen et al. (2007, 2008), Ruddy et al. (2012)]. However, the natural rubber is not easy to process and need to be cured at high temperature and high pressure. Normally, natural rubber does not have such ideal thermal resistant when comparing with silicone rubber (begins to melt at approximately 180 °C). This characteristic make the MRE based on natural rubber not suitable for high temperature working environment. Shen et al. (2004) used natural rubber and polyurethane (PU) as the matrix to fabricate the MRE samples. The experimental results indicated that MRE made of polyurethane sealant had better controllable properties than MRE made of natural rubber. Chen et al. (2008) used silicon rubber (SiR), natural rubber (NR), chloroprene rubber (CIIR) to fabricate MRE materials and compared their damping ratios in Figure 2.1. It can be seen from this figure that the damping ratio of the MRE based on NR is lower than that of MRE based on SiR and CIIR. Yu et al. (2015) fabricated MRE sample based on polyurethane (PU)/epoxy resin (EP) graft interpenetrating polymer networks (IPNs). Based on his study, it can be noticed this type of MRE material has much better thermal stability than other previous MRE materials.

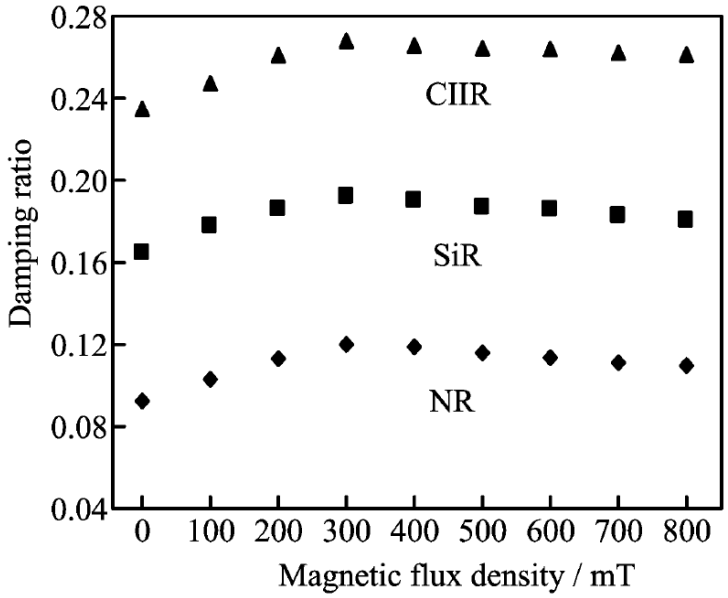


Figure 2. 1 Damping ratio of MREs based on different types of matrix. [Chen et al. (2008)]

Table 2. 1 Summary of the matrix material selected for MRE in previous researches

| Matrix | Author and time |
|---|---|
| Natural rubber | Lokander and Stenberg (2003), Shen et al. (2004), Chen et al. (2007, 2008), Yang et al. (2013), Zhang et al. (2011), Khimi and Pickering (2015, 2016), Yunus et al. (2016), Olabide and Elejabarrieta (2017), An et al. (2017) , Aziz et al. (2018), Fan et al. (2019) |
| Silicon rubber (SiR) | Gong et al. (2005), Wang et al. (2006), Chen et al. (2007, 2008), Song et al. (2009), Popp K et al. (2010), Park et al. (2011), Kumbhar et al. (2013), Hegde et al. (2014), Schubert and Harrison (2015), Gao and Wang (2016), Bastola et al. (2017), Damiani and Sun (2017), Olabide and Elejabarrieta (2017), Sun et al. (2018), Gavrilovici et al. (2019), Shabdin et al. (2019) |
| Polydimethylsiloxane (PDMS) | Varga et al. (2005), Böse (2007), Böse and Röder (2009), Borin et al. (2012), Tian et al. (2013), Li and Nakano (2013). Martínez et al. (2017), Pineda et al. (2017) |

| | |
|---|---|
| Cis-polybutadiene rubber (BR) | Fan et al. (2010, 2012), Zhang et al. (2011), Gong et al. (2012) |
| Thermoplastic (Tefabloc TO 222) | Zając et al. (2010), Kaleta et al. (2011, 2012), Królewicz et al. (2012, 2013) |
| Polyurethane (PU) rubber | Shen et al. (2004), Sławiński et al. (2011), Boczkowska et al. (2012), Wu et al. (2012), Xu et al. (2013) |
| Segmented urea-urethane (EPU) | Boczkowska and Awietjan (2011) |
| Nitrile rubbers | Lokander and Stenberg (2003) , Stenberg et al. (2004) |
| Poly methyl methacrylate (PMMA) | Li et al. (2009) |
| Poly(Vinyl Butyral) (PVB) | Park et al. (2009) |
| Polytetramethylene ether glycol (PTMEG)-based polyurethane (PU) | Wu et al. (2010), Wei et al. (2010) |
| Chloroprene rubber (CIIR) | Chen et al. (2008) |
| Poly(styrene-b-ethyleneco-butylene-b-styrene) (SEBS) | Lu et al. (2012) |
| Polyurethane (PU)/Silicone rubber (SiR) hybrid | Hu et al. (2005) |
| Immiscible silicon rubber/polystyrene (SiR/PS) blend | Wang et al. (2007) |

### 2.2.2 Magnetic particle

Introducing magnetic particles into elastomer matrix may influence the mechanical performance of the material while applying external magnetic field. The mechanical properties of MRE materials are dependent on its matrix and magnetic particles. As shown in Table 2.2 the iron particles and carbonyl iron are most popular magnetic particle fillers for MREs. The magnetic fillers are iron, nickel and cobalt with a diameter from 1 to 100 microns [Li and Zhang (2008)]. Most of previous researchers preferred using iron particles to fabricate MREs due to its high permeability, low permanent magnetization and high saturation magnetization [Zhu et al. (2013), Carlson and Jolly (2000)]. This may generate large interaction between the magnetic particles to achieve large MR effect. According to passed experimental research, the increment of MR effect is not remarkable when the volume fraction of the fillers is over 30 vol%

[Lokander and Stenberg (2003)].

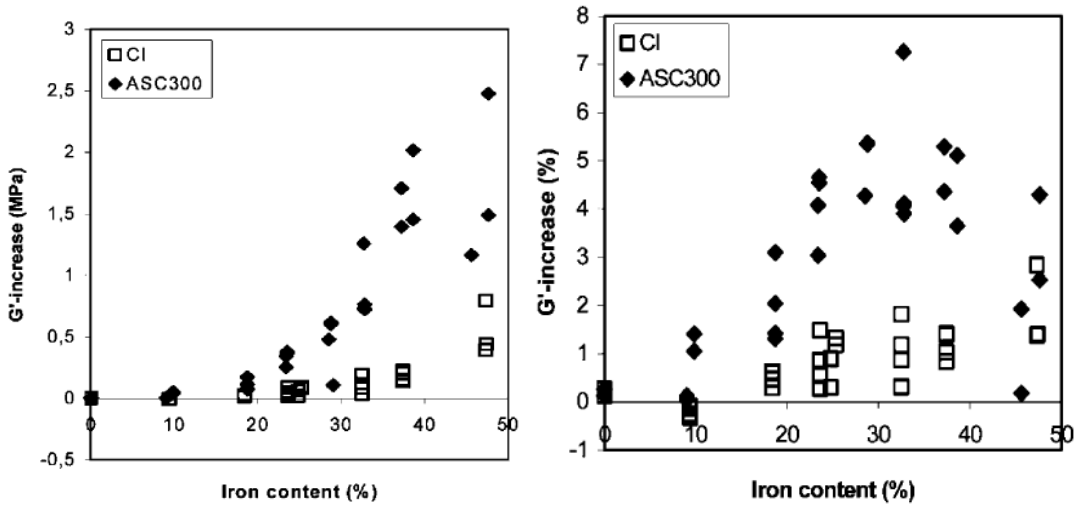


Figure 2. 2 The MR effect of Perbunan 3445 with ASC300 and carbonyl iron (CI), displayed in left as the absolute increase in shear modulus (in MPa), and in right as the relative increase in shear modulus (in vol%). [Lokander and Stenberg (2003)]

As show in Figure 2.2, the stiffening of the material caused by increased content of filler is larger than the increase in MR effect at high concentrations. MRE materials with high volume fractions of filler normally have large zero-field modulus. This means the MR effect of these material may be quite low. In conclusion, the ideal iron volume concentration is about 30 vol%, which can achieve the maximum modulus or stiffness of MRE [Eem et al. (2013), Koo et al. (2010)]. Wang et al. (2006) fabricated MRE based on carbonyl iron (CI) particles and various weight percentages of silicon rubber without magnetic field but γ-ray radiation. Scanning electron microscope (SEM) and differential scanning calorimetry (DSC) were applied to investigate the MR effect, mechanical properties of MREs and the rubber/magnetic particle interactions. Park et al. (2011) produced MRE specimen with siloxane polymer and iron, nickel, cobalt powder to investigate their vibration characteristics. The principle of natural frequency shifting with the change of stiffness was explained in their research.

The size of the filler particles also has significant influence on MRE materials' MR effect and other mechanical properties. Yang et al. (2013) used 10 wet% SiC (silicon carbide) particles with diameters of 0.06, 0.6, 6, and 60 μm to synthesize MRE samples to compare the shear storage modulus (as shown in Figure 2.3). This result showed that the storage modulus was depended on the size of the filler, this effect may become more obvious with increased the external magnetic field. Leong et al. (2016) reported the performance of the MREs made with

nano-sized magnetic particles. The results indicated both the rheological and viscoelastic properties of the material were enhanced by adding the nano-sized particles. Chen et al. (2016) developed a carbonyl iron powder surface modification method which can avoid the magnetic energy loss originating from the particle gaps. This surface modification can help to develop MRE with both good mechanical performance and high MR effect, meanwhile reduce the loss factor. Sapouna et al. (2017) examined both anisotropic and isotropic MRE made of extra-large iron particles (diameter < 220 μm). Their experimental results indicated that MRE with larger particles was slightly stiffer but had lower MR effect when comparing with the regular MREs at the same volume fraction conditions.

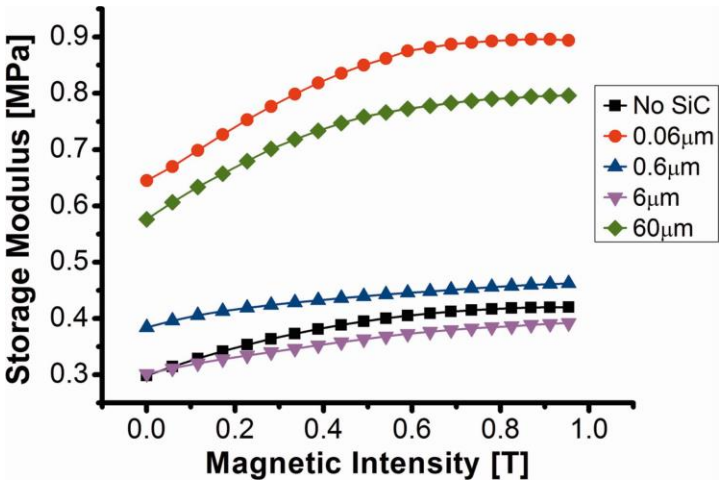


Figure 2. 3 The storage modulus of different diametric MRE samples. [Yang et al. (2013)]

Table 2. 2 Summary of the filler particles selected for MRE in previous researches

| Particles | Author and time |
|---|---|
| Carbonyl iron | Gong et al. (2005, 2012), Hu et al. (2005), Varga et al. (2005), Wang et al. (2006, 2007), Jiang et al. (2008), Boczkowska and Awietjan (2008, 2009, 2011), Wu et al. (2010), Fan et al. (2010, 2012, 2019), Wei et al. (2010), Chertovich et al. (2010), Lu et al. (2010, 2012), Zhang et al. (2010, 2011) , Sławiński et al. (2011), Wu et al. (2012), Dong et al. (2012), Fan et al. (2012), Xu et al. (2013), Yang et al. (2013), Hegde et al. (2014), Schubert and Harrison (2015), Gao and Wang (2016), Damiani and Sun (2016), Yunus et al. (2016), Bastola et al. (2017), Olabide and Elejabarrieta (2017), An et al. (2017), Aziz et al. (2018), Tang et al. (2018), Sun et al. (2018), Gavrilovici et al. |

| | |
|---|---|
| | (2019), Dargahi et al. (2019), Shabdin et al. (2019) |
| Iron particles | Lokander and Stenberg (2003), Stenberg et al. (2004), Lokander et al. (2004), Shen et al. (2004), Gong et al. (2005), Li et al. (2008), Böse and Röder (2009), Kaleta et al. (2011), Borin et al. (2012), Keinänen et al. (2007), Chen et al. (2007), Popp et al. (2010), Park et al. (2011), Kaleta et al. (2011, 2012), Królewicz et al. (2012, 2013), Kumbhar et al. (2013) |
| Cobalt (Co) particles | Song et al. (2009), Park et al. (2011) |
| Nickel (Ni) particles | Park et al. (2011) |

### 2.2.3 Additive

Additives are normally applied as a part of MRE ingredients to improve the mechanical performances of MRE. The common additives for MRE fabrication are reinforcing agent, vulcanizing agent, plasticizer, accelerator, age-resistor and crosslinking. The reinforcing agent such as carbon black [Fu et al. (2013)] may increase the shear strength of the rubber. The amount of reinforcing agent normally varies with the purpose and application. Stearic acid which act like lubricant can improve the rubber mechanism and increase the properties of magnetic particle [Chen et al. (2007)]. Other common additives used in MRE material fabrication are zinc oxide (ZnO) and sulphur [Lokander et al. (2004), Shen et al. (2004), Lokander and Stenberg (2003)]. ZnO normally acts as an activator, but for some particular matrix such as polychlorophene rubber, it works as vulcanizing agent. Antioxidant is used to reduce speed of the deterioration of MRE, the amount usually around 1-3 pphr.

Fan et al. (2010) selected maleic anhydride (MA) to modify the interfaces of the MREs based on cis-polybutadiene rubber and CI particles to improve the damping property. Their experiment results showed that the content of bound-rubber and the compatibility between the magnetic particles and rubber matrix were enhanced. Fan et al. (2012) fabricated samples with different cross-link densities and plasticizer contents to investigate the effect of cross-link density of the matrix on the controllable damping properties of cis-polybutadiene rubber and CI based MRE. Ge et al. (2013) fabricated a rosin glycerine ester/natural rubber mixed matrix based MREs to get high MR effects. This type of material had ideal MR effect and lower loss factor which can be applied to many fields such as adaptive tuned absorbers. Yang et al. (2013) developed a kind of SiC-strengthened MREs which had higher storage modulus, magneto-induced modulus, and damping property than traditional MREs.

### 2.2.4 Microstructure

The spatial distribution of the particles in the matrix can be either homogenous (isotropic) or chain-like columnar (anisotropic). Anisotropic MRE is normally fabricated with applying an external magnetic field during its curing process. It normally has a strictly directed particle orientation and become a uniform particle distribution as shown in Figure 2.4 (b), this is due to the magnetic field induced dipole interaction between these particles. The anisotropic structure of material is also preserved without a magnetic field because the particles are permanently embedded in the matrix material. It is worth noting that the stiffness of the MREs increases along with the same direction as the intensity of the applied magnetic field increases [Jung et al. (2009), Li et al. (2010)].

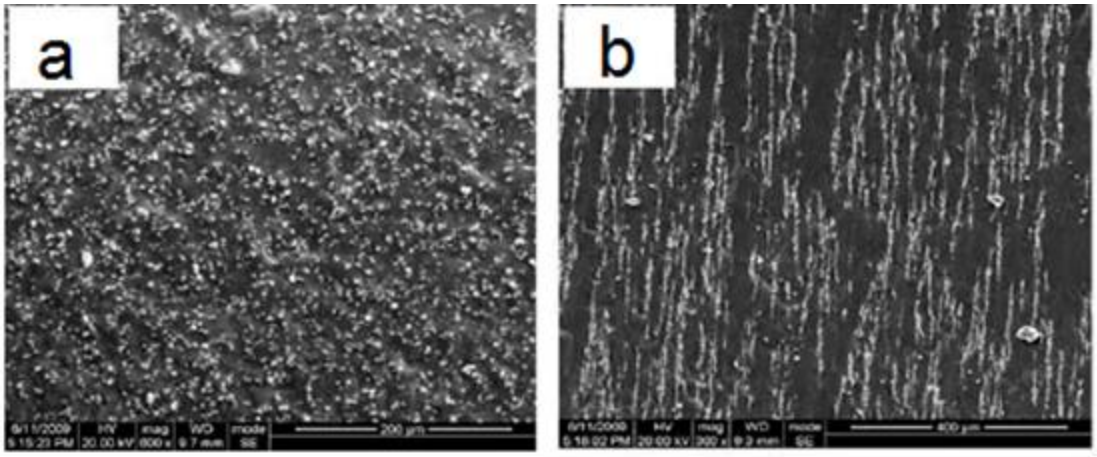


Figure 2. 4 SEM images of (a) isotropic MREs and (b) anisotropic MREs. [Wu et al. (2012)]

Gong et al. (2005) fabricated isotropic MRE under natural conditions with carbonyl iron (CI) particles, silicon rubber and silicone oil to investigate the effects of iron particles and additives on the MR effect and the relationship between microstructure and mechanical properties. Kaleta et al. (2011) examined the magneto mechanical properties of tefabloc-iron particles based MRE specimens with both isotropic and anisotropic structure. Lu et al. (2010) introduced styrene-ethylene-butylene-styrene (SEBS) into the traditional rubber matrix to prepare the thermoplastic CI filled MREs and studied the influence of temperature, holding time, magnetic field intensity and CI concentration on the properties of specimens. Królewicz et al. (2012) presented the manufacturing process of magnetically polarized (anisotropic) MRE. Téfabloc was selected as a thermoplastic matrix to mix up with iron particles. Kaleta et al. (2012) tested the MRE material samples with cyclic shearing at a constant frequency of 1 Hz. Samples with polarized (anisotropic) particle alignments were fabricated. The tested material was modelled

with a simple viscoelastic model. Gong et al. (2012) studied the influences of mass ratios, magnetic field, and temperature on the dynamic mechanical properties. The tensile strength, the modulus, and the MR effect were also evaluated in their research. The influence on material loss factors are shown in Figure 2.5 and Figure 2.6.

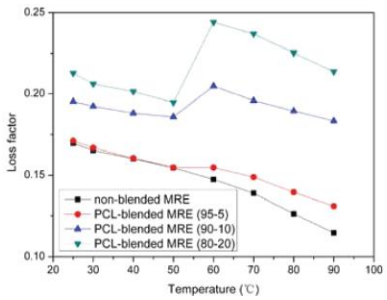


Figure 2. 5 Loss factors of MRE samples under different temperatures. [Gong et al. (2012)]

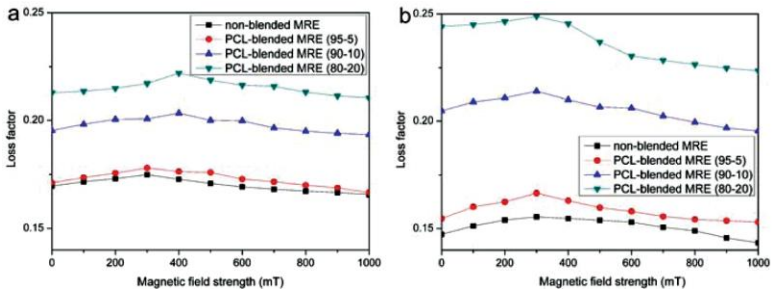


Figure 2. 6 Loss factors of MRE samples under different magnetic field strengths: (a) testing at 25 °C; (b) testing at 60 °C. [Gong et al. (2012)]

Gao and Wang (2016) investigated the steady-shear behaviors of MR elastomer composites with different volume fractions of ferromagnetic particles. Bastola et al. (2017) developed a novel MR hybrid elastomer by using 3D printing method. Their research showed that the 3D printing technique was feasible for fabrication of MREs with controlled microstructures including magnetic particles/MR fluid. Sapouna et al. (2017) combined isotropic and anisotropic MREs in parallel and series configurations. This type of new MRE materials appeared to have higher tangent of the loss angle than isotropic ones, but lower stiffness than anisotropic ones.

## 2.3 Physical phenomena of MRE

### 2.3.1 MR effect

The MR effect is the fraction of the magnetic-induced value to the non-magnetized condition value of the related parameter. The MRE normally works in the linear viscoelastic region with small deformations. Rheological properties of MRE can be changed by varying the external magnetic field as shown in Figure 2.7.

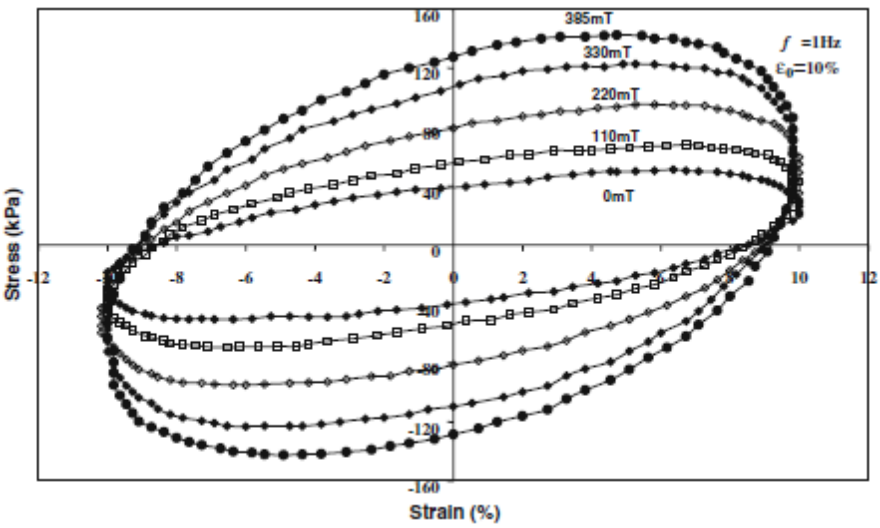


Figure 2. 7 Stress–strain relationships with various magnetic fields. [Li et al. (2010)]

The field-dependent modulus of the material can be controlled continuously, rapidly and reversibly in the pre-yield regime through adjusting the external magnetic field. The MR effect is defined by equation as follow:

$$\mathbf{G_{MR\ effect}} = \frac{\mathbf{G_{Max} - G_0}}{\mathbf{G_0}} \times \mathbf{100}\% \qquad (2.1)$$

where, $\mathbf{G_{Max}}$ is the maximum modulus (also the storage modulus when the particles are at magnetic saturation), $\mathbf{G_0}$ is the initial modulus when the magnetic flux density is 0 mT. The magnetic force between magnetisable particles is main effect to the modulus of MRE. The stiffness of MRE material is dependent on the number of particle chains per unit cross section. After applying an external magnetic field, the ferromagnetic particles will be magnetised and interact with surrounding particles. This can effectively increase the stiffness of particle chains. In most cases, the stiffness of anisotropic MREs seemed to be more sensitive to magnetic field and thus the MR effect for anisotropic MREs was slightly larger than isotropic ones in most cases [Böse and Röder (2009)]. Technically, the MR effect can be treated as the theory of a temporary reinforcement method for this material. Normally, the MR effects increased with the increment of magnetic particles content, and MREs with vertically aligned particles usually achieved higher MR effects as shown in Figure 2.8 [Schubert and Harrison (2015)].

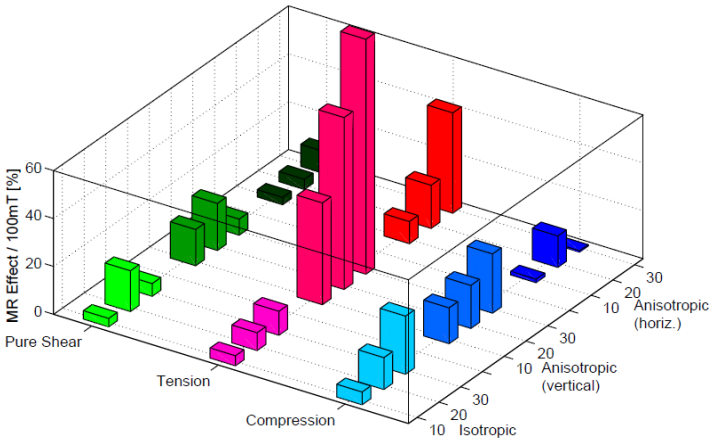


Figure 2. 8 Comparison of relative MR response for all deformation modes, and all types of MREs with particle concentrations from 10 vol% to 30 vol%. [Schubert and Harrison (2015)]

The magnetically induced deformations are related to the applied magnetic field. The deformation of anisotropic MRE under applied magnetic field is smaller than that of isotropic MRE with the same volume fraction. This is due to the fact that anisotropic MRE is stiffer than isotropic MRE in the chain direction. The test results [Kaleta et al. (2011)] in Figure 2.9 have shown that the MR effect was slightly larger for the anisotropic samples in most cases. The stiffness of MREs increased as the intensity of the applied magnetic field increased [Jung et al. (2009), Li et al. (2010)] and the maximum MR effect can be achieved when the iron particle volume fraction was about 30 vol% [Lokander and Stenberg (2003), Eem et al. (2013)].

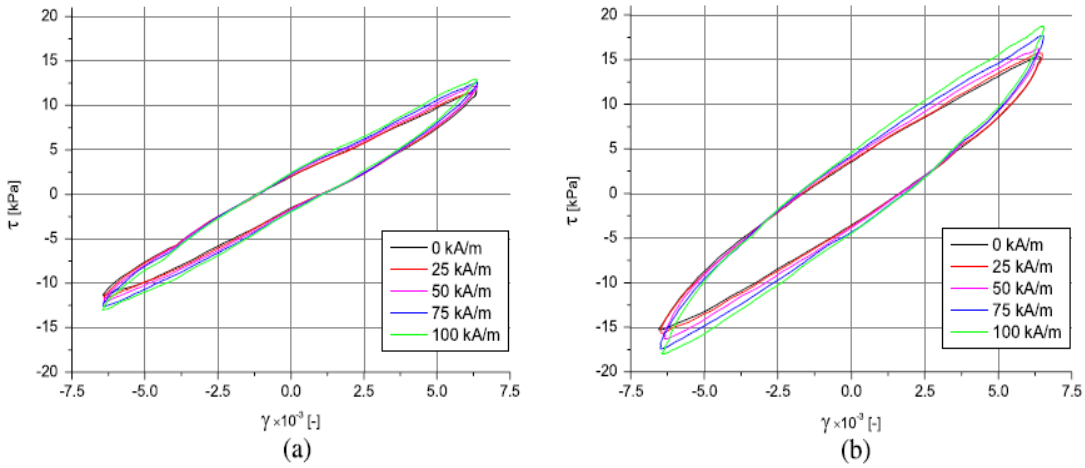


Figure 2. 9 Hysteresis loops of (a) isotropic and (b) anisotropic samples for various magnetic field strength values. Minimum strain amplitude $\gamma_a = 6.25 \times 10^{-3}$. [Kaleta et al. (2011)]

### 2.3.2 Mullins effect

The Mullins effect (as shown in Figure 2.10) is a particular mechanical response in filled

rubbers of which the stress–strain curve depends on the maximum loading previously encountered. This behaviour can be idealized as an instantaneous and irreversible softening of the stress–strain curve. Nonlinear elastic behaviour appears when the load is less than maximum value. The main features of the Mullins softening can be characterized as follows: The stress strain curve of a virgin material (previously undeformed) follows the virgin loading curve. The stress softening occurs in the first unloading curve and the subsequent loading curve is close to the first unloading curve unless the strain exceeds the previous maximum strain. After a few number of cycles (up to ten cycles in the literature depending on the material nature), the material responses coincide during the successive cycles. If the subsequently loading is beyond the previous maximum strain, the loading curve follows the path of virgin loading [Ogden and Roxburgh (1999), Diani et al. (2009), Mai et al. (2017)].

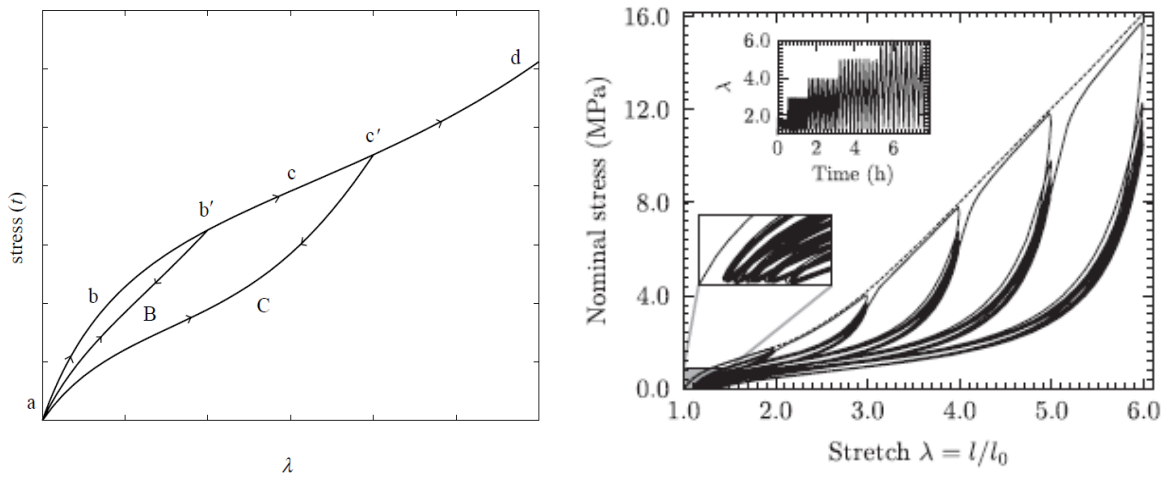


(a) (b)

Figure 2. 10 Schematic representation of the Mullins effect: (a) loading-unloading curves in simple tension (λ is stretch) [Ogden and Roxburgh (1999)]; and (b) stress-stretch response of a filled rubber under cyclic uniaxial conditions. [Merckel et al. (2012)]

If the material left unloaded for a long period, the material will recover part of its original stiffness. This recovery procedure usually takes more than 24 hours and can be speed up by heating the material for a certain time. However, some materials never recover to their original state completely depending on the strain they experienced. Normally, the material will become softer under loading cycles until the composite comes to a stable point after certain number of cycles [Lion et al. (1996)].

MREs are generally regarded as a class of rubber-like materials filled with micron sized magnetic particles. Therefore, the Mullins softening phenomena of MREs in the absence of

magnetic field is similar to that of filled rubbers. Under external magnetic field, the Mullins effect of MREs becomes larger because the stretch results in high local stresses in the gap area between two adjacent magnetic particles and favours the detachment of the polymer from the particles through a debonding process [Coquelle and Bossis (2006)]. In order to investigate the Mullins phenomenon of magnetoactive elastomers (MAEs) in the presence of a magnetic field, Shariff and Bustamante (2016) proposed a phenomenological model based on the direction-dependent damage parameters and a set of spectral invariants. The influence of the external magnetic field on the Mullins of MAEs under simple tension and simple shear was discussed. The Mullins softening phenomena of MREs in the absence of magnetic field is similar to that of particle filled rubbers. Under external magnetic field, the Mullins effect of MREs becomes larger.

### 2.3.3 Payne effect

The Payne effect is a particular feature of the nonlinear stress-strain behaviour of filled rubbers subjected to cyclic loading within small strain. One of the typical features of this behaviour is the dynamic moduli are dependent on the applied strain amplitude. The storage modulus decreases significantly and the loss modulus shows a more or less pronounced maximum with increasing strain amplitude [Rendek and Lion (2010), Pan and Zhong (2017)]. When the applied strain amplitude is sufficiently small, it can be considered that both storage modulus and loss modulus are weakly dependent on the strain amplitude and can be described by using linear viscoelastic model. This strain amplitude dependence of dynamic moduli is usually interpreted as a dynamic state of equilibrium between breakage and recovery of physical bonds linking adjacent filler clusters. A phenomenological model was proposed by Kraus (1984) to describe the strain amplitude dependence of the dynamic moduli [Lion et al. (2003), Clément et al. (2005), Luo et al. (2010)].

For MRE material, the Payne effect significantly increased in the presence of an external magnetic field and varied with the cyclic loading which reached saturation after several cycles [Sorokin et al. (2014)]. Additionally, anisotropic MRE has a more pronounced Payne effect than isotropic MRE. As Figure 2.11 shown, the storage modulus monotonically decreases while the loss modulus first increases and then decreases with increasing strain amplitude. The cyclic increasing-decreasing strain amplitude in the constant external magnetic field leads to an increment in both dynamic moduli [Sorokin et al. (2017)]. Yu et al. (2017) investigated the magnetic-induced Payne effect of the MRE by experiments and a modified Maier and Goritz

model. The results showed that that the Payne effect increased with increasing magnetic flux density and can be reduced by improving the interfacial interactions between magnetic particle and elastomeric matrix.

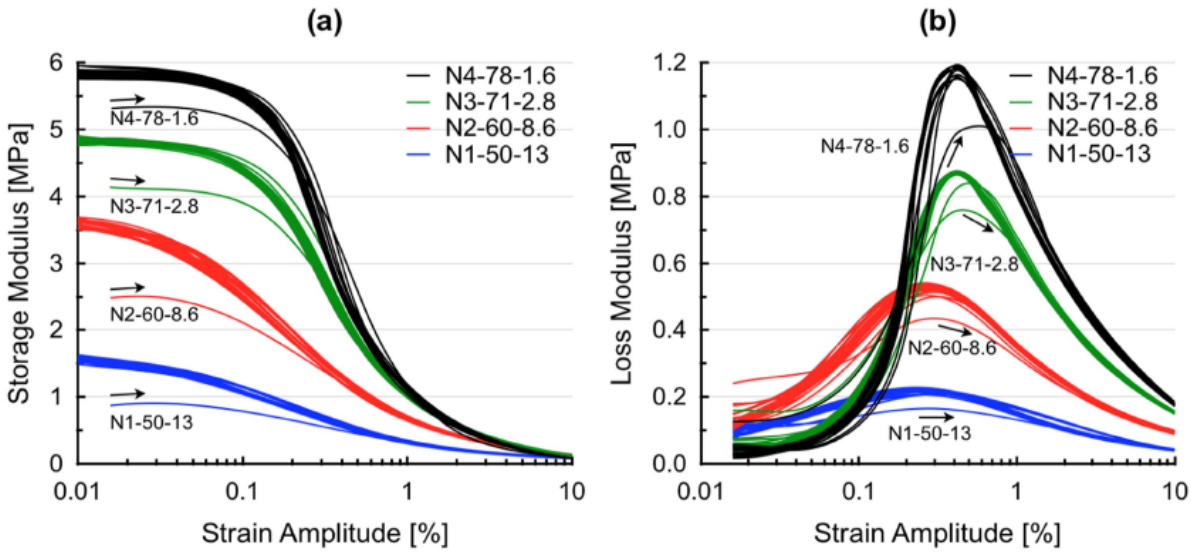


Figure 2. 11 Storage modulus (a) and loss modulus (b) versus increasing–decreasing strain amplitude in a maximum magnetic field of 600 mT. Initial curves are indicated by arrows. [Sorokin et al. (2017)]

Recently, a series of experiments were performed to investigate the strain dependence of dynamic moduli of MREs under different magnetic fields. The linear viscoelastic limit of MREs in presence of magnetic field is determined [Watanabe et al. (2018), Qi et al. (2018), Aziz et al. (2018)]. Various phenomenological models were proposed based on the Kraus model [Suo et al. (2018), Xin et al. (2016)] and the Maier-Goritz model [Yu et al. (2017)] to describe the strain amplitude and frequency dependent shear moduli of MREs. The good agreement was found between the experiment data and predicted results.

## 2.4 Dependent properties of MREs

### 2.4.1 Magnetic field dependence

The dynamic modulus of MREs is influenced by the magnetic force between the filler particles inside the matrix material. The filler particles are magnetized and start to interact with the surrounding particles while applying the external magnetic field to MREs [Chen et al. (2007)]. Magnetic flux density is one of the most important factors which can affect the magnetic force. The magnetic force increased with the risen magnetic field and so is the stiffness of MREs.

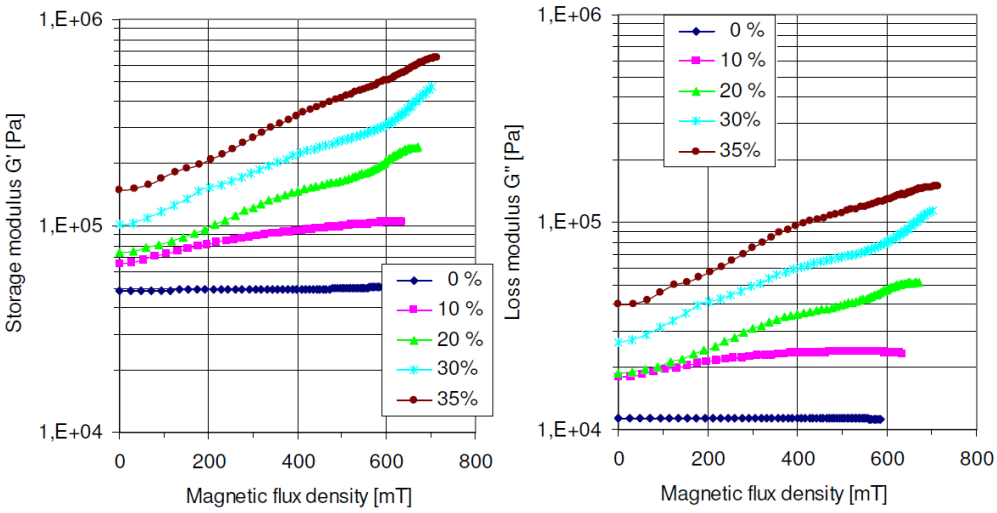


Figure 2. 12 Dependence of storage modulus (left) and loss modulus (right) of isotropic MRE with different concentrations of small iron particles (in vol%) in silicone on the magnetic flux density. [Böse and Röder (2009)]

As shown in Figure 2.12, the storage and loss moduli of MRE with various contents of iron particles increased with rising magnetic flux density. When the saturation occurs, the magnetization of each particle will remain constant and the magnetic force between the particles does not change much with the applied field [Huber et al. (2005)]. Additionally, the stiffness of anisotropic MREs seems to be more sensitive to the external magnetic field and thus the MR effect for anisotropic MREs is greater than isotropic ones [Böse and Röder (2009)]. However, it is necessary to notice that according to the exact particle distribution, there may be some areas inside the material has higher local magnetic forces than the rest. Therefore, both damping factor and stiffness may stay at constant value or even decrease while reach the magnetic saturation of the filler particles. This value is mainly dependent on the type and the size of selected particles but usually around 800 mT. However, for normal industry applications, it is difficult to generate magnetic fields over 800 mT. Thus, any device where MRE material is applied should be designed to work below this value. According to published MRE experiment data, it can be concluded that the stiffness of the material increase significantly with the increment of external magnetic field. But for the damping factor, it only changes slightly depending on the selected matrix and the type of the mechanical test. It can be assumed that the damping factor is not mainly affected by the external magnetic field.

### 2.4.2 Strain amplitude and frequency dependence

The MR effect of MRE materials also depends on the applied strain amplitude and applied exciting frequency due to the magnetic forces are dependent on the distance between the dipole particles. According to existing research results, the dynamic modulus of elastomer is a function of the amplitude of the applied strain and thus the material is described as nonlinear. However, the strain-stress curves for rubber and rubber-like material are not perfect ellipses but deformed depending on the loading amplitude. The effective modulus and damping factor can be considered as linear only at very low strain amplitudes to simplify the calculation.

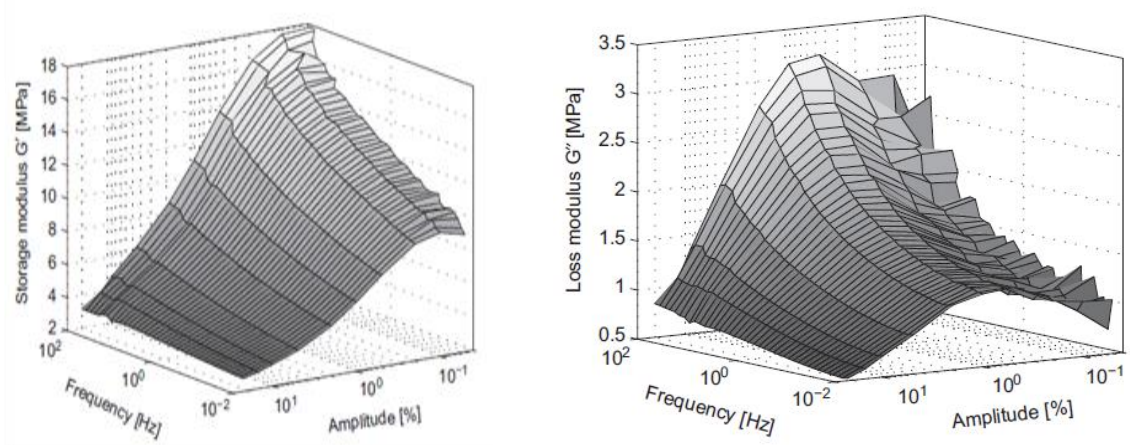


Figure 2. 13 Storage modulus and loss modulus as a function of amplitude and frequency. [Li and Su (2011)]

According to Li and Sun (2011) experiment result, the storage modulus and the loss factor changed with the strain amplitude and exciting frequency are shown in Figure 2.13. The maximum value of MR effect can be obtained at relatively small strain amplitudes. This is due to the strongest interaction between the particles occurs at this moment. Normally, the MR effect decreases obviously with the increment of strain amplitude. This is caused by the particle chains subjected to external load start to yield the MR effect will diminish. There are strain limitations exist, above which the stress reaches a saturation and starts to decrease steadily.

### 2.4.3 Temperature dependence

The environment temperature normally has a significant influence on rubber and rubber-like materials. When temperature is decreased, the thermal motion of the molecules is reduced and the material appears to be stiffer. At particular low temperature, the motion of the molecules almost stopped which made the material behave more like glass than elastomer with large

dynamic modulus. This temperature is usually referred to the material's glass transition temperature. Zhang et al. (2011) carried out the experimental research of MRE samples to investigate their steady-state and dynamic properties under different temperature conditions. The MRE samples in their research were fabricated with mixed rubber matrices (cis-polybutadiene rubber and natural rubber) and in different mass ratios. The results revealed that storage modulus and loss modulus of samples, which contained only cis-polybutadiene rubber, decreased linearly with the temperature increment. This behaviour is quite different from the samples which only contained natural rubber (as shown in Figure 2.14).

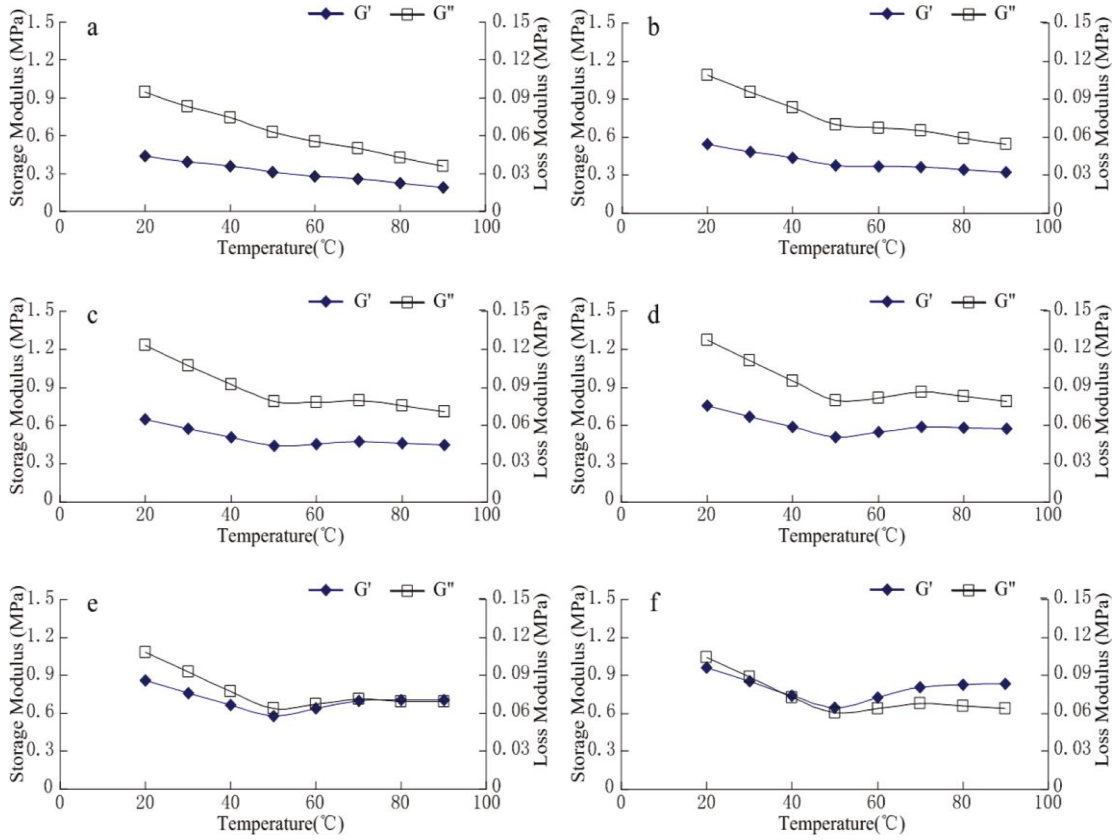


Figure 2. 14 Temperature-dependent storage modulus of samples with different ratios of cis-polybutadiene rubber and natural rubber at 800 mT: (a) 100:0, (b) 80:20, (c) 60:40, (d) 40:60, (e) 20:80, and (f) 0:100. [Zhang et al. (2011)]

The dynamic modulus of the samples which contained more natural rubber showed different characteristic, and the relationships between stress and strain also exhibited different characteristics with different matrix. A constitutive equation was developed to predict the trend of properties of MRE at different temperatures. However, this model only works on the material parameters which can be easily measured in experiments. Yu et al. (2016) performed the experiments of the temperature effects on MRE samples in shear mode and laminated MRE

isolator in the running process. It was found that the shear storage modulus and shear loss modulus of MRE samples increased with increasing magnetic flux densities and decreased with rising temperature nonlinearly. The internal temperature of the MRE isolator was increased due to the heating of the electromagnetic coil when current was passed through it. The resonant frequency, stiffness and damping of the MRE isolator were mainly influenced by the internal temperature and the excitation current.

## 2.5 Modelling of MRE

### 2.5.1 Phenomenological models

The complex magneto-mechanical coupled behaviour of MREs makes the modelling process become a difficult task. The distribution of microstructure has great influence on the dynamic performance of MREs. The experimental research has shown that the MREs still reveal linear viscoelastic properties when the strain amplitude was below 10%, indicating the curve of input strain and response stress can be simplified as elliptical loops [Li et al. (2010)]. Enhance, the dynamic response of MRE under harmonic load with small amplitude can be described well by linear models. When a sinusoidal load is applied to MRE material, the material does not respond instantaneously but the resulting stress will be lagging the input by an angle which named loss angle. The modulus of elasticity is considered to be a complex modulus $M^*$ which consists of a real elastic element and an imaginary viscous element to represent this situation mathematically.

$$M^* = M' + iM'' \tag{5.2}$$

where, the complex modulus $M^*$ can be either shear modulus or Young's modulus. The storage modulus $M'$ indicates the ability of viscoelastic material to store the energy due to deformation, which contributes to the material stiffness. The loss modulus $M''$ represents the ability of viscoelastic material to dissipate the energy of deformation.

The magnitude of complex modulus $M^*$ can be calculated by the slope of the line from the maximum strain to the minimum strain. It is defined as:

$$|M^*| = \sqrt{M'^2 + M''^2} \tag{5.3}$$

The ratio between the loss module and storage module is another widely used term to present the property of viscoelastic material:

$$\tan\varphi = \frac{M''}{M'} \tag{5.4}$$

where, $\tan\varphi$ is called the loss factor, which can be used for describing the efficiency of damping caused by the viscoelastic material. The loss angle $\varphi$ is relevant to the energy dissipation per volume within an oscillatory cycle, which is the area enclosed by the hysteresis loop.

It needs to be noticed that the dynamic modulus of filled rubbers is always higher than the modulus determined by static loading conditions due to the dynamic load. There are several linear viscoelastic models have been developed to process the stiffness and damping capability of MRE, among which the Kelvin-Voigt model is the simplest one (as shown in Figure 2.15).

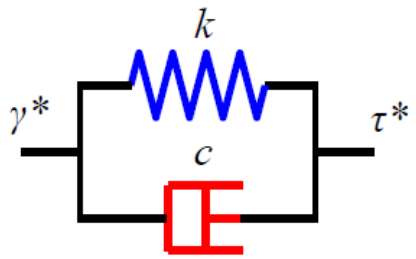


Figure 2. 15 Kelvin-Voigt model for MRE ($\gamma^*$ is input strain and $\tau^*$ is response stress)

This model is widely used in designing vibration control systems where both stiffness and damping can be considered nonlinear with strain or frequency when necessary. For MRE material, the mechanical properties are strain, frequency and magnetic field dependent while the equations predicting the manner of the dependence are derived directly from the experiment data. However, interfacial slippages also occur between the matrix and particles. As a result, the relationship between applied strain amplitude and the response stress is nonlinear. Most of previous researches were focused on the linearity. When it comes to some theoretical problems due to the nonlinearity of MRE is quite important.

Chen and Jerrams (2011) developed a rheological model (as shown in Figure 2.16) to simulate the dynamic behaviour of MRE. It modelled the viscoelasticity of the MRE material, magnetic field induced properties, and interfacial slippage between the matrix and particles. This model can be used to predict the dynamic behaviour of MREs with various volume fractions of particles and matrix materials.

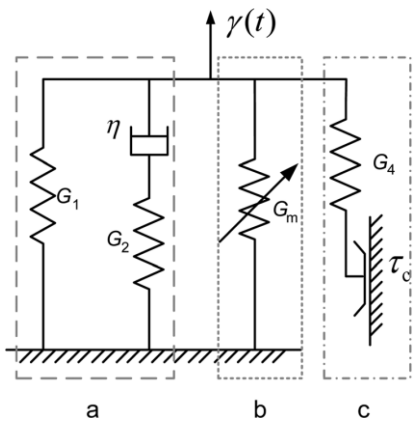


Figure 2. 16 A rheological model for examining dynamic properties of MREs comprising three components to simulate (a) the viscoelasticity of the polymer composite, (b) the magnetic-field-induced mechanical properties, and (c) interfacial slippage between the matrix and the particles. [Chen and Jerrams (2011)]

Yang et al. (2013) proposed a phenomenological model for MRE isolator as shown in Figure 2.17 which incorporated a Bouc–Wen component to reproduce hysteresis loops in parallel with a Kelvin–Voigt element describing solid-material behaviours.

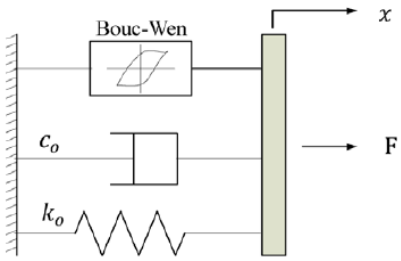


Figure 2. 17 Schematic diagram of the MRE model. [Yang et al. (2013)]

The Bouc–Wen component described by the evolutionary variable was applied to represent the function of the time history of displacement. Due to its mathematical simplicity and ability to represent a large class of hysteretic behaviours, it was widely accepted in structural engineering to describe the MR behaviour.

Daniel et al. (2014) improved their previous model in order to consider the hysteresis effect. This irreversible model was fully multiaxial and allowed the description of typical hysteresis, butterfly loops and the calculation of magnetic losses as a function of magneto-mechanical loadings. Figure 2.18 provides the modelling process of the material.

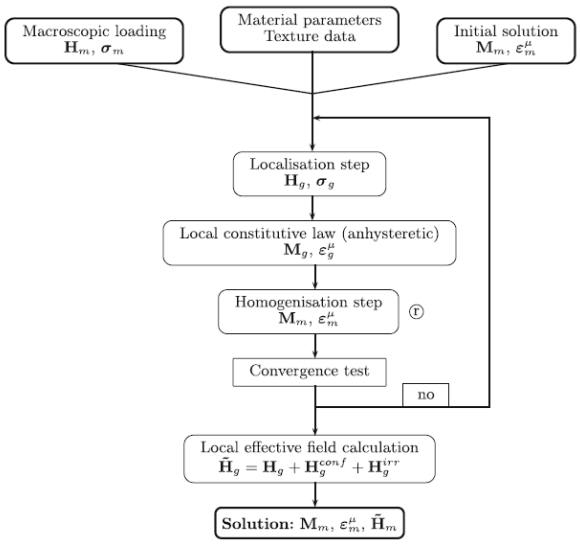


Figure 2. 18 Calculation principles. [Daniel et al. (2014)]

Li et al. (2015) assumed that magnetic particles were organized in layer with applied magnetic field, and MREs were kind of anisotropic materials which stack the reinforced layers and matrix layers together (as shown in Figure 2.19). The Mori-Tanaka method was used to build the theoretical model to investigate the zero-field modulus of anisotropic MRE material.

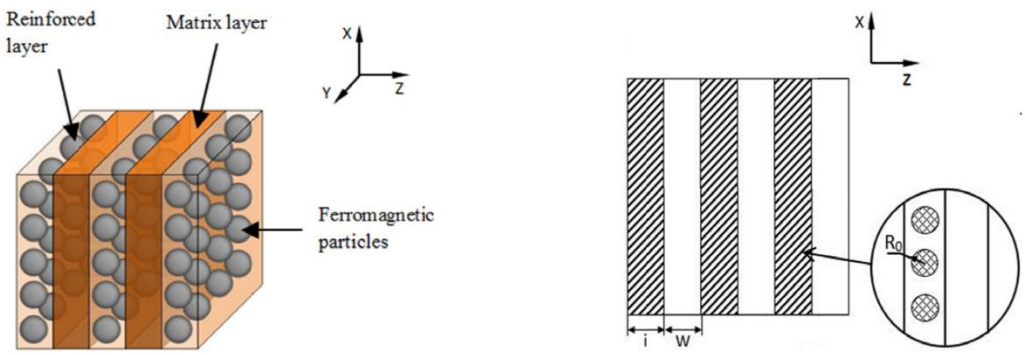


Overall view Cross-sectional view

Figure 2. 19 Layer-like unit cell. [Li et al. (2015)]

### 2.5.2 Micromechanical models

Several theoretical models have been proposed to describe the MR behaviour of MRE. Davis (1999) first assumed that the particles formed an infinite chain in the matrix. The saturated field-induced shear modulus was calculated by:

$$G = \frac{3\emptyset\mu_0 M_s^2 d^3}{5h^3} \tag{5.5}$$

where, $M_s$ was the saturation magnetization and d were the diameter of the particle.

Borcea and Bruno (2001) set up a model that took the fully coupled magneto-elastic interactions into account. The calculations assumed that the ferromagnetic particles were uniformly magnetized. The distribution of the magnetization inside the composite material was calculated according to the basic minimum energy principle of magneto-elasticity. Shen et al. (2004) developed a quasi-static model which also involved the effect of magnetic field and presented the nonlinear stress–strain relationship of the MRE material. In their model, the dipole interactions caused by all the dipoles in a chain were considered. The accuracy of their model was improved when comparing with the previous models which only considered two nearby dipole interactions. Chen et al. (2007) proposed a finite-column model to calculate the field induced shear modulus from the observation of microstructures. The field-induced shear modulus can be expressed as:

$$G = \frac{(\mu_{\parallel} - \mu_{\perp})H_0^2 \sin\gamma \cos\gamma}{\gamma} \tag{5.6}$$

where, $\gamma$ was the shear strain, $H_0$ was the applied magnetic field strength, $\mu_{\parallel}$ was the permeability of the block parallel to the column axes and $\mu_{\perp}$ was the permeability of the block perpendicular to the column axes.

Linnemann and Klinkel (2006) presented a 3D macroscopic constitutive law for hysteresis effects in magnetostrictive materials based on the thermodynamically consistent model. An additive decomposition of the magnetic and the strain field in a reversible and an irreversible part were implemented in FEM. A numerical example demonstrated the capability of the proposed model to reproduce the ferromagnetic hysteresis loops of a Terfenol-D sample. Daniel and Galopin (2008) presented a multiscale model of hysteretic magneto-elastic behaviour based on a statistical energetic description of the domain microstructure evolution. This method was applied to predict the magneto-elastic behaviour of Terfenol-D single crystal and polycrystalline samples respectively and compared with experiment data. Daniel et al. (2008) proposed a multiscale approach (as shown in Figure 2.20) to modelling the reversible magneto-elastic behaviour of ferromagnetic materials which approached standards between macroscopic phenomenological modelling and micro-magnetic simulations. This multiscale model can be described as a simplified micro-magnetic model. The first scale was the magnetic domains scale, which the magnetization can be considered as homogeneous. The second scale was the single crystal scale where elastic properties were homogeneous. The last scale was the representative volume element (RVE) scale, which was large enough to define the average material behaviour and properties.

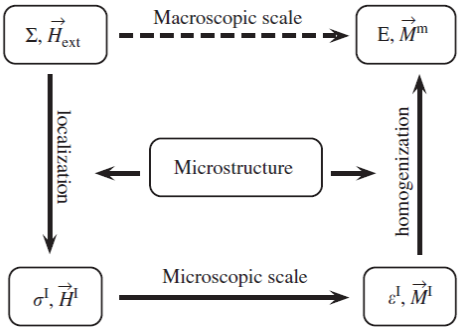


Figure 2. 20 Multiscale approach—principle. [Daniel et al. (2008)]

This model was applied to predict the magnetic behaviour, elastic behaviour and magnetostrictive behaviour. The influence of multiaxial stress state on both the magnetization and the magnetostrictive behaviour were taken into consideration. The main disadvantages of the model were that the magnetic and mechanical fields were considered as homogeneous within a single crystal and the domain walls were not taken into account which led to an increase of energy due to exchange energy contribution. The last limitation was that the domain configuration was only seen through volumetric fractions, which was insufficient when considering the importance of the domains distribution on the local demagnetizing fields. Li et al. (2010) presented an effective permeability model which took the magnetic saturation and the magnetic energy of MREs into consideration to predict the mechanical performances of MREs with complex structures. Melenev et al. (2011) carried out experimental investigation on the mechanical properties of soft magnetic elastomer samples subjected to cyclic uniaxial loading. The residual strain was observed when the external field was present and it disappeared as long as the external field switching-off. A phenomenological model was proposed based on the observation and discussion of experiment to describe the field-induced plasticity of soft magnetic elastomer composites under an external field. Keip and Rambausek (2016) also used the multiscale method to investigate the MRE characterization. On the microscopic scale, the governing equations were solved by the RVE of the material with a coupled large-strain finite element (FE) formulation. A FE scheme based on the same set of variables along with the large-strain continuum formulation was applied for macroscopic scale study.

Jolly et al. (1996) proposed a quasi-static model based on the magnetic dipole interactions between two adjacent particles within a chain to investigate the mechanical and magnetic properties of MR materials as shown in Figure 2.21. The effect of magnetic interactions apart from those between two adjacent particles of the chain was also considered by adjusting the

model parameter which determined by comparing the theoretical results with the experimental data. The calibrated model provided a good agreement with published experimental study results and was capable of predicting both the magnetic and mechanical properties of MR materials, including magnetic induction curves and field dependent yield stress for MRF, field induced change in modulus for MRE. It should be noted that there was a small mistake in the expression of $J_p = |m|V_i$ and the correct form should be $J_p = \frac{|m|}{V_i}$.

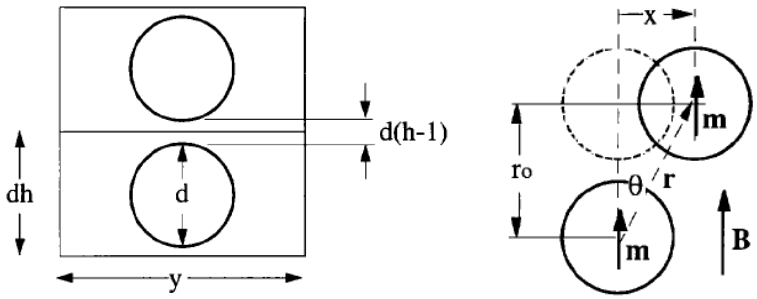


(a) Geometry (b) Magnetic interaction

Figure 2. 21 The single-chain model of two adjacent magnetic particles. [Jolly et al. (1996)]

Zhu et al. (2006) presented a multi-chain model to predict the magnetic-induced shear modulus of MRE by taking the derivative of the magnetic energy density with respect to shear strain as shown in Figure 2.22. The influences of particles in the same chain and the particles in all adjacent chains on the shear modulus of MRE can be calculated by using the multi-chain model. The obtained results showed that the single dipole model overestimated the magnetic-induced shear modulus of the MRE. The smaller the ratio of the distance between adjacent chains to the distance between adjacent particles in the same chain was, the bigger the difference between the multi-chain model and the single-chain model was. The comparative calculations were performed between chain-like structure and columnar structure containing body-centered tetragonal (BCT) cells. From the point of increasing the magnetic-induced shear modulus, the performance of chain-like structure was better when the particle volume fraction was low, and the performance of the columnar structure with BCT cells was better when the particle volume fraction was large.

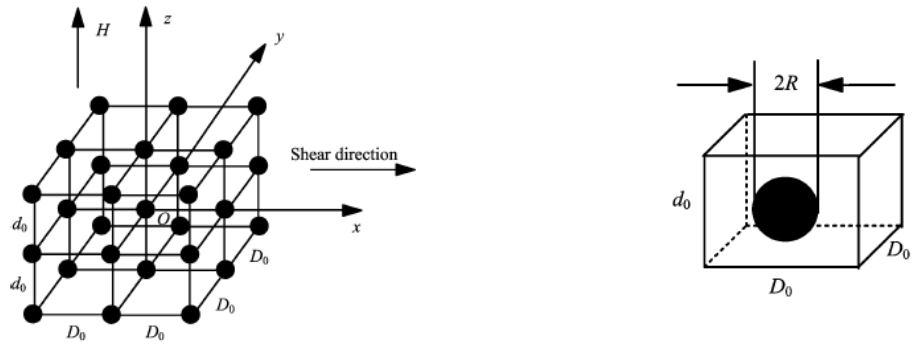


(a) Schematic model (b) Unit cell

Figure 2. 22 The multi-chain model of the magnetic particles. [Zhu et al. (2006)]

Zhang et al. (2008) presented an effective permeability model to predict the field-induced modulus of MRE with complex structure and components. The effects of the nano-particles additives around micron-particles and the particle's saturation were taken into account. In order to verify the proposed model, MRE samples was designed in which the iron particles were coated with magnetisable soft shell composed of nano-size ferrite particles and polymer gel. The calculation results showed this type of MRE had the much larger field-dependent shear modulus than that of conventional MRE and can only slightly increase the zero-field shear modulus. Zhang et al. (2008) carried out theoretical and experimental investigations on the field-dependent mechanical properties of the patterned MREs with uniform lattice and body centered cubic (BCC) structures. A quasi-static model was proposed by taking account the effects of both the local magnetic field and the dipole interaction magnetic energy of all the particles inside the patterned MRE. These MREs samples were manufactured by precisely positioning magnetic iron particles in the polydimethylsiloxane (PDMS) matrix. The shear modulus and the stress-strain curves of the patterned MREs samples with low particle volume fraction were recorded at different external magnetic field intensities. The good agreements were observed between prediction results and experimental data. The obtained results showed that the effects of interactions between different particle chains on the shear modulus of the lattice patterned MRE was too small to be neglected while on the shear modulus of the BCC patterned MRE was large enough to be considered. Zhang et al. (2010) proposed a Gaussian distribution model to calculate the field-induced shear modulus of anisotropic MRE with body-centered tetragonal (BCT) structures. The column length of the BCT structures was assumed to follow the Gaussian distribution. The nonlinearity and saturation of particle magnetization was considered in the model. The comparative calculations were performed between the proposed model and existing model as well as the published experiment data. The obtained

results showed that their distribution of the column length had significant effect on MRE material's shear modulus. The shear modulus increased with the increment of the mean value and decrement of standard variance of the Gaussian distribution. The column width had a slight influence on the field-induced modulus, the thin columns can result in slightly higher MR effect than the thick ones. Miedzińska et al. (2010) described how to use the n-body simulation model to predict the interactions between iron particles (dipoles) and the motion of the particles in the liquid elastomer under an applied magnetic field. The three forces vectors: magnetic, gravity, viscosity and uplift pressure were considered for each two dipoles in the numerical simulation of the MRE microstructure forming process. Ivaneyko et al. (2012) derived a mechanical model based on the free energy of the deformed MREs with isotropic distribution of the magnetic particles in an external magnetic field. Three different isotropic spatial distributions of magnetic particles including simple cubic, body-centered cubic and hexagonal close-packed lattices were considered in the present model by extending their previous research work [Ivaneyko et al. (2011)] which only took account for simple cubic lattice. The calculation results showed that the magneto-mechanical behaviour of MREs was very sensitive to the spatial distribution of the magnetic particles. The Young's modulus of MREs with simple cubic and body-centered cubic lattices decreased when increasing the external magnetic field. However, for MREs with hexagonal close-packed lattice, their Young's modulus increased when increasing the external magnetic field. The MREs with simple cubic and hexagonal close-packed lattices exhibited contraction while the MRE with body-centered cubic lattice exhibited expansion along the direction of external magnetic field. Based on Li's work, a micromechanical model was proposed by Chen et al. (2016) to investigate the tensile modulus of anisotropic MRE. This model was incorporated with the macroscopic constitutive laws which derived from the equivalent effective medium theory. A three-parameter representative volume element (RVE) was applied to describe the microscopic structure of the MRE material. Their research showed that the field response effect of tensile modulus was affected by the magneto-induced stress, magneto-induced spatial structure, and far-field strain. The simulation results also indicated that there was an optimal particles volume fraction for structured MRE with the largest changing rate of tensile modulus in one direction.

## 2.6 Applications of MRE

The applications of MR materials have been commercialization and industrialization, including varies of fields such as automotive industry like earthquake resistance and vibration control.

This is due to the MR materials dynamic yield stress can be controlled continuously, rapidly and reversely according to the applied magnetic field. The main difference between MREs and MRFs was that the MR effect of MREs is the field-dependent modulus with in pre-yield regime, while the MR effect of MRFs is the field-dependent yield stress with in the post-yield region [Jung et al. (2003)]. MREs are promising for many applications, including adaptive tuned vibration absorbers, stiffness tuneable mounts and suspension, variable impedance surfaces [Deng et al. (2006), Ginder et al. (1999), Carlson and Jolly (2000), Zhang et al. (2009), and Li et al. (2009)].

The mechanism of vibration control system based on MRE material is its elastic modulus can be changed by external magnetic field enhancement to change the natural frequency of dynamic system. Therefore, the vibration response is reduced at low frequencies where active control method is usually applied. On the other hand, passive control method is not so suitable due to its incapability to adjust with the external environment very well. As the active control system need a lot of additional power supply while operating, it is necessary to develop an adaptive-passive control system combined the advantages of both passive and active control systems. This type of system can be considered as passive system with changeable dynamical factors such as mass, damping property, and stiffness.

### 2.6.1 MRE absorbers

Deng and Gong (2008) developed an adaptive tuned vibration absorber (ATVA) based on unique characteristics of MRE with controllable shear modulus as shown in Figure 2.23. The theoretical and experimental results both indicated their ATVA had the capability of frequency shift. In addition, the shift-frequency properties of the ATVA were analysed and simulated through the vibration theory and the dipole model. [Deng and Gong (2007)]

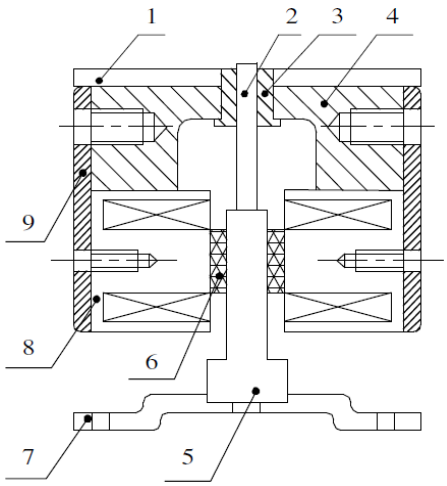


Figure 2. 23 The schematic diagram of the ATVA: 1. cover; 2. guide rod; 3. linear bearing; 4. magnetic conductor; 5. shear plate; 6.MREs; 7. base; 8. electromagnet; 9. mounting shell. [Deng and Gong (2008)]

Collette et al. (2009) demonstrated the characteristics of MRE TVA subjected to a broad band random excitation. The characteristic of MRE was described by using a simple Kelvin-Voigt model, in which some parameters (i.e. stiffness, damping coefficient) were assumed to change with the applied magnetic field linearly. Liao et al. (2011) developed an active-adaptive tuned vibration absorber (AATVA) by adding an activation force exciter between the MRE TVA and the primary system is shown in Figure 2.24. The experimental studies were carried out to demonstrate the vibration attenuation property and the capability of frequency shift.

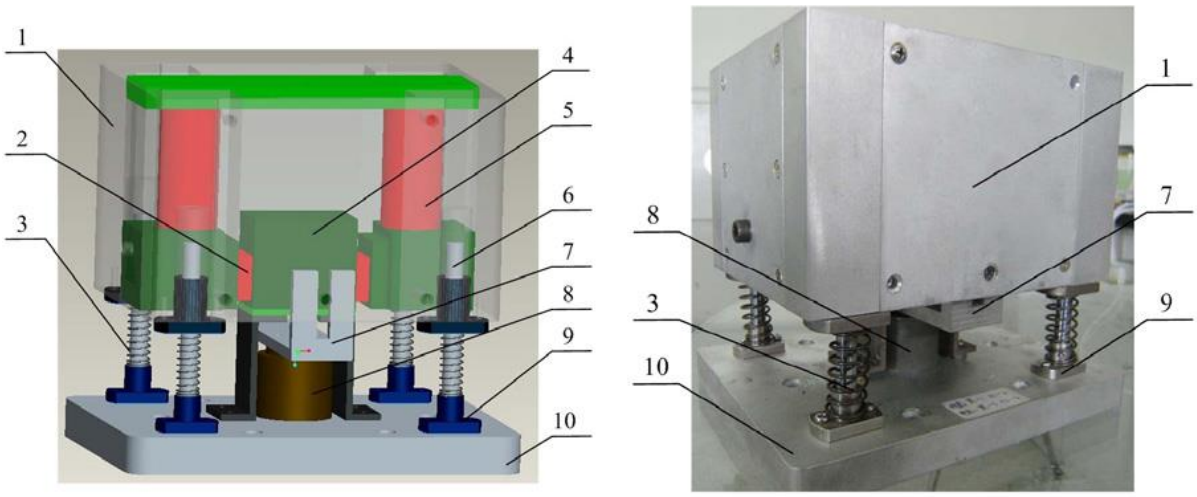


Figure 2. 24 The MRE AATVA (a) schematic diagram and (b) photograph: (1) mounting shell; (2) MRE; (3) helical spring; (4) shear block; (5) magnetic conductor; (6) guide rod; (7) connector of the voice coil motor and the shell; (8) voice coil motor; (9) flange; (10) base. [Liao et al. (2011)]

Liao et al. (2014) proposed a phase-based stiffness tuning algorithm to overcome the uncertainty of the relation between the magnetic current and the natural frequency for MRE TVA caused by the nonlinearity of MRE. Sun et al. (2015) designed and prototyped an ATVA (as shown in Figure 2.25) based on multilayer MRE sheets. The proposed device had the capability of frequency shift and demonstrated more effective performances than the passive vibration absorber over a wide frequency range. In addition, they also fabricated two kinds of MRE absorbers with squeeze and shear working mode, respectively [Sun et al. (2015)]. According to their test results, it can be noticed that the squeeze MRE absorber has a larger frequency-shift range than that working in the shear mode.

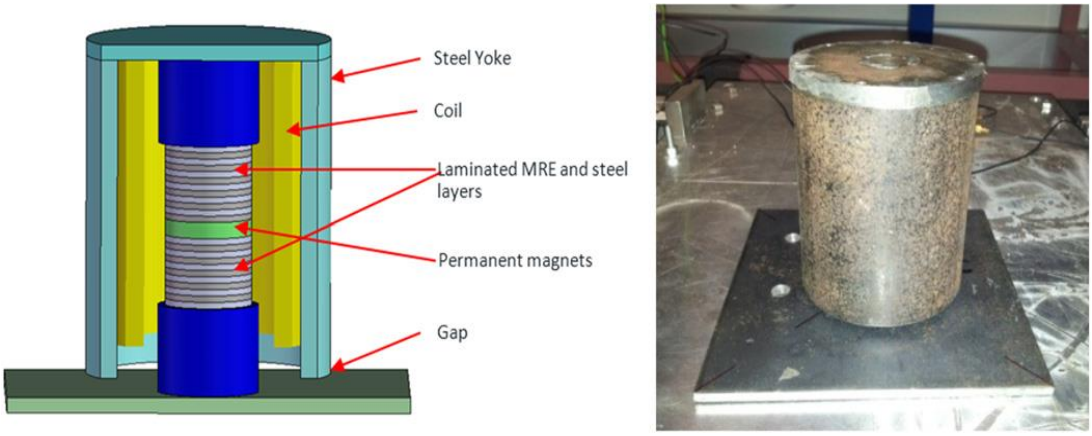


Figure 2. 25 The structure and prototyping of laminated MRE absorber. [Sun et al. (2015)]

Komatsuzaki et al. (2016) also used the MRE in the vibration absorber in order to provide the natural frequency tenability and the self-sensing ability.

### 2.6.2 MRE isolators

Usman et al. (2009) introduced a hybrid isolation system by applying MRE into the passive base isolator. It showed this new system can significantly reduce the response compared with the passive isolation system using rubber bearings for various excitations. Behrooz et al. (2012) proposed a new semi-active variable stiffness and damping isolator (VSDI) which consisted of MRE and traditional steel-rubber vibration absorber. The Bouc-Wen model was employed to represent the force-displacement relationship of VSDI, and Lyapunov based control strategy was used to control the scaled structural vibration. The obtained results showed that the proposed VSDI can significantly reduce the displacement and acceleration when experience seismic excitation. At the same time, it can shift the natural frequency by adjusting the damping and stiffness of scaled structure with electric current [Behrooz et al. (2014)].

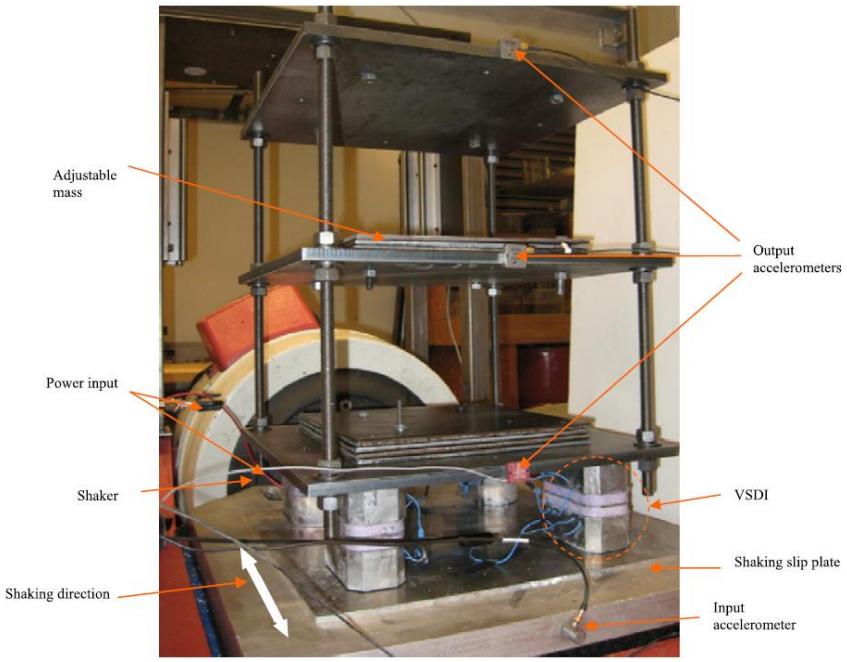


Figure 2. 26 Shake table vibration experiment setup. [Behrooz et al. (2014)]

In the following research, Behrooz et al. (2014) developed a feedback control loop consisted of the hysteretic model of VSDIs. The comparative experiments were carried out of the three levels scaled building with fixed base, off-state, on-state, passive VSDIs, and controlled VSDIs. The obtained results showed that the passive VSDIs significantly reduced the acceleration and slightly increased the displacement comparing to others. The controlled VSDIs reduced the maximum acceleration and slightly increased the displacement of each floors. Yu et al. (2014) proposed a simplified hysteretic model based on Bouc-Wen model to represent the relationship between force and displacement of MRE isolator. The model parameters were identified and validated by experiment results, and optimization was used the modified artificial fish swarm algorithm (AFSA). Li and Li (2015) designed a highly adjustable laminated MRE base isolator (as shown in Figure 2.27). A phenomenological model was proposed to characterize the dynamic behaviour of the designed isolator by incorporating with power-law function to represent the strain-stiffening behaviour. The identification of the model parameters in the proposed model was less complicated than those in the Bouc-Wen model. Comparison between the experimental data and calculation results by proposed model showed good agreement and demonstrated the effectiveness of proposed model in representing the characteristics of MRE base isolator, including the strain-stiffening phenomenon.

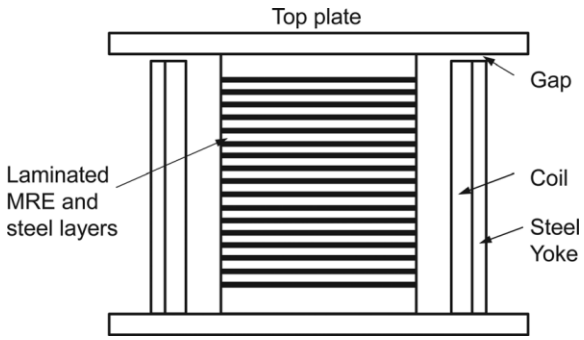


Figure 2. 27 Cross section of the MRE base isolator. [Li and Li (2015)]

Fu et al. (2013) designed a new MRE based buffer (as shown in Figure 2.27). The variable stiffness of the buffer was regulated by the human simulated intelligent control (HSIC) algorithm. The Kelvin-Voigt model was employed to represent the variation of MRE shear modulus when applied external magnetic field. Both numerical simulation and actual drop test results showed that the proposed MRE buffer and the control strategy can reduce the impact acceleration effectively.

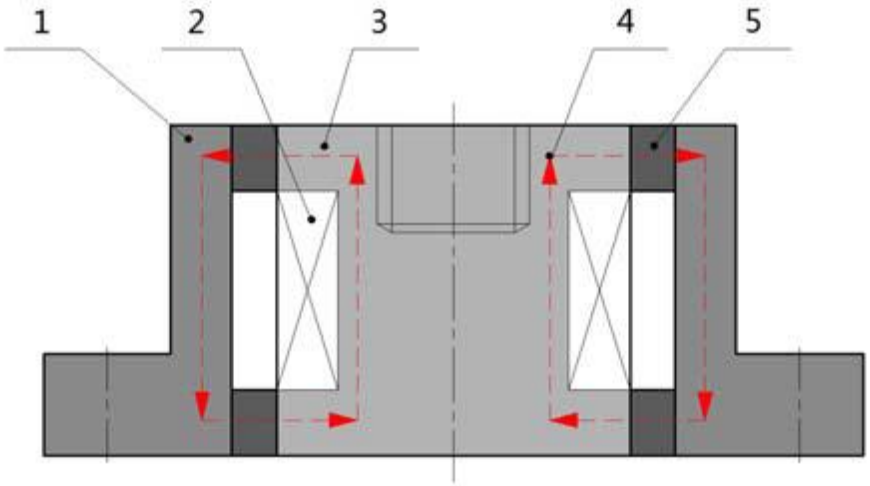


Figure 2. 28 Schematic configuration of MRE buffer: 1-Outer cylinder; 2-Coil; 3-Piston; 4-Primary flux; path 5-MRE). [Fu et al. (2013)]

Zhu and Rui (2014) introduced a semi-active vibration control system with a MR damper and MRE connected in series. The Bouc-Wen model was employed to represent the relationship between force and displacement/velocity. A corresponding parameter identification method was developed and validated by experiment data. The results showed that the MR damper can reduce the large-range and low frequency vibration and the MRE can reduce the small-range and high-frequency vibration as shown in Figure 2.29.

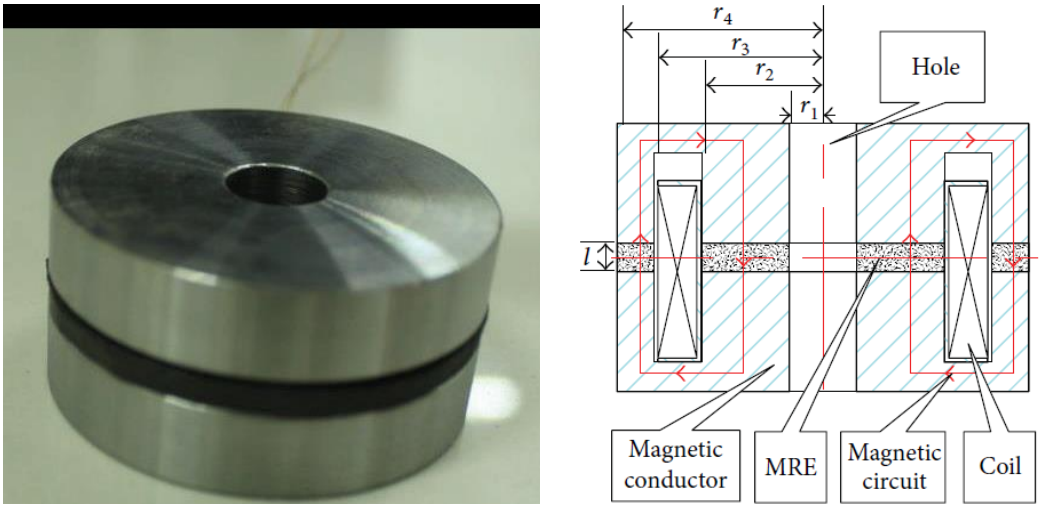


(a) (b)

Figure 2. 29 (a) MRE device and (b) device structure [Zhu and Rui (2014)]

Wahab et al. (2016) designed an isolator with multilayer MRE sheets associated with the natural rubber (NR) as the matrix. The test for force-displacement of isolator with vary external magnetic field was carried out with both static and dynamic compression mode. Their research proofed that the laminated MRE based isolator system can be effectively applying the actuating force or shifting the natural frequency of the device by changing the current (magnetic intensity). Yu et al. (2016) investigated the temperature characteristics of the laminated MRE isolator. They have noticed that the rising temperature of MRE in the working process can largely affect the stiffness and damping. They carried out a series of temperature sweeping-frequency tests and found out that the resonant frequency of the isolator is decrease linearly with the internal temperature. They also used both silicon grease and air cooling system to reduce the temperature effect during the working period to improve the stability of the MRE isolator. Mikhailov and Bazinenkov (2016) tested an active isolation platform on base of MRE. The MRE material can provide millisecond response speed and nano-meter running accuracy for the control system. In addition, the MRE based isolator can also shift the natural frequency of the system and reduce the amplitude of vibration [Poojary et al. (2016)]. Yu et al. (2016) developed a parametric model for the hysteretic shear force–displacement relationship of MRE base isolator which adopts a strain stiffening component. This model has four parameters which were identified by solving the linear equations through the least square method. Yang et al. (2016) fabricated and tested the scaled MRE isolator with a scaled three levels building under the motion induced by a scaled El Centro earthquake. Ladipo et al. (2016) used a four-parameter model to imitate the MRE engine mount and carried out the simulation work. The

performance of the MRE mounts were compared with the passive rubber mounts. According to their simulation results, the reduction in vibration was 50% while in the relative displacement plots. Fu et al. (2017) carried out a series of experiments to evaluate and characterize the dynamic behaviours of the designed MRE based isolator in shear-compression mode. These experiments were conducted under harmonic load and different magnetic fields. The experiment results showed that the maximum increment of the force generated by the designed MRE isolator can be up to 190%, and the increment of equivalent stiffness and damping were up to 175% and 216%, respectively. Sun et al. (2017) also designed, fabricated, tested and modelled an MRE-F isolator which combined both MRE and MRF. In their device, the MRF unit controled the device damping and the MRE component dominated the stiffness variation. They study showed the reliability and efficiency of MRE-F isolator against the sudden vibration. Gu et al. (2019) developed radial basis function neural network based fuzzy logic control (RBF-NFLC) to solve the inherent nonlinearity and hysteresis of the MRE isolator. The controller was able to accomplish the intended gain of smart base isolation.

### 2.6.3 Vibration control structures

As an ideal smart material for vibration control systems, MRE can be used to solve vibration problems with various control schemes for ship structures and civil engineering. Due to MRE has the ability to change elastic modulus with the magnetic field, this type of materials can be used in dynamic structures to adjust their natural frequency. The natural frequency of the structure becomes higher when the elastic modulus increased. This method can protect the structure from attaining the resonance phenomena by adjusting its natural frequency.

Yalcintas et al. (2004) studied the vibration suppression capabilities of MRE materials in adaptive structures: a homogeneous sandwich beam with MR materials between two elastic layers (as shown in Figure 2.30). Both theoretical and experimental results showed that for simply supported boundary condition, the application of MR adaptive beam resulted in a reduction of 20dB in the vibration amplitudes and a shift of 30% in natural frequencies.

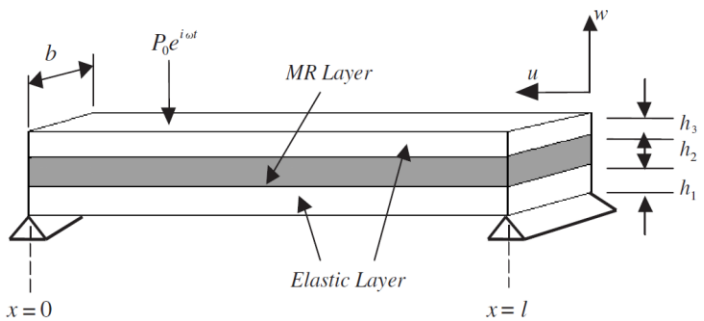


Figure 2. 30 Three-layered adaptive beam with MR material situated in the middle layer. [Yalcintas et al. (2004)]

Choi et al. (2010) investigated the dynamic behaviours of a sandwich beam with MRE core between two pieces of steel skins. The MR effects at 300 mT were studied by comparing the simply supported beam with clamped beam. Ni et al. (2010) investigated the micro-vibration control efficiency of both MRE based composite wall and MRE based composite floor. This material was used as cores of sandwich structures to support equipment under stochastic support motion excitations, as shown in Figure 2.31. The analytical results of velocity response showed that the composite structure incorporating MRE material possessed great micro-vibration suppression capability. Additionally, the parameters of the MREs, such as thickness, storage modulus and loss factor had great influence on the system RMS velocity response reduction.

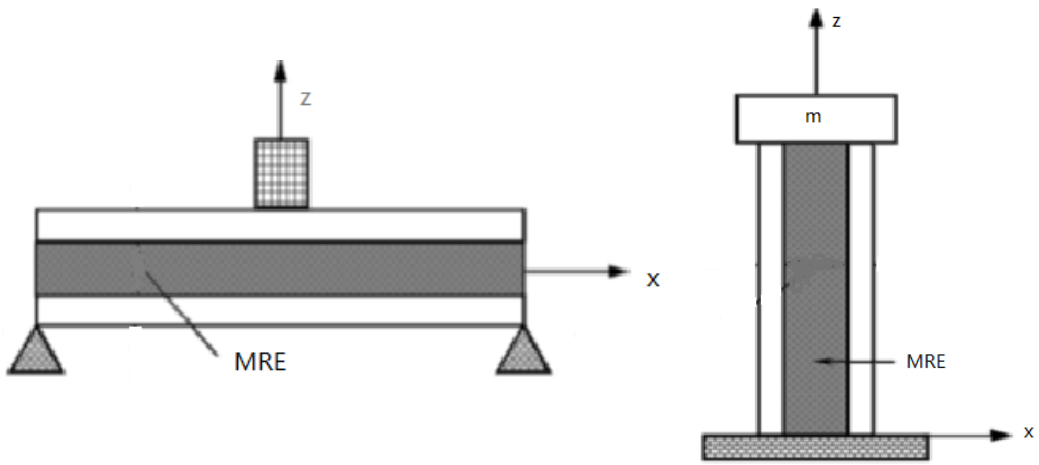


Figure 2. 31 MRE-based composite floor supporting equipment (a) and MRE-based composite wall supporting equipment (b). [Ni et al. (2010)]

Nayak et al. (2012) presented a symmetric three-layered beam with conductive skins and MRE patch between two soft viscoelastic patches in the core layer as shown in Figure 2.32. Second-order multiple scales method was used to solve the temporal equation of motion which

contained two frequency parametric excitation terms. According to their research, the stability of the system was improved significantly by the MRE material when the sandwich beam was subjected to periodic axial load.

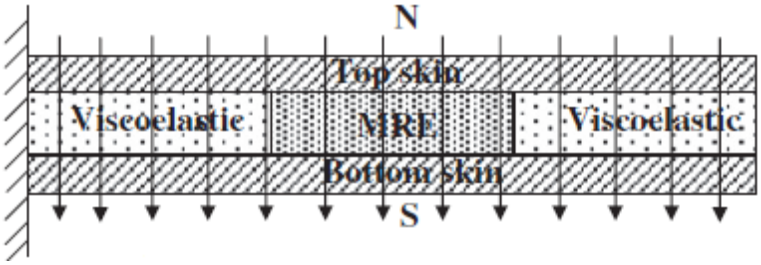


Figure 2. 32 MRE embedded viscoelastic cored sandwich beam subjected to periodic magnetic field and axial load. [Nayak et al. (2012)]

Yildirim et al. (2015) investigated the nonlinear dynamic response of an MRE sandwich beam. They have carried out several cases of experiments and one of them was MRE in the presence of a small external magnetic field. It needs to be noticed that the sandwich beam with MRE in the presence of a small magnetic field appears to have two resonant peaks. Komatsuzaki et al. (2016) investigated the dynamic properties of the different tapered laminated composite MRE sandwich plates. The natural frequency of the plate increased with the raised aspect ratio, but decreased with taper angle of the face layers. Aguib et al. (2016) studied both static behaviour and the dynamic response of sandwich beam which fabricated with two aluminium skins and a MRE core. This beam can rapidly stabilize under the magnetic field even under large vibration amplitudes. This technique can be used to reduce, or even eliminate the structural resonances in short time.

### 2.6.4 Other applications

Tang et al. (2018) presented a novel MRE micro actuator (as shown is Figure 2.33) for microfluidic systems including pumps and mixers using an innovative actuation mechanism. The presented MRE micro actuators are small size, simple, and efficient, offering a great potential to significantly advance the current research on complex microfluidic systems. Kawasetsu et al (2018) proposed a flexible tactile sensor consists of a magnet, magnetic transducer and dual-layer elastomer, which composed of a magnetorheological and nonmagnetic elastomer sheet. This sensor appears to has a high sensitivity that can respond to the applied with high contact speed.

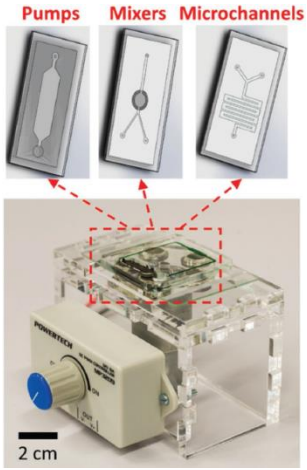


Figure 2. 33 MRE micro actuator. [Tang et al. (2018)]

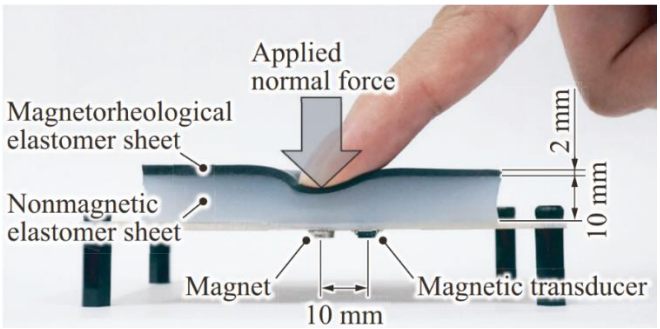


Figure 2. 34 MRE sensor. [Kawasetsu et al (2018)]

Qi et al. (2018) developed a magnetic-field sensor based on MRE material for the sensing of time-varying/uniform magnetic field. In their design, triboelectric nanogenerator (TENG) was used for detecting the deformation of MRE film. The designed sensor showed high sensitivity and stability in the measurement of magnetic field, and the response time and reset time were about 20 and 30 ms. Their experiment data also showed that the sensitivity of the sensor could be adjusted by MRE and device parameters.

## 2.7 Research gaps

A series of research studies on MRE material have been carried out by the researchers and engineers in recent years. Vibration control devices based on MRE materials have been designed and tested as well. From previous studies, it can be noticed that the MRE material mechanical performance can be affected by several factors, such as vibration frequency, strain amplitude, external magnetic field, temperature, etc. However, there are still some research gaps need to be solved as follow:

(1) Up to now, most of existing studies are mainly focus on the MRE material properties under room temperature conditions. However, MRE and MRE based device are usually operating in wide range of temperature. For example, the environment temperature of the ship engine and electric generator is about 40 ℃ in these areas. It is necessary to investigate the temperature effect on the dynamic properties of MREs.

(2) A lot of previous experimental studies have already investigated the mechanical properties of MRE material. It is necessary to use the time-temperature superposition

principle to construct dynamic modulus master curve with different temperatures and vibration frequencies.

(3) The micro-structure of MRE have significant influence on material properties. There is still no reliable calculation method nor existing statistic data to predict the particle distribution situation in MRE material.

(4) New smart composite material manufacture technology such as 3D printing method can be used to control the micro-structure of the MRE material. Based on these new methods, the microstructure of the material can be design and optimize to achieve better mechanical performance.

(5) There is no reliable generalized model for MRE material which take into account the influence of strain amplitude, excitation frequency, external magnetic field and environment temperature.

(6) For MRE application, the previous researchers designed the isolator and absorber without considering the temperature effect. It is necessary to design a vibration control system considering the temperature compensation component.

# 3 Methodology

MREs are usually anisotropic and inhomogeneous although their component materials are isotropic and homogenous. It is very difficult to determine the material properties of MREs by laboratory experiments or theoretical studies separately. Therefore, both numerical modelling and mechanical experiments should be used to investigate the magneto-mechanical properties of MREs. In this thesis, the dynamic mechanical properties of anisotropic MREs under different magnetic fields, environment temperatures, strain amplitudes, and excitation frequencies are obtained by using dynamic mechanical analysis (DMA) test and mathematical modelling. The experimental and modelling studies are presented to demonstrate the capabilities and effectiveness of the designed MRE based devices for semi-active vibration control in marine engineering. The research work is performed in three parts: DMA experiment, mathematical modelling, and design of MRE mount. The flow chart of the project is shown in the Figure 3.1.

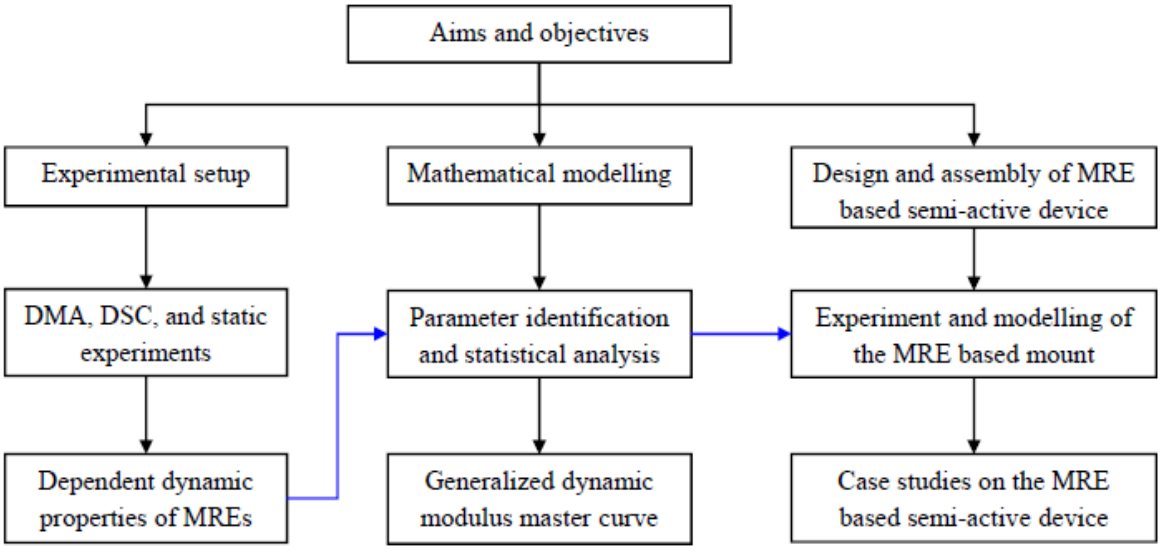


Figure 3. 1 Flow chart of the project

## 3.1 Experimental investigation on the mechanical properties of MREs

Experimental investigation on mechanical properties of MREs plays an important role in characterization and modelling of MRE materials and MRE based devices. The controllable dynamic properties of MREs are dependent on many factors, among which temperature is very important yet lack of understanding due to limited studies. The main purpose of this part is to

investigate the nonlinear dynamic properties of MRE samples under the combined magnetic-thermal-mechanical load by DMA experiments. The effects of magnetic field, environment temperature, pre-strain, strain amplitude, and excitation frequency on dynamic mechanical properties of MRE were measured and discussed. The detail of the research work in DMA experiment (Part I) includes:

- Choose the suitable matrix material and filler particles for the MRE fabrication. Prepare the anisotropic MRE specimens according to the BS ISO standards for dynamic mechanical test.
- Design and manufacture an oven consisting of a thermos-detector, the aluminum shell with thermal insulation material, and the heating wire and its control panel. It can provide maximum 70 °C testing temperature when room temperature is 20 °C.
- Integrate the self-manufactured oven and the electromagnets/permanent magnets into the Instron mechanical testing machine, which can be applied to perform DMA tests on MRE sample under the combined magnetic-thermal-mechanical load.
- Perform the DMA experiments on nonlinear dynamic properties of the MRE specimens under uniaxial harmonic compression. The effects of external magnetic field, environment temperature, pre-strain, strain amplitude, and the excitation frequency on the dynamic properties of the MRE samples are investigated though the DMA experiments.
- Carry out the static mechanical experiments and the differential scanning calorimetry (DSC) test to study the mechanical behaviour of MRE under the static load and different temperature. The DSC test results present a good physical interpretation of the transition behaviour of the MRE material observed in the DMA experiment. With the help of the DSC result, the potential applicability range of the time-temperature superposition (TTS) principle is also achieved.

The flow chart of Part I is shown in Figure 3.2.

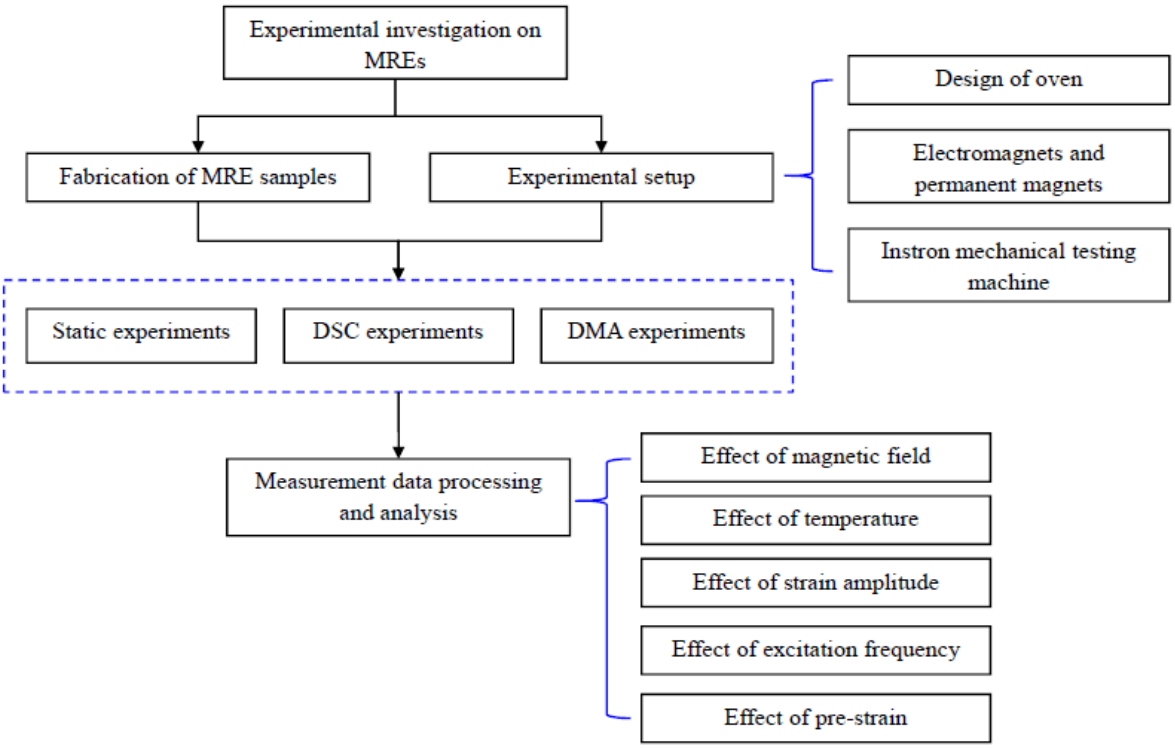


Figure 3. 2 Flow chart of Part I: DMA experiment

## 3.2 Mathematical modelling of MRE materials

A lot of models have been developed and proposed in the previous research so far to describe the dynamic properties of MREs under the combination of magnetic and mechanical load conditions. To our knowledge, there is still a research gap in the development of generalized mathematical model for describing the dependent dynamic properties of MREs considering combined impact factors such as magnetic field, environment temperature, and mechanical load. This part focus on developing a generalized mathematical model for the elastic and rheological properties of MREs under different magnetic fields, environment temperatures, strain amplitudes, and excitation frequencies. The research work in mathematical modelling (Part II) in introduced as follows:

- Propose a new approach to model the viscoelastic behaviour of MREs based on modified Kelvin-Voigt model in which both the stiffness of spring and viscosity of dashpot are dependent on the excitation frequency and have a clear physical interpretation. Comparative analysis is performed between the existing model (e.g. the fractional Zener model and the CAM model) and proposed new model with the experiment data.

- Extend the time-temperature superposition (TTS) principle to construct the dynamic modulus master curve of the MREs by using the horizontal shift factor and vertical shift factor. The applicability of the TTS principle to the MRE samples is verified by the logarithmic Cole-Cole plot and the semi-logarithmic Black diagram. Then the WLF empirical equation, the Arrhenius equation, quadratic polynomial function are used to model the horizontal shift factor and the vertical shift factor respectively. The good correlation between DMA experiment data and predicted results of dynamic modulus is confirmed and evaluated by the goodness-of-fit statistical analysis.
- Present new fractional functions to fit the experiment data of the magnetic field influence on dynamic modulus of MREs under uniaxial harmonic compression. The comparative analysis is performed between the proposed functions and existing equations developed by Blom and Kari (2011), Norouzi et al. (2016), and Xin et al. (2016). The statistical analysis results of goodness-of-fit show the proposed functions provide the better fitting results than the existing equations.
- Adopt the Kraus model to describe the strain amplitude effect on dynamic modulus of the MRE under uniaxial harmonic compression. The linear viscoelastic limit of MRE is discussed.
- Develop a generalized mathematical model for dynamic properties of MREs under uniaxial harmonic compression, which can take into account the influence of magnetic field, temperature, strain amplitude, and vibration frequency. The good correlation between DMA experiment data and predicted results of the storage modulus and loss modulus are evaluated respectively by the goodness-of-fit statistical analysis.

The flow chart of Part II is presented in Figure 3.3

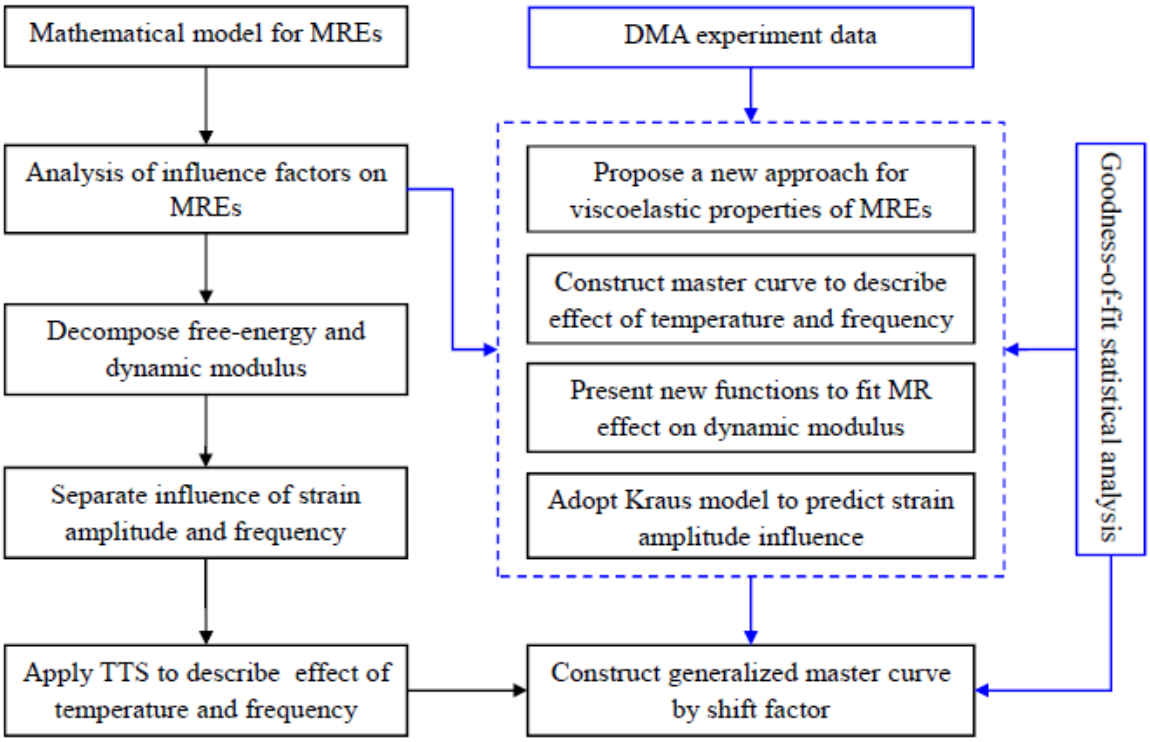


Figure 3. 3 Flow chart of Part II: Mathematical modelling

## 3.3 Design of MRE based devices for semi-active vibration control

Base on both numerical and experimental investigation results, a prototype of MRE based vibration control system is designed, manufactured and tested. Its performance is demonstrated by several case studies. The main worm in design of MRE mount (Part III) includes:

- Design and assembly of the semi-active vibration control device based on MRE materials. The MRE based mount system consists of signal processing and control subsystem, MRE material, electrical magnets and power supply. The signal processing and control subsystem processes the signal from thermometer and accelerator and controls the current and the magnetic flux intensity by using Labview and Arduino.
- Investigate the dynamic properties of the MRE mount by DMA experiment and mathematical modelling under the different magnetic fields and temperature conditions. The comparative analysis is performed between experimental data and modelling results. The force transmissibility and frequency shift are evaluated by experiment and modelling under different magnetic fields and environment temperatures.
- Carry out case studies on the performance of the MRE mount with real-time semi-active control strategy and subsystem. The capability of the MRE mount system to reduce the

force transmissibility and shift natural frequency is demonstrated under various load conditions.

The flow chart of Part III is shown in Figure 3.4.

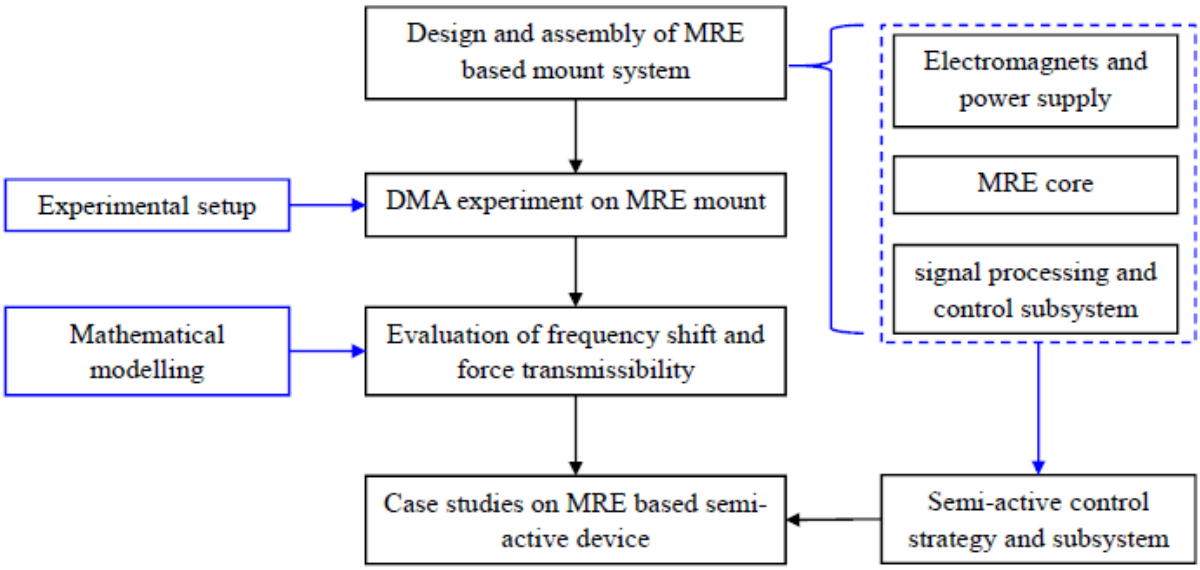


Figure 3. 4 Flow chart of Part III: Design of MRE based mount

# 4 Experimental investigation on MRE

## 4.1 Introduction

Experimental investigation on material properties of magnetorheological elastomers (MREs) plays an important role in developing MRE materials, understanding mechanical properties of MREs, and designing MRE-based devices for semi-active vibration control. Therefore, extensive experimental studies have been carried out in the past decades to achieve the mechanical properties of MREs with different size and volume fraction of particles, load amplitude, excitation frequency, and intensity of magnetic field etc. (as shown in Chapter 2). However, there is a few published research works investigated the temperature dependent mechanical properties of MRE material and MRE based device [Zhang et al. (2011), Yu et al. (2016)].

MRE based devices are often exposed to a wide temperature range. The temperature changes in MREs and MRE based devices may be caused by the environmental temperature variations and/or internal temperature rises due to energy dissipation. MRE exhibits a temperature dependent softening and stiffening ability at low and high temperature respectively, which can have a significant effect on material properties of MREs and the performance of MRE based devices. It is necessary to carry out the experiments on nonlinear dynamic properties of MRE materials under the combined magnetic-thermal-mechanical load. In order to achieve this goal, a reliable measuring system has been designed which includes:

(1) Electromagnets and permanent magnets, which are applied to produce the external magnetic field in different directions.
(2) A self-manufactured oven, which can provide maximum 70 °C testing temperature when room temperature is 20 °C.
(3) The Instron mechanical testing machine, which is applied to perform dynamic mechanical analysis (DMA) tests on MRE sample under uniaxial harmonic compression.

The DMA tests are performed in the Transport Systems Research Laboratory in University of Southampton. The test standard is selected as BS ISO standard. The influence of external magnetic field, environment temperature, strain amplitude, excitation frequency, and applied pre-strain on the dynamic properties of anisotropic MRE samples under uniaxial harmonic compression is measured and determined. Firstly, Section 4.2 presents the experimental setup including the sample manufacture, experiment plan design, test machine, and data processing method. The DMA experiment results of the anisotropic MRE samples are presented and

discussed in Section 4.3. The static experiments and the differential scanning calorimetry (DSC) test on the MRE sample are carried out in Section 4.4 and Section 4.5, respectively. In the end, Section 4.6 gives the chapter summary.

## 4.2 Experimental setup

### 4.2.1 MRE sample manufacture

The most popular rubber and rubber-like materials for MRE matrix are natural rubber and silicone rubber (as shown in Table 2.1). All these materials are not recyclable, there is no possibility of reprocessing once the matrix is cured. Silicone rubber is selected for this project due to it is easy for processing, especially can be cured at room temperature. This advantage makes silicone rubber quite suitable for laboratory experimental study. Silicone rubber also offers highly thermal resistance to the extreme environment temperatures, which is more appropriate for ship engine or electric generator system.

According to the published experiment results of MRE samples in the literature, the maximum MR effect normally was achieved when the iron particle volume fraction was around 30 vol% [Eem et al. (2013), Koo et al. (2010), Lokander and Stenberg's (2003)]. The stiffness of anisotropic MREs appeared to be much more sensitive to magnetic field when the external magnetic field flux had the same direction as the particles chain line inside the MRE. Thus the MR effect of anisotropic MREs was larger than isotropic ones in most cases [Böse and Röder (2009), (Kaleta et al. (2011), Varga et al. (2005)]. In our experimental research, the anisotropic (or considered as transversely isotropic) MRE samples are fabricated by using silicone rubber with volume fraction of 70 vol% and iron particles with the particle volume fraction of 30 vol% cured under room temperature.

The iron particles are purchased from Sigma-Aldrich company (iron particles volume ≥ 99.5 vol%, grain size 5-9 um), and the silicone rubber is purchased from Wacker Chemie AG (Germany). According to the instructions from the company for the silicon rubber, Elastosil A is mixed with Elastosil B (as shown in Figure 4.1) as 10:1 in volume fraction and then the iron particles (as shown in Figure 4.2) are added. The mixture is blended by stirrer over 10 minutes to make sure the iron particles are well distributed in the silicone matrix. Then the mixture is placed in a vacuum chamber for more than 20 minutes to reduce the air bubbles trapped inside the material during mixing progress (as shown in Figure 4.3).

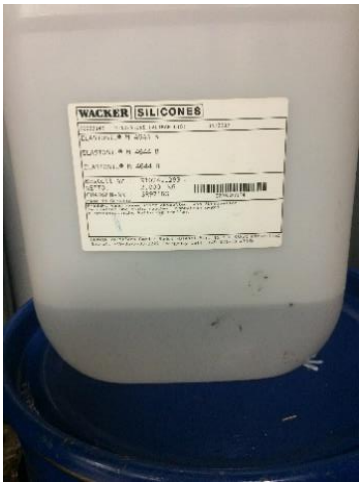


Figure 4. 1 Silicone rubber A and B

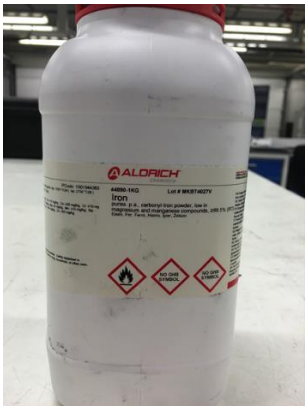

Figure 4. 2 ALDRICH iron particles

Figure 4. 3 Vacuum chamber and vacuum pump

Finally, the mixed material (as shown in Figure 4.5) is placed in the aluminium moulds (as shown in Figure 4.4) with the inner diameter of 28mm, height of 13mm, and thickness of 1mm, then left in the room temperature to cure for more than 20 hours. In addition, the moulds are placed between two permanent magnets producing a stable magnetic field of about 265 mT to achieve anisotropic MRE samples. During curing and testing, the external magnetic field is generated by two cylindrical grade N42 neodymium permanent magnets (purchased from E-magnets UK) with diameter 40 mm, thickness 5 mm and 14 kg pull. The magnetic flux values are measured by gaussmeter GM08 (purchased from Hirst Magnetic Instruments Ltd UK) as shown in the following figures.

Figure 4. 4 Aluminium moulds

Figure 4. 5 MRE mixture

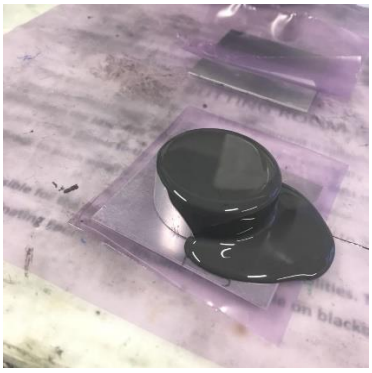

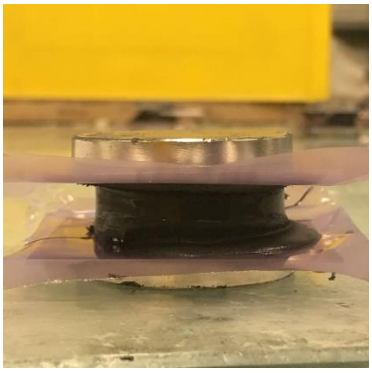

Figure 4. 6 Anisotropic MRE sample curing

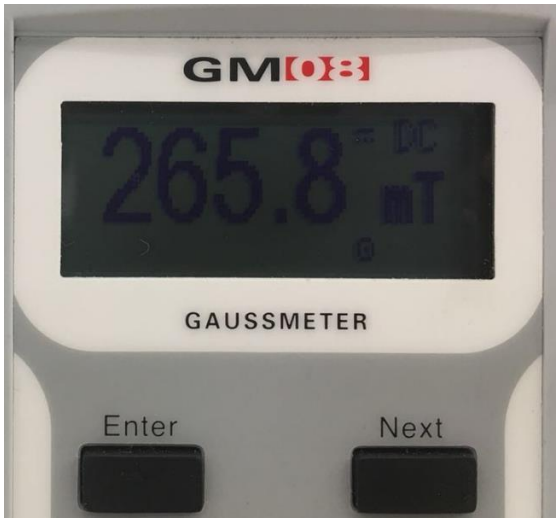


Figure 4. 7 One pair of N42

Figure 4. 8 Two pairs of N42

When only using one pair of magnets, it can produce a constant magnetic field with 265 mT (as shown in Figure 4.7) between the magnets with a gap of 12 mm (model height). When two pairs are used (two magnets are stacked together), the produced magnet field is about 465 mT (Figure 4.8). A serial of other permanent magnets purchased from the same company are used

to generate the stable external magnetic field for the MRE samples from 30mT to 210mT.

### 4.2.2 Experiment design for mechanical characterization of MREs

The DMA experiments of the MRE samples are performed according to the BS ISO 4664-1:2011, and the static mechanical experiments are following the guidance of BS ISO 7743:2017. The mechanical properties of the MRE based on silicon rubber and iron particle are investigated through uniaxial harmonic compression tests in certain range of frequencies and applied strain amplitudes. The storage modulus and loss modulus of the MRE are calculated following the guidance of the manual of Instron Plus for DMA measurements. A large quant of the MRE samples are tested at different pre-strains, strain amplitudes, excitation frequencies, external magnetic fields, environment temperatures. The experiment data are recorded though the force and displacement channels during DMA test. The parameters of test samples and the basic DMA test plan are given in Table 4.1 and the photo of the MRE specimens are shown in Figure 4.9.

Table 4. 1 Test specimen dimension and the test conditions for MRE samples

| | |
|---|---|
| Iron particle size (μm) | < 10 (80 vol%), < 100 (20 vol%) |
| Mode of deformation | Compression |
| Shapes | Cylinder |
| Dimensions (mm) | h=13 and d=28 |
| Pre-strain (%) | 3%, 5%, 7%, 10% |
| Strain amplitude (%) | ±0.01, ±0.25, ±0.5, ±0.75, ±1, ±1.25, ±1.5 |
| Test temperature (°C) | RT, 30, 35, 40, 45, 50, 55, 60 |
| Test frequency (Hz) | 10, 20, 30, 40, 50, 60 |
| Magnetic field (mT) | 0, 30, 60, 90, 120, 150, 180, 210, 265, 300, 465, 500 |

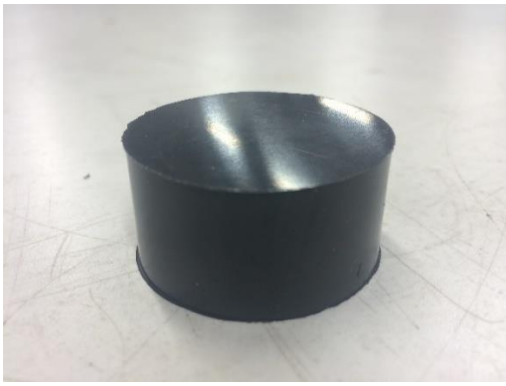

Figure 4. 9 MRE sample according to the BS ISO standard

Each test is operated with a specific number of cycles and all these data are recorded. The detail of the loading cycles for varying excitation frequency is shown as follow:

Table 4. 2 Test loading cycles with excitation frequency

| Excitation frequency (Hz) | 10 | 20 | 30 | 40 | 50 | 60 |
|---|---|---|---|---|---|---|
| Cycles | 100 | 200 | 300 | 400 | 500 | 600 |

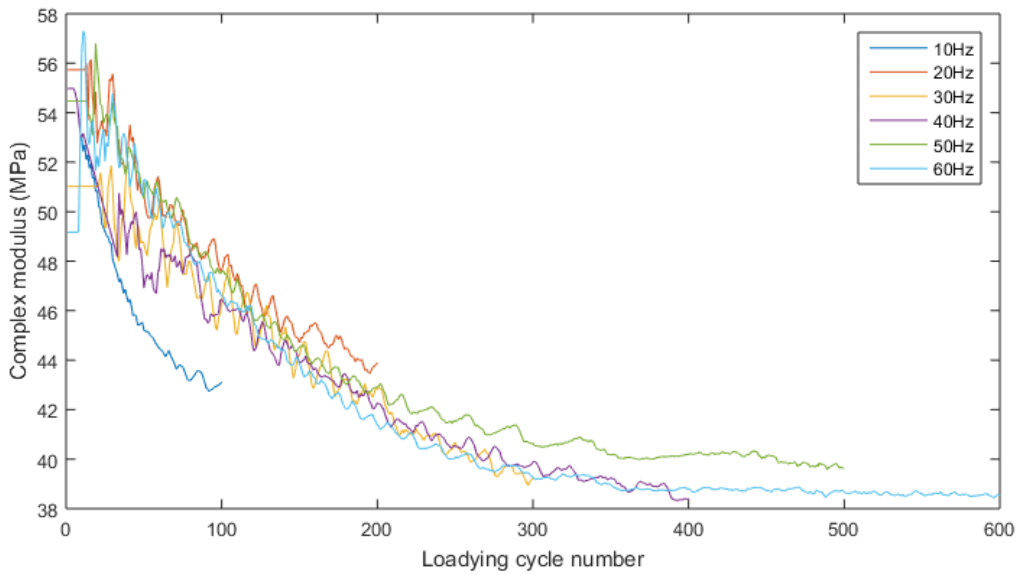


Figure 4. 10 The complex modulus of different excitation frequencies and loading cycles

According to Figure 4.10 above, the experiment results of the complex modulus appear to be stable when the test cycle is increased. Simply increasing the number of loading cycle may significantly improve the reliability of the measurement data. However, this will result in

longer test time and potential sample damaged. It is necessary to select suitable loading cycles to ensure the corrective data may have achieved with less loading cycles.

### 4.2.3 Oven design

For practical industry applications, especially in maritime engineering, the vibration control devices are usually operated with environmental temperature range from 40 ℃ to 60 ℃. However, most of previous experimental studies about the mechanical properties of silicone rubber based MRE are carried out under room temperature test condition which is normally 20 ℃. In order to achieve the mechanical properties of MRE materials in the high temperature condition, it is necessary to carry out the DMA test under various temperatures. For this study, the testing temperature is range from 20 ℃ to 60 ℃ with each 5 ℃ as the test step. An oven has been designed and manufactured for the DMA experiment under various temperatures.

The oven shell is manufactured of aluminium alloy and a special glass which can be used in high temperature (as shown in Figure 4.11). The thickness of the selected glass is 20 mm to reduce the heat loss.

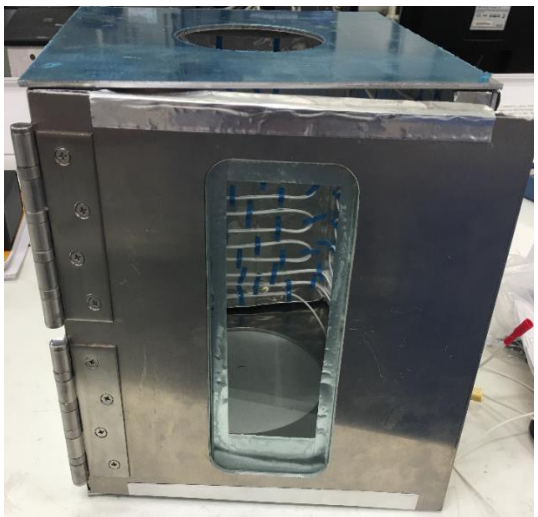

Figure 4. 11 The high temperature glass

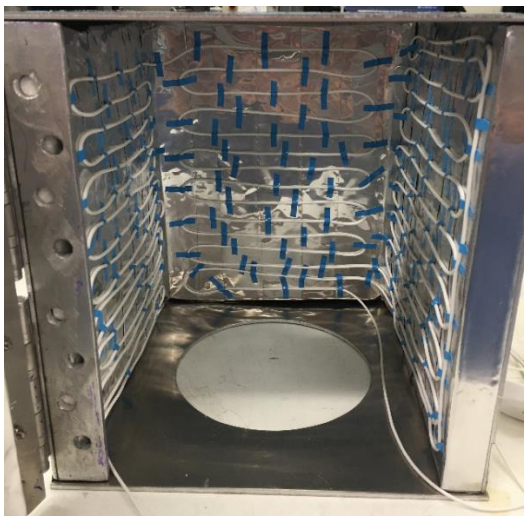

Figure 4. 12 Heating wire

Aluminium silicate layer has been placed between the shell and the aluminium foil to reduce heat conduction, enhance to guarantee the specimen temperature stay at the target temperature. Heating wire is well arranged inside the oven (as shown in Figure 4.12). A temperature control panel (Inkbird ITC-308) has been applied to control the heating system and make sure the inside temperature remains at the target range. The specimen temperature is monitored by a thermos-detector (TM902C).

### 4.2.4 Experiment test machine

The DMA experiments are performed by Instron test machine (E1000 Electro plus) in the Transport Systems Research Laboratory. During the test, the displacement and force are the original tracking channels. The strain amplitude and vibration frequency are controlled through the displacement channel and the resulting force is measured by the force channel. The applied strain is calculated by the displacement and the sample thickness, and the resulting stress is achieved by calculating the force and the cross section area of the MRE sample. The experimental setup for dynamic compression test is shown in Figure 4.14.

For industry application, electro-magnets are capable of continuously controlling the magnetic field intensity of the adaptive MRE vibration control devices. In this study, the magnet field is provided by cylindrical neodymium permanent magnets (as shown in Figure 4.13). This is due to electro-magnets may generate large amount of heat during its operating period which can affect the experiment results. The magnetic flux density can be varied by changing the type and the number of neodymium permanent magnets.

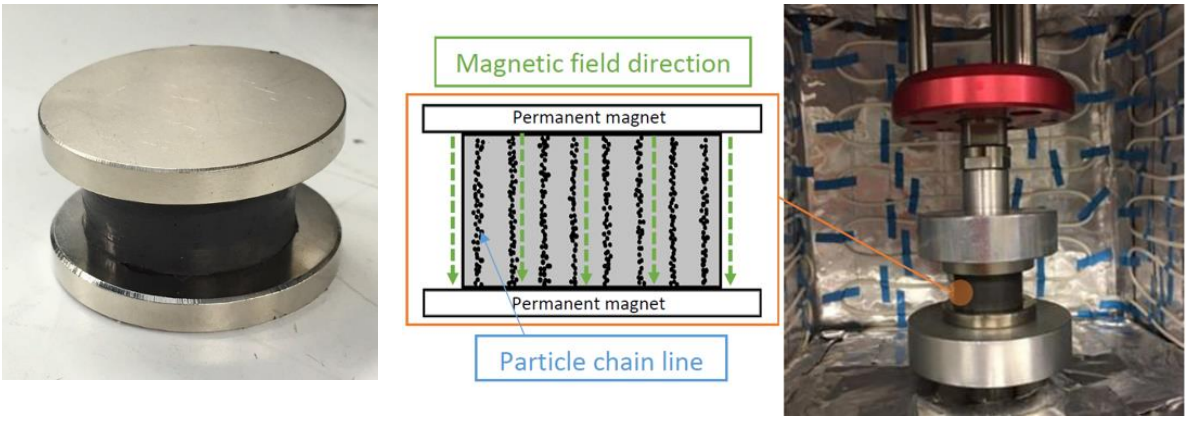


Figure 4. 13 MRE sample with two permanent magnets

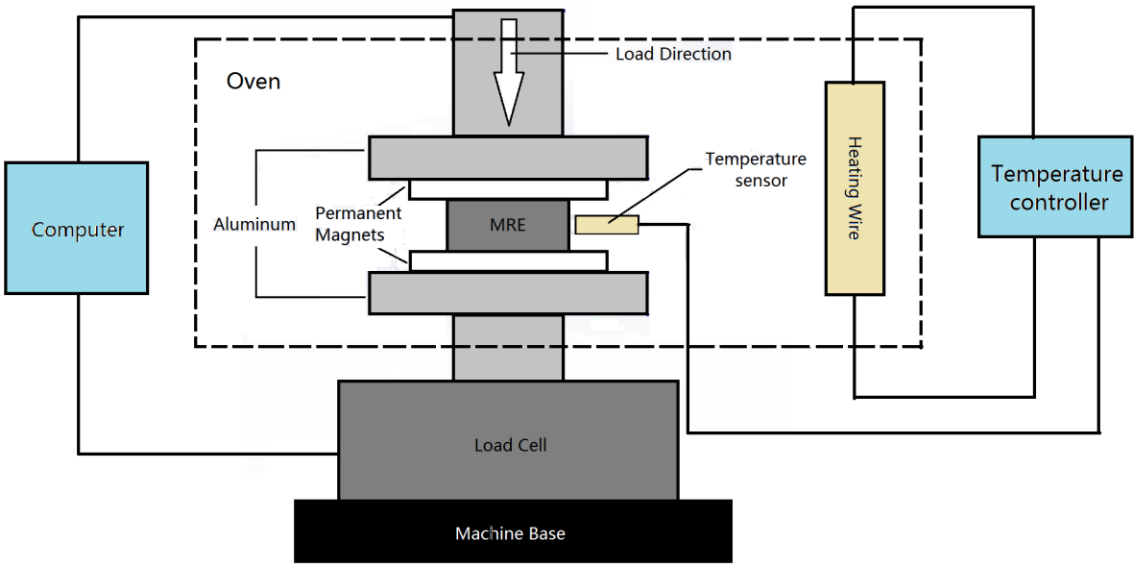


Figure 4. 14 Experimental setup for uniaxial harmonic compression test

All the MRE samples are preloaded and unloaded for ten cycles before the DMA test to avoid the Mullins effect. Each test conditions will have at least three samples in order to obtain reliable results. In the temperature effect investigation, the inside part of the MRE samples needs more than 10 min to reach the same temperature as the material surface. For this reason, each samples are pre-heated and remain at the target temperature at least 30 min before the DMA test.

### 4.2.5 Experimental data processing

The experimental data of frequency, load, and position are recorded through the data channels to obtain the force-displacement curves for the MRE samples. The DMA tests of the MRE samples are performed under uniaxial harmonic compression in a range of frequencies from 1 Hz to 60 Hz, strain amplitudes from 0.01% to 1.5%, pre-strain from 3% to 10%, environmental temperature from room temperature (about 20 ℃) to 60 ℃, and external magnetic field intensities from 0 mT to 500 mT. The storage modulus and loss modulus of the MRE samples can be calculated following the manual of Instron machine E1000 Electro plus for DMA measurements. Each set of tests is carried out with at least three samples independently, and every test is repeated at least twice for each pair of the MRE samples. The experimental data are averaged to present the curve or surface to guarantee the reliability of the test data. During the mechanical test, it can be noticed that the experiment data change slightly for the same samples when the dynamic tests are repeated.

MRE is a kind of filled rubber-like material which cannot respond instantaneously when a sinusoidal strain is applied due to its viscosity. The resultant stress will normally lag the input with a loss angle or factor. Take this situation into consideration, mathematically the complex modulus of MRE, namely the storage modulus and loss modulus, is expressed as follow:

$$E^* = E' + iE'' \tag{4.1}$$

where $E^*$ denotes the complex modulus, E' and E'' are the real part and imaginary part of the complex modulus, called the storage modulus and the loss modulus, respectively. The magnitude of complex modulus $|E^*|$ can be obtained by calculating the ratio of the stress range to the strain range. The loss angle $\varphi$ is relevant to the energy dissipation per volume within an oscillatory cycle, which is the area enclosed by the hysteresis loop. This can be calculated according to the DMA directions of the manual for the Instron machine E1000 Electro Plus measurements. The magnitude of complex modulus $|E^*|$, storage modulus E', loss modulus E'' and loss angle $\varphi$ are defined as follows:

$$E' = |E^*| \cos\varphi \tag{4.2}$$

$$E'' = |E^*| \sin\varphi \tag{4.3}$$

$$|E^*| = \frac{A_{stress}}{A_{strain}} \tag{4.4}$$

$$\varphi = \arcsin \frac{E_{loop}}{\pi A_{strain} A_{stress}} \tag{4.5}$$

where $E_{loop}$ is the energy enclosed by the hysteresis loops, $A_{strain}$ denotes the strain amplitude and $A_{stress}$ the stress amplitude.

## 4.3 Dynamic mechanical analysis measurement result

During the experimental process, the testing machine continuously measures and records the number of cycles, the load, and the displacement. Based on these, the complex modulus, storage modulus, loss modulus, loss angle, and dynamic damping coefficient etc. are calculated by using energy method at the same time.

The hysteresis loops based on strain-stress data are plotted in the following paragraphs. The dynamic properties of MRE material are calculated and analysed. The influence of the external magnetic field, load frequency, strain amplitude, and environmental temperature on mechanical properties of the MRE are discussed. The error analysis of the test results is shown as follow:

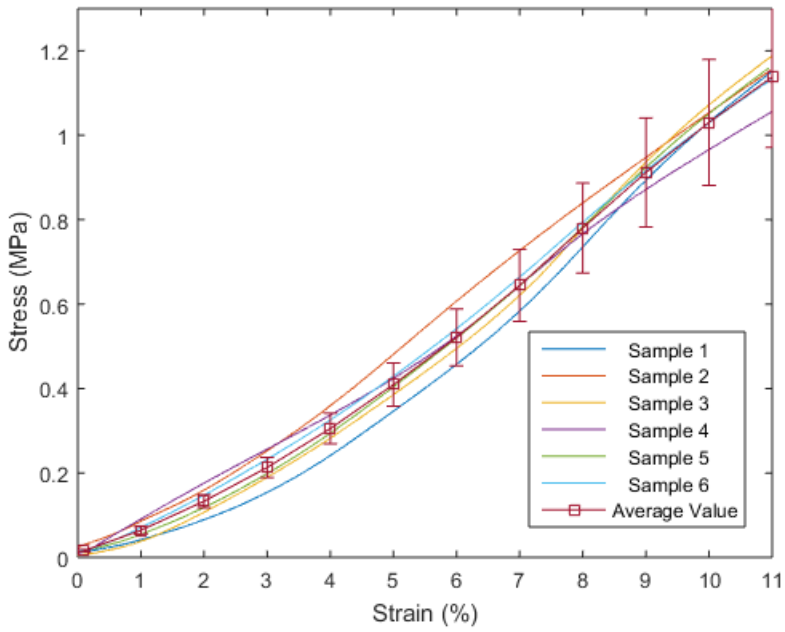


Figure 4. 15 Results comparison and error analysis for static compression test

Figure 4.15 shows the comparison of the strain-stress curves between different MRE samples under static compression test. This test is carried out under the room temperature and zero external magnetic field. The stress and strain curves of the MRE samples are calculated from the load and displacement data. Six samples are manufactured and tested for different conditions according to BS ISO 7743:2017. The standard deviation of the measurement data is increased with the applied strain, and reaches its maximum value at strain of 11% which is 0.31. In this research, the authors only focus the small amplitude strain which is within 6.5%. The standard deviation is always below 0.08 (at strain of 6.5%) when the applied strain is range from 0% to 6.5%. According to this, the measurement data of the static compression test is achieved and their reliability is proofed.

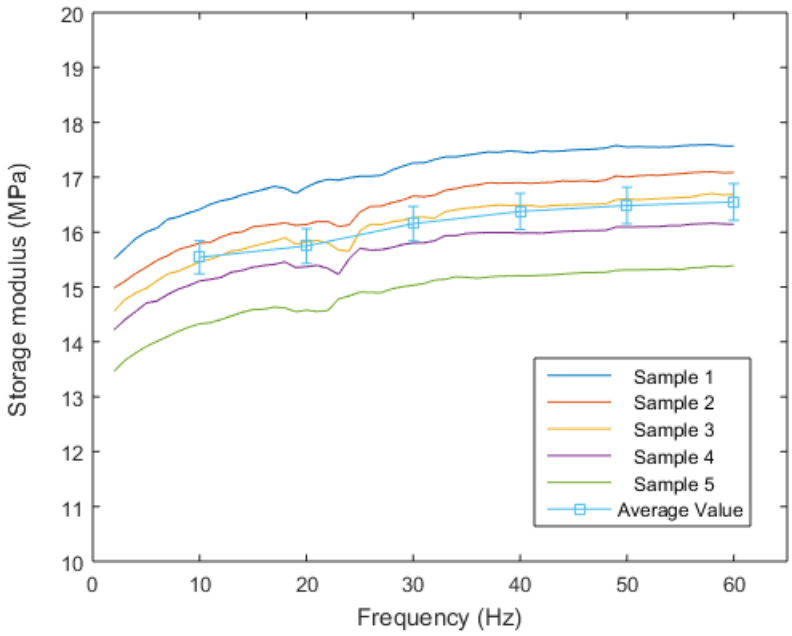


(a)

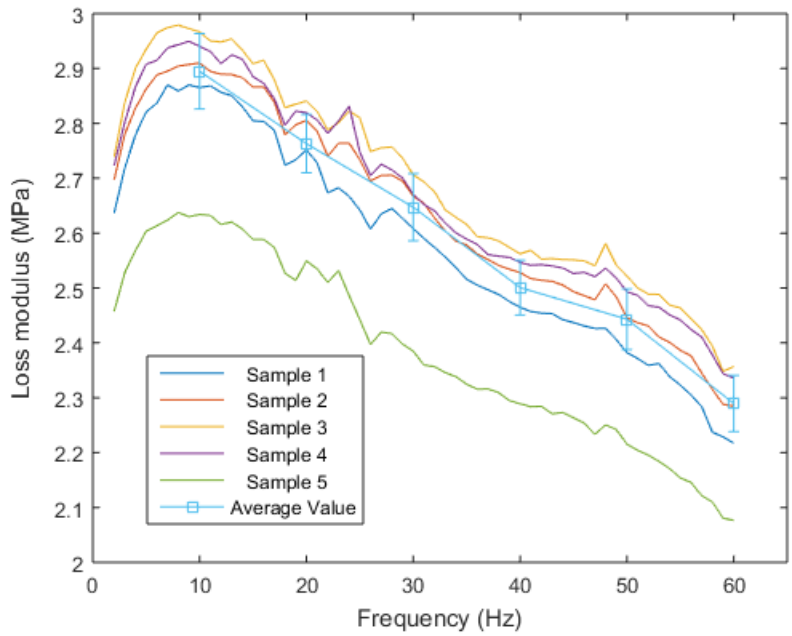


(b)

Figure 4. 16 Results comparison and error analysis of dynamic compression test. (a) storage modulus and (b) loss modulus

Figure 4.16(a) and Figure 4.16(b) show the comparison of frequency dependent storage modulus and loss modulus curves between different MRE samples under uniaxial harmonic compression load. These tests are carried out under the room temperature and zero external magnetic field. For each test conditions, five MRE samples are used at least to achieve at least

three reliable data, which means the green curve data in Figure 4.16b is not selected in our research. The standard deviation of the magnitude of complex modulus and storage modulus are remained at a stable value approximately 0.17. The standard deviation of the loss modulus is much lower which is 0.12. Based on the data error analysis results, the measurement data of the dynamic compression test is proofed to be reliable.

### 4.3.1 Hysteresis loop

MRE and other rubber-like materials exhibit a nonlinear stress–strain behaviour known as hysteresis under cyclic loading and unloading. When a sinusoidal load is applied to the MRE sample, it does not respond immediately. The resulting displacement usually lags the input load by an angle which is called the loss angle. This property leads to a displacement-force hysteresis loop curve is shown as a phase difference between displacement and force. Each of the hysteresis loops forms an elliptical shape within linear viscoelastic regime. The area enclosed by the hysteresis loop indicates the amount of energy dissipated in each cycle and thus the damping capability of the material while the main axis of the hysteresis loop characterizes the stiffness i.e. the magnitude of the complex modulus.

#### 4.3.1.1 Magnetic field dependence

As mentioned early in this thesis, MRE is a kind of smart material with its properties can be affected by the external magnetic field. Figure 4.17 shows the stress-strain curves of the anisotropic MRE samples at 0 mT, 265 mT, and 465 mT magnetic field density. The environment temperature is around 20℃ (room temperature). The pre-strain is 5% and this point is set as the zero position, the strain amplitude is fixed as 1.5%. The excitation frequency is set constant as 10 Hz.

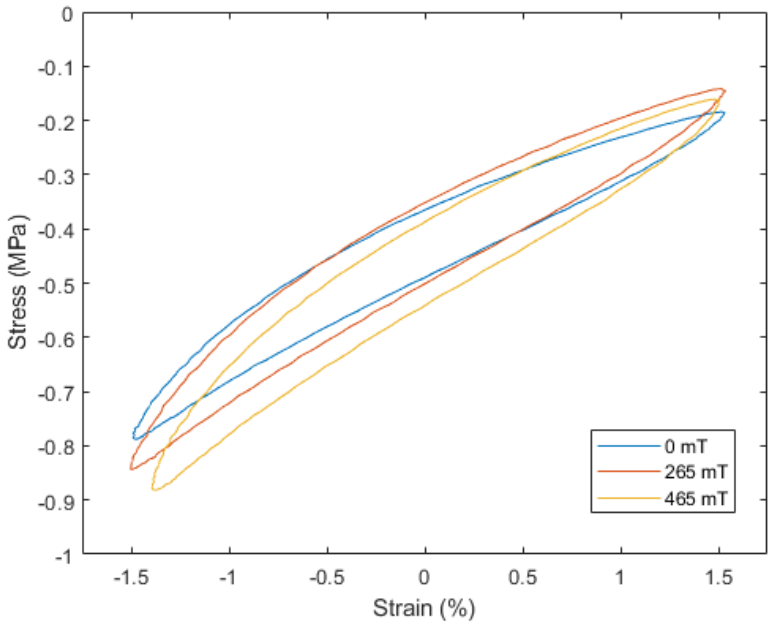


Figure 4. 17 Hysteresis loop of MRE samples under uniaxial compression with pre-strain of 5%, test frequency of 10 Hz, strain amplitude of 1.5 %, and external magnetic field varying from 0 to 465 mT in room temperature

It can be observed from Figure 4.17 that the slope of the stress-strain curve changes with increasing magnetic flux density. The MRE samples obviously become stiffer when increasing the magnetic intensity. Based on the stress-strain hysteresis loops, the magnitude of complex modulus can be obtained from the slope of the line from the point of minimum strain to the maximum strain point. The loss angle is calculated from the area enclosed by the hysteresis loop. Then the storage and loss moduli can be achieved as well.

#### 4.3.1.2 Frequency dependence

The following figures present the stress-strain relationship of the anisotropic MRE samples with different excitation frequencies from 10 Hz to 60 Hz. In this experiment, the pre-strain of the MRE sample is 5% and the strain amplitude is 1.5%. This DMA test is carried in room temperature condition which is 20 °C. Figure 4.18 shows the hysteresis loops of the MRE sample under non-magnetic field, and Figure 4.19 shows the test results of MRE samples under external magnet field of 265 mT.

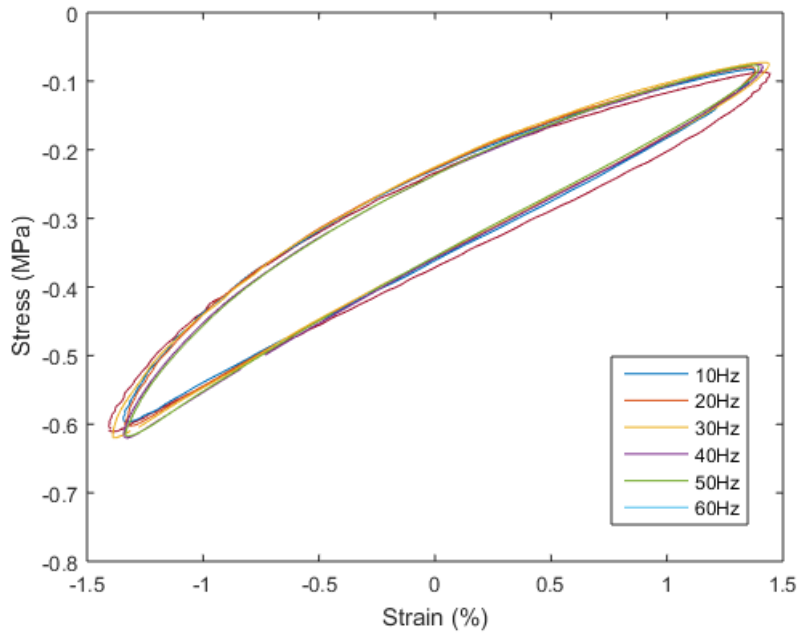


Figure 4. 18 Hysteresis loops of MRE samples under uniaxial compression with pre-strain of 5%, strain amplitude of 1.5%, non-magnetic field, and different vibration frequencies from 10 Hz to 60Hz in room temperature

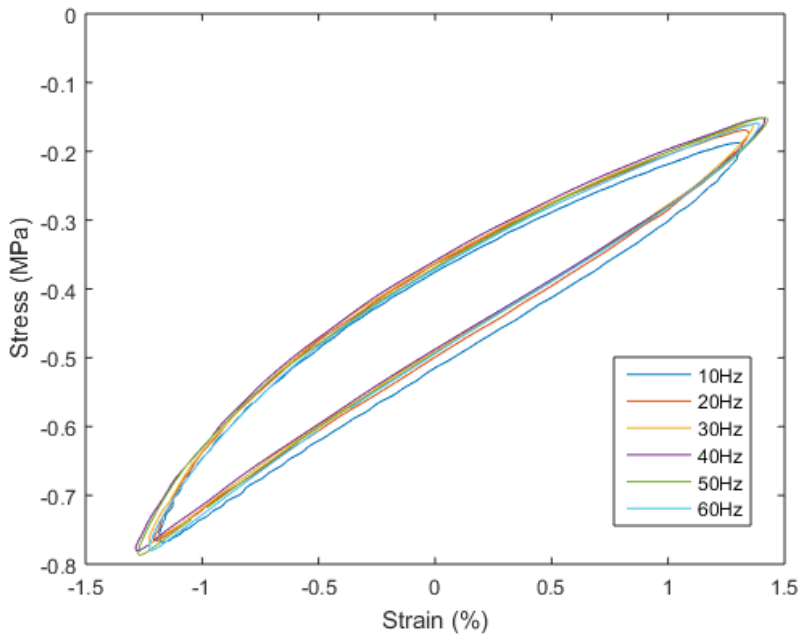


Figure 4. 19 Hysteresis loops of MRE samples under uniaxial compression with pre-strain of 5%, strain amplitude of 1.5%, external magnetic field of 265 mT, and different vibration frequencies from 10 Hz to 60Hz in room temperature

It can be observed from Figure 4.18 and Figure 4.19 that the ellipse of the hysteresis loops shift to higher values with the increasing frequency indicating that the stiffness of the MRE material is slightly increased for both non-magnetic field and 265 mT magnetic field. However, the influence of the excitation frequency on material damping capability is not significant because

the area of the hysteresis loop almost remains the same for different loading frequency conditions.

#### 4.3.1.3 Strain amplitude dependence

The following figures present the strain-stress hysteresis curves for the anisotropic MRE samples that corresponds to uniaxial dynamic strain amplitudes of 0.25%, 0.5%, 0.75%, 1%, 1.25%, and 1.5%. The first step of the test is to quasi-statically compress the MRE sample to the target loading state which is 5% in this experiment. The following step is vibration test of the MRE sample under different strain amplitudes. The vibration test of each strain amplitude will run 100 cycles for 10 Hz excitation test condition, and 600 cycles for 60 Hz test. Therefore, the total cycle number is 600 for 10 Hz vibration test, and 3600 for 60 Hz vibration test. The details of these two test plans are listed in Table 4.3 and Table 4.4 respectively. No.80 cycle and No. 580 cycle are selected respectively as the representative cycles for 10 Hz compression test and 60 Hz compression test.

Table 4. 3 Test plan for 10 Hz compression test

| Test step | 1 | 2 | 3 | 4 | 5 | 6 | 7 | 8 |
|---|---|---|---|---|---|---|---|---|
| Strain amplitude | Test start | 0.25% | 0.50% | 0.75% | 1.00% | 1.25% | 1.5% | End Test |
| Cycles | 0 | 100 | 100 | 100 | 100 | 100 | 100 | 0 |

Table 4. 4 Test plan for 60 Hz compression test

| Test step | 1 | 2 | 3 | 4 | 5 | 6 | 7 | 8 |
|---|---|---|---|---|---|---|---|---|
| Strain amplitude | Test start | 0.25% | 0.50% | 0.75% | 1.00% | 1.25% | 1.5% | End Test |
| Cycles | 0 | 600 | 600 | 600 | 600 | 600 | 600 | 0 |

Figure 4.20 shows the experimental result of the MRE samples under non-magnetic field, and Figure 4.21 is the test result of the MRE sample under 265 mT magnet field. The test frequency is 10 Hz and the test temperature are 30 ℃.

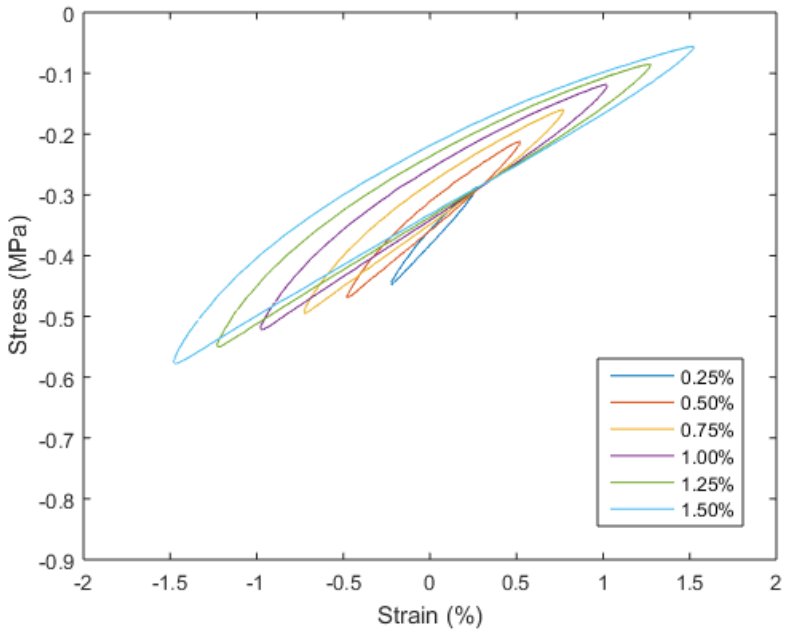


Figure 4. 20 Hysteresis loops of MRE samples under uniaxial compression with vibration frequency of 10 Hz, non-magnetic field, pre-strain of 5%, and different strain amplitudes from 0.25% to 1.5% in test temperature of 30 °C

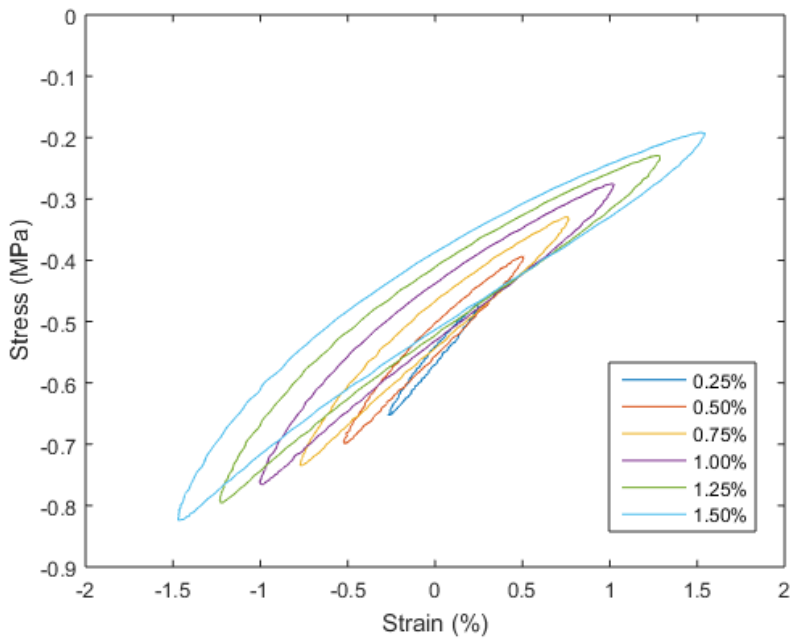


Figure 4. 21 Hysteresis loops of MRE samples under uniaxial compression with vibration frequency of 10 Hz, external magnetic field of 265 mT, pre-strain of 5%, and different strain amplitudes from 0.25% to 1.5% in test temperature of 30 °C

From Figure 4.20 to Figure 4.23, it can be noticed that the main axis of hysteresis loop has shown a shift to lower values with increasing of strain amplitude for both test frequency

conditions. This mechanical phenomenon indicates that the stiffness of the MRE sample decreases as the strain amplitude is increased. The nonlinear relationship between stress and strain appears much more obvious when the strain amplitude is increased. At the same time, the slope of stress-strain loop decreases slightly with the rising of strain amplitudes which is caused by the Mullins effect of filled rubber and rubber-like material. Each test sample runs hundreds of cycles, and appears to become much softer when the number of the cycle increased.

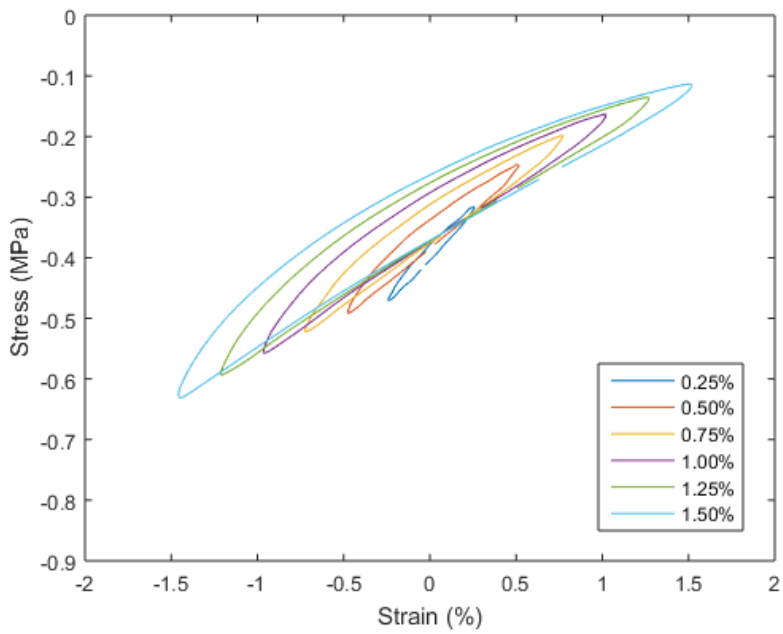


Figure 4. 22 Hysteresis loops of MRE sample under uniaxial compression with vibration frequency of 60 Hz, non- magnetic field, pre-strain of 5%, and different strain amplitudes from 0.25% to 1.5% in test temperature of 30 °C

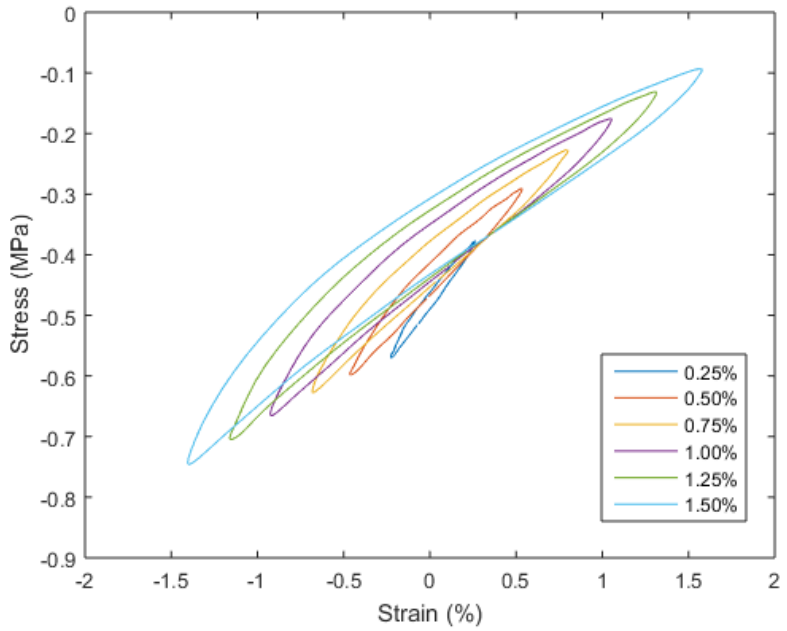


Figure 4. 23 Hysteresis loops of MRE sample under uniaxial compression with vibration frequency of 60 Hz, external magnetic field of 265 mT, pre-strain of 5%, and different strain amplitudes from 0.25% to 1.5% in test temperature of 30 ℃

Figure 4.22 shows the test result of MRE samples under non-magnetic field, and Figure 4.23 is the experiment result under 265 mT magnetic field. The test frequency is 60 Hz and the test temperature are 30 ℃. It is also found from Figure 4.20 to Figure 4.23 that the shape of the hysteresis loops changes from an elliptical to an approximate elliptical as the increasing of strain amplitude. The little deviation occurs in the vicinity of strain peaks which may be caused by the interfacial friction due to a change in applied strain direction.

#### 4.3.1.4 Temperature dependence

For temperature dependent dynamic mechanical test, the pre-strain of the MRE sample is 5% and strain amplitude is 1.5%. The loading frequency is 60 Hz and the test temperature range is from room temperature (20 ℃) to 60 ℃. In the DMA experiment, each MRE sample has run enough cycles before data recording to reduce the impact of the Mullins effect.

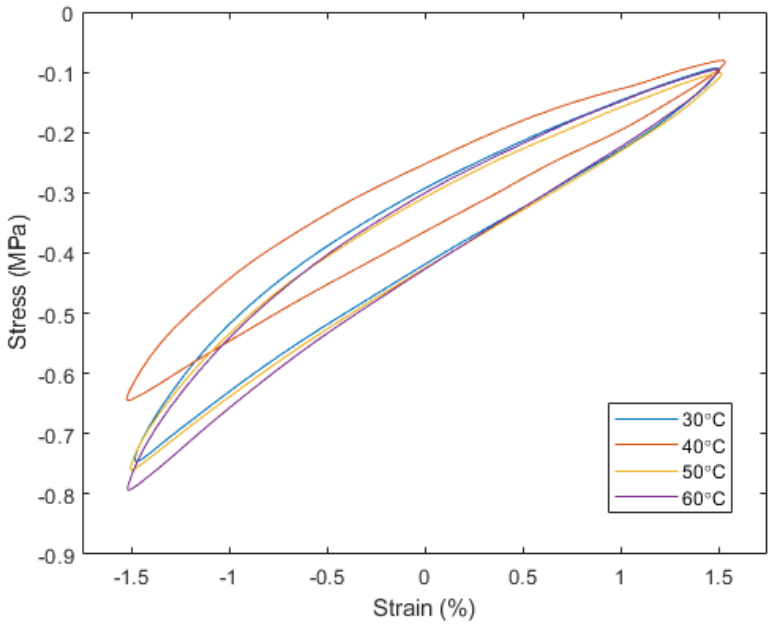


Figure 4. 24 Hysteresis loops of MRE sample under uniaxial compression with pre-strain of 5%, strain amplitude of 1.5%, vibration frequency of 60 Hz, and external magnetic field of 265 mT in different test temperatures

Figure 4.24 shows the stress-strain relationships of anisotropic MREs with different temperature. Large differences in the shape and position of hysteresis loops can be observed between various test temperature conditions. Compering with the other impact factors above, the test temperature has more significant influence on dynamic mechanical properties of MREs, and much more complicated.

### 4.3.2 Dynamic mechanical properties

#### 4.3.2.1 Dependence on strain and frequency

Figure 4.25 to Figure 4.27 show that the effects of the strain amplitude and frequency on the storage modulus and loss modulus of the MRE samples under uniaxial harmonic compression with the pre-strain of 5%. The test temperature is room temperature which is about 20 ℃ and the external magnetic field is 0 mT. The results are obtained by calculating the average of the DMA measurement data of three samples for each test conditions.

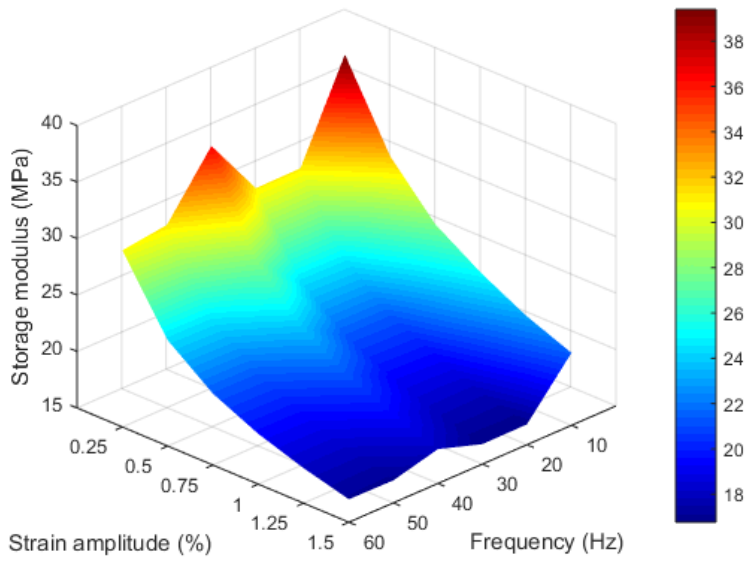


Figure 4. 25 Dependence of storage modulus on strain amplitude at room temperature, pre-strain of 5%, magnetic field of 0 mT

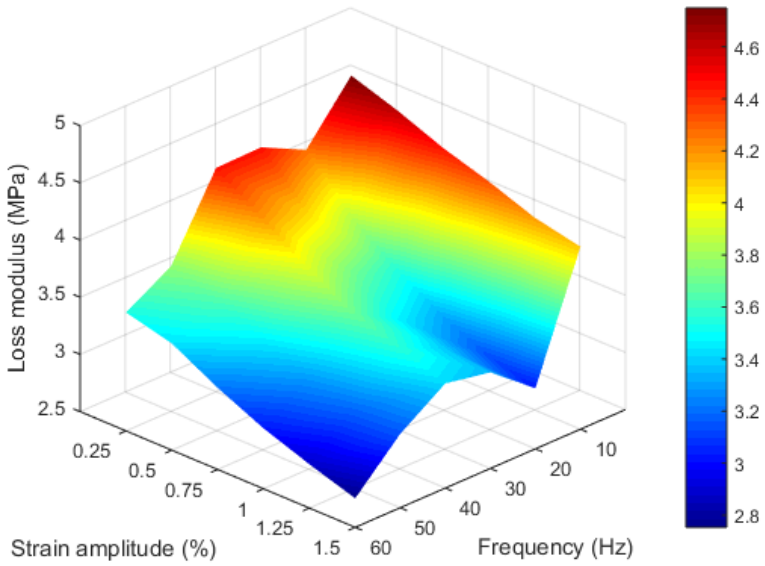


Figure 4. 26 Dependence of loss modulus on strain amplitude at room temperature, pre-strain of 5%, magnetic field of 0 mT

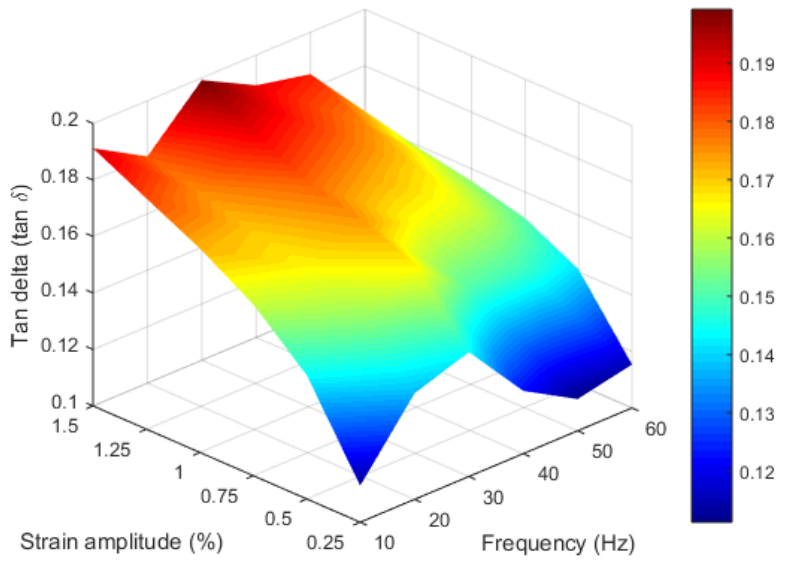


Figure 4. 27 Dependence of tan delta on strain amplitude at room temperature, pre-strain of 5%, magnetic field of 0 mT

Figure 4.25 reveals that the storage modulus of the MRE samples decreases with increasing strain amplitude under various loading frequencies. It can be noticed the tendencies of each curve are almost the same, which indicates the strain amplitude is an independent impact factor on dynamic modulus of the MRE material. The storage modulus decreases rapidly from 0.25% to 0.75% strain amplitude, and then becomes slowly from 0.75% to 1.5% strain amplitude. As shown in Figure 4.26, the loss modulus of the MRE samples also decreases with increasing strain amplitudes. In the meanwhile, the variation tendency of loss modulus with vibration frequency displays a more or less sigmoidal shape. It is obvious that the loss modulus of the MRE specimens at low excitation frequency is higher than that under high excitation frequency. Figure 4.27 shows the dependence of tangent delta value on strain amplitude and vibration frequency at room temperature. The maximum tan delta value is achieved when the vibration frequency is around 30 Hz and the strain amplitude is 1.5%. In low strain amplitude test conditions, the tangent delta first increases with the increasing of vibration frequency reaches the perk value at 30Hz and then decreases with the increment of vibration frequency. The tendency of the curve in high strain amplitude condition is different. The tangent delta first decreases and then increases with increasing vibration frequency. After reaching the perk value, it decreases again with the increment vibration frequency.

Figure 4.28 to Figure 4.30 show that the effects of the strain amplitude and frequency on the storage modulus and loss modulus of the MRE samples under external magnetic field of 265 mT. The test temperature is around 20 °C (room temperature) and the pre-strain is 5%. The

results are obtained by calculating the average of the DMA measurement data of three samples for each test conditions.

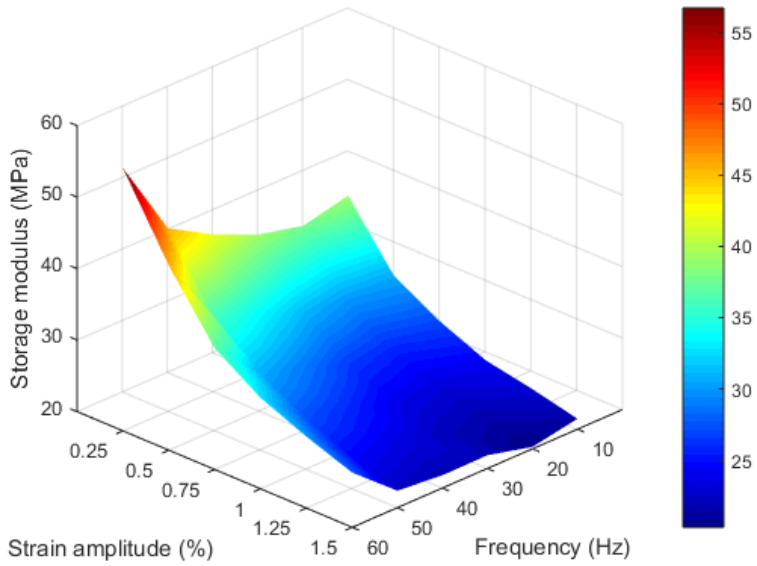


Figure 4. 28 Dependence of storage modulus on strain amplitude at room temperature, pre-strain of 5%, magnetic field of 265 mT

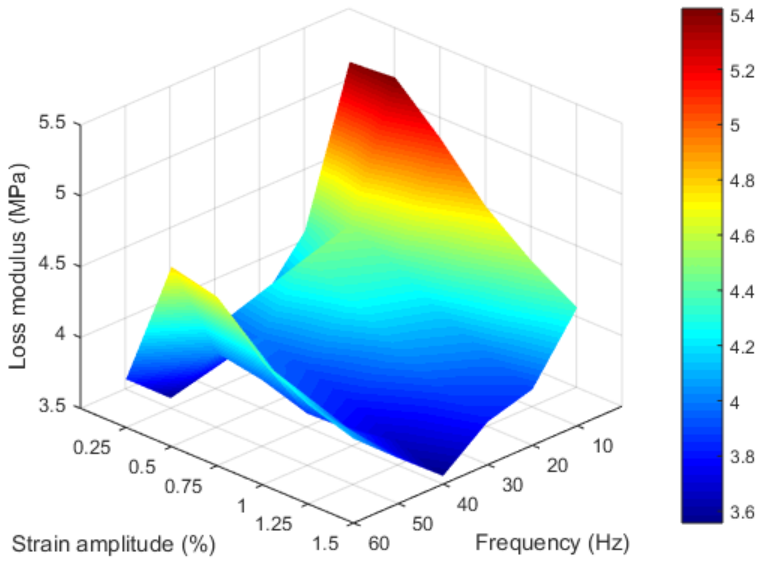


Figure 4. 29 Dependence of loss modulus on strain amplitude at room temperature, pre-strain of 5%, magnetic field of 265 mT

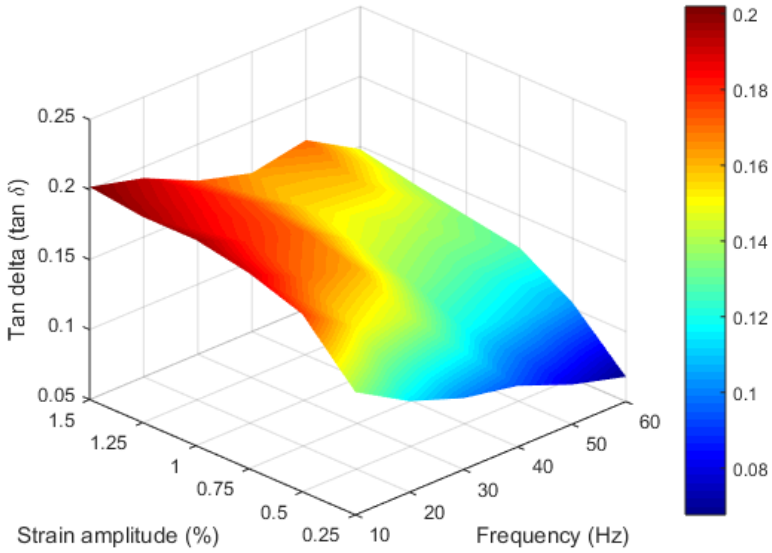


Figure 4. 30 Dependence of tan delta on strain amplitude at room temperature, pre-strain of 5%, magnetic field of 265 mT

It can be seen from Figure 4.28 that the storage modulus increases when the strain amplitude decreases and excitation frequency increases. However, the dependence of storage modulus on frequency does not change significantly with the variation of strain amplitude. For the same frequency and external magnetic field (as shown in Figure 4.25 and Figure 4.28), the MRE under lower strain amplitude always possess higher storage modulus than that under large strain amplitude. Furthermore, MRE material under lower strain amplitude shows greater dependence on excitation frequency than the higher ones. This phenomenon is due to the change of storage modulus with increasing frequency is much more obvious especially when the vibration frequency over 40 Hz. It can be observed from Figure 4.29 that the loss modulus decreases with the increasing of excitation frequency in the range of 10 Hz to 40 Hz and starts to rise up with increasing frequency in the range of 40 Hz to 50 Hz, then drop again with the increment of vibration frequency until 60 Hz. For the same frequency and magnetic field (as shown in Figure 4.26 and Figure 4.29), the loss modulus of the MRE under high strain amplitude is always greater than that under the lower strain amplitude when the strain amplitude is over 0.25%. Figure 4.30 shows that the tangent delta of the MRE in the presence of 265 mT external magnetic field increases with the increasing of strain amplitude and decreases as vibration frequency is increased. It indicates that the higher tangent delta of the MRE normally achieved at the high strain amplitude and low vibration frequency in the presence of external magnetic field.

Figure 4.31 to Figure 4.33 illustrate the variation of the dynamic properties of MRE samples

with different pre-strains and strain amplitudes under zero and 265 mT magnetic field. The DMA experiments are carried out in the room temperature condition and the excitation frequency is set as 60 Hz.

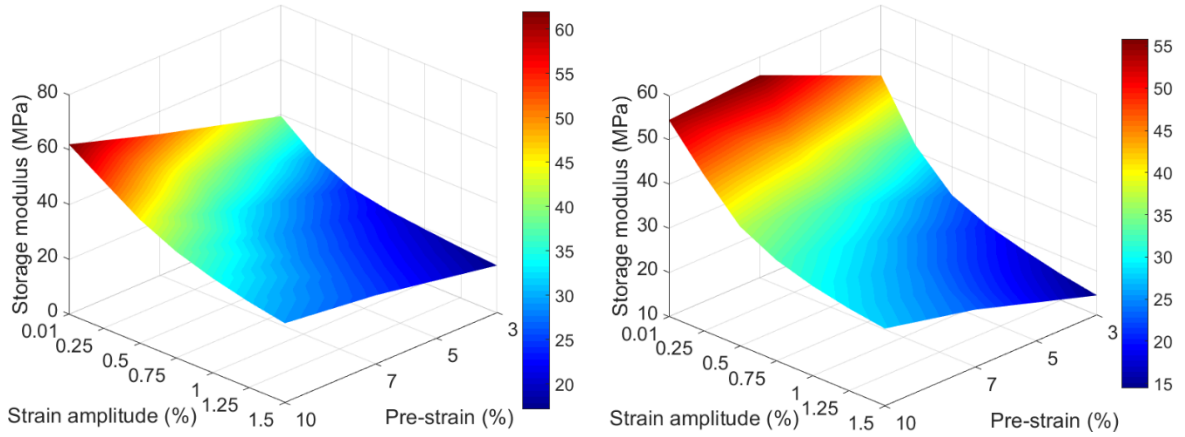


(a) (b)

Figure 4. 31 Dependence of storage modulus on strain amplitude and pre-strain at room temperature, excitation frequency of 60 Hz with (a) 0 mT, (b) 265 mT magnetic field

Figure 4.31 shows that the storage modulus of the MRE samples decreases with increasing strain amplitude in the absence and application of an external magnetic field. It can be found that the external magnetic field has little effect on the tendency of the storage modulus with the strain amplitude but affects the storage modulus value. The variation tendency is almost the same for the MRE sample with or without application of external magnetic field. However, when the strain amplitude changes from 0.01% to 1.5%, the storage modulus decreases by 67% under external magnetic field of 265 mT while the decrement of the storage modulus is about 50% in the absence of external magnetic field. Under the same strain amplitude, the MRE owns higher storage modulus when the pre-strain is increased, the increments are 52% and 30% respectively when the pre-strain varies from 3% to 10%.

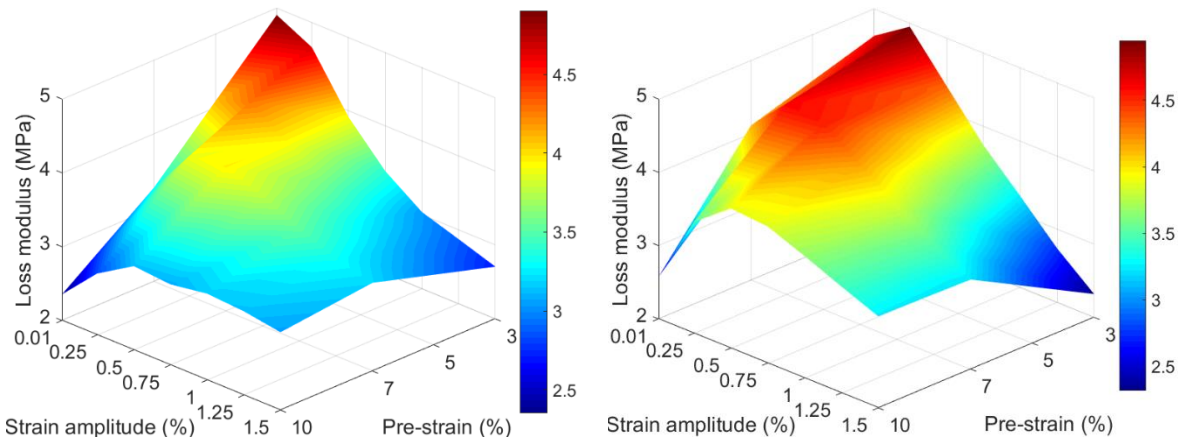


(a) (b)

Figure 4. 32 Dependence of loss modulus on strain amplitude and pre-strain at room temperature, excitation frequency of 60 Hz with (a) 0 mT, (b) 265 mT magnetic field

According to Figure 4.32, the loss modulus of the MRE samples displays an obvious dependence on the strain amplitude and pre-stain. In zero external magnetic field condition, the loss modulus of the MRE samples increases with the increasing of strain amplitude under high pre-strain (e.g. 7% and 10% as shown in Figure 4.32), and then starts to decrease. Otherwise, the loss modulus only decreases with the increment of stain amplitude when the pre-strain is 3% as shown in Figure 4.32. However, in high external magnetic field condition, the loss modulus of the MRE samples increases and then decreases with the increasing of strain amplitude in all pre-strain tests. This means the relationship between the MRE's loss modulus and the strain can be significant affected by the external magnetic field.

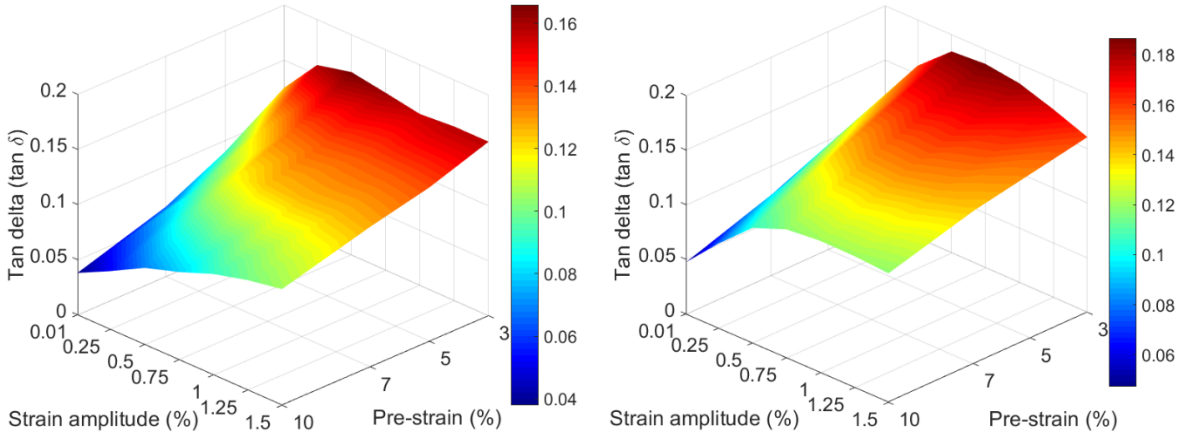


(a) (b)

Figure 4. 33 Dependence of tangent delta on strain amplitude and pre-strain at room temperature, excitation frequency of 60 Hz with (a) 0 mT, (b) 265 mT magnetic field

Figure 4.33 shows that the tangent delta decreases with increasing the pre-strain for the MRE samples both without and with the application of external magnetic field. It also indicates that the tangent delta increases with the increasing of strain amplitude when the pre-stain is over 7%.

#### 4.3.2.2 Dependence on magnetic field

The following Figure 4.34 to Figure 4.36 show that the influence of the external magnetic field and vibration frequency on the storage modulus and loss modulus of the MRE samples under uniaxial harmonic compression with the strain amplitude of 1.5% and the pre-strain of 5%. The DMA tests are carried out in room temperature (about 20 ℃).

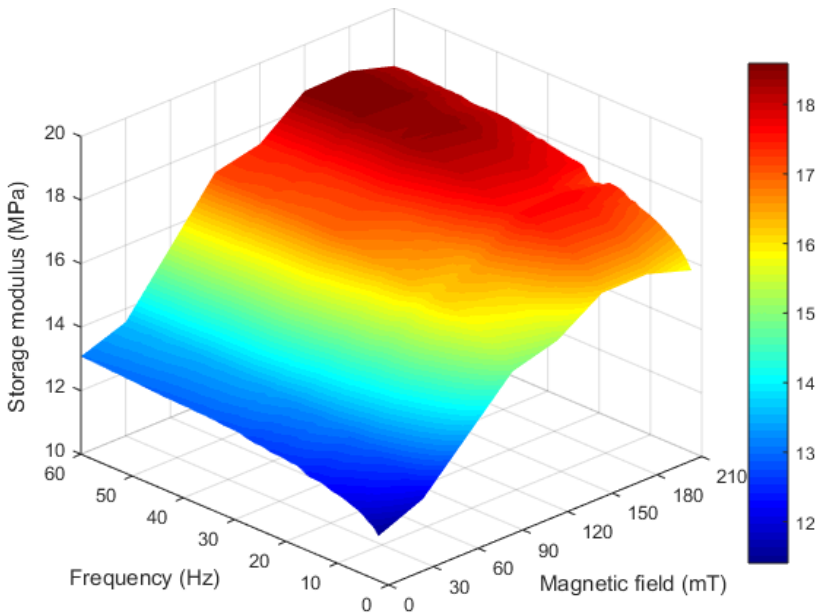


Figure 4. 34 Dependence of storage modulus on external magnetic field and frequency at room temperature, pre-strain of 5%, and strain amplitude of 1.5%

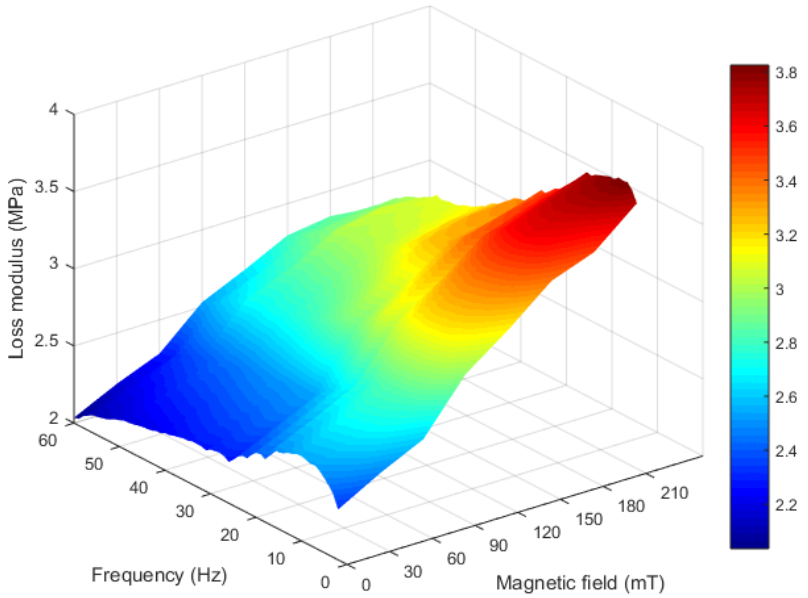


Figure 4. 35 Dependence of loss modulus on external magnetic field and frequency at room temperature, pre-strain of 5%, and strain amplitude of 1.5%

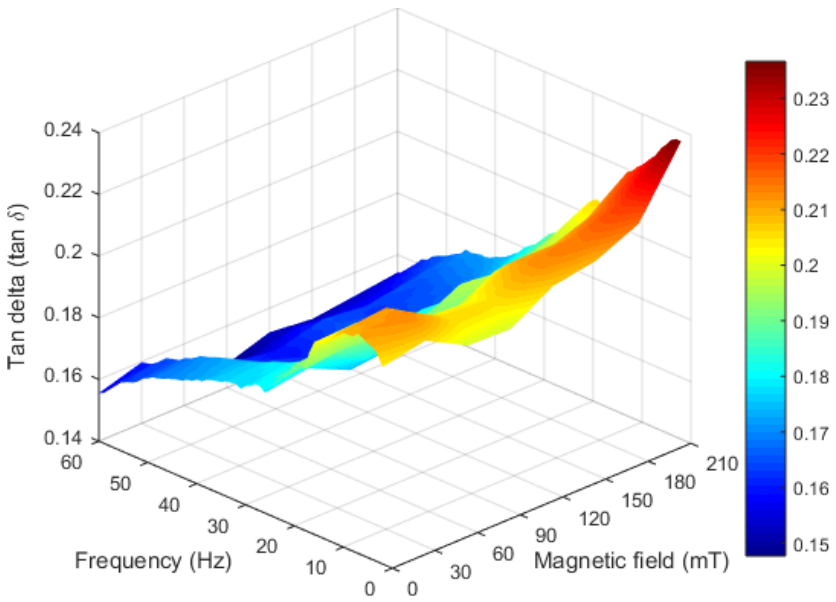


Figure 4. 36 Dependence of tan delta on external magnetic field and frequency at room temperature, pre-strain of 5%, and strain amplitude of 1.5%

Figure 4.34 shows that the storage modulus of the MRE samples increases with the increasing of magnetic field and excitation frequency. For the same frequency, the MRE under higher external magnetic field always possess higher storage modulus than the MRE with lower magnetic field. When an external magnetic field is applied, the magnetic forces are generated between iron particles that force them to move inside the silicon matrix. Furthermore, the MRE without magnetic field shows greater dependence on frequency than the MRE under higher external magnetic field. Figure 4.35 indicates that at the same frequency, the MRE samples under external magnetic field always have much higher loss modulus than the MRE samples in the absence of magnetic field. The influence of the excitation frequency is more significant when the MRE under external magnetic field than the MRE without application of external magnetic field. Furthermore, when the test is carried out in the absence of external magnetic field, the change of the loss modulus under 30 Hz is not such obvious as the results over 40 Hz. According to Figure 4.36, the maximum value of the tangent delta occurs at high external magnetic field and low vibration frequency. It also indicates that the tangent delta increases when the external magnetic field is increased. This tendency is more clearly and typically at low vibration frequency condition.

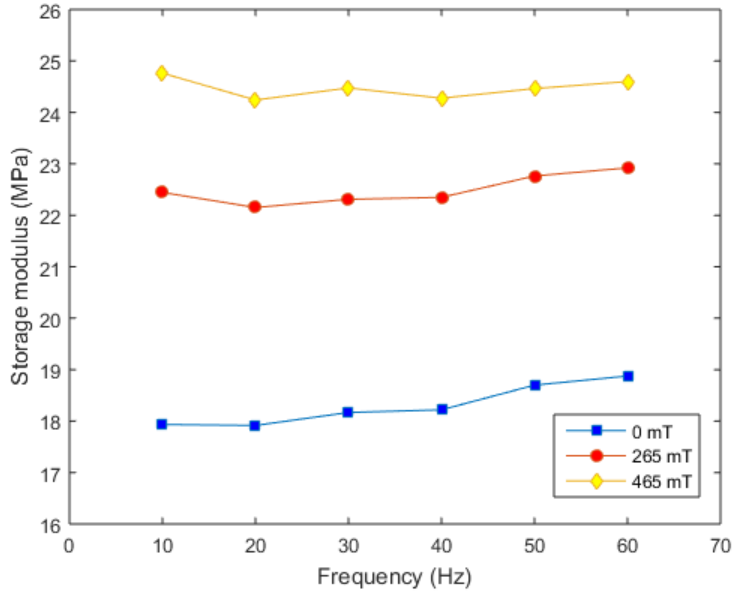


Figure 4. 37 Dependence of storage modulus on external magnetic field and frequency at room temperature, pre-strain of 5%, and the strain amplitude is 1.5%

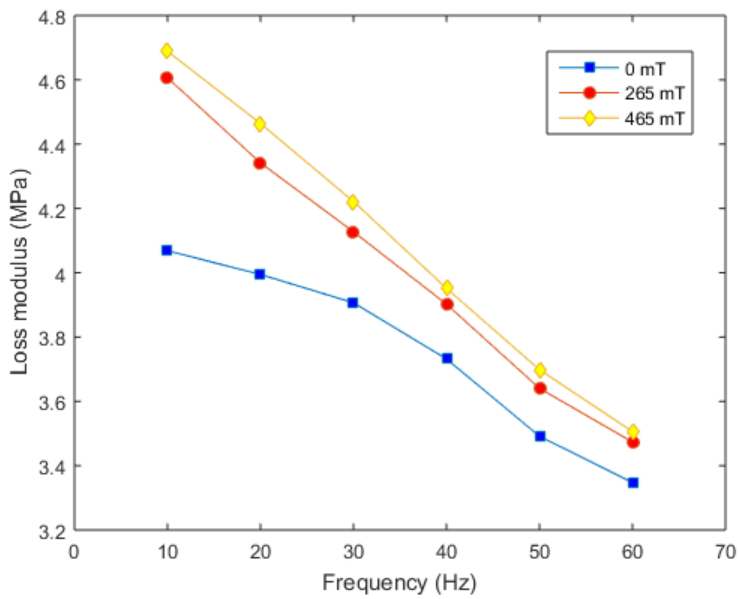


Figure 4. 38 Dependence of loss modulus on external magnetic field and frequency at room temperature, pre-strain of 5%, and the strain amplitude is 1.5%

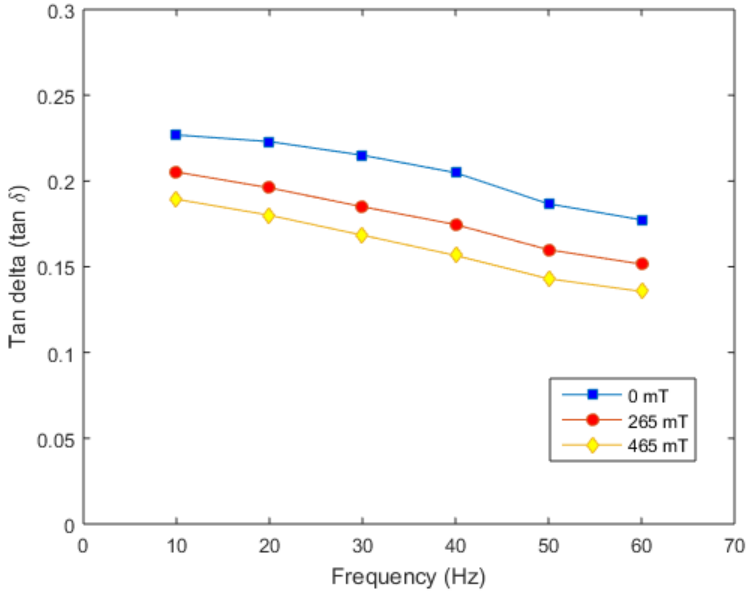


Figure 4. 39 Dependence of tangent delta on external magnetic field and frequency at room temperature, pre-strain of 5%, and the strain amplitude is 1.5%

Figure 4.37 to Figure 4.39 show the frequency dependent dynamic modulus of the MRE samples under uniaxial harmonic compression with the pre-strain of 5% and the strain amplitude of 1.5%. The DMA experiments are performed in room temperature and external magnetic field of 0 mT, 265 mT, and 465 mT, respectively. It can be seen from Figure 4.37 that the increment of the storage modulus between 265 mT and 465 mT magnetic field is smaller than that between 0 mT and 265 mT magnetic field. It may due to the MRE material approaching its magnetic saturation state. This means that the storage modulus of the MRE increases with the increasing of magnetic field but its incremental rate is gradually slowed down until stopping due to magnetic saturation. The storage modulus of the MRE will not become higher obviously while further increasing the external magnetic field. This phenomenon is much more clearly showed by the loss modulus of the MRE samples as shown in Figure 4.38. The loss modulus of the MRE samples at low vibration frequency with zero magnetic field is much lower than that under higher magnetic field. Figure 4.39 shows the tangent delta changes with the vibration frequency under different magnetic fields. The tangent delta is decreased with the increment of both vibration frequency and external magnetic field. However, even the DMA test is carried out under the extraordinary large external magnetic field, the tangent delta does not change too much with the magnetic field.

The following figures show that the coupling influence of the external magnetic field and strain amplitude on the material dynamic modulus. The test temperature is 20 °C, the pre-strain of

this test is 5% and the test frequency are 10 Hz and 60 Hz.

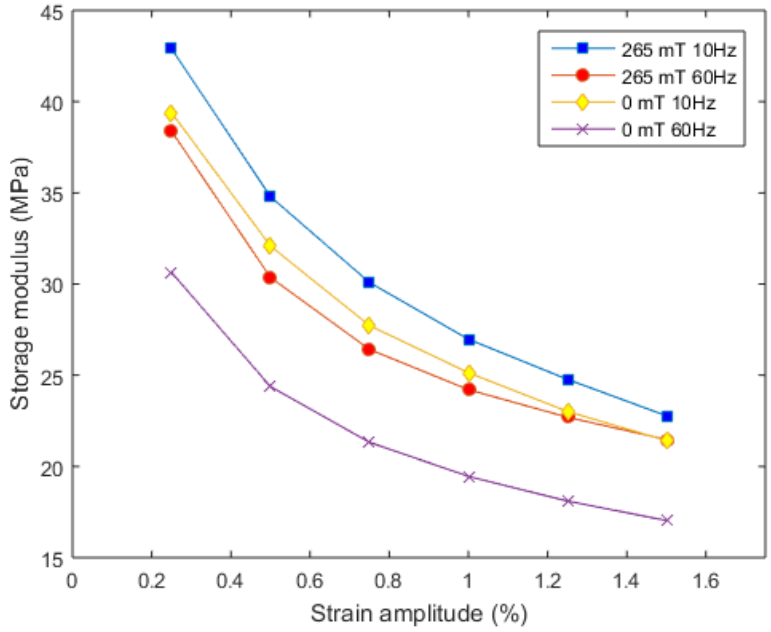


Figure 4. 40 Dependence of storage modulus on external magnetic field and strain amplitude at room temperature, pre-strain of 5%, and the test frequency is 10 Hz and 60 Hz

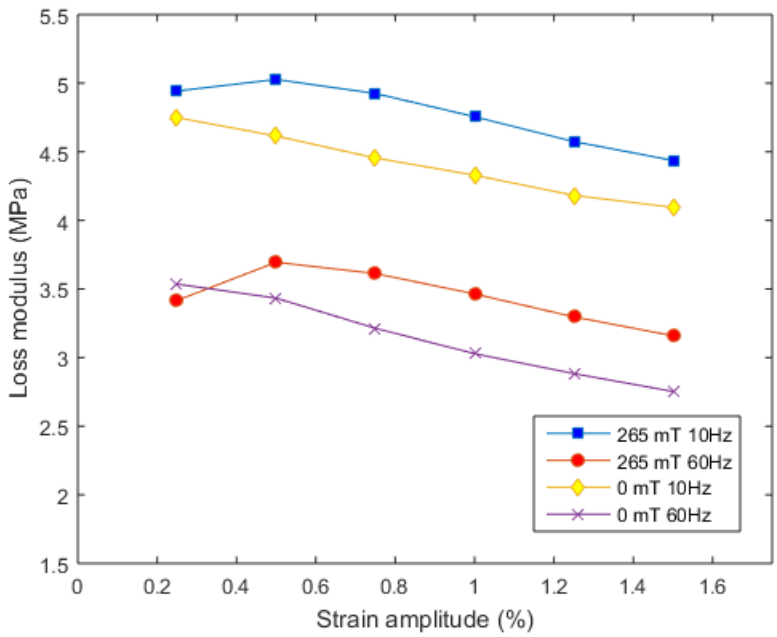


Figure 4. 41 Dependence of loss modulus on external magnetic field and strain amplitude at room temperature, pre-strain of 5%, and the test frequency is 10 Hz and 60 Hz

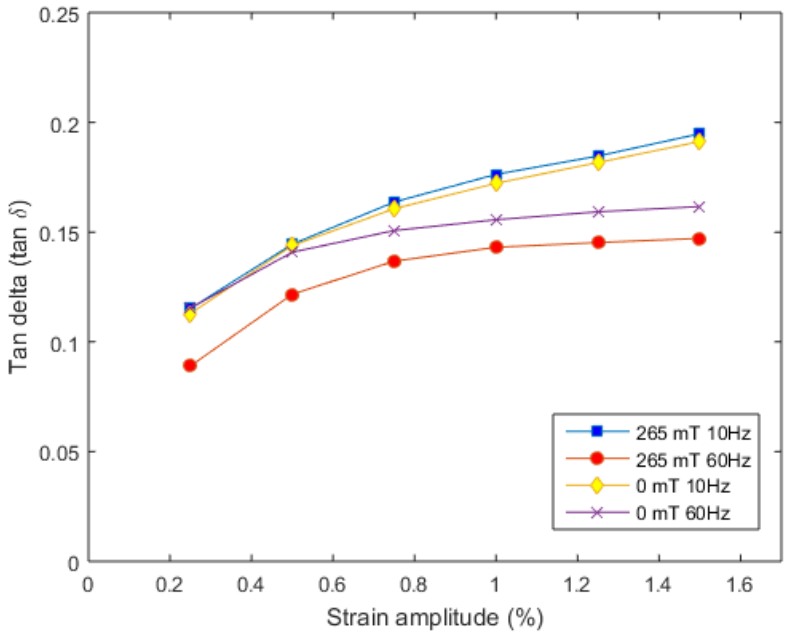


Figure 4. 42 Dependence of tangent delta on external magnetic field and strain amplitude at room temperature, pre-strain of 5%, and the test frequency is 10 Hz and 60 Hz

It can be observed that the MRE samples under external magnetic field always have higher storage modulus than the samples without external field at both high frequency and low frequency as shown in Figure 4.40. Furthermore, under high strain amplitude condition, the influence of the external magnetic field is much more significant. Figure 4.41 exhibits that the loss modulus decreases with the increasing of strain amplitude under non-magnetic field. However, the test results are a bit more complicate when MRE samples subjected to external magnetic field. The loss modulus first increases and reaches the highest value at 0.5% strain amplitude and then decreases with the strain amplitude. It needs to be noticed that the loss modulus of the MRE under 265 mT external magnetic field and 0.25% strain amplitude is lower than that in the absence of external magnetic field. Figure 4.42 shows the tangent delta of the MRE samples changes with the strain amplitude. According to the experiment results, the tangent delta is always increased with the increment of strain amplitude. This tendency is much more obvious in low vibration frequency conditions than that in high vibration frequency conditions.

### 4.3.3 Temperature effect

#### 4.3.3.1 Coupling effect of temperature and vibration frequency

Following figures show the DMA test results of the MRE samples under uniaxial harmonic compression with the pre-strain of 5% and the strain amplitude of 1%. Each test is carried out under various magnetic fields and the test temperatures ranging from 25℃ to 60℃ with the interval of 5 ℃.

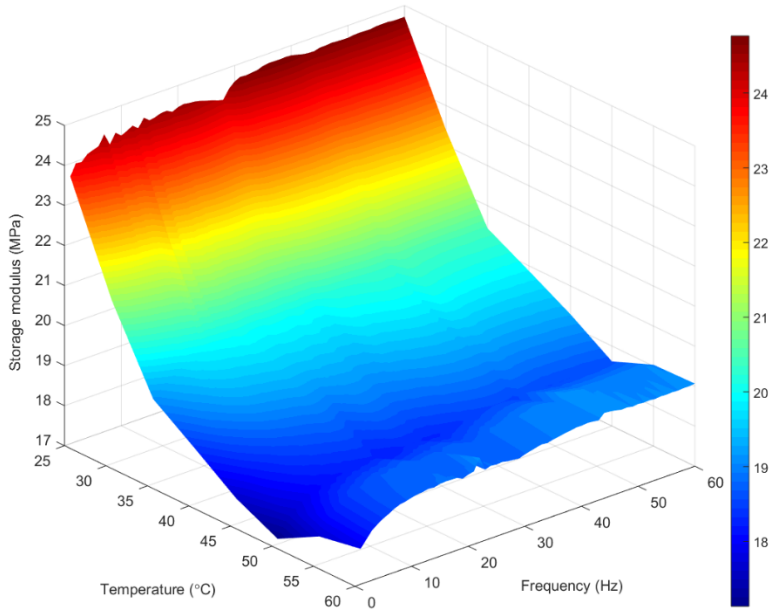


Figure 4. 43 Dependence of storage modulus on temperature and frequency at pre-strain of 5%, strain amplitude of 1%, and magnetic field of 0 mT

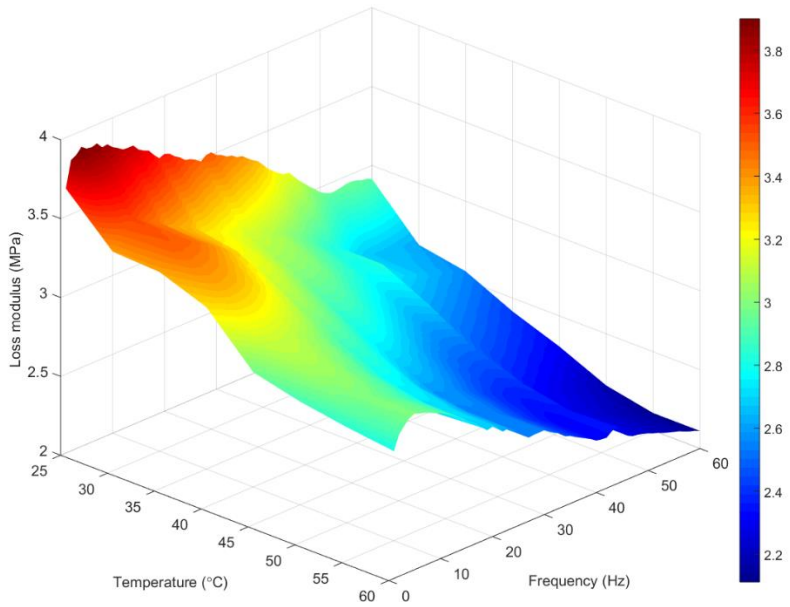


Figure 4. 44 Dependence of loss modulus on temperature and frequency at pre-strain of 5%, strain amplitude of 1%, and magnetic field of 0 mT

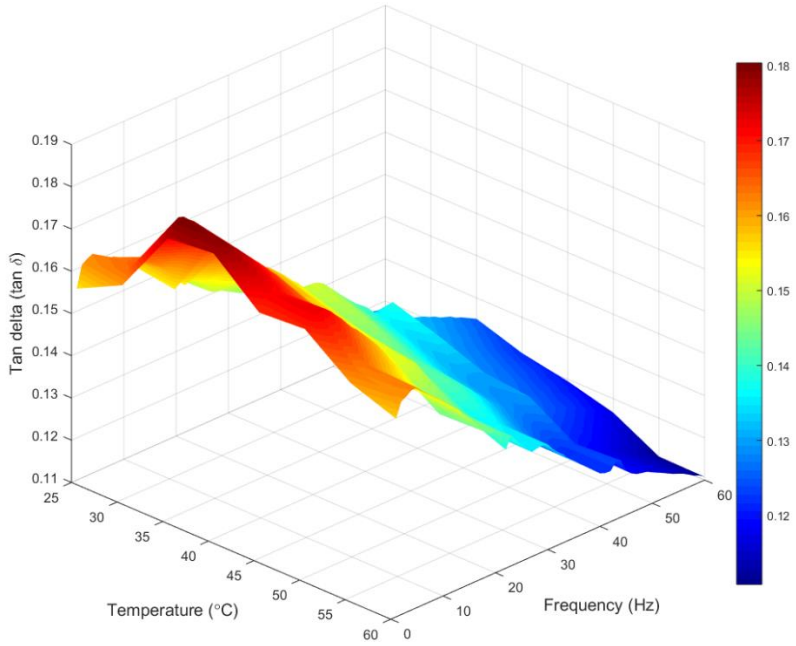


Figure 4. 45 Dependence of tan delta on temperature and frequency at pre-strain of 5%, strain amplitude of 1%, and magnetic field of 0 mT

Figure 4.43 shows the temperature effect on the storage modulus of the MRE samples under different test frequencies without external magnetic field. According to the DMA test results under various temperaures, the storage modulus first drops when the temperature gets higher and reaches its minimum value at about 50 °C, and then starts increasing with the rising temperature until 60 °C. This DMA test result is similar to the test data published by Zhang et al. (2011), although their MRE samples were fabricated by using the different matrix materials. Both the cis-polybutadiene rubber and natural rubber are selected as the MRE matrix material in their experiment. However, based on their experiment result, only the MRE contains the natural rubber appears to have this phenomenon. In order to investigate the causes of this phenomenon, the differential scanning calorimetry (DSC) test are carried out in this research. Based on the DSC test results, this material behaviour may be due to the MRE samples approaching its transition temperature. This transition behaviour is normally caused by the matrix material are usually rubber and rubber-like material which have various phase transition temperature.

Figure 4.44 shows the loss modulus changes with environment temperature and vibration frequency. The loss modulus drops roughly 25% while the environment temperature increases from 25 °C to 60 °C or vibration frequency increases from 1Hz to 60Hz. In addition, the loss modulus is reduced by 50% while the MRE material changes from the low frequency and low temperature to the high frequency and high temperature. This means both the environment

temperature and vibration frequency may have significant effect on the loss modulus of the MRE samples. Figure 4.45 indicates the dependence of tangent delta varies with the environment temperature and vibration frequency. The tangent delta reaches its maximum value at 35 °C then starts to decrease with the temperature. According to the experiment result, both the loss modulus and the tangent delta increase with the increasing of vibration frequency at low frequency (below 10 Hz) then start to decreases with further increasing vibration frequency at zero external magnetic field.

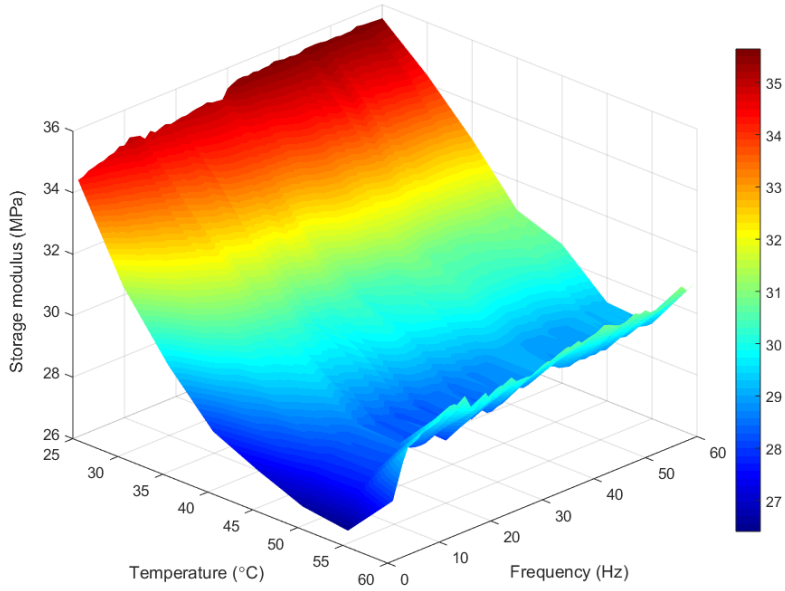


Figure 4. 46 Dependence of storage modulus on temperature and frequency at pre-strain of 5%, strain amplitude of 1%, and magnetic field of 265 mT

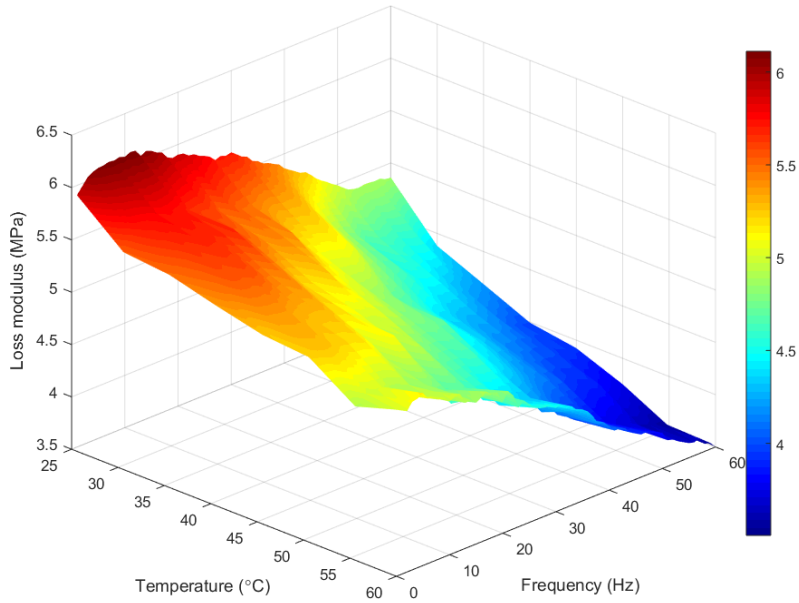


Figure 4. 47 Dependence of loss modulus on temperature and frequency at pre-strain of 5%, strain amplitude of 1%, and magnetic field of 265 mT

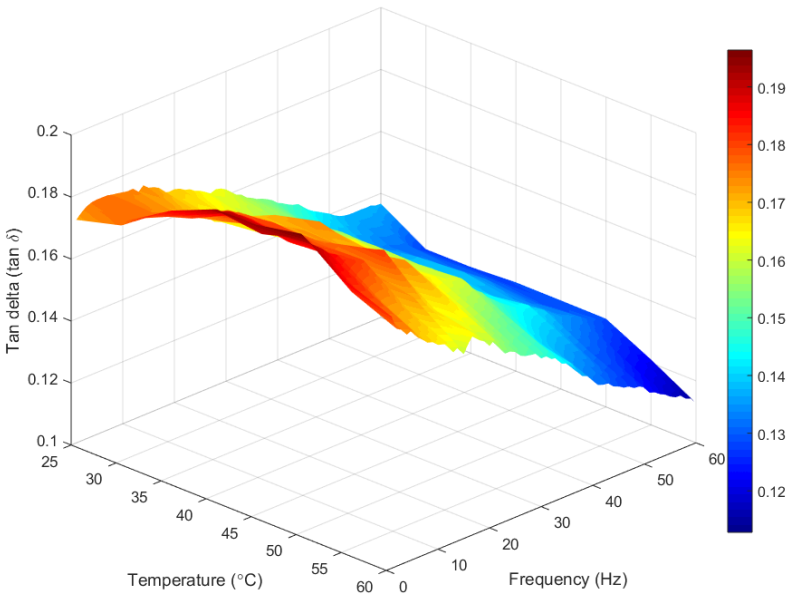


Figure 4. 48 Dependence of tan delta on temperature and frequency at pre-strain of 5%, strain amplitude of 1%, and magnetic field of 265 mT

Figure 4.46 reveals the relationship between the storage modulus of the MRE samples and the test temperature via different test frequency under external magnetic field of 265 mT. The variation tendency of the storage modulus are similar but much more obvious when comparing with the zero magnetic field condition. The curve of storage modulus changes with the environment temperature at low frequency is more obvious than that at high vibration frequency. The MRE material sample has its minimum storage modulus at temperature of 55 °C and excitation frequency of 1 Hz. When comparing with Figure 4.43, the storage modulus is increased almost 10 MPa while the external magnetic field changes from 0 mT to 265 mT. Figure 4.47 performs the loss modulus changes with the test temperature and vibration frequency. The loss modulus decreases with rising temperature when the vibration frequency is below 30 Hz. When the vibration frequency is over 30 Hz, the results is different from that in the low frequency conditions. The loss modulus falls off at the beginning, then increases to the second peak value at 50 Hz and decreases to the minimum value at 60 Hz. Figure 4.48 shows the tangent delta changes with both vibration frequency and environment temperature under 265 mT external magnetic field. The variation tendency of the tangent delta is totally different from that in the absence of magnetic field. The tangent delta is increased with the environment temperature and reaches the maximum value between 40 °C and 50 °C.

Figure 4.49 to Figure 4.51 show the DMA test results of the MRE samples under uniaxial harmonic compression with the pre-strain of 5% and the strain amplitude of 1% in different temperatures. Each test is carried out under external magnetic field of 465 mT and the test

temperature ranging from 25 °C to 60 °C with the interval of 5 °C.

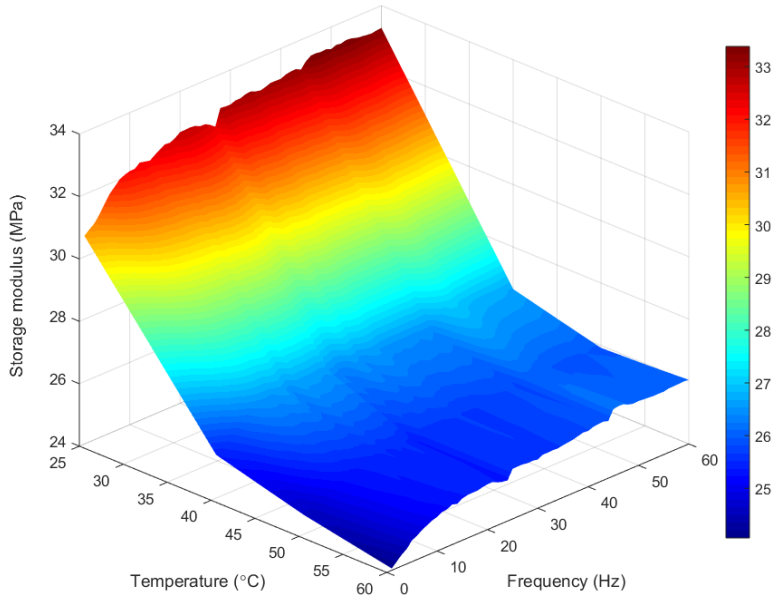


Figure 4. 49 Dependence of storage modulus on temperature and frequency at pre-strain of 5%, strain amplitude of 1%, and magnetic field of 465 mT

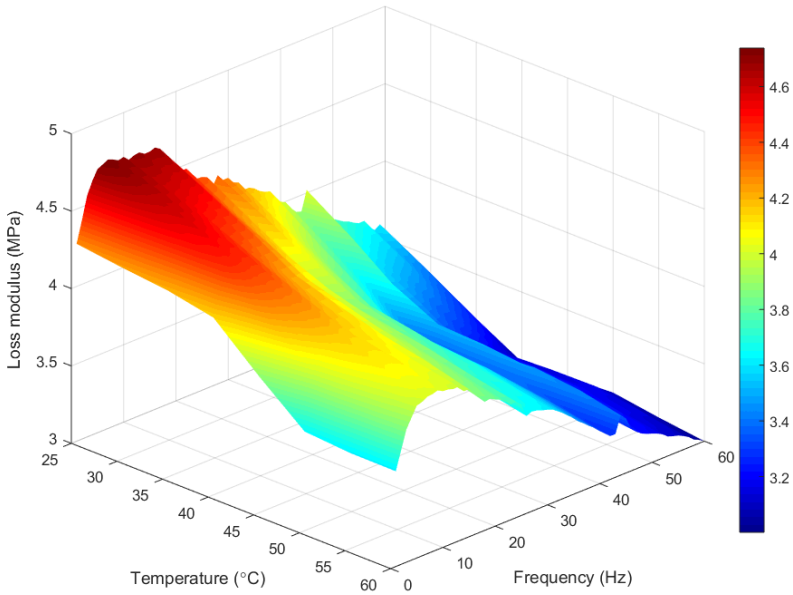


Figure 4. 50 Dependence of loss modulus on temperature and frequency at pre-strain of 5%, strain amplitude of 1%, and magnetic field of 465 mT

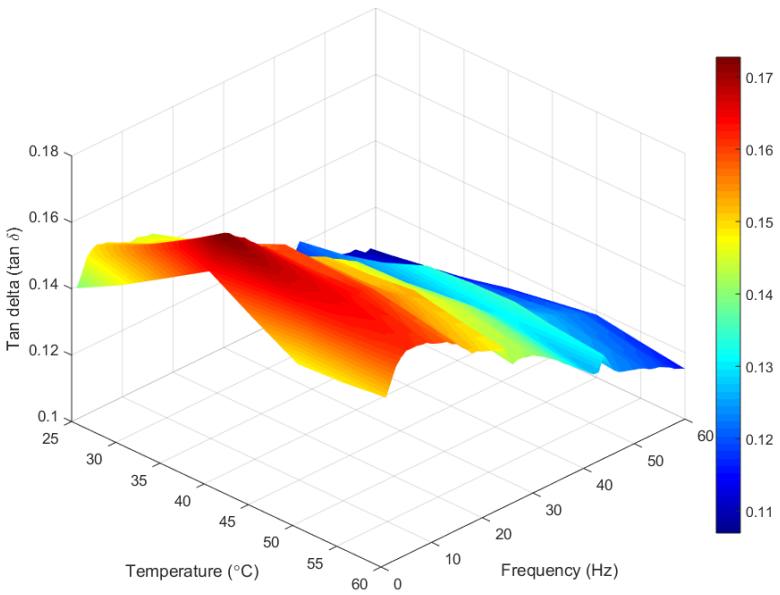


Figure 4. 51 Dependence of tan delta on temperature and frequency at pre-strain of 5%, strain amplitude of 1%, and magnetic field of 465 mT

Figure 4.49 shows the changes of the storage modulus with the test temperature and excitation frequency. For test frequency above 20 Hz, the storage modulus of the MRE falls off when the test temperature rises and reaches the minimum value at 50 °C, then starts to remain at a stable value or even slightly decreases until 60 °C. For test frequency below 10 Hz condition, the storage modulus curve is a bit different. It first drops with the environment temperature rapidly at the beginning stage and slows down when the temperature over 40 °C. Figure 4.50 indicates the relationship between the loss modulus and the test temperature and excitation frequency. It can be notice that the loss modulus is cut down linearly with the temperature when the vibration frequency is between 10 Hz and 30 Hz. For vibration frequency over 30 Hz, the loss modulus decreases from the maximum value at the first stage, then remains at a constant value when the temperature is between 40 °C and 50 °C. At last, the loss modulus drops again when the temperature increases until 60 °C. Figure 4.51 is dependence of tangent delta on the environment temperature and vibration frequency under high external magnetic field. The tangent delta achieves its maximum value at temperature of 40 °C and 10 Hz vibration frequency. The change tendency of the tangent delta with vibration frequency under magnetic field of 465 mT is similar at different environment temperature condition. The tangent delta first rises from 1 Hz to 10 Hz then starts to decrease. The environment temperature is another important factor, the tangent delta increases with the environment temperature at the first stage until 40 °C then starts to decrease.

#### 4.3.3.2 Coupling effect of pre-strain and strain amplitude with environment temperature

From the experiment results above, it can be noticed that the influence of excitation frequency on MRE dynamic modulus is not obvious comparing with that of other impact factors. Based on these, the DMA experiment results under 60 Hz excitation frequency are presented and discussed in this section. Figure 4.52 to Figure 4.57 are the DMA experiments results of the coupling effect of pre-strain and strain amplitude on the MRE samples near their transition temperature, which is around 45 °C. Therefore, the test temperature is selected at 40 °C and 50 °C to compare the DMA experiment data achieved in room temperature. The experimental results at zero magnetic field are presented only in this section, due to the tendency of coupling effect on the dynamic modulus with different external magnetic field are similar. The pre-strain is set as 3%, 5%, 7%, and 10%. The strain amplitude is range from 0.01% to 1.5%.

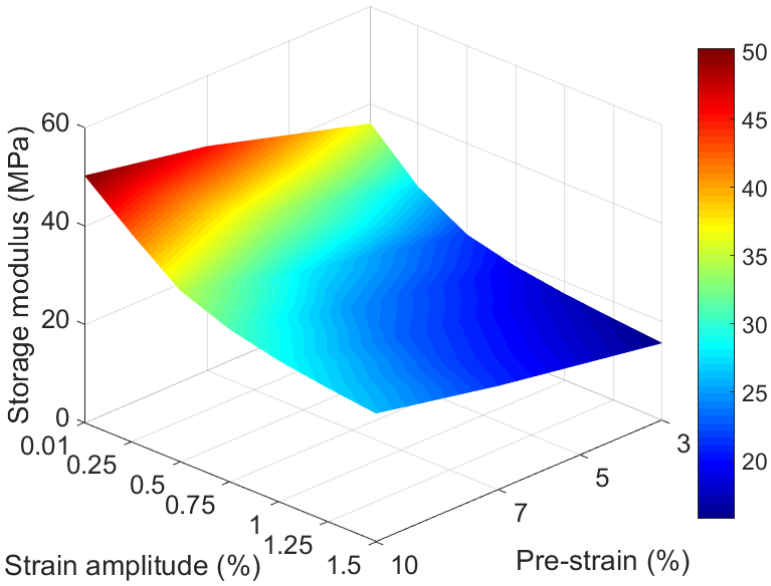


Figure 4. 52 Dependence of storage modulus on strain amplitude and pre-strain at 40 °C, 60 Hz excitation frequency and in absence of external magnetic field

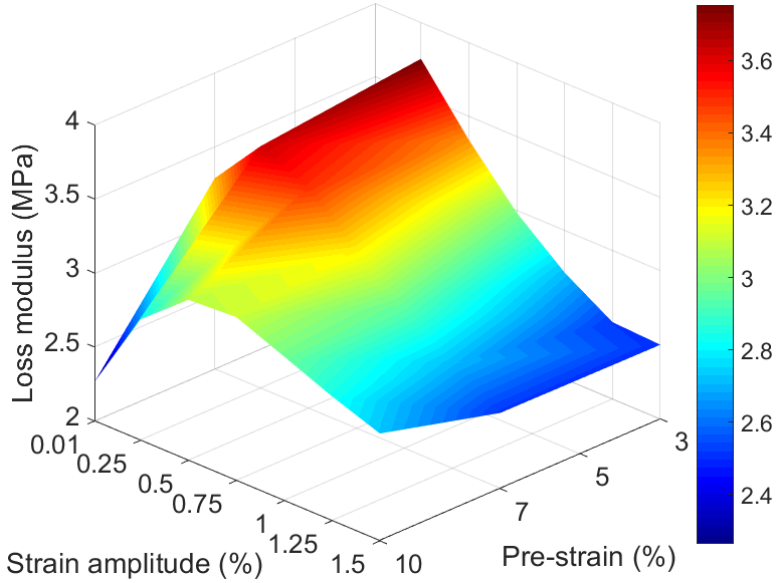


Figure 4. 53 Dependence of loss modulus on strain amplitude and pre-strain at 40 ℃, 60 Hz excitation frequency and in absence of external magnetic field

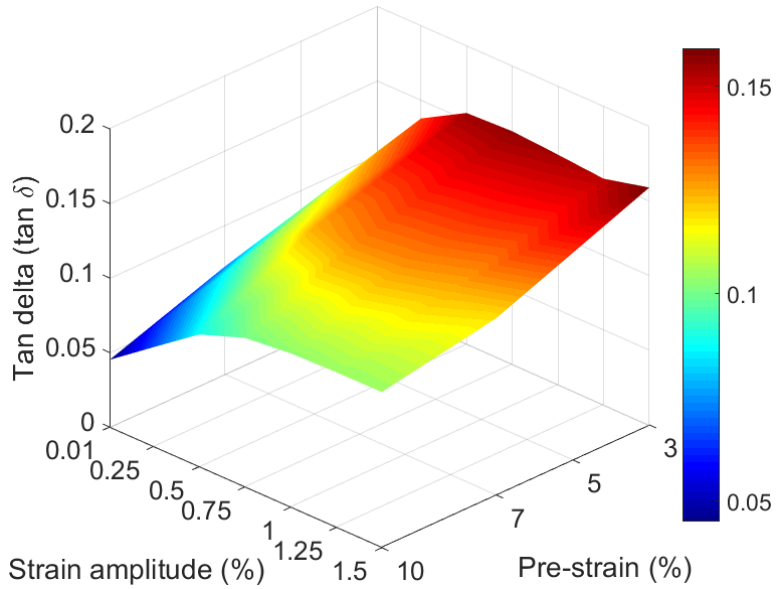


Figure 4. 54 Dependence of tan delta on strain amplitude and pre-strain at 40 ℃, 60 Hz excitation frequency and in absence of external magnetic field

Figures 4.52 to 4.54 illustrate the variation of dynamic modulus under 40 ℃ with different strain amplitudes and pre-strains. The storage modulus decreases by almost 50% when the strain amplitude is changed from 0.01% to 1.5%. The tendency of storage-strain amplitude curve does not change too much when the pre-strain varies. The loss modulus increases rapidly with the strain amplitude by around 25% between 0.01% and 0.25% when the pre-strain is 3%, 5% and 7%. This change of the loss modulus is more obvious when the pre-strain of the MRE is 10%. The increment of loss modulus becomes 33% when the strain amplitude varies from

0.01% to 0.5%. After reaching the peak value, the loss modulus then starts to decrease with the increasing of strain amplitude. The tangent delta increases with the strain amplitude and remains at a stable value after the strain amplitude is greater than 1%, in the meantime, it keeps decreasing with the increasing of pre-strain in this case.

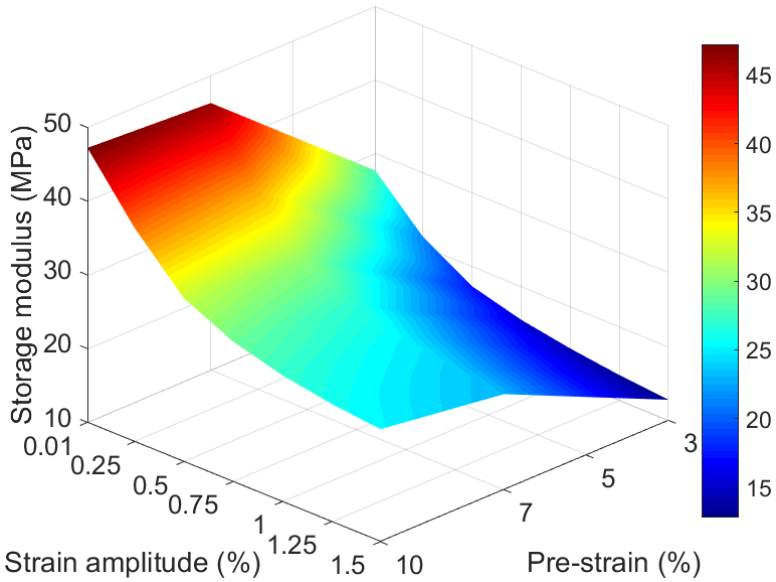


Figure 4. 55 Dependence of storage modulus on strain amplitude and pre-strain at 50 °C, 60 Hz excitation frequency and in absence of external magnetic field

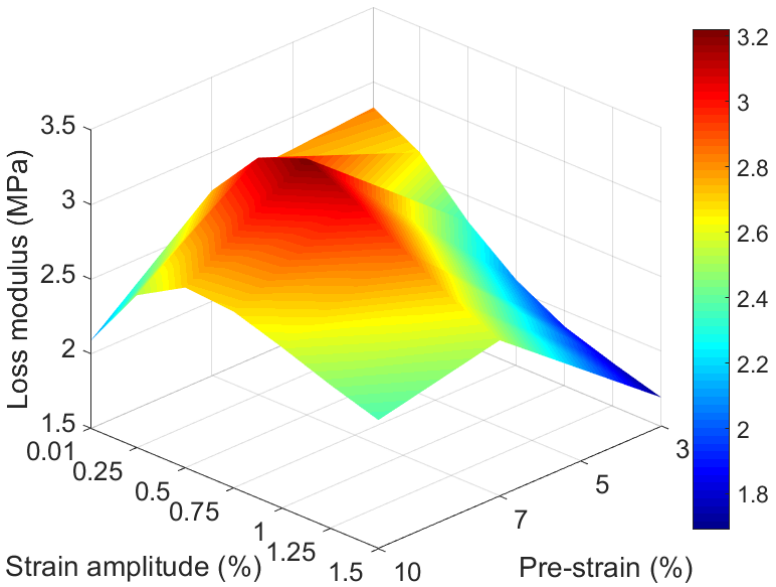


Figure 4. 56 Dependence of loss modulus on strain amplitude and pre-strain at 50 °C, 60 Hz excitation frequency and in absence of external magnetic field

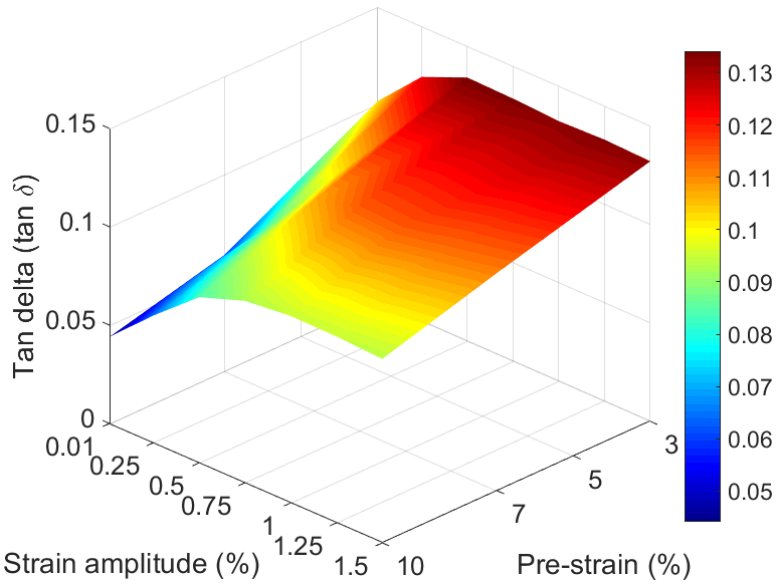


Figure 4. 57 Dependence of tan delta on strain amplitude and pre-strain at 50 °C, 60 Hz excitation frequency and in absence of external magnetic field

Figure 4.55 to Figure 4.57 illustrate the variation of dynamic modulus under 50 °C with different strain amplitudes and pre-strains. The storage modulus decreases by more than 60% when the strain amplitude is changed from 0.01% to 1.5%. This change of the storage modulus is more significant when comparing with the DMA experiment data achieved at 40 °C. The tendency of the storage modulus varies with the pre-strain is also slightly different, it remains at a stable value when the pre-strain is over 7%. The variation of the loss modulus with strain amplitude under temperature of 50 °C is the same as that under temperature of 40 °C when the pre-strain is over 7%. However, the loss modulus simply decreases with the strain amplitude when the pre-strain is below 5%.

According to experiment results, the coupling effect of pre-strain and strain amplitude with environment temperature on dynamic properties of the MRE is mainly caused by the complex variation of the loss modulus with strain and temperature. The relationship between the loss modulus curve and the dynamic strain is complicate in high temperature conditions, especially when the environment temperature is over MRE's transition temperature.

## 4.4 Static mechanical test

The static mechanical test is carried out in the Transport Systems Research Laboratory. Testing machine of Instron E plus 1000 with software Bulehill is selected for static test. The compression load speed is fixed at 0.01 mm/s. The original data is tracked by the load channel and displacement channel. The compressive stress and compressive strain are calculated

through the load data and sample dimensions. Through the static compression tests, the static mechanical properties of the MRE material is determined. These test results can be used to determine the pre-strain conditions for the DMA experiments of the MRE samples.

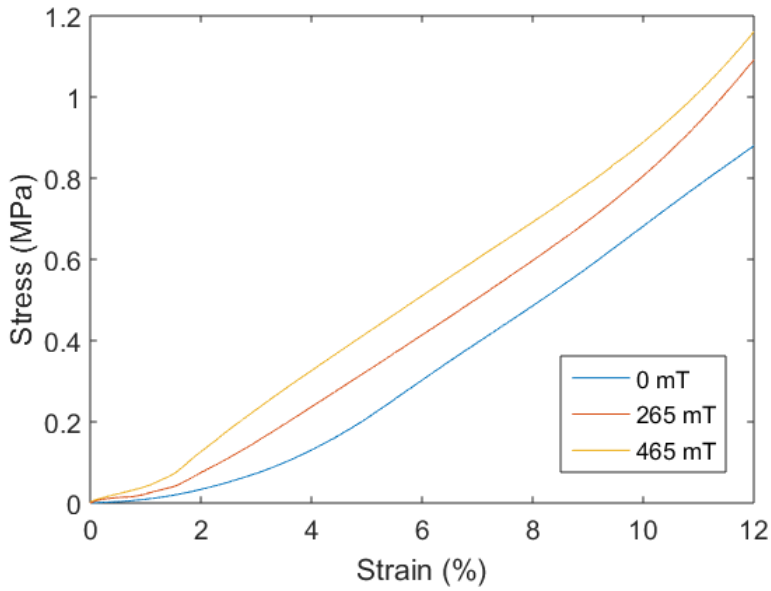


Figure 4. 58 The static stress-strain curve of MRE

It can be observed from Figure 4.58 that the stress-strain curves of the MRE samples under different external magnetic field conditions have the similar tendency. The higher external magnetic field, larger stress of MRE samples under the same strain. This is due to the interaction between magnetic particles inside the MRE material makes it become stiffer. The increasing curve can be divide into three parts. In the first phase, the uniaxial stress is slowly increased with the applied strain when the strain is varying from 0 to 3.5% in 0 mT, 1.6% in 265 mT and 1.5% in 465 mT, respectively. In the second phase, the stress is linearly increased with the strain, during this period, the Young's modulus, which is represented as the slope of the curve, remains at a constant value until the strain reaches 10%. In the last phase, the stress becomes rapidly increasing with the applied strain, Young modulus of the MRE material also starts to slightly increase at the same time.

## 4.5 Differential scanning calorimetry test

The glass-transition temperature ($T_g$) of the viscoelastic material represents the temperature range when glass transition behaviour occurs. Hard plastics such as polystyrene and poly (methyl methacrylate) are normally used below their glass transition temperatures (in their glassy state). Their $T_g$ values are normally higher than room temperature, at around 100 °C.

Rubber and rubber-like elastomers, for example, polyisoprene and polyisobutylene are usually used above their $T_g$, where they are soft and flexible. In this project, the silicone rubber is selected as the matrix material of MRE which belong to the rubber-like elastomers, thus, in their rubbery state.

Despite the change in the physical properties of a viscoelastic material through its glass transition, the transition is not only considered as a phase transition but also a phenomenon extending over a range of temperature and defined by one of several conventions. At the glass transition point, the thermal expansion, heat capacity, shear modulus, and many other properties of the material appears a relatively sudden change. Any such step or kink can be used to define $T_g$. To make this definition reproducible, the cooling and heating rate must be specified. The Tg is frequently defined by the energy release on heating in differential scanning calorimetry (DSC) test. The DSC is a thermal analysis technique in which the difference in the amount of heat required to increase the temperature of a sample and reference is measured as a function of temperature. Generally, the temperature program for a DSC analysis is designed such that the sample holder temperature increases linearly as a function of time. There are normally two main types of DSC test method: power-compensated DSC which keeps power supply constant and heat-flux DSC which keeps heat flux constant. In this tudy, the power-compensated DSC is selected and carried out by TA Instruments Trios. The starting temperature point of the test is -70.00 °C, with the heating speed 10.00 °C/min increases until reaching the end temperature point which is 250.00 °C. The DSC experiment result is shown as follow:

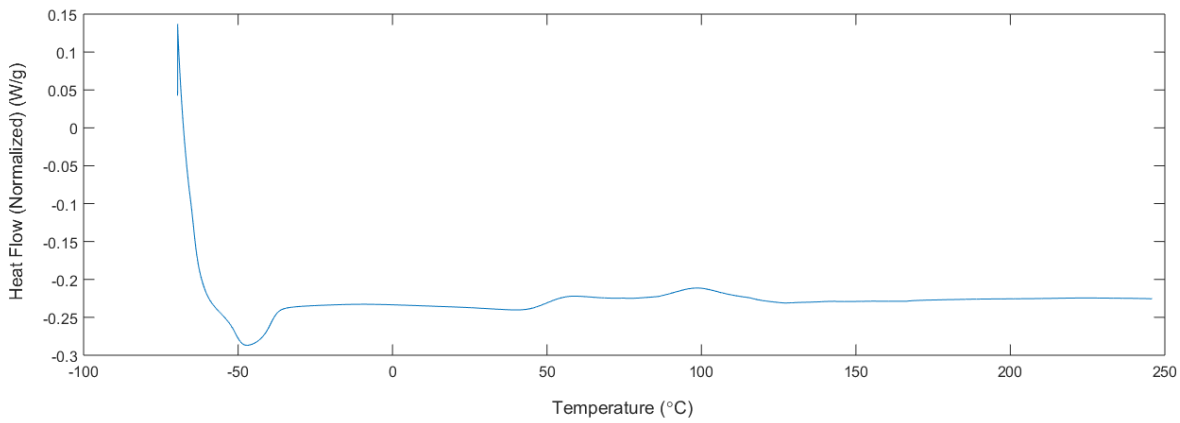


Figure 4. 59 Differential scanning calorimetry (DSC) test result of the MRE sample

According to the temperature-heat flow figure, the minimum value of the curve is at -48.81 °C which is the glass transition temperature of the MRE material. Normally the glass transition temperature of silicone rubber is around -40.00 °C. In this case, the change of the glass

transition temperature maybe due to the MRE introduced the iron particles as filler which affect the heat flow. It needs to be noticed there are two exothermic peaks at 58.66 °C and 98.6 °C. This maybe the main reason causes the transition behaviour of the MRE material in the DMA test. With the help of the DSC result, the potential applicability range of the time-temperature superposition (TTS) principle is also achieved.

## 4.6 Summary

This chapter mainly focus on the DMA experiment investigation on MRE material properties in order to achieve a better understanding in mechanical properties of MREs. DMA test, Static mechanical test and DSC test are carried out in this chapter. A reliable test system, consisting of a self-designed oven, electromagnets and permanent magnets, and the Instron test machine, is applied to perform the DMA experimental investigation of the anisotropic MRE samples under uniaxial harmonic compression. The influence of excitation frequency, strain amplitude, pre-strain, external magnetic field, and environment temperature on MRE dynamic properties are measured and discussed. The main experimental results obtained are summarized as follows:

(1) The effect of environment temperature on dynamic properties of MRE material based on silicone rubber are first observed through the DMA test. From the experiment results, it can be noticed that the relationship between the storage modulus and the environment temperature can be divide into two phases. It first decreases with the rising environment temperature and then turning to increase with the environment when pass the transition temperature point. In the meanwhile, the loss modulus is always decreased with the environment temperature. The DSC test is carried out to further investigate the cause of this phenomenon in storage modulus. In the DSC test, the glass transition temperature of MRE material based on silicone rubber is monitored. An inflection point of the heat flow curve is also observed at around 50 °C which is the main reason of the transition behaviour of MRE storage modulus at the same temperature. In addition, the external magnetic field appears to have a significant coupling influence on the temperature effect. The transition behaviour of storage modulus is more obvious in the low magnetic field condition and reduced in the high external magnetic field condition.

(2) The influence of both pre-strain and strain amplitude on dynamic mechanical properties of the MRE samples are presented. According to the DMA test results in room temperature, the storage modulus decreases with the rising strain amplitude. The loss modulus is fast

increased when the strain amplitude varies from 0.1% to 0.5% then starts to remain at a constant value in the absence of the external magnetic field or start to decrease with the strain amplitude under external magnetic field, respectively. In the meanwhile, the storage modulus increases with the pre-strain and decreases with the dynamic strain amplitude. There is no obvious change in the shape of the dynamic properties curves of MRE samples when the temperature is increased.

(3) The external magnetic field plays an important role in MRE dynamic mechanical properties. In the DMA test at room temperature, both storage modulus and loss modulus are significantly increase with the increasing of external magnetic field. It also generates a series of coupling effect with the environment temperature on dynamic properties. In the zero external magnetic field, the storage is first decreased with the environment temperature and then starts to increase with the rising temperature. In the high external magnetic field test condition, the storage remains at a constant value after the transition temperature point.

(4) The experimental results lay the foundation for the development of mathematical models and can be utilized to identify the model parameters of mathematical models. The experiment results are also used for designing the MRE based semi-active vibration control device.

# 5 Mathematical modelling of MREs

## 5.1 Introduction

Magnetorheological elastomers (MREs) show the potential application in semi-active vibration control due to their dynamic properties can be adjusted rapidly and reversibly by changing the external magnetic field [e.g. Molchanov et al. (2014), Jang et al. (2018), Bornassi and Navazi (2018)]. It is well known that the dynamic mechanical properties of MREs are affected not only by their components and fabrication process [e.g. Boczkowska and Awietjan (2011), Qiao et al. (2015), Sapouna et al. (2017)] but also by the in-service conditions such as load amplitude, excitation frequency, external magnetic field, and temperature etc. [Zhang et al. (2011), Sorokin et al. (2014), Qi et al. (2018)]. In order to achieve an optimal damping or vibration isolation system for practical application of MRE based active or semi-active vibration control device, the characterization and modelling of MREs under various load conditions are essential to be determined.

Plenty of models have been developed and proposed so far for describing the dynamic properties of MREs under the combination of magnetic and mechanical load conditions. Among these modelling approaches, the parametric model has been received considerable attention due to its efficient and rapid simulation of the dynamic behaviours of MREs and MRE based devices under various loading conditions (please see Chapter 2 for detail). To our knowledge, there is a research gap in the development of generalized mathematical model for describing the dependent dynamic properties of MREs in combined magnetic-thermal-mechanical load conditions.

This chapter aims to develop a new mathematical model to describe the elastic and rheological properties of MREs under the combination of magnetic-thermal-mechanical loads. In order to achieve this, the influence of magnetic field, temperature, strain amplitude and frequency on the dynamic properties of MREs under uniaxial harmonic compression is investigated. A generalized dynamic modulus master curve of MREs is constructed, which can take these influence factors into account. The good correlation between the experimental data and modelling results was confirmed by the goodness-of-fit statistical analysis.

This chapter is organized as follows. In Section 5.2, a new approach is proposed to model the viscoelastic behaviour of MREs. The master curve of MREs' dynamic modulus is constructed in Section 5.3. The new fractional functions are proposed to fit the magnetic field induced

dynamic moduli of MREs in Section 5.4. The Kraus model is adopted to predict the influence of strain amplitude on dynamic moduli of MREs in Section 5.5. A mathematical model for dynamic moduli of MREs is presented in Section 5.6. Finally, Section 5.7 gives a summary of the chapter.

## 5.2 Linear viscoelastic model

### 5.2.1 Viscoelastic models in literature

There are many viscoelastic models available in literature to describe the dynamic modulus and phase angle, which can be categorized into two groups: the mechanical models and the mathematical models. The mechanical models (also called analogical models) simulate the elastic and rheological response of viscoelastic materials by using a particular combination of springs and dashpots (or springpots) in series and/or parallel, e.g. the generalized Maxwell model, the generalized Kelvin-Voigt model, and the fractional Zener model [e.g. Sasso et al. (2011), Jóźwiak et al. (2015), Yin et al. (2017)]. While the mathematical models (also called empirical algebraic models) utilize an analytical expression to fit experimental data, such as the CAM model and modified CAM model, the sigmoidal model and generalized logistic sigmoidal model [e.g. Shan et al. (2016); Christensen et al. (2017), Xu and Engquist (2018)]. For the sake of comparison with proposed model, the fractional Zener model and the CAM model are regarded as the typical mechanical and mathematical viscoelastic models and presented respectively as follows.

#### 5.2.1.1 The fractional Zener model

The fraction Zener model is comprised of a spring and a fractional Maxwell element (also called the Scott-Blair element) in parallel. It was developed based on the Zener model by replacing the dashpot with a springpot as shown in Figure 5.1. The constitutive equation for stress and strain relation in the linear isothermal isotropic case can be written as: [Metzler et al. (1995), Dinzart and Lipinski (2009), Kontou and Katsourinis (2016)]

$$\sigma(t) + \tau^{\alpha}\frac{\mathrm{d}^{\alpha}\sigma(t)}{\mathrm{d}t^{\alpha}} = E_0\varepsilon(t) + E_{\infty}\tau^{\alpha}\frac{\mathrm{d}^{\alpha}\varepsilon(t)}{\mathrm{d}t^{\alpha}} \tag{5.1}$$

in which, $E_0$ is the long time or relaxed modulus, $E_{\infty}$ is the unrelaxed or instantaneous modulus, $\tau$ denotes the relaxation time which is equal to the ratio between the viscosity of the dashpot and the stiffness of the spring in the fractional Maxwell model, $\alpha$ is the order of the fractional

derivative in the range of 0 to 1. The springpot changes to a linear spring in the extreme case of α = 0, and leads to the dashpot in the extreme case of α = 1.

According to the Riemann-Liouville fractional derivative with 0 < α < 1, the fractional derivative operator is defined as [Bagley and Torvik (1983, 1986), Sasso et al. (2011)],

$$\frac{d^{\alpha} f(t)}{dt^{\alpha}} = \frac{1}{\Gamma(1-\alpha)} \frac{d}{dt} \int_0^t \frac{f(s)}{(t-s)^{\alpha}} ds \tag{5.2}$$

Where $\Gamma(x)$ is the Eulerian Gamma function.

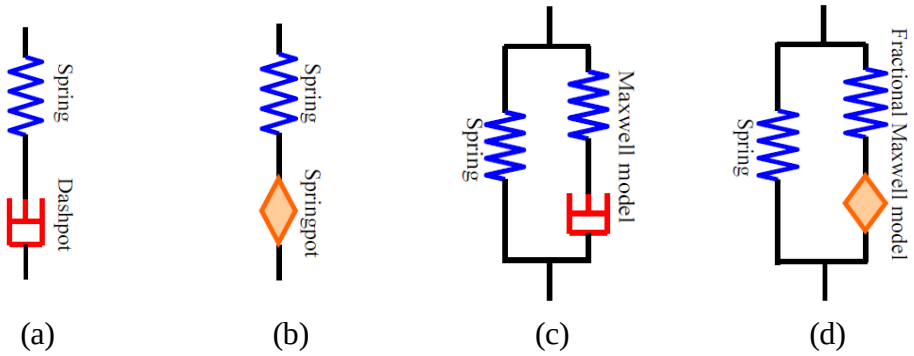


Figure 5. 1 Diagram of linear viscoelastic models: (a) the Maxwell model, (b) the fractional Maxwell model, (c) The Zener model, and (d) the fractional Zener model.

The corresponding complex modulus of the fractional Zener model can be expressed in the following form:

$$E^*(\omega) = E_0 + (E_\infty - E_0) \frac{(i\omega\tau)^{\alpha}}{1 + (i\omega\tau)^{\alpha}} \tag{5.3}$$

The complex modulus is distinguished between the real and imaginary parts, defined respectively as storage modulus and loss modulus,

$$E'(\omega) = E_0 + (E_\infty - E_0) \frac{(\omega\tau)^{\alpha} \cos\frac{\alpha\pi}{2} + (\omega\tau)^{2\alpha}}{1 + 2(\omega\tau)^{\alpha} \cos\frac{\alpha\pi}{2} + (\omega\tau)^{2\alpha}} \tag{5.4a}$$

$$E''(\omega) = (E_\infty - E_0) \frac{(\omega\tau)^{\alpha} \sin\frac{\alpha\pi}{2}}{1 + 2(\omega\tau)^{\alpha} \cos\frac{\alpha\pi}{2} + (\omega\tau)^{2\alpha}} \tag{5.4b}$$

The fractional Zener model have been widely adopted to describe the creep, stress relaxation, and dynamic response of viscoelastic materials and MREs [e.g. Mainardi and Spada (2011), Markou and Manolis (2016), Olabide et al. (2018)]. Recently, the fractional Zener model was

used to describe the dynamic modulus master curve of MREs in the absence of external magnetic field [Olabide and Elejabarrieta (2016)] and under different magnetic fields [Wan et al. (2019)].

#### 5.2.1.2 The CAM model

The CAM model was developed by Marasteanu and Anderson (1996) based on the CA model [Christensen and Anderson (1992)] for characterizing the dynamic modulus of asphalt binders as a function of frequency. As the modified version of the CA model, the capability and accuracy of the model were enhanced in the lower and higher frequency range by providing greater flexibility in the rate at which the phase angle approaches the viscous flow and glassy modulus asymptotes [Christensen et al. (2017)]. Shortly thereafter, the generalized form of the CAM model was proposed by Zeng et al. (2001) which can be applied to describe the elastic and rheological properties of both bituminous binders and mixes [Bayane et al. (2017)].

According to the generalized form of CAM model, the magnitude of dynamic modulus can be expressed as follow:

$$|E^*(\omega)| = E_e + \frac{E_g - E_e}{[1 + (\omega_c/\omega)^k]^{m/k}} \tag{5.5}$$

in which, $E_e$ and $E_g$ are the equilibrium modulus and the glassy modulus respectively, $\omega_c$ denotes the crossover frequency, k and m are shape parameters (dimensionless).

The corresponding phase angle can be derived by the approximations of the Kramers-Kronig relations as follow: [Booij and Thoone (1982), Pritz (1999)]

$$\delta(\omega) \approx \frac{\pi}{2}\frac{d\log|E^*(\omega)|}{d\log\omega} \tag{5.6}$$

A modified expression of phase angle is introduced by adding a correct factor η in Eq. (5.6), it leads to:

$$\delta(\omega) = \frac{\eta\pi}{2}\frac{m}{1 + (\omega_c/\omega)^k} \tag{5.7}$$

The other expressions for phase angle were presented by Shan et al. (2016) and Bayane et al. (2017) for constructing the dynamic modulus master curve of asphalt binders and hot-mix asphalt concrete mixtures respectively.

The storage modulus and loss modulus can be expressed as follow:

$$E'(\omega) = |E^*(\omega)| \cos\delta(\omega) \tag{5.8a}$$

$$E''(\omega) = |E^*(\omega)| \sin\delta(\omega) \tag{5.8b}$$

### 5.2.2 The proposed model for viscoelastic properties of MREs

On the basis of the modified Kelvin-Voigt model [Norouzi et al. (2016)] in which the stiffness of spring and the viscosity of dashpot are not constants and dependent on the excitation frequency in small strain range as shown in Figure 5.2.

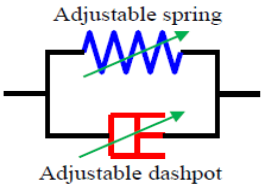


Figure 5. 2 Diagram of the proposed viscoelastic model.

The viscoelastic stress-strain relationship is expressed as,

$$\sigma(t) = E(\omega)\varepsilon(t) + \eta(\omega)\dot{\varepsilon}(t) \tag{5.9}$$

Inspired by our DMA experiment, the stiffness of the spring and viscosity of the dashpot in Figure 5.2 are given as follow:

$$E(\omega) = E_s\left[1 + A\left(\frac{\omega}{\omega_s}\right)^{\alpha}\right] \tag{5.10a}$$

$$\eta(\omega) = \frac{C}{\omega_s}\left(\frac{\omega}{\omega_s}\right)^{\alpha-1} e^{-\left(\frac{\omega}{\omega_s}\right)^{\beta}} \tag{5.10b}$$

In which $E_s$ is the static stiffness, A is the coefficient of frequency dependent stiffness, C denotes the viscosity coefficient of dashpot, $\omega_s$ is scalar parameter, α and β are shape parameters respectively. The stiffness of spring and viscosity of dashpot are correlated by the scalar parameter $\omega_s$ and the shape parameter α.

Besides the DMA experiment results, the physical reason in selecting the Eq. (5.10) to characterize the stiffness and viscosity of MREs can be interpreted as follows. The stiffness of spring takes the function form of the Cowper-Symonds model, which are widely used to characterize the influence of strain rate on the stress-strain relationship of materials. The stiffness is associated with the storage energy and the strain rate is related to the vibration

frequency. It indicates that this function form can take the frequency effect on the dynamic modulus of MREs into consideration.

The viscosity of dashpot takes the similar form of the Weibull distribution function because the function in Eq. (5.10b) can be transformed into the two-parameter Weibull function by setting $\alpha = C = \beta$). The viscosity is associated with the dissipative energy, which is dependent not only on the movement of molecular chains but also on the interaction between the elastomeric matrix and the filler particles. The Weibull function has been proven to be capability of matching historical failure and repair data, which represent the characteristics of a given failure mode in the course of industrial process. Therefore, it can represent the dynamic equilibrium between breakage and recovery of weak physical bonds linking the elastomeric matrix and the filler particles.

The complex modulus and corresponding storage modulus and loss modulus can be expressed as follow by turning Eq. (5.9) into the frequency domain.

$$E^*(\omega) = \frac{\sigma^*(\omega)}{\varepsilon^*(\omega)} = E'(\omega) + iE''(\omega) \tag{5.11a}$$

$$E'(\omega) = E_s\left[1 + A\left(\frac{\omega}{\omega_s}\right)^{\alpha}\right] \tag{5.11b}$$

$$E''(\omega) = C\left(\frac{\omega}{\omega_s}\right)^{\alpha} e^{-\left(\frac{\omega}{\omega_s}\right)^{\beta}} \tag{5.11c}$$

where, the model parameters ($E_s$, A, C, $\omega_s$, α, and β) can be identified by DMA experiment data. The storage modulus and loss modulus are correlated by the scalar parameter of $\omega_s$ and the shape parameter of α.

### 5.2.3 Fitting procedure and goodness-of-fit statistics

There are different number of parameters in different predictive models for viscoelastic properties, e.g. five parameters in the fractional Zener model, and six parameters in the CAM model and our proposed model respectively. These parameters can be identified by minimizing the sum of square of error (SSE) between the experimental data and model predicted results using the least square method and optimization algorithm such as the genetic algorithm (GA).

The sum of square of error (SSE) between the predicted and measured data is

$$\mathrm{SSE} = \gamma \sum \left(1 - \frac{E'_{pred}}{E'_{exp}}\right)^2 + (1-\gamma) \sum \left(1 - \frac{E''_{pred}}{E''_{exp}}\right)^2 \tag{5.12}$$

in which $E'_{exp}$ and $E'_{pred}$ are experimental and predicted data of storage modulus, $E''_{exp}$ and $E''_{pred}$ are experimental and predicted data of loss modulus respectively, $\gamma$ is a weight factor for better optimization in the range of 0 to 1.

The fitting results can be evaluated in detail by using the statistical analysis of goodness-of-fit. The standard error ratio ($S_e/S_y$) and the coefficient of determination ($R^2$) are expressed respectively in the statistical analysis as follow: [Yusoff et al. (2011)]

$$S_e = \sqrt{\frac{\sum\left(y_{exp} - y_{pred}\right)^2}{n-k}} \tag{5.13a}$$

$$S_y = \sqrt{\frac{\sum\left(y_{exp} - \bar{y}_{pred}\right)^2}{n-1}} \tag{5.13b}$$

$$R^2 = 1 - \frac{n-k}{n-1}\left(\frac{S_e}{S_y}\right)^2 \tag{5.13c}$$

where n and k are the number of the samples and the independent model parameters respectively, $y_{exp}$ and $y_{pred}$ are the experimental data and predicted results of the sample respectively, and $\bar{y}_{exp}$ denotes the mean value of the experimental data, e.g. experimental data of storage modulus or loss modulus. The related criteria of the goodness-of-fit is listed in Table 5.1 [Yusoff et al. (2011)].

Table 5. 1 The criteria for statistical analysis [Yusoff et al. (2011)].

| Criteria | $S_e/S_y$ | $R^2$ |
|---|---|---|
| Excellent | $\leq 0.35$ | $\geq 0.90$ |
| Good | $0.36 - 0.55$ | $0.70 - 0.89$ |
| Fair | $0.56 - 0.75$ | $0.40 - 0.69$ |
| Poor | $0.76 - 0.89$ | $0.20 - 0.39$ |
| Very poor | $\geq 0.90$ | $\leq 0.19$ |

In order to assess the model's capability of fitting, the maximum geometrical deviation (MGD) and average geometrical deviation (AGD) are introduced as follows:

$$MGD = \max_{n} \left| \frac{y_{exp} - y_{pred}}{y_{exp}} \right| \tag{5.14a}$$

$$AGD = \frac{1}{n} \sum \left| \frac{y_{exp} - y_{pred}}{y_{exp}} \right| \tag{5.14b}$$

These parameters represent the maximum and average geometrical deviation from the experimental data respectively. The perfect fit can be achieved when the MGD and AGD are equal to zero.

### 5.2.4 Comparative analysis of viscoelastic models

The comparative analysis has been performed between the DMA experimental data and the predicted results of isothermal dynamic modulus by using linear viscoelastic models for the MRE samples under various load cases, including magnetic field, test temperature, and strain amplitude and excitation frequency. Figure 5.3 to Figure 5.6 present the comparison of fitting capability among our proposed model, the fractional Zener model and the CAM model for the isothermal dynamic modulus of the MRE samples under typical load cases (magnetic field, test temperature, and strain amplitude) with the excitation frequency range from 1 Hz to 60 Hz.

Load case 1: Uniaxial harmonic compression with 1% strain amplitude, test temperature of 35°C, and non-magnetic field.

Load case 2: Uniaxial harmonic compression with 0.25% strain amplitude, test temperature of 25°C, and magnetic field of 300 mT.

Load case 3: Uniaxial harmonic compression with 0.25% strain amplitude, test temperature of 60°C, and magnetic field of 300 mT.

Load case 4: Uniaxial harmonic compression with 1% strain amplitude, test temperature of 60°C, and magnetic field of 500 mT.

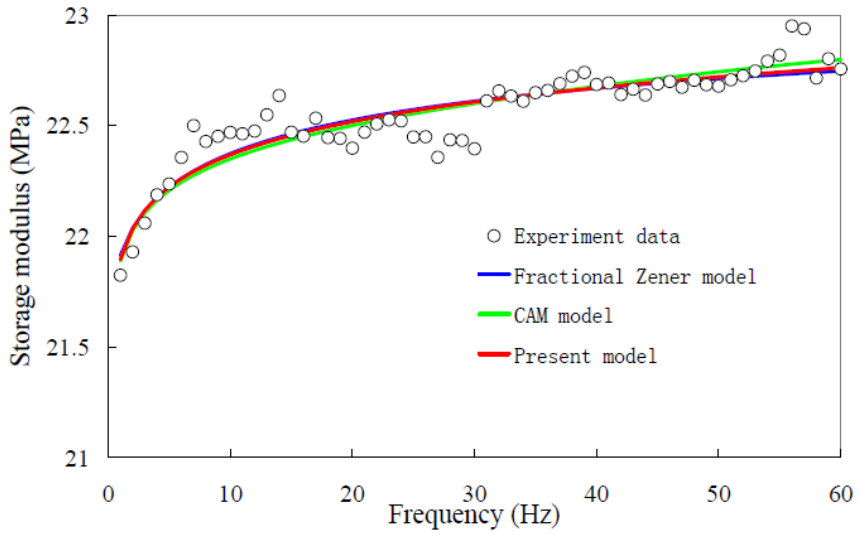


(a)

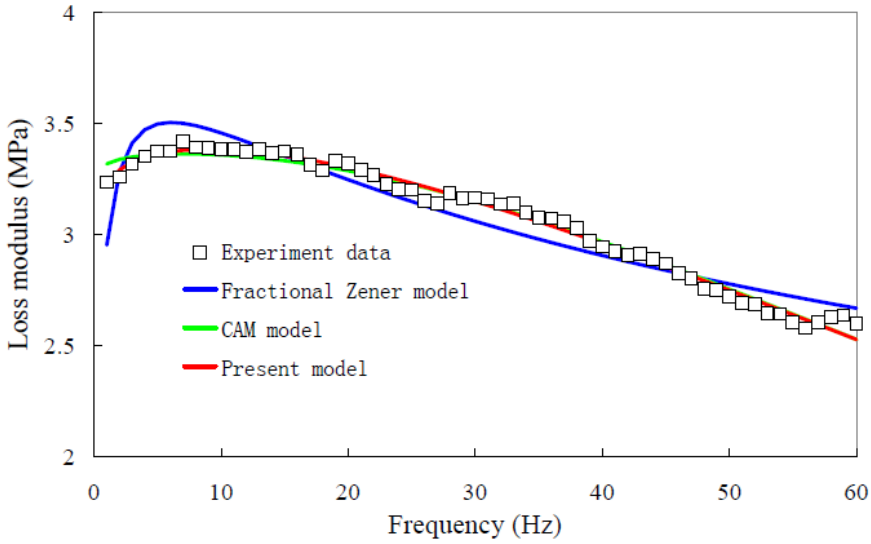


(b)

Figure 5. 3 Comparison fitting capability between our proposed model and the fractional Zener model and the CAM model for the MRE sample: (a) storage modulus, and (b) loss modulus of the MRE sample subjected to uniaxial harmonic compression with 1% strain amplitude in the temperature of 35°C and non-magnetic field.

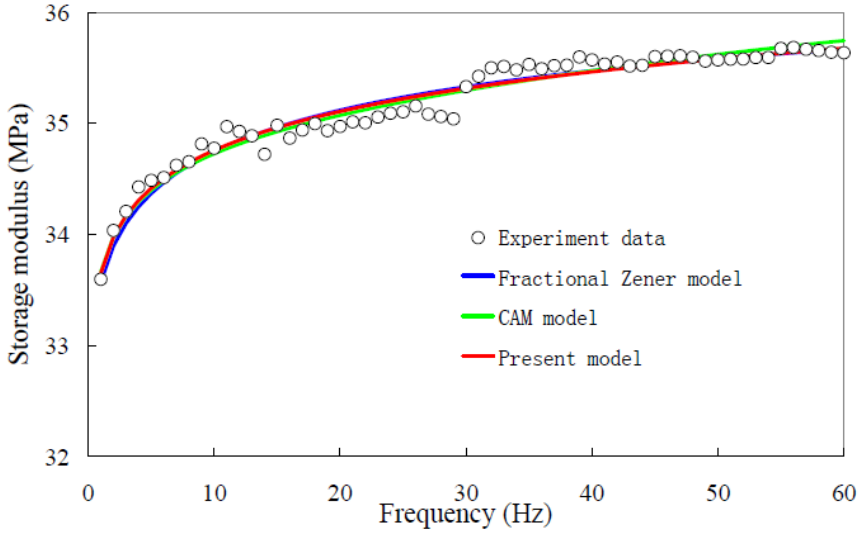


(a)

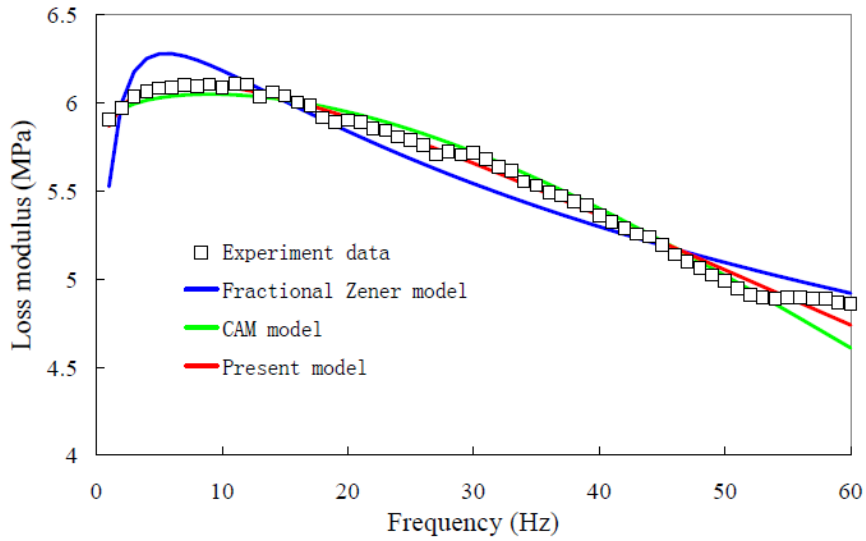


(b)

Figure 5. 4 Comparison fitting capability between our proposed model and the fractional Zener model and the CAM model for the MRE sample: (a) storage modulus, and (b) loss modulus of the MRE sample under uniaxial harmonic compression with 0.25% strain amplitude, the temperature of 25°C and the magnetic field of 300 mT.

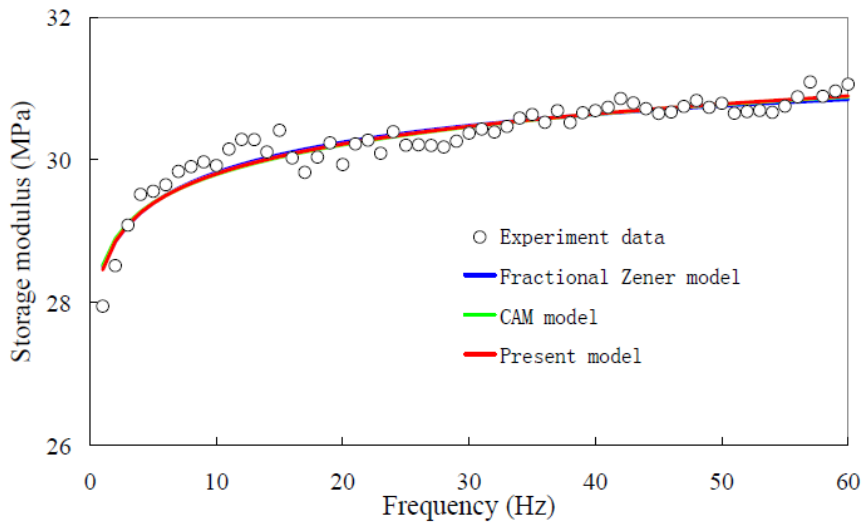


(a)

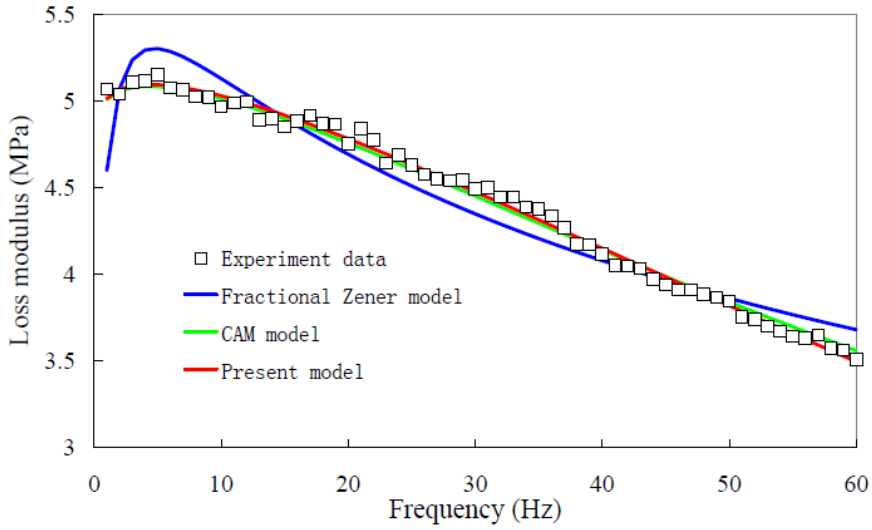


(b)

Figure 5. 5 Comparison fitting capability between our proposed model and the fractional Zener model and the CAM model for the MRE sample: (a) storage modulus, and (b) loss modulus of the MRE sample under uniaxial harmonic compression with 0.25% strain amplitude, the temperature of 60℃ and the magnetic field of 300 mT.

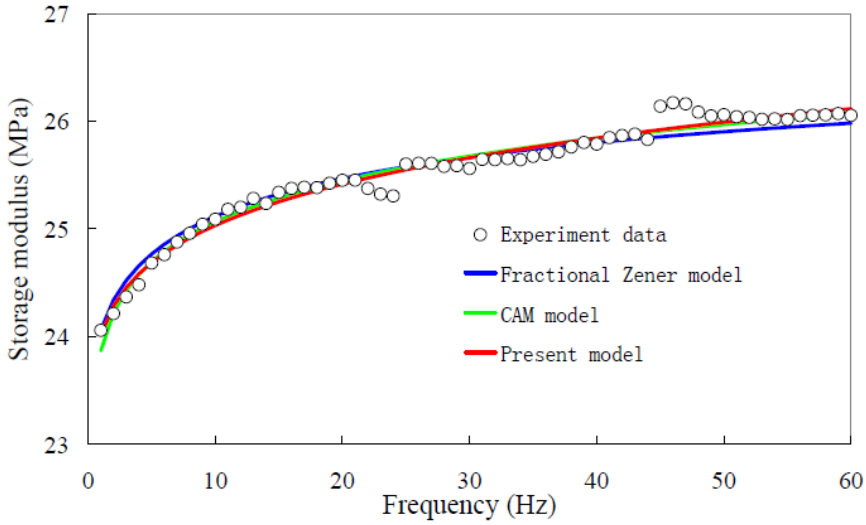


(a)

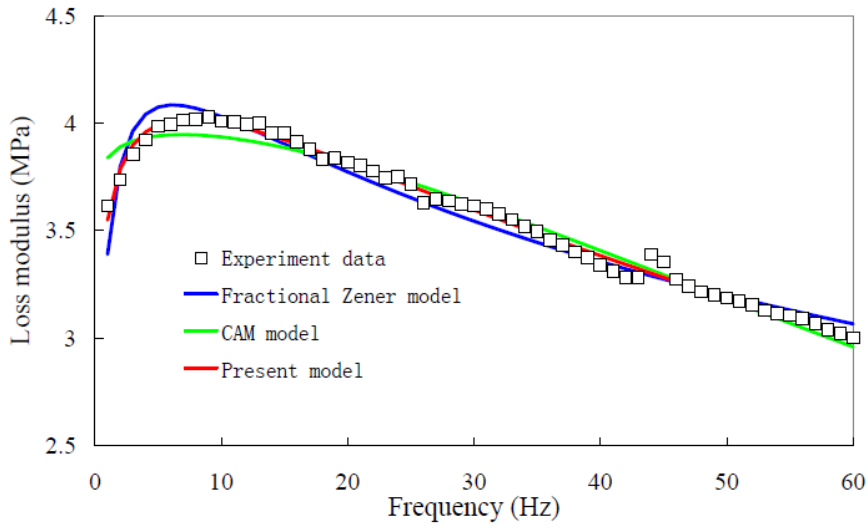


(b)

Figure 5. 6 Comparison fitting capability between our proposed model and the fractional Zener model and the CAM model for the MRE sample: (a) storage modulus, and (b) loss modulus of the MRE sample under uniaxial harmonic compression with 1% strain amplitude, the temperature of 60℃ and the magnetic field of 500 mT.

The standard error ratio ($S_e/S_y$), the coefficient of determination ($R^2$), the maximum geometrical deviation (MGD), and average geometrical deviation (AGD) of the predicted results as shown in Figure 5.3 to Figure 5.6 are also presented in Table 5.2 to Table 5.5 for comparative analysis of the proposed model, the fractional Zener model, and the CAM model. It can be observed that the very good agreement exists between the experimental data and the proposed model for both storage modulus and loss modulus. The maximum deviation and mean normalized error are less than 5% and 1% respectively. Both the CAM model and the fractional Zener model present the good fitting results of storage modulus, while a little difference exists

between the experimental data and predicted results of loss modulus. The maximum discrepancy of loss modulus occurs in the low frequency range. The maximum deviation and mean normalized error of the results predicted by the CAM model and the fractional Zener model are less than 10% and 5% respectively.

The goodness-of-fit statistical analysis results in Table 5.2 and Table 5.3 show that all these linear viscoelastic models can be applied to describe the isothermal dynamic moduli including storage modulus and loss modulus. According to the criteria for statistical analysis in Table 5.1, all these models present the excellent fitting results for loss modulus and the good fitting results for storage modulus. The proposed model gives a better fitting result than the CAM model and the fractional Zener model.

Table 5. 2 Goodness-fit-statistics of the proposed model, the fractional Zener model, and the CAM model for storage modulus of the MRE sample under uniaxial harmonic compression with different magnetic fields, test temperatures, and strain amplitudes.

| | Index of statistics | Fractional Zener model | CAM model | Proposed model |
|---|---|---|---|---|
| Load case 1 | $S_e/S_y$ | 0.455 | 0.449 | 0.450 |
| | $R^2$ | 0.807 | 0.816 | 0.815 |
| Load case 2 | $S_e/S_y$ | 0.331 | 0.336 | 0.328 |
| | $R^2$ | 0.898 | 0.897 | 0.902 |
| Load case 3 | $S_e/S_y$ | 0.237 | 0.218 | 0.224 |
| | $R^2$ | 0.948 | 0.956 | 0.954 |
| Load case 4 | $S_e/S_y$ | 0.172 | 0.182 | 0.185 |
| | $R^2$ | 0.972 | 0.970 | 0.969 |

Table 5. 3 Goodness-fit-statistics of the proposed model, the fractional Zener model, and the CAM model for loss modulus of the MRE sample under uniaxial harmonic compression with different magnetic fields, test temperatures, and strain amplitudes.

| | Index of statistics | Fractional Zener model | CAM model | Proposed model |
|---|---|---|---|---|
| Load case 1 | $S_e/S_y$ | 0.319 | 0.136 | 0.115 |
| | $R^2$ | 0.905 | 0.983 | 0.988 |
| Load case 2 | $S_e/S_y$ | 0.268 | 0.096 | 0.080 |
| | $R^2$ | 0.933 | 0.992 | 0.994 |
| Load case 3 | $S_e/S_y$ | 0.271 | 0.168 | 0.094 |
| | $R^2$ | 0.931 | 0.974 | 0.992 |
| Load case 4 | $S_e/S_y$ | 0.210 | 0.171 | 0.104 |
| | $R^2$ | 0.959 | 0.973 | 0.990 |

Table 5. 4 The maximum geometrical deviation (MGD) and average geometrical deviation (AGD) of the predictive models for storage modulus.

| | Fractional Zener model | | CAM model | | Proposed model | |
|---|---|---|---|---|---|---|
| | MGD | AGD | MGD | AGD | MGD | AGD |
| Load case 1 | 1.04 | 0.300 | 0.99 | 0.302 | 1.01 | 0.295 |
| Load case 2 | 0.78 | 0.240 | 0.68 | 0.232 | 0.74 | 0.224 |
| Load case 3 | 1.98 | 0.474 | 2.03 | 0.468 | 1.82 | 0.462 |
| Load case 4 | 1.17 | 0.315 | 0.96 | 0.243 | 0.90 | 0.256 |

Table 5. 5 The maximum geometrical deviation (MGD) and average geometrical deviation (AGD) of the predictive models for loss modulus.

| | Fractional Zener model | | CAM model | | Proposed model | |
|---|---|---|---|---|---|---|
| | MGD | AGD | MGD | AGD | MGD | AGD |
| Load case 1 | 8.75 | 2.274 | 3.27 | 0.973 | 3.30 | 0.787 |
| Load case 2 | 6.46 | 1.711 | 5.16 | 0.952 | 2.49 | 0.537 |
| Load case 3 | 9.28 | 2.440 | 2.29 | 0.893 | 1.79 | 0.745 |
| Load case 4 | 6.27 | 1.273 | 6.15 | 1.162 | 2.53 | 0.555 |

## 5.3 Temperature effect

The elastic and rheological properties of MREs in addition to an external magnetic field are also dependent on the thermal-mechanical load conditions. The temperature has a significant influence on material properties of MREs and the performance of MRE based devices [Zhang et al. (2011), Yu et al. (2016)]. Compared with the extensive research on the characterization and modelling of the frequency-, amplitude-, and magnetic field-dependent viscoelastic properties of MREs, to our knowledge, there is a limited number of published studies on the characterization and modelling of the temperature-dependent viscoelastic properties of MREs.

The relationship between frequency and temperature, named master curve, can be established base on the time-temperature superposition (TTS) principle for the thermorheologically simple materials such as single-phase, single-transition amorphous homopolymers and random copolymers [Tschoegl et al. (2002)]. The elastic constants are independent of temperature and the time constants have the same dependence of temperature. The isotherms of dynamic modulus can be shifted into a smooth master curve by using the horizontal shift factor. The master curve constructed by TTS principle has been successfully applied to predict the elastic

and rheological properties of viscoelastic materials over a range of frequencies within linear viscoelastic region [Madigosky et al. (2006), Moreira et al. (2010), Rouleau et al. (2015)]. At the same time, many research efforts were delivered to extend the application of TTS to multi-phase composites that the deviations from the thermorheologically simple behaviour are not too large [Guedes (2011), Nakano (2013), Çakmak et al. (2014)]. The results revealed that the TTS principle did not hold for a multi-phase system in general but held for a multi-component system in which all components had the same temperature dependence and identical shift factors, or some components had the same temperature dependence and the others had no or nearly no temperature dependence [Nakano (2013), Çakmak et al. (2014)]. The results showed that the storage modulus of iron particle filled poly (norbornene) (PNB) was independent on the iron particle content and the PNB represented a perfectly thermorheologically simple material behaviour. The master curve presented a good fit for the storage modulus and loss factor of the PNB with varying contents of spherical iron particles. A phenomenological frequency-temperature shift was presented with a good fit for storage modulus of poly (dimethylsiloxane) (PDMS) filled with varying contents of spherical iron particles. Although the PDMS was not thermorheologically simple material, but it had linearly dependence of temperature and the same shift factor [Çakmak et al. (2014)]. The dynamic modulus master curve of an isotropic magnetosensitive elastomer in the absence of magnetic field, and the magnitude of complex modulus master curve of MR fluids under magnetic field were constructed respectively in the literature [Chool and Oyadiji (2005), Olabide and Elejabarrieta (2016)]. However, the statistical analysis of the good-of-fitness were not presented.

### 5.3.1 Shift factor equations

The isothermal dynamic moduli, including storage modulus and loss modulus, can be shifted respectively into a unique master curve at a reference temperature when the applicable of the TTS principle has been verified [Çakmak et al. (2014), Moreira et al. (2010), Rouleau et al. (2015)].

$$E'(\omega_r, T_r) = b_T E'(\omega, T) \tag{5.15a}$$

$$E''(\omega_r, T_r) = b_T E''(\omega, T) \tag{5.15b}$$

$$\omega_r = a_T \omega \tag{5.15c}$$

Where, $\omega_r$ and $T_r$ denote reduced frequency and reference temperature, $a_T$ and $b_T$ are the horizontal and vertical shift factors respectively.

The shift factor definition is mainly based on the observation that isothermal dynamic modulus curves obtained from DMA experiments can be shifted into a smooth master curve with the goodness of fit between measured and predicted data: higher value of the coefficient of determination ($R^2$) and lower value of the standard error ratio ($S_e/S_y$). The numerical shift factor for each isotherm of dynamic modulus produced the best fit between experimental and predicted data [Rowe and Sharrock (2011)]. While the functional shift factor has an advantage over the numerical shift factor in mathematical expression and application to computer software [Kim et al. (2015)]. In addition, if a functional form with some thermodynamic basis is used then the resulting master curve and shift factor equations can be employed to predict the viscoelastic behaviour beyond the measurement data range of temperatures and frequencies. In general, the horizontal shift factor is commonly expressed by simple temperature dependent equations, such as the Arrhenius model and the WLF model of Williams-Landel-Ferry equation [Williams et al. (1955)] because of their strong thermodynamic basis, and the quadratic polynomial function for the sake of fitting accuracy [Dealy and Plazek (2009), Kim et al. (2015)].

The Arrhenius equation and the WLF empirical equation:

$$\log a_T = C_0\left(\frac{1}{T} - \frac{1}{T_r}\right) \tag{5.16a}$$

$$\log a_T = \frac{C_1(T - T_r)}{C_2 + (T - T_r)} \tag{5.16b}$$

in which, $C_0$, $C_1$, and $C_2$ are model parameters respectively, $T_r$ is the reference temperature chosen for the master curve.

The quadratic polynomial function:

$$\log a_T = a_1(T - T_r) + a_2(T - T_r)^2 \tag{5.17}$$

where $a_1$ and $a_2$ are model parameters, $T_r$ is the reference temperature chosen for the master curve.

The WLF shift equation is based on the free-volume concept and has been widely used for thermorheologically simple materials such as single-phase, single-transition amorphous homopolymers and random copolymers. However, the WLF shift equation does not work well for filled polymers. Some overlapping of the master curves occurs in the lower frequency range

and/ or the high temperature region due to the interactions of polymer-filler and filler-filler. This overlapping indicates that the filler network dominates the dynamic mechanical properties of the filled polymers. The vertical shift factor is usually utilized to reduce the effect of these overlapping and obtain a master curve with better fit [Chen and Jerrams (2011), Blom and Kari (2011), Guo et al. (2014)].

The vertical shift factor represents temperature induced density changes and supplements for polymers with vertical shifts of the dynamic modulus [Dealy and Plazek (2009), Guedes (2011)].

$$b_T = \frac{\rho_r T_r}{\rho T} \tag{5.18}$$

in which, ρ and $\rho_r$ are density of the material at current temperature, and reference temperature.

Where the temperature ratio represents an effect of entropy-based restoring force in the flexible chains and the ratio of density represents an effect of thermal expansion. The vertical shift factor is weakly dependent on temperature, and normally can be neglected in most cases [Dealy and Plazek (2009)]. Under the assumptions about densities that the mass of the material remains constant when temperature varying, the approximations of vertical shift factor can be derived as follow [Guedes (2011)].

$$b_T = 1 + b_1(T - T_r) + b_2(T - T_r)^2 \tag{5.19}$$

where $b_1$ and $b_2$ are model parameters dependent on reference temperature and the thermal expansion coefficient of the material.

### 5.3.2 Applicability of the time-temperature superposition principle

The time-temperature superposition (TTS) principle holds for the thermorheologically simple materials [Tschorgl et al. (2002)] and has been extended to a multi-component system in which some components have the same temperature dependence and the others have no temperature dependence [Nakano (2013), Çakmak et al. (2014)]. Therefore, the applicability of the TTS principle should be verified before the construction of the master curve. The Cole-Cole plot and the Black diagram (also called the van Gurp-Palmen plot) are two general methods to verify whether the viscoelastic material is thermorheologically simple or not.

When the Cole-Cole plot and the Black diagram form a single smooth curve, the material is

thermorheologically simple. The elastic constants are independent of temperature and the time constants have the same dependence of temperature. The isotherms of dynamic modulus can be shifted into a unique master curve by only using the horizontal shift factor [Madigosky (2006), Moreira et al. (2010), Rouleau et al. (2015)]. When the Cole-Cole plot and the Black diagram are temperature dependent, the material does not exhibit simple thermorheological behaviour. Both horizontal and vertical shift factors should be applied to construct the master curve based on TTS principle [Dealy and Plazek (2009), Guedes (2011), Nakano (2013)].

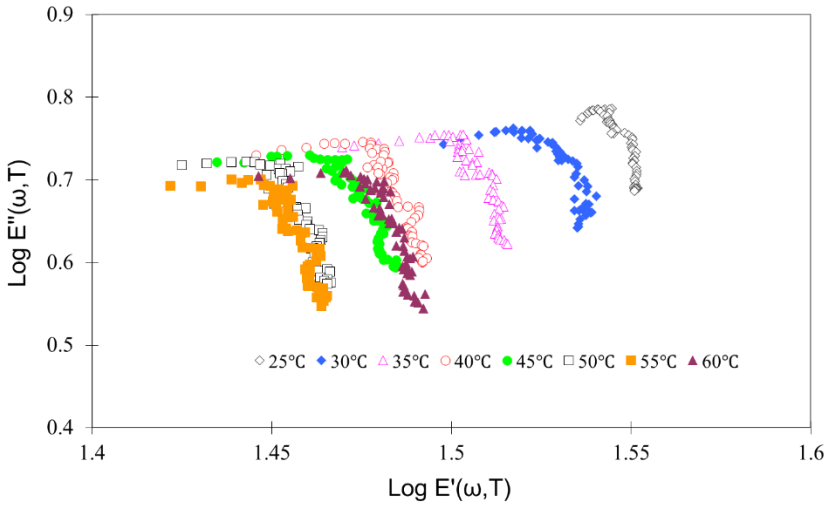


(a)

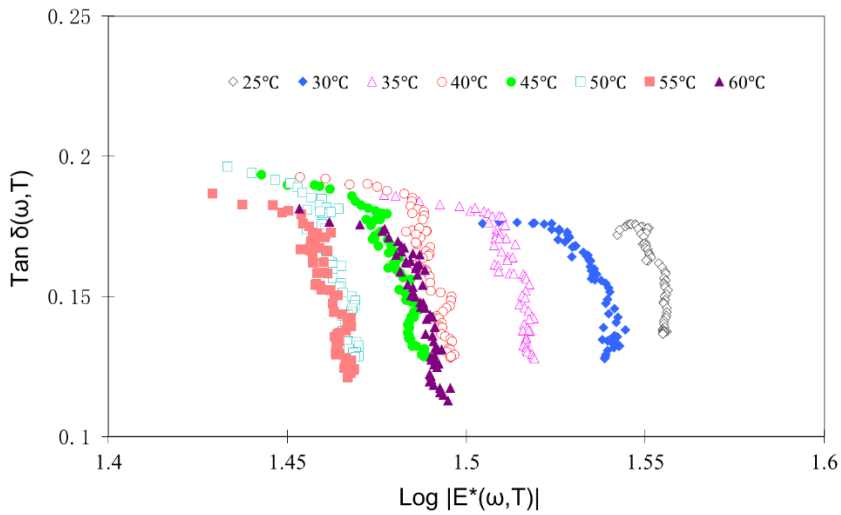


(b)

Figure 5. 7 (a) The Cole-Cole plot, and (b) the Black diagrams of the MRE samples under 0.25% uniaxial harmonic compression and 300 mT magnetic field.

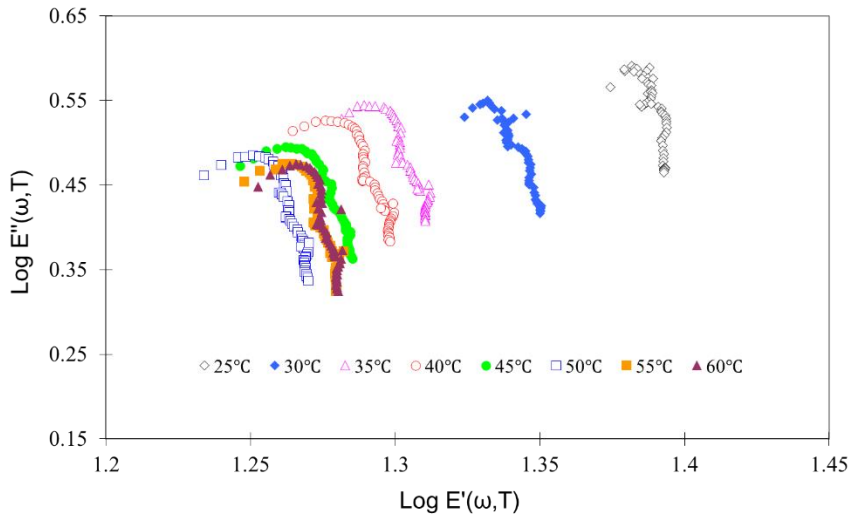


(a)

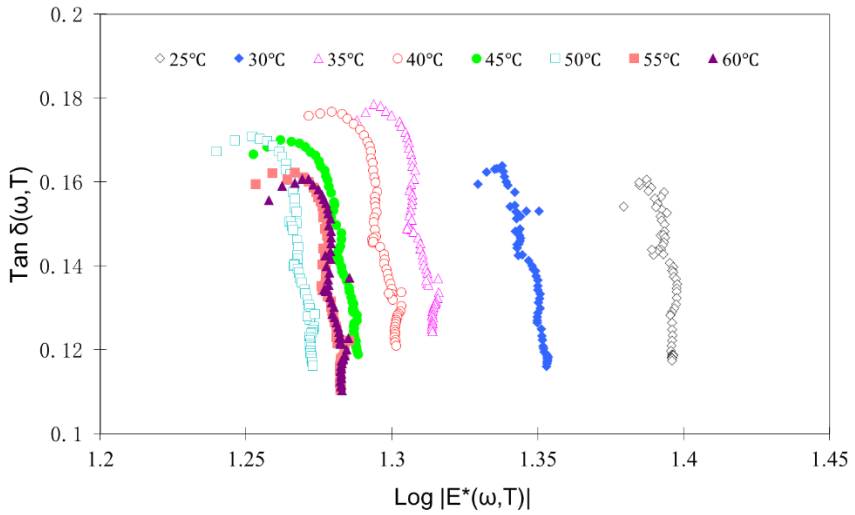


(b)

Figure 5. 8 (a) The Cole-Cole plot, and (b) the Black diagrams of the MRE samples under 1% uniaxial harmonic compression and non-magnetic field.

Figure 5.7 and Figure 5.8 show the logarithmic Cole-Cole plot and the semi-logarithmic Black diagram of the DMA measurement data of the MRE samples under 0.25% uniaxial harmonic compression in the presence of 300 mT magnetic field and the samples subjected to 1% uniaxial harmonic compression in the absence of a magnetic field respectively. It can be observed that the logarithmic Cole-Cole plot and the semi-logarithmic Black diagram does not form a single smooth curve, but the sets of each curve are dependent on temperature and exhibit a similar shape at different temperatures. This indicates that the MRE samples are not thermorheologically simple material, but the TTS may be applied to construct the master curve by using the horizontal shift factor and vertical shift factor [Dealy and Plazek (2009), Guedes (2011), Nakano (2013)].

In fact, the isothermal curves with a similar shape in Figure 5.7 and Figure 5.8 can be merged respectively into a single curve (as shown in Figure 5.9 and Figure 5.10) at a reference temperature of 40°C by applying the vertical shift factor. The similar shape of the Wicket plot obtained in Figure 5.9 and Figure 5.10 indicates that the TTS can be applied to construct the dynamic modulus master curve of the MRE samples under uniaxial harmonic compression within linear viscoelastic region. The scatter of calculated data in Figure 5.9 and Figure 5.10 are partly caused by the measurement noise. This graphical representation may assist in enhancing data analysis with measurement noise removal [Moreira (2010)].

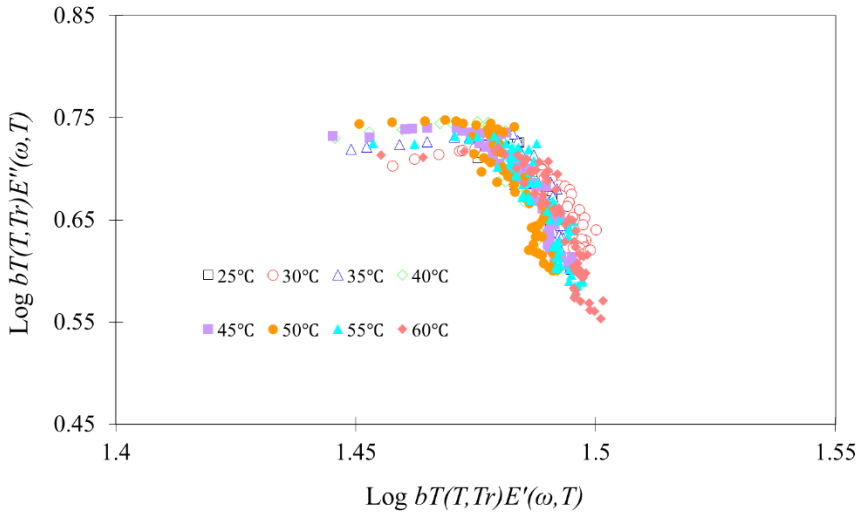


(a)

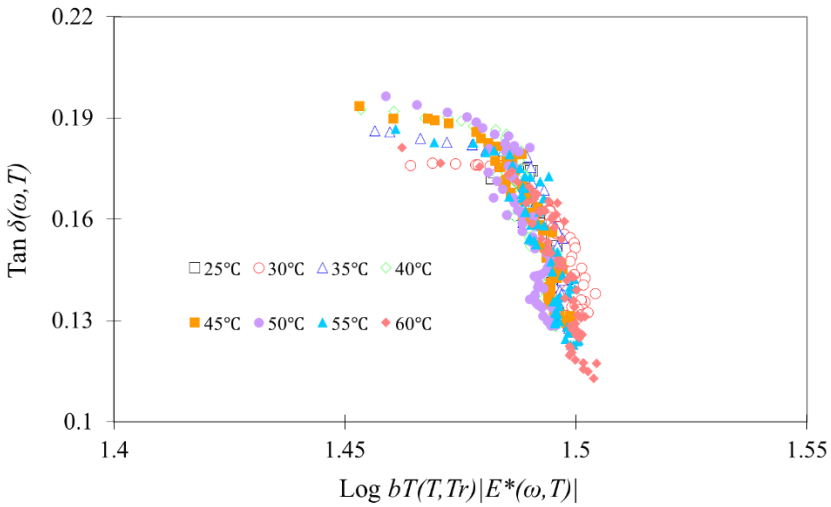


(b)

Figure 5. 9 The wicket plot calculated by applying the vertical shift factor to: (a) Cole-Cole plot, and (b) the Black diagrams of the MRE samples under 0.25% uniaxial harmonic compression and 300 mT magnetic field.

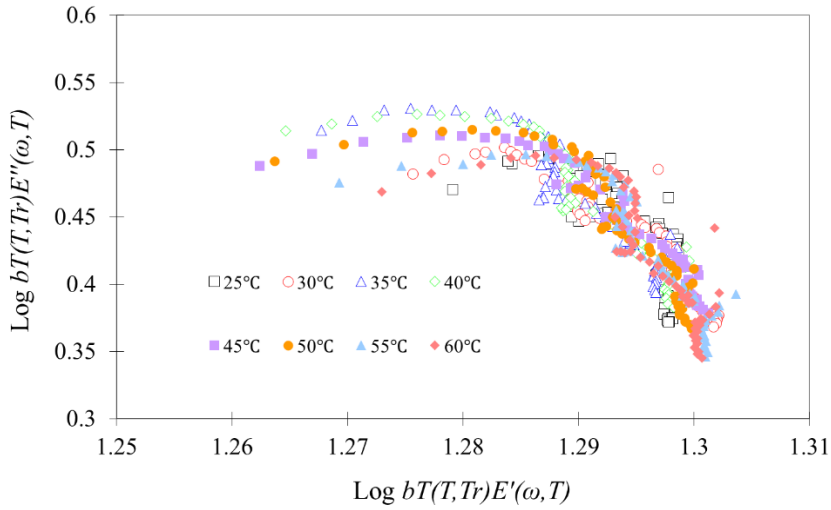


(a)

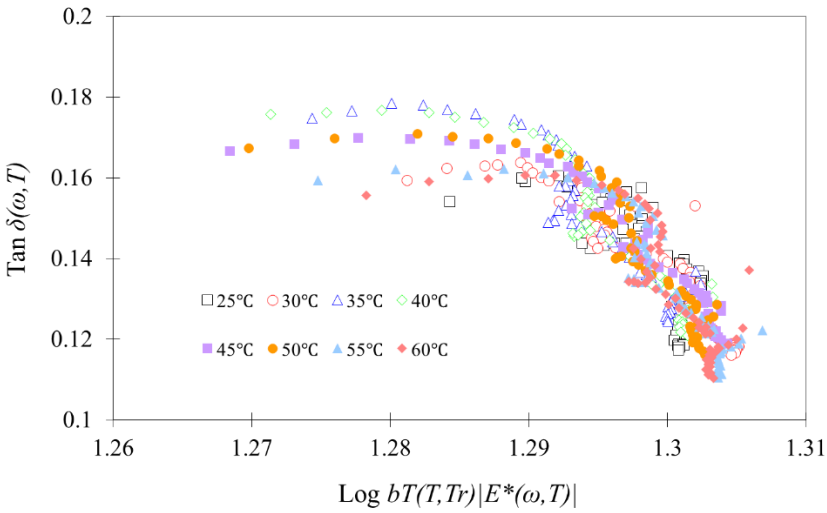


(b)

Figure 5. 10 The wicket plot calculated by applying the vertical shift factor to: (a) Cole-Cole plot, and (b) the Black diagrams of the MRE samples under 1% uniaxial harmonic compression and non-magnetic field.

### 5.3.3 Master curves construction

The dynamic modulus master curve of the MRE samples is constructed by applying the TTS principle at a reference temperature of 30°C. The model parameters for master curve and the numerical shift factors for each individual dynamic modulus are identified by minimizing the sum of square of error (SSE) between the predicted and measured data.

The frequency dependent storage modulus and loss modulus at different temperatures as shown in Figure 5.11 and Figure 5.13 are merged respectively into the master curves (as shown in

Figure 5.12 and Figure 5.14) by using the horizontal and vertical shift factors. Figure 5.12 shows the dynamic modulus master curves of the MRE samples subjected to uniaxial harmonic compression with small strain amplitude of 0.25% in the magnetic field of 300 mT. Figure 5.14 shows the dynamic modulus master curves of the MRE samples subjected to 1% strain amplitude harmonic compression in absence of magnetic field. A reasonable good superposition of frequency and temperature is observed despite a few points are not superposition well with the others and deviate from the master curve. The discrepancy occurs in the low frequency band of the master curve (as shown Figure 5.12(b) and Figure 5.14(b)) may be caused partly by the measurement data noise in DMA experiment. The goodness-of-fit parameters in Table 5.6 and Table 5.7, the standard error ratio ($S_e/S_y$) and the coefficient of determination ($R^2$), indicate that the excellent fitting results of dynamic modulus master curves.

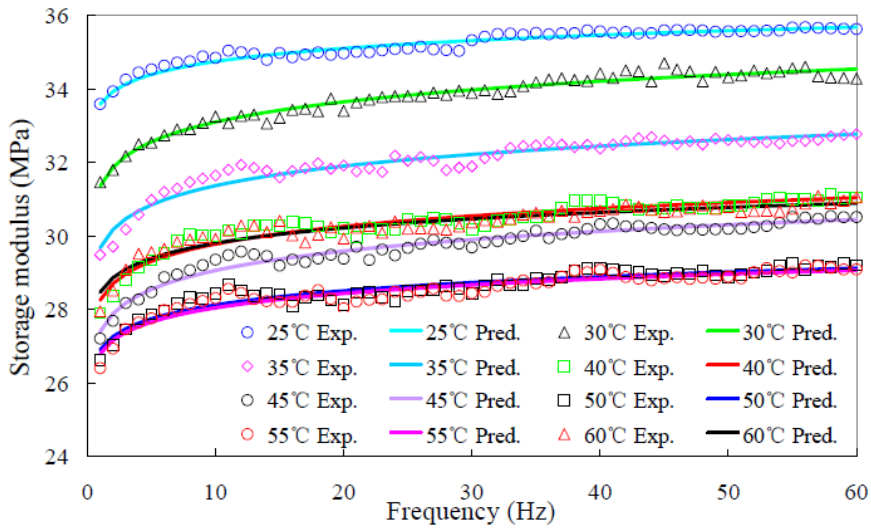


(a)

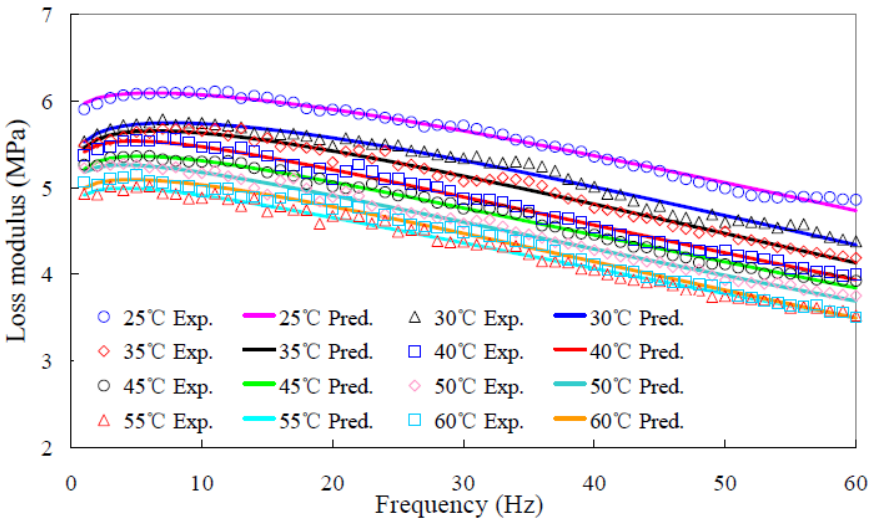

(b)

Figure 5. 11 Comparison between experimental and predicted data of: (a) storage modulus, and (b) loss modulus of the MRE samples under 0.25% strain amplitude and 300 mT magnetic field.

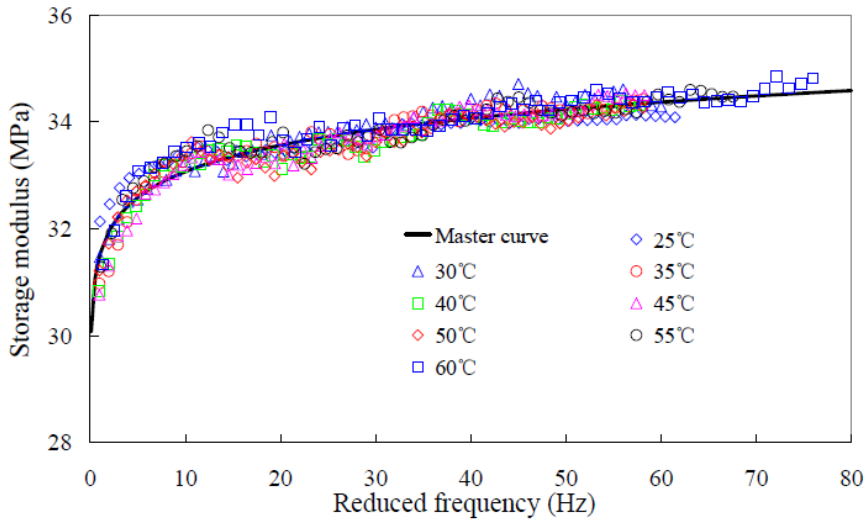


(a)

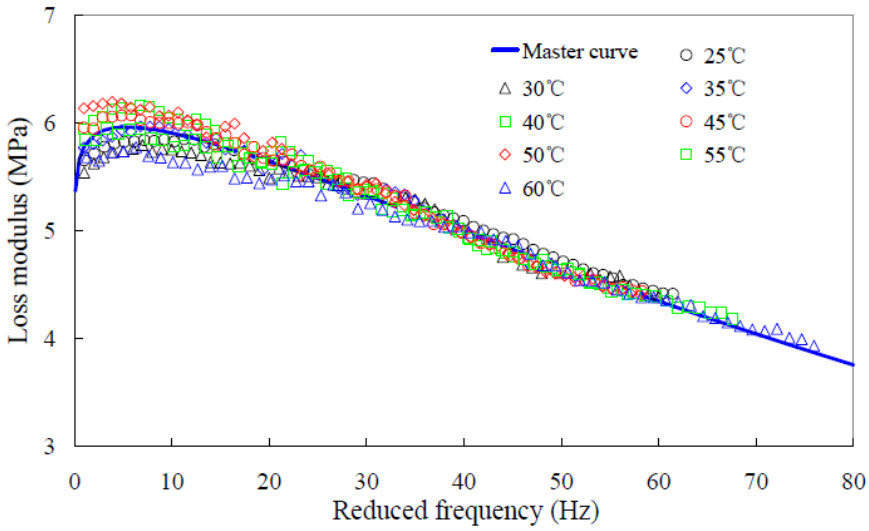


(b)

Figure 5. 12 Dynamic modulus master curve of the MRE samples under 0.25% strain amplitude and 300 mT magnetic field, (a) storage modulus, and (b) loss modulus.

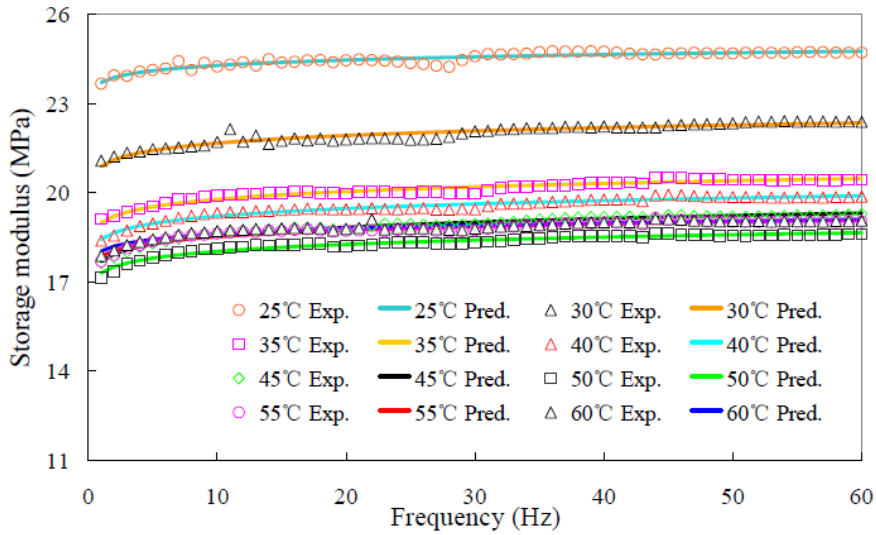


(a)

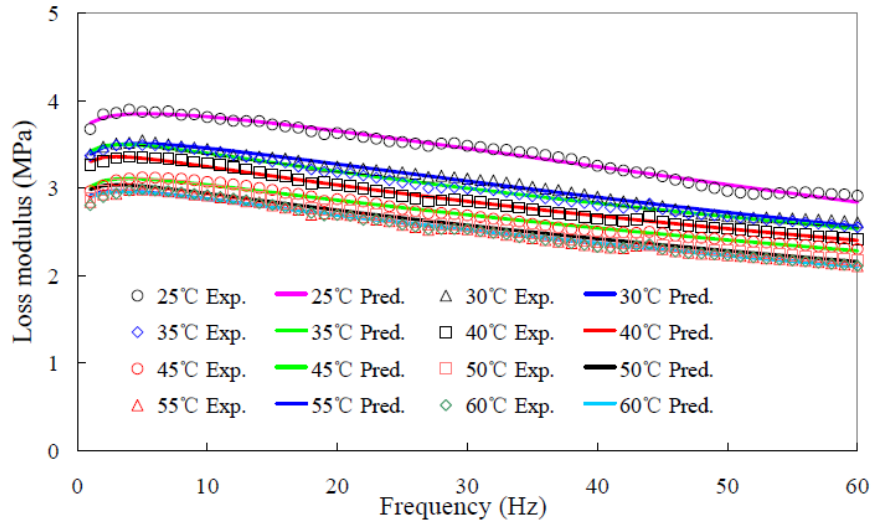


(b)

Figure 5. 13 Comparison between experimental and predicted data of: (a) storage modulus, and (b) loss modulus of the MRE samples under 1% strain amplitude and non-magnetic field.

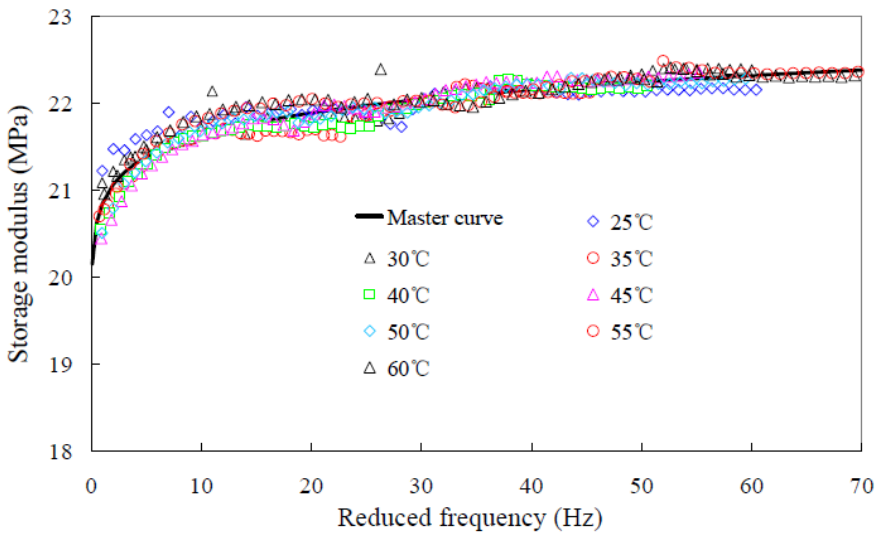


(a)

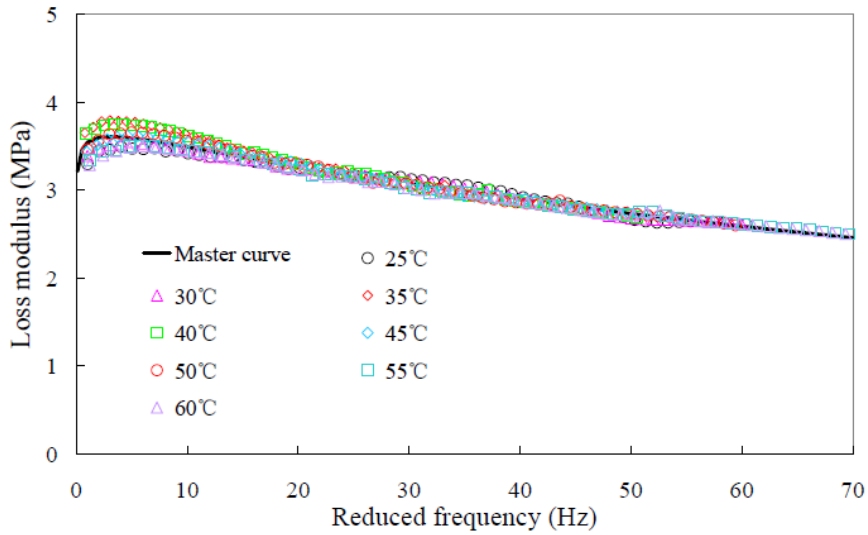


(b)

Figure 5. 14 The frequency and temperature dependent (a) storage modulus and (b) loss modulus of the MRE samples under 1% strain amplitude and non-magnetic field.

The goodness-of-fit statistical analysis results of the temperature dependent dynamic modulus and the fitting results by the proposed model as shown in Figure 5.11 and Figure 5.13 are also presented in Table 5.6 and table 5.7 for comparative analysis. The master curve and the proposed model fitting have similar correlations between experimental and predicted data of storage modulus and loss modulus. It indicates that the points deviate from the master curve is partly due to the fitting results of the viscoelastic model.

Table 5. 6 Goodness-of-fit analysis of the master curve and the proposed model for the MRE sample under uniaxial compression with 0.25% strain amplitude in the magnetic field of

300mT.

| | | 25°C | 30°C | 35°C | 40°C | 45°C | 50°C | 55°C | 60°C | Master curve |
|---|---|---|---|---|---|---|---|---|---|---|
| Storage modulus | $S_e/S_y$ | 0.263 | 0.208 | 0.250 | 0.290 | 0.228 | 0.365 | 0.349 | 0.320 | 0.090 |
| | $R^2$ | 0.937 | 0.960 | 0.942 | 0.923 | 0.952 | 0.878 | 0.888 | 0.906 | 0.992 |
| Loss modulus | $S_e/S_y$ | 0.273 | 0.317 | 0.281 | 0.227 | 0.249 | 0.230 | 0.239 | 0.271 | 0.147 |
| | $R^2$ | 0.932 | 0.908 | 0.928 | 0.953 | 0.943 | 0.951 | 0.948 | 0.933 | 0.979 |

Table 5. 7 Goodness-of-fit analysis of the master curve and the proposed model for the MRE sample under uniaxial compression with 1% strain amplitude in absence of magnetic field.

| | | 25°C | 30°C | 35°C | 40°C | 45°C | 50°C | 55°C | 60°C | Master curve |
|---|---|---|---|---|---|---|---|---|---|---|
| Storage modulus | $S_e/S_y$ | 0.398 | 0.386 | 0.307 | 0.239 | 0.136 | 0.189 | 0.252 | 0.303 | 0.060 |
| | $R^2$ | 0.853 | 0.861 | 0.912 | 0.947 | 0.983 | 0.967 | 0.941 | 0.915 | 0.997 |
| Loss modulus | $S_e/S_y$ | 0.221 | 0.183 | 0.100 | 0.103 | 0.104 | 0.085 | 0.103 | 0.097 | 0.161 |
| | $R^2$ | 0.954 | 0.969 | 0.991 | 0.990 | 0.990 | 0.993 | 0.990 | 0.991 | 0.975 |

### 5.3.4 Goodness-of-fit statistics of shift factors

The numerical shift factors present the best fit between experimental and predicted data in the construction of the dynamic modulus master curve as shown in Table 5.6 and Table 5.7. However, the functional shift factors, especially those with some thermodynamic basis, are still preferred to use because they are rapid and easy to apply in computer software [Rowe and Sharrock (2011), Kim et al. (2015)]. Figure 5.15 and Figure 5.16 show the comparison between the numerical shift factors and the functional shift factors for constructing the dynamic modulus master curve of the MRE samples under uniaxial harmonic compression. The functional horizontal shift factor is usually expressed by the WLF empirical equation, the Arrhenius equation, and the quadratic polynomial function, respectively. The DMA experiment results (as shown in the Chapter 4) indicate that the viscoelastic behaviour of the MRE samples under uniaxial compression can be identified into two regions by the transition temperature (about 50 °C). The DMA measurement data within the temperature range of 25 °C to 50 °C are considered for the application of the Arrhenius equation and the WLF empirical equation according to their thermodynamic basis.

Figure 5.15 and Figure 5.16 plot the numerical and functional shift factors versus temperature. It can be found that the quadratic equation presents the excellent correlation between the numerical and the functional vertical shift. The statistical analysis results show that the standard error ratio ($S_e/S_y$) is less than 0.27 and the coefficient of determination ($R^2$) is greater than 0.91. This indicates the quadratic equation can be utilized to predict the vertical shift factor.

A little difference exists between the numerical and functional horizontal shift factor. However, the Goodness-of-fit parameters of the resulting dynamic modulus master curve in Table 5.8 reveal that the functional horizontal shift factor works well for constructing the dynamic modulus master curve of the MRE samples under uniaxial harmonic compression. They present the excellent fitting results of the dynamic modulus master curves.

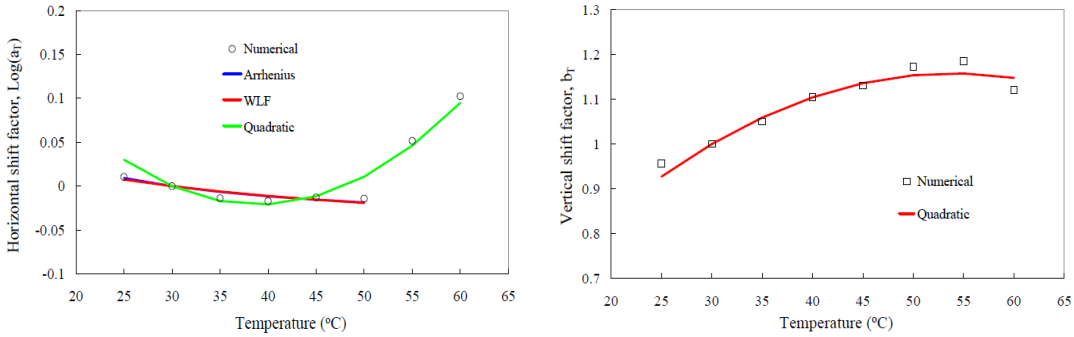


(a) (b)

Figure 5. 15 Comparison between numerical and functional shift factors: (a) horizontal shift factor and vertical shift factor of the MRE samples under 0.25% strain amplitude and 300 mT magnetic field.

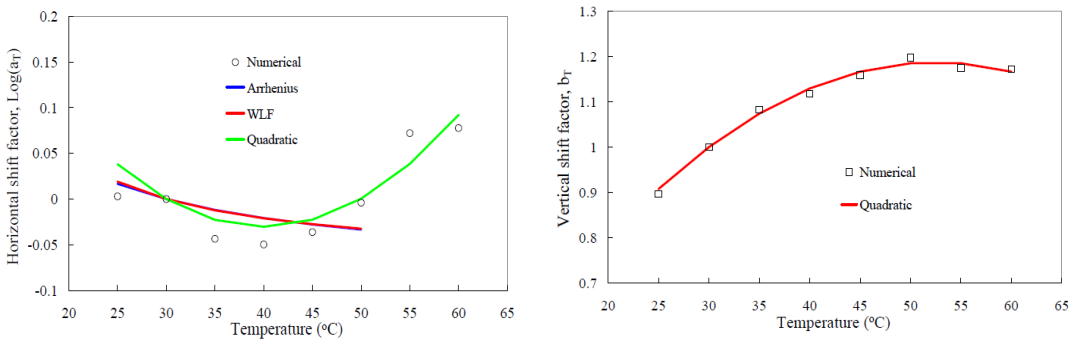


(a) (b)

Figure 5. 16 Comparison between numerical and functional shift factors: (a) horizontal shift factor and vertical shift factor of the MRE samples under 1% strain amplitude and non-magnetic field.

Table 5. 8 Goodness-of-fit statistical analysis of the dynamic modulus master curve constructed by different horizontal shift factors.

| | | | numerical | WLF equation | Arrhenius equation | Quadratic polynomial |
|---|---|---|---|---|---|---|
| 0.25% and 300 mT | Storage modulus | $S_e/S_y$ | 0.090 | 0.282 | 0.240 | 0.276 |
| | | $R^2$ | 0.992 | 0.922 | 0.944 | 0.925 |
| | Loss modulus | $S_e/S_y$ | 0.147 | 0.190 | 0.189 | 0.179 |
| | | $R^2$ | 0.979 | 0.965 | 0.965 | 0.969 |

| | | | | | | |
|---|---|---|---|---|---|---|
| 1% and 0 mT | Storage modulus | $S_e/S_y$ | 0.060 | 0.141 | 0.111 | 0.113 |
| | | $R^2$ | 0.997 | 0.981 | 0.988 | 0.987 |
| | Loss modulus | $S_e/S_y$ | 0.161 | 0.175 | 0.175 | 0.159 |
| | | $R^2$ | 0.975 | 0.970 | 0.970 | 0.975 |

## 5.4 Dependence of magnetic field

### 5.4.1 Basic equation

MREs are a class of smart composite materials which consist of micron-sized magnetic particles embedded in an elastomeric matrix. Their dynamic properties in addition to mechanical load are dependent on the external magnetic field. According to the magneto-elastic theory [Castanda and Galipeau (2011)], the free-energy function for these smart composites can be additively decomposed into a mechanical part $\varphi_{mech}(\varepsilon, B)$ and a magnetic part $\varphi_{magn}(\varepsilon, B)$,

$$\varphi(\varepsilon, B) = \varphi_{mech}(\varepsilon, B) + \varphi_{mech}(\varepsilon, B) \tag{5.20}$$

In which ε is the strain of MREs and B is the external magnetic flux intensity.

The magnetic part $\varphi_{magn}(\varepsilon, B)$ is dependent on strain amplitude, excitation frequency, and external magnetic flux intensity while the mechanical part $\varphi_{mech}(\varepsilon)$ is dependent on strain amplitude and excitation frequency. This indicates the complex modulus of MREs under magnetic-mechanical loads can be divided into mechanical part $E^*_{mech}(\varepsilon)$ and magnetic part $E^*_{magn}(\varepsilon, B)$ as follow:

$$E^*(\varepsilon, B) = E^*_{mech}(\varepsilon) + E^*_{magn}(\varepsilon, B) \tag{5.21}$$

where the magnetic part $E^*_{magn}(\varepsilon, B)$ denotes magnetic field induced dynamic modulus, the mechanical part $E^*_{mech}(\varepsilon)$ is the isothermal dynamic modulus of particle filled elastomers and dependent on temperature and strain including strain amplitude and excitation frequency.

The temperature effect on dynamic modulus has been discussed in Section 5.3. The dynamic modulus master curve can be constructed by using TTS principle to predict the viscoelastic properties of the MREs beyond the DMA experiment range of temperatures and frequencies. In the case of linear viscoelastic regime, the stress-strain hysteresis loop forms an elliptical shape, and the effect of strain amplitude can be neglected. The isothermal dynamic modulus can be modelled by using linear viscoelastic model within linear viscoelastic regime, which

has been discussed in Section 5.2. The influence of strain amplitude on the dynamic modulus will be discussed in Section 5.5.

### 5.4.2 The magnetic field induced modulus

The magnetic field induced dynamic modulus can be decomposed into the magnetic field induced storage modulus and loss modulus in small strain range.

$$E^*_{magn}(\varepsilon, B) = E'_{magn}(\varepsilon, B) + iE''_{magn}(\varepsilon, B) \tag{5.22}$$

in which $E'_{magn}(\varepsilon, B)$ and $E''_{magn}(\varepsilon, B)$ are magnetic field induced storage modulus and loss modulus respectively.

They can be described by the magnetorheological (MR) effect.

$$E'_{magn}(\varepsilon, B) = c'_{MR} E'_{mech}(\varepsilon) \tag{5.23a}$$

$$E''_{magn}(\varepsilon, B) = c''_{MR} E''_{mech}(\varepsilon) \tag{5.23b}$$

where $c'_{MR}$ and $c''_{MR}$ are the MR effect on storage modulus and loss modulus respectively, which are mainly dependent on the magnetic flux density and applied strain amplitude. $E'_{mech}(\varepsilon)$ and $E''_{mech}(\varepsilon)$ are isothermal storage modulus and loss modulus, the real and imaginary part of the complex modulus $E^*_{mech}(\varepsilon)$.

$$c'_{MR} = \frac{E'_{magn}(\varepsilon, B)}{E'_{mech}(\varepsilon)} \tag{5.24a}$$

$$c''_{MR} = \frac{E''_{magn}(\varepsilon, B)}{E''_{mech}(\varepsilon)} \tag{5.24b}$$

Substituting Eq. (5.22) – Eq. (5.24) into Eq. (5.21), it leads to

$$E^*(\varepsilon, B) = (1 + c'_{MR})E'_{mech}(\varepsilon) + i(1 + c''_{MR})E''_{mech}(\varepsilon) \tag{5.25}$$

The MR effect, regarded as the unique characteristic of MREs, has attracted a great deal of attentions from researchers and engineers. The experimental results revealed that the MR effect was mainly dominated by the dipole interaction force of magnetic particles in the presence of magnetic field [Böse and Röder (2009), Kaleta et al. (2011), Lokander and Stenberg (2003)]. Theoretical models, such as the dipole model and the effective permeability model, were developed to predict the MR effect of MREs based on a pre-assumed microstructure [Jolly et

al. (1996), Zhu et al. (2006), Dong et al. (2012)]. The theoretical results showed that the dipole interaction of magnetic particles was proportional to the square of magnetic flux intensity or the particle magnetization until the magnetic saturation. The MR effect of MREs can be expressed as quadratic polynomial function of the magnetic flux density or the particle magnetization as follow [Norouzi et al. (2016), Blom and Kari (2011)]:

$$c'_{MR} = c'_0 + c'_1 B + c'_2 B^2 \tag{5.26a}$$

$$c''_{MR} = c''_0 + c''_1 B + c''_2 B^2 \tag{5.26b}$$

where $c'_0$, $c'_1$, $c'_2$, $c''_0$, $c''_1$, and $c''_2$ are model parameters which can be identified by DMA experiment data. B is the external magnetic flux intensity.
and

$$c'_{MR} = \delta \left(\frac{M}{M_s}\right)^2 \tag{5.27}$$

where δ is model parameter which can be identified by DMA experiment data. M the magnetization and $M_s$ is the saturation magnetization.

On the basis of the observation in the DMA experiment, Xin et al. (2016) proposed a polynomial function with three order for representing the MR effect of MREs,

$$c'_{MR} = \left(\alpha_1 + \beta_1 \frac{B}{B_{max}}\right) B^2 \tag{5.28a}$$

$$c''_{MR} = \left(\alpha_2 + \beta_2 \frac{B}{B_{max}}\right) B^2 \tag{5.28b}$$

where $\alpha_1$, $\alpha_2$, $\beta_1$, and $\beta_2$ are model parameters which can be identified by DMA experiment data. B is the external magnetic flux intensity and $B_{max}$ is the saturation magnetic flux intensity.

Figure 5.17 to Figure 5.19 present the comparative analysis between the DMA experimental data and the fitting results of magnetic field dependent dynamic modulus by using Eq. (5.26) to Eq. (5.28). It is clearly observed from Table 5.9 and Figure 5.17 to Figure 5.19 that these models provide the excellent fitting results for storage modulus while the fair fitting results for loss modulus. The magnetic field dependent loss modulus has a peak value in the range of magnetic flux intensity considered. These models cannot represent the larger changes near the peak value of the loss modulus. In order to model this larger changes and obtain the better fitting results, a new approach is proposed as follows for fitting the storage modulus and loss

modulus respectively.

$$c'_{MR} = \frac{c_1 B^m}{1 + d_1 B^m} \tag{5.29a}$$

$$c''_{MR} = \frac{c_2 B^n}{1 + d_2 B^{2n}} \tag{5.29b}$$

where $c_1$, $c_2$, $d_1$, $d_2$, $m$, and $n$ are model parameters which can be identified by DMA experiment data. B is the external magnetic flux intensity.

Comparative analysis is performed between the proposed model and the existing models for MR effect of MRE sample under uniaxial harmonic compression with 5% pre-strain, 1% strain amplitude, and 1 to 60 Hz excitation frequency in room temperature. Figure 5.17 to Figure 5.19 show the results obtained in the frequency case of 10 Hz, 30 Hz, and 50Hz. It is clearly observed that the proposed model presents the better fitting results than the existing models. It is very good agreement with the experimental data for both storage modulus and loss modulus. The existing models fit very well with storage modulus but fair with loss modulus. The standard error ratio ($S_e/S_y < 0.27$) and the coefficient of determination ($R^2 > 0.94$) as shown in Table 5.10 indicate that the excellent fitting results of both storage modulus and loss modulus are obtained by the proposed model.

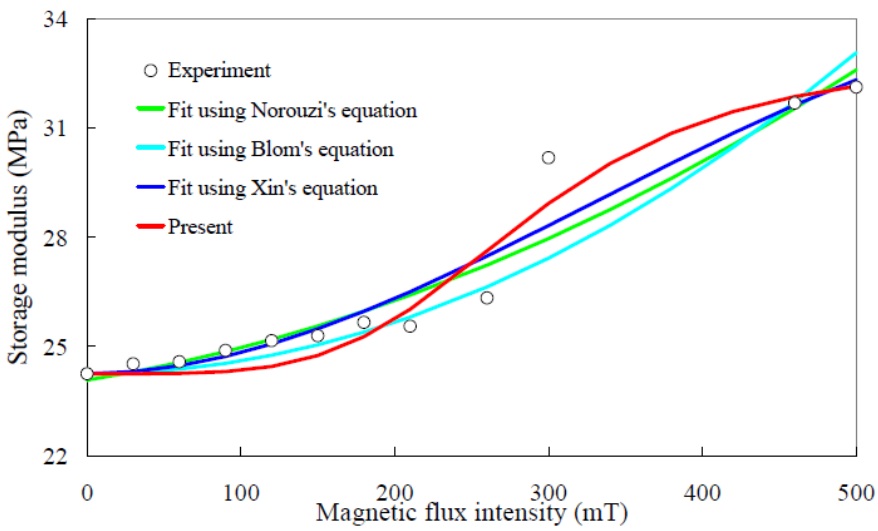


(a)

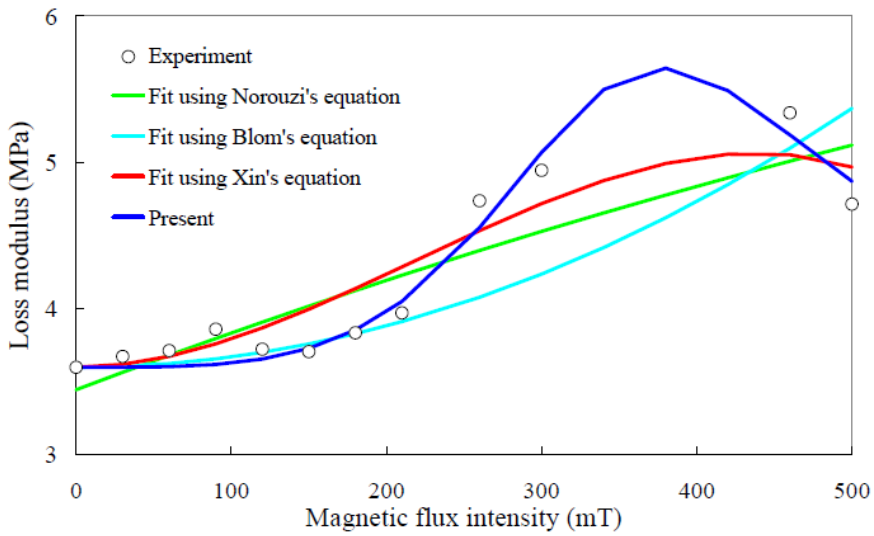


(b)

Figure 5. 17 The Comparison of magnetic field dependent: (a) storage modulus and (b) loss modulus between experimental data and fitting results of the MRE sample under uniaxial compression with 5% pre-strain, 1% strain amplitude, and 10 Hz excitation frequency in room temperature.

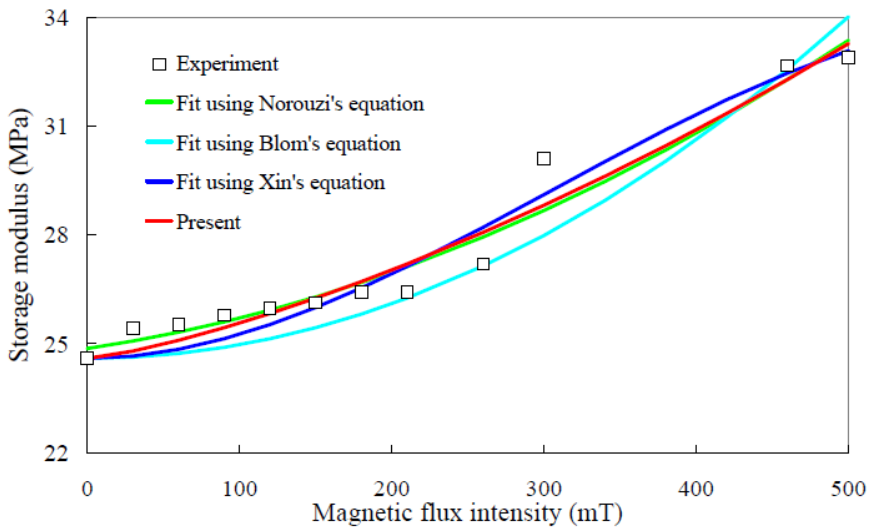


(a)

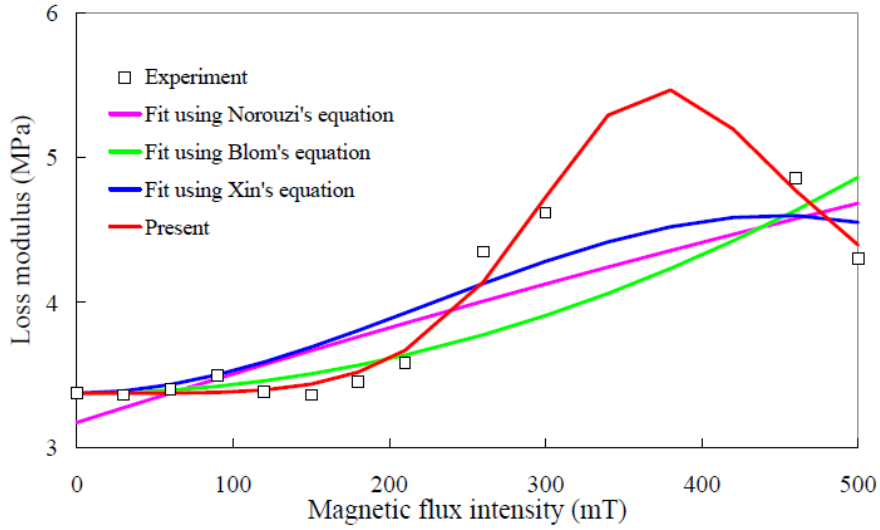


(b)

Figure 5. 18 The Comparison of magnetic field dependent: (a) storage modulus and (b) loss modulus between experimental data and fitting results of the MRE sample under uniaxial compression with 5% pre-strain, 1% strain amplitude, and 30 Hz excitation frequency in room temperature.

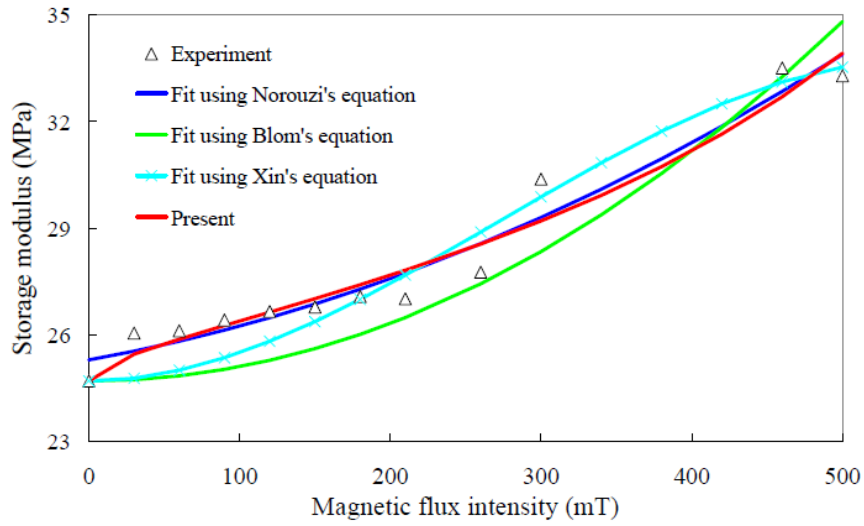


(a)

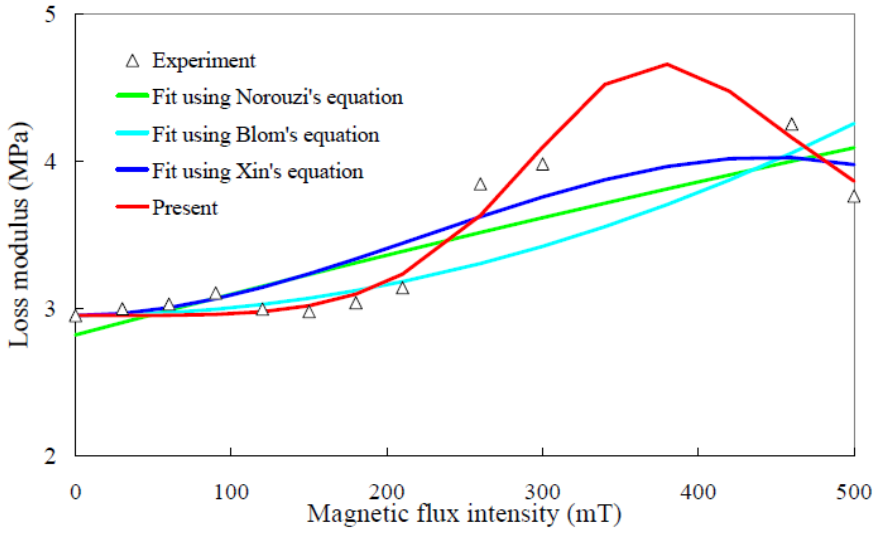


(b)

Figure 5. 19 The Comparison of magnetic field dependent: (a) storage modulus and (b) loss modulus between experimental data and fitting results of the MRE sample under uniaxial compression with 5% pre-strain, 1% strain amplitude, and 50 Hz excitation frequency in room temperature.

Table 5. 9 Statistical analysis results of Goodness-of-fit for magnetic field dependent storage modulus and loss modulus of MREs under uniaxial harmonic compression with 5% pre-strain and 1% strain amplitude in room temperature.

| | | | Norouzi's equation | Blom's equation | Xin's equation | Present |
|---|---|---|---|---|---|---|
| Frequency of 10 Hz | Storage modulus | $S_e/S_y$ | 0.304 | 0.316 | 0.267 | 0.257 |
| | | $R^2$ | 0.924 | 0.900 | 0.935 | 0.946 |
| | Loss modulus | $S_e/S_y$ | 0.517 | 0.607 | 0.388 | 0.236 |
| | | $R^2$ | 0.781 | 0.631 | 0.863 | 0.955 |
| Frequency of 10 Hz | Storage modulus | $S_e/S_y$ | 0.231 | 0.326 | 0.232 | 0.240 |
| | | $R^2$ | 0.956 | 0.894 | 0.951 | 0.953 |
| | Loss modulus | $S_e/S_y$ | 0.569 | 0.596 | 0.463 | 0.190 |
| | | $R^2$ | 0.735 | 0.644 | 0.805 | 0.971 |
| Frequency of 10 Hz | Storage modulus | $S_e/S_y$ | 0.224 | 0.430 | 0.294 | 0.242 |
| | | $R^2$ | 0.959 | 0.815 | 0.922 | 0.952 |
| | Loss modulus | $S_e/S_y$ | 0.559 | 0.610 | 0.455 | 0.243 |
| | | $R^2$ | 0.716 | 0.628 | 0.811 | 0.952 |

### 5.4.3 Magnetic field dependent dynamic properties

The magnetic field dependent dynamic moduli of MREs in linear viscoelastic regime can be predicted by using Eq. (5.11), Eq. (5.25), and Eq. (5.29). Figure 5.21 presents the dynamic modulus master curve, which take into account for magnetic field effect. Twelve curves of the storage modulus and loss modulus of MREs under various magnetic fields (as shown in Figure

5.20) are merged respectively into a single curve of the storage modulus and loss modulus of MREs in the absence of magnetic field (as shown in Figure 5.21).

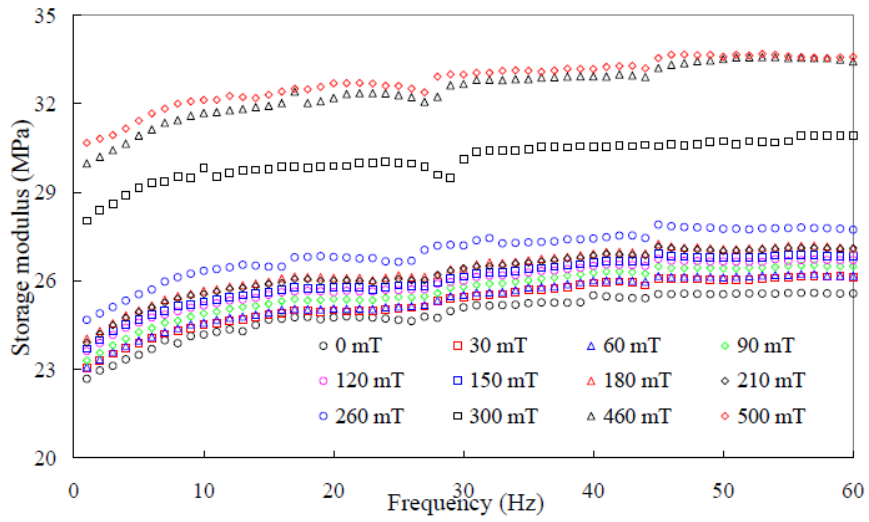


(a)

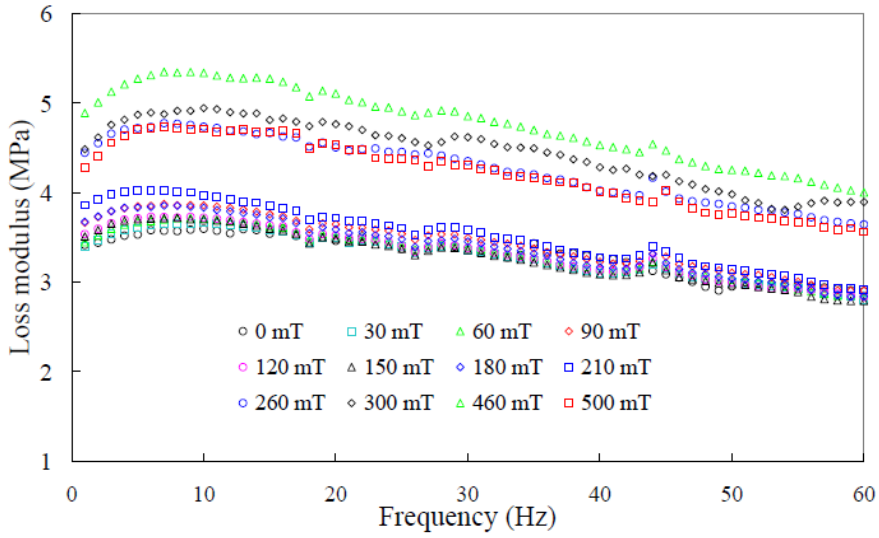


(b)

Figure 5. 20 Measured data of magnetic field dependent: (a) storage modulus, and (b) loss modulus of the MRE sample under uniaxial compression with 5% pre-strain and 1% strain amplitude in room temperature

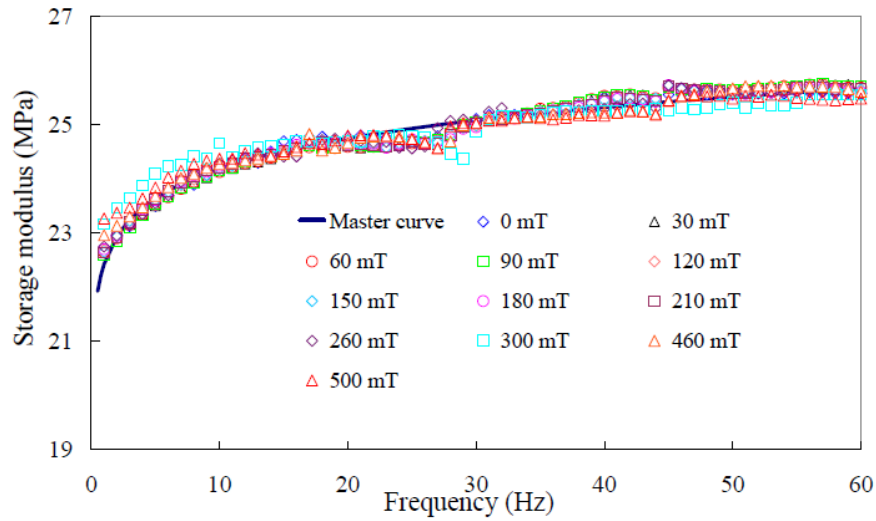


(a)

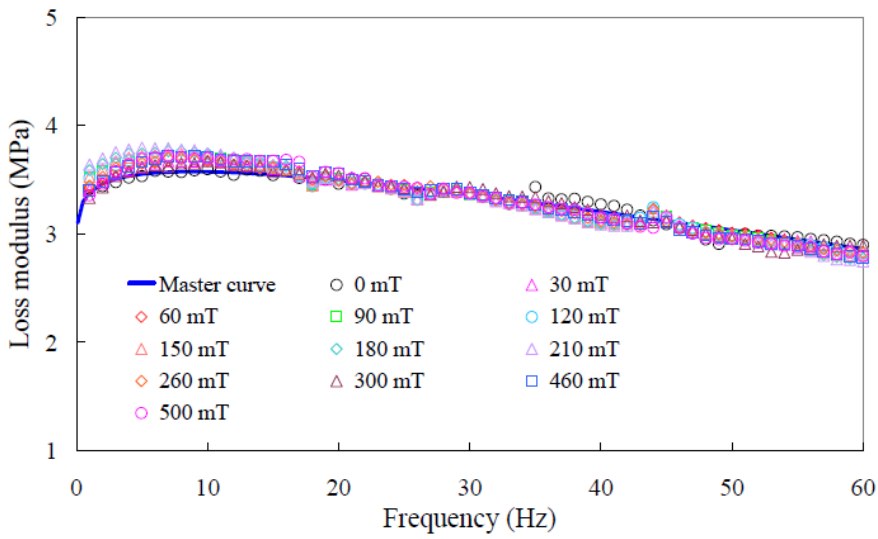


(b)

Figure 5. 21 Predicted results by using the proposed model for magnetic field dependent: (a) storage modulus, and (b) loss modulus of the MRE sample under uniaxial compression with 5% pre-strain and 1% strain amplitude in room temperature.

The statistical analysis results of goodness-of-fit show that the proposed model provides the very good fitting results for storage modulus ($S_e/S_y < 0.28$ and $R^2 > 0.92$) and the excellent fitting results for loss modulus ($S_e/S_y < 0.33$ and $R^2 > 0.89$). This indicates that the effects of magnetic field and excitation frequency on the dynamic moduli of MREs are separable within linear viscoelastic regime. The external magnetic field affects the dynamic moduli value of MREs without affecting the vibration frequency. The master curve of magnetic field dependent dynamic modulus can be constructed by using the MR effect and viscoelastic model in linear viscoelastic regime. The constructed master curve can be used to predict the influence of

magnetic field on dynamic modulus by interpolating or even extrapolating experimental results.

## 5.5 Dependence of strain amplitude

### 5.5.1 Linear viscoelastic limit

The dynamic response of particle filled elastomers can be classified into linear and nonlinear viscoelastic regimes by the strain amplitude. In the linear regime, the strain amplitude is sufficiently small that dynamic modulus is independent on strain amplitude and the hysteresis loop forms an elliptical shape. The dynamic properties can be described by using linear viscoelastic model.

As the strain amplitude rises higher than the linear viscoelastic limit, the dynamic properties tend toward nonlinear viscoelastic and the consequent reduction in modulus with increasing strain amplitude (called the Payne effect). This physical phenomenon is commonly interpreted as the deformation induced changes in material's microstructure, a dynamic equilibrium between breakage and recovery of weak physical bonds linking the polymer and the filler particles [Cassagnau and Mélis (2003), Robertson et al. (2008)].

The linear viscoelastic limit of filled elastomers is dependent on the volume fraction and distribution of particles, material properties of elastomeric matrix, excitation frequency, and temperature etc. In additional to these dependent factors like filled elastomers, the linear viscoelastic limit of MREs is also dependent on the external magnetic field [Olabide et al. (2014, 2015), Nanpo et al. (2016), Sorokin et al. (2017)]. The linear viscoelastic limit decreases with increasing of external magnetic field. However, there is no standardized procedure for defining the linear viscoelastic limit [Starkova and Aniskevich (2007)]. It is usually determined by the distortion in regular elliptical shape of hysteresis loop [Li et al. (2010), Poojary and Gangadharan (2016)], the intersection of the inflectional tangent with the tangent extrapolated from the plateau below the linear viscoelastic limit [Sorokin et al. (2017)], and the percentage deviation from linear relationship of stress and strain [Qi et al. (2018), Olabide and Elejabarrieta (2018)].

The experimental results revealed that the linear viscoelastic limit of MREs were strongly dependant on external magnetic field and weak dependent on excitation frequency [Poojary and Gangadharan (2016)]. The linear viscoelastic limit of MREs varies from 0.01% to 10% according to the published results [Li et al. (2010), Gong et al. (2012), Tian et al. (2013), Nappo

et al. (2016), An et al. (2017)]. As a semi-active vibration control device, MREs usually work beyond the linear viscoelastic regime. Their dynamic properties of MREs should be described by using the nonlinear viscoelastic theory.

According to the nonlinear viscoelastic theory, the nonlinear stress response to an input sinusoidal strain $\varepsilon(t) = \varepsilon_0 \sin \omega t$ can be expressed by using Fourier series and power series respectively [Hyun et al. (2011), Song et al. (2016), Singh et al. (2018)].

$$\begin{aligned}\sigma(t) &= \sum_{n,odd} [\sigma_n'(\omega,\varepsilon_0)\sin(n\omega t) + \sigma_n''(\omega,\varepsilon_0)\sin(n\omega t)] \\ &= \varepsilon_0 \sum_{n,odd} [E_n'(\omega,\varepsilon_0)\sin(n\omega t) + E_n''(\omega,\varepsilon_0)\sin(n\omega t)]\end{aligned} \tag{5.30}$$

in which $\varepsilon_0$ denotes strain amplitude, $\sigma_n'(\omega,\varepsilon_0)$ and $\sigma_n''(\omega,\varepsilon_0)$ are elastic and viscous stress Fourier coefficients, $E_n'(\omega,\varepsilon_0)$ and $E_n''(\omega,\varepsilon_0)$ are elastic and viscous modulus Fourier coefficients.

$$\begin{aligned}\sigma(t) &= \sum_{m,odd}\sum_{n,odd}^{m} \varepsilon_0^n\,[E_{mn}'(\omega)\sin(n\omega t) + E_{mn}''(\omega)\sin(n\omega t)] \\ &= \varepsilon_0[E_{11}'(\omega)+\varepsilon_0^2E_{31}'(\omega) + O(\varepsilon_0^4) + \cdots]\sin(\omega t) \\ &\quad +\varepsilon_0[E_{11}''(\omega)+\varepsilon_0^2E_{31}''(\omega) + O(\varepsilon_0^4) + \cdots]\cos(\omega t) \\ &\quad +\varepsilon_0^3[E_{33}'(\omega)+\varepsilon_0^2E_{53}'(\omega) + O(\varepsilon_0^4) + \cdots]\sin(3\omega t) \\ &\quad +\varepsilon_0^3[E_{33}''(\omega)+\varepsilon_0^2E_{53}''(\omega) + O(\varepsilon_0^4) + \cdots]\cos(3\omega t) + \cdots\end{aligned} \tag{5.31}$$

where $E_{mn}'(\omega)$and $E_{mn}''(\omega)$ are frequency dependent elastic and viscous modulus coefficients in power series.

Since the Eq. (5.30) and Eq. (5.31) describe the same nonlinear viscoelastic phenomena using different mathematical descriptions, these two expressions can be mathematically related for first and third terms of modulus coefficients in Fourier series and power series.

The first term:

$$E_1'(\omega,\varepsilon_0) = E_{11}'(\omega)+\varepsilon_0^2E_{31}'(\omega) + O(\varepsilon_0^4) + \cdots \tag{5.32a}$$

$$E_1''(\omega,\varepsilon_0) = E_{11}''(\omega)+\varepsilon_0^2E_{31}''(\omega) + O(\varepsilon_0^4) + \cdots \tag{5.32b}$$

and the third term:

$$E_3'(\omega,\varepsilon_0) = \varepsilon_0^2 E_{33}'(\omega) + \varepsilon_0^4 E_{53}'(\omega) + O(\varepsilon_0^6) + \cdots \quad (5.33a)$$

$$E_3''(\omega,\varepsilon_0) = \varepsilon_0^2 E_{33}''(\omega) + \varepsilon_0^4 E_{53}''(\omega) + O(\varepsilon_0^6) + \cdots \quad (5.33b)$$

in which $E_{11}'(\omega)$ and $E_{11}''(\omega)$ are two linear Fourier coefficients of the small strain regime. It is clearly found from Eq. (5.30) to Eq. (5.33) that $E_1'(\omega,\varepsilon_0) = E_{11}'(\omega) = E'(\omega)$ and $E_1''(\omega,\varepsilon_0) = E_{11}''(\omega) = E''(\omega)$ within linear viscoelastic regime. $E_{31}'(\omega)$, $E_{31}''(\omega)$, $E_{33}'(\omega)$, and $E_{33}''(\omega)$ are four nonlinear Fourier coefficients of the medium strain regime, which are quadratic dependence on strain amplitude in medium strain range.

Functions $E_{31}'(\omega)$ and $E_{31}''(\omega)$ represent the intercycle nonlinearities which explain average changes of hysteresis loops. While functions $E_{33}'(\omega)$, and $E_{33}''(\omega)$ represent the intracycle nonlinearities which explain instantaneous deviation from linear viscoelastic response within a single cycle [Ewoldt et al. (2008), Nie et al. (2016), Singh et al. (2018)].

These functions present an asymptotic nonlinearity of viscoelastic materials in small strain range. Both storage modulus and loss modulus can be separated into a strain-amplitude dependent part and an excitation frequency dependent part within small strain regime [Lin and Lee (1996), Li et al. (2017)]. The change of dynamic modulus is quadratic dependent on strain amplitude and should be taken into account in the viscoelastic model.

The detailed discussion on the degree of nonlinearities can be referred to published papers [e.g. Hyun and Kim (2011), Merger and Wilhelm (2014), Poulos et al. (2015)]. The nonlinear parameter $Q(\omega,\varepsilon_0)$ and the zero-strain nonlinearity $Q_0(\omega)$, which based on the ratio of first and third term, are introduced to characterize the intrinsic nonlinearity in medium strain range.

### 5.5.2 The Kraus model

Our experiment results (as shown in the Chapter 4) reveal that the hysteresis loop forms an approximate elliptical shape. The little deviation is found nearby strain peaks, which may be caused by the interfacial friction due to a change in applied strain direction. The slope of the stress-strain hysteresis loop decreases when strain amplitude increases. The Payne effect occurs as increasing of strain amplitude.

These observations indicate that the dynamic response of the MRE samples can be separated into a strain dependent part and a frequency dependent part. The frequency dependent dynamic modulus can be described by using linear viscoelastic models. However, the influence of strain

amplitude on the dynamic modulus should be taken into consideration in the viscoelastic model [Luo et al. (2010), Suo et al. (2018)].

For a fixed vibration frequency, the Kraus model is employed to describe the strain amplitude dependent dynamic modulus.

$$E'(\varepsilon_0) = E'_\infty + \frac{E'_0 - E'_\infty}{1 + (\varepsilon_0/\varepsilon_c)^{2k}} \tag{5.34a}$$

$$E''(\varepsilon_0) = E''_\infty + \frac{2(E''_m - E''_\infty)(\varepsilon_0/\varepsilon_c)^k}{1 + (\varepsilon_0/\varepsilon_c)^{2k}} \tag{5.34b}$$

in which $\varepsilon_0$ is strain amplitude, $E'_0$ is storage modulus at small strain amplitude, $E'_\infty$ and $E''_\infty$ are the asymptotic values of storage modulus and loss modulus at large strain amplitude respectively, $\varepsilon_c$ is the characteristic strain amplitude where the loss modulus reaches its maximum $E''_m$, and k is a model parameter.

Figure 5.22 to Figure 5.25 present the comparison of predicted results and measured data of the MRE samples by strain amplitude sweep in frequency range of 10 Hz to 60 with interval of 10 Hz, and non-magnetic field and 300 mT magnetic field respectively. It can be found that the predicted results are very agreement with the measured data of the MRE samples under uniaxial harmonic compression in different excitation frequencies, external magnetic fields, and temperatures. The model parameter $E''_\infty$ can be approximately considered equal to zero. The Eq. (5.34b) can be simplified to the following expression.

$$E''(\varepsilon_0) \approx \frac{2E''_m(\varepsilon_0/\varepsilon_c)^k}{1 + (\varepsilon_0/\varepsilon_c)^{2k}} \tag{5.34c}$$

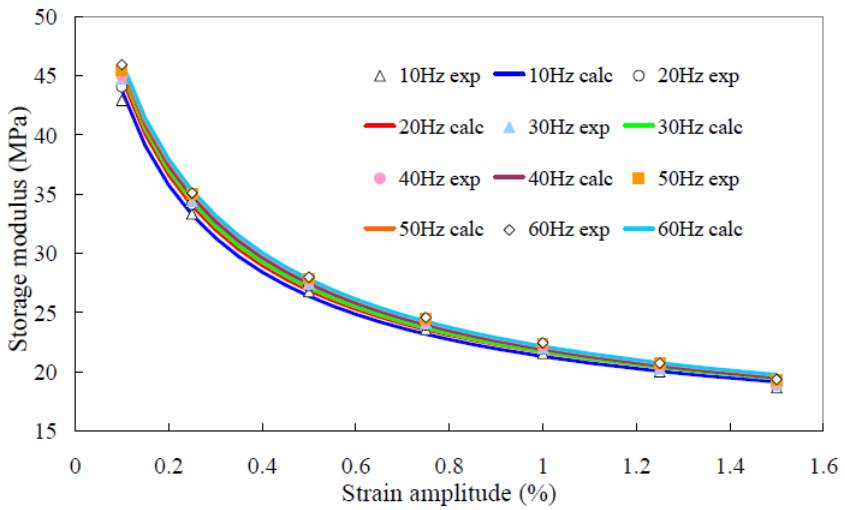


(a)

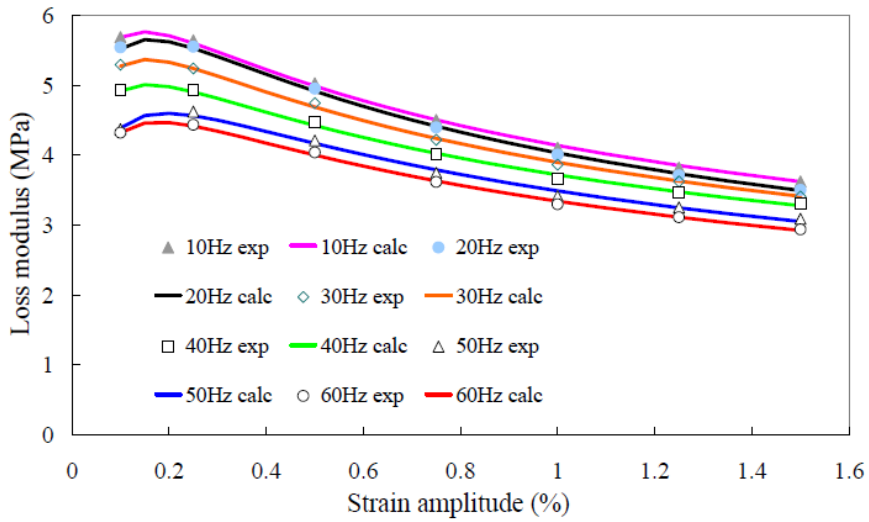


(b)

Figure 5. 22 Comparison of predicted results and measured data of strain amplitude dependent: (a) storage modulus, and (b) loss modulus of the MRE sample under uniaxial compression with 3% pre-strain, in non-magnetic field and room temperature.

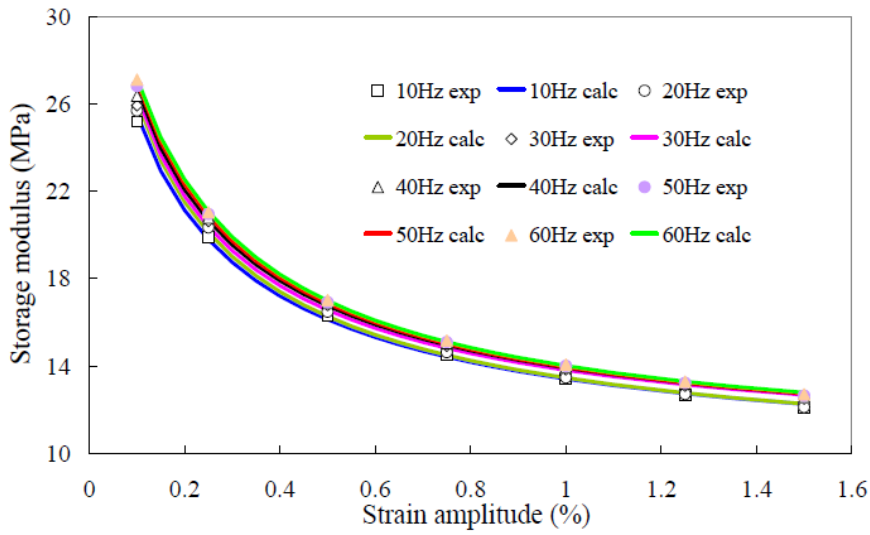


(a)

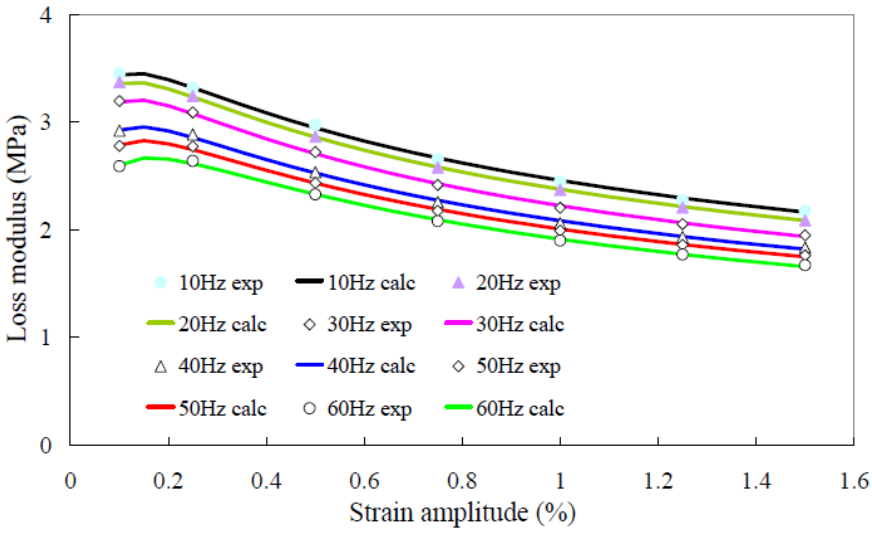


(b)

Figure 5. 23 Comparison of predicted results and measured data of strain amplitude dependent: (a) storage modulus, and (b) loss modulus of the MRE sample under uniaxial compression with 3% pre-strain, in non-magnetic field and temperature of 50 °C.

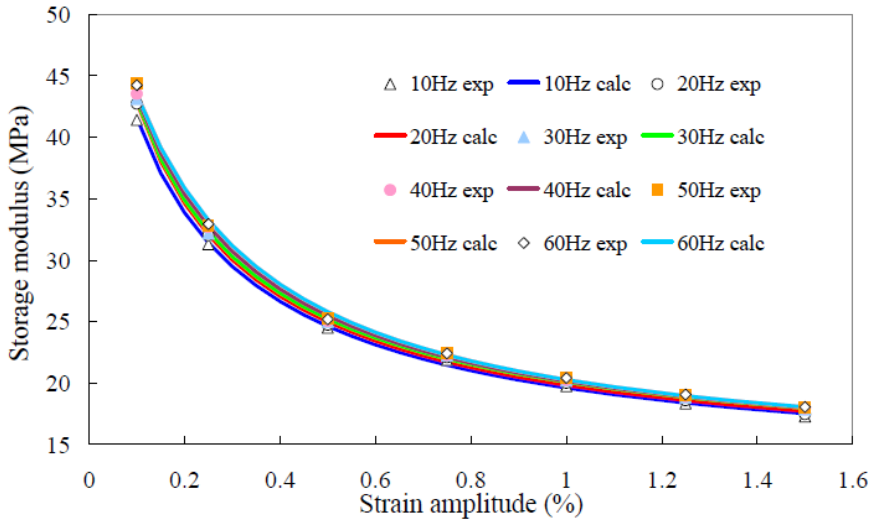


(a)

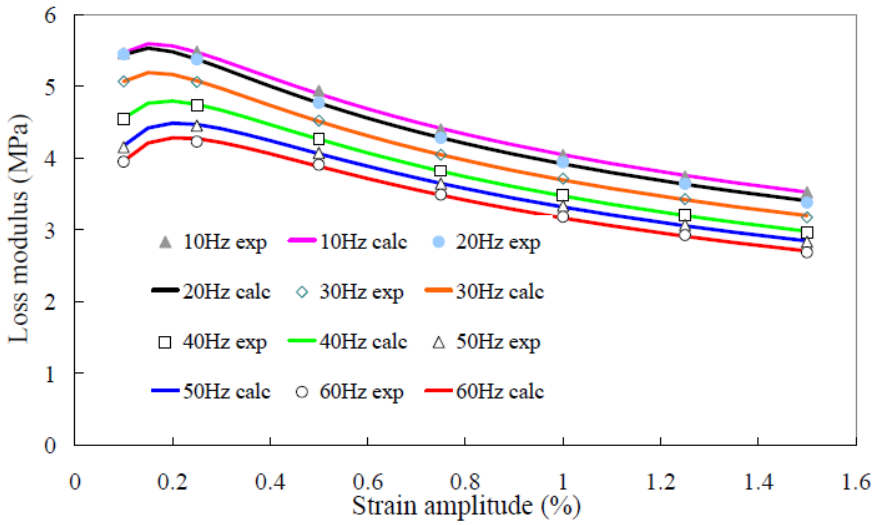


(b)

Figure 5. 24 Comparison of predicted results and measured data of strain amplitude dependent: (a) storage modulus, and (b) loss modulus of the MRE sample under uniaxial compression with 3% pre-strain, in magnetic field of 300 mT and temperature of 30 °C.

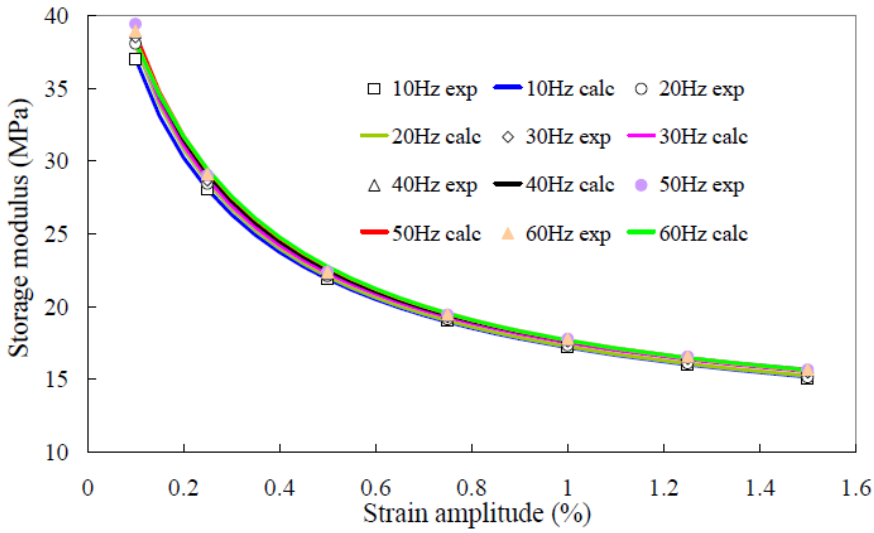


(a)

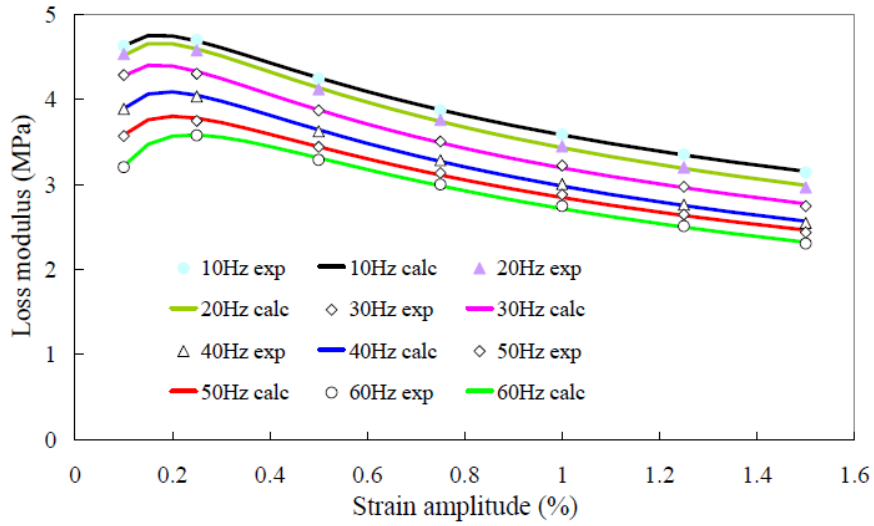


(b)

Figure 5. 25 Comparison of predicted results and measured data of strain amplitude dependent: (a) storage modulus, and (b) loss modulus of the MRE sample under uniaxial compression with 3% pre-strain, in magnetic field of 300 mT and temperature of 40 °C.

### 5.5.3 Strain amplitude dependent dynamic properties

The Kraus model as presented in Eq. (5.34) is a phenomenological model to describe the influence of strain amplitude on the dynamic modulus of filled rubbers. The storage modulus at small strain amplitude is dependent on vibration frequency, which can be described by using linear viscoelastic model. While the asymptotic values of storage modulus at large strain amplitude appear to be nearly independent on vibration frequency in a certain range of frequencies. The maximum of the loss modulus can be regarded as a weak function of frequency for most samples with different filler levels. For natural rubber/carbon blacks, the

loss modulus at high and low dynamic amplitudes appears to be independent of frequency in the investigated frequency range. However, it needs further experimental investigations [Heinrich and Klüppel (2002)].

In order to investigate the influence of asymptotic values of storage modulus and loss modulus at large strain amplitude on the fitting results, the comparative analysis is performed for three cases:

(1) Both of $E'_\infty$ and $E''_\infty$ are assumed to be functions of frequency,
(2) Both of $E'_\infty$ and $E''_\infty$ are assumed to be constant model parameters,
(3) $E'_\infty$ is set to a constant model parameter while $E''_\infty$ is set to zero.

The statistical analysis results of goodness-of-fit are listed in Table 5.10 and Table 5.11. It is clearly found that setting the model parameters to constant does not affect the accuracy of fit, although the fitting results also depend on the parameter identification method and process. In this chapter, the asymptotic values of storage modulus and loss modulus at large strain amplitude are set to constants. The strain amplitude and frequency dependent dynamic moduli of MREs can be modeled by using the following form:

$$E'(\varepsilon_0,\omega) = E'_\infty + \frac{E'_0(\omega) - E'_\infty}{1 + (\varepsilon_0/\varepsilon_c)^{2k}} \tag{5.35a}$$

$$E''(\varepsilon_0,\omega) = E''_\infty + \frac{2[E''_m(\omega) - E''_\infty](\varepsilon_0/\varepsilon_c)^k}{1 + (\varepsilon_0/\varepsilon_c)^{2k}} \tag{5.35b}$$

where $\varepsilon_c$, $E'_\infty$, $E''_\infty$, and k are model parameters which can be identified by DMA experiment data.

Table 5. 10 Goodness-of-fit statistical analysis of different expressions for the asymptotic values of storage modulus and loss modulus at large strain amplitude under prestrain of 3% prestrain, magnetic field of 0 mT, and temperature of 20°C

| | | $S_e/S_y$ | $R^2$ | MGD | AGD |
|---|---|---|---|---|---|
| Case (1) | Storage modulus | 0.022 | 1.000 | 3.03% | 0.48% |
| | Loss modulus | 0.078 | 0.994 | 7.61% | 0.95% |
| Case (2) | Storage modulus | 0.023 | 0.999 | 3.64% | 0.50% |
| | Loss modulus | 0.082 | 0.994 | 7.59% | 0.92% |
| Case (3) | Storage modulus | 0.027 | 0.999 | 5.06% | 0.50% |
| | Loss modulus | 0.100 | 0.990 | 7.91% | 1.12% |

Table 5. 11 Goodness-of-fit statistical analysis of different expressions for the asymptotic values of storage modulus and loss modulus at large strain amplitude under prestrain of 3% prestrain, magnetic field of 300 mT, and temperature of 20°C

| | | $S_e/S_y$ | $R^2$ | MGD | AGD |
|---|---|---|---|---|---|
| Case (1) | Storage modulus | 0.024 | 0.999 | 3.39% | 0.56% |
| | Loss modulus | 0.105 | 0.989 | 8.42% | 1.22% |
| Case (2) | Storage modulus | 0.023 | 0.999 | 4.00% | 0.59% |
| | Loss modulus | 0.110 | 0.988 | 7.98% | 1.39% |
| Case (3) | Storage modulus | 0.026 | 0.999 | 4.12% | 0.54% |
| | Loss modulus | 0.108 | 0.989 | 8.33% | 1.22% |

Figure 5.27 and Figure 5.29 present the dynamic modulus master curve taking into account for strain amplitude and frequency effect. The seven curves of the storage modulus and loss modulus of MREs under uniaxial harmonic compression with various strain amplitudes as shown in Figure 5.26 and Figure 5.28 are merged respectively into a single curve of the storage modulus and loss modulus of MREs under uniaxial harmonic compression with strain amplitude of 0.1% as shown in Figure 5.27 and Figure 5.29. It is found that the constructed master curves of strain amplitude dependent dynamic moduli in non-magnetic field and room temperature (as shown in Figure 5.26) and in magnetic field of 300 mT and temperature of 40 °C (as shown in Figure 5.28) have the similar variation trend with frequency although their values are different. It indicates that the model parameters in Eq. (5.35) are less dependent on the vibration frequency in different magnetic fields and environment temperatures. The influence of strain amplitude and excitation frequency on dynamic modulus is separable.

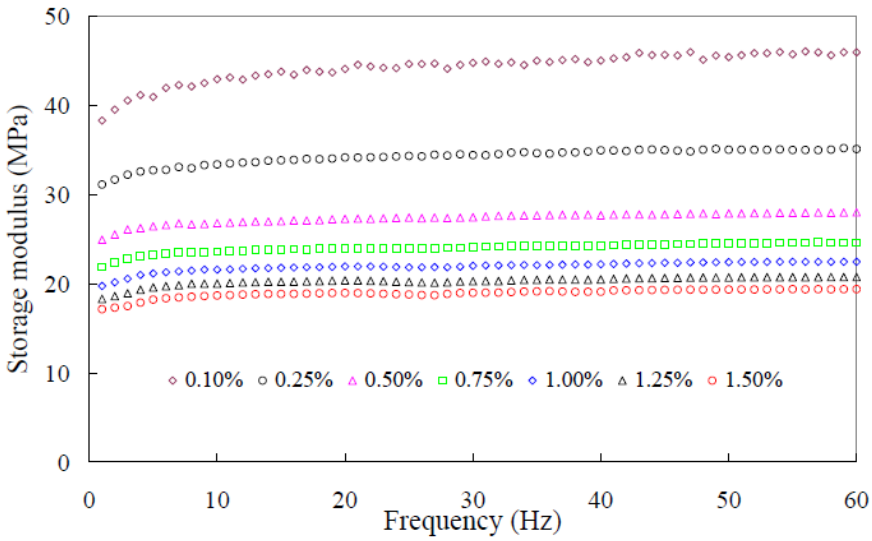

(a)

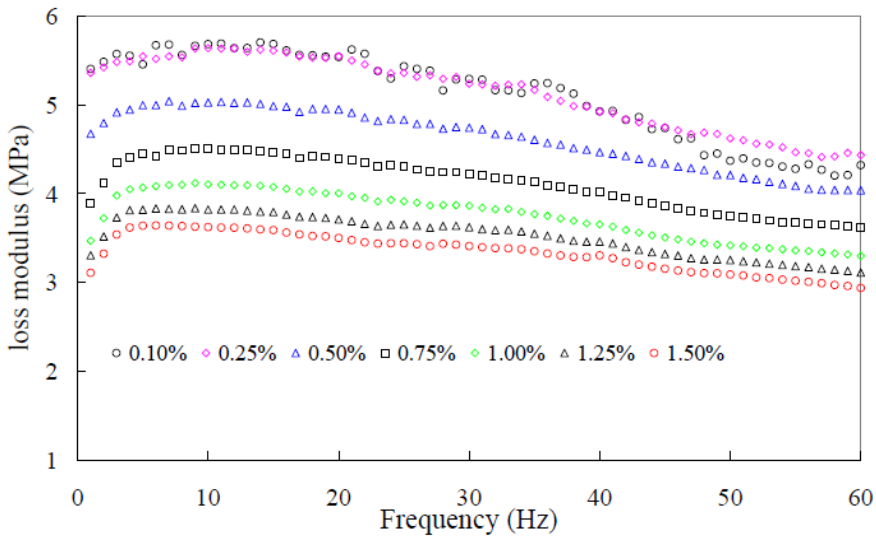


(b)

Figure 5. 26 Measured data of strain amplitude dependent: (a) storage modulus, and (b) loss modulus of the MRE sample under uniaxial compression with 3% pre-strain in non-magnetic field and room temperature

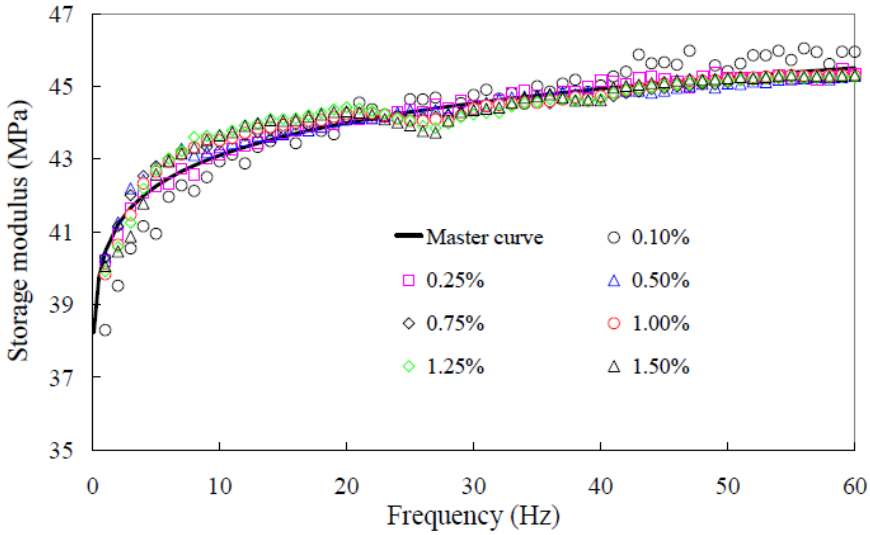


(a)

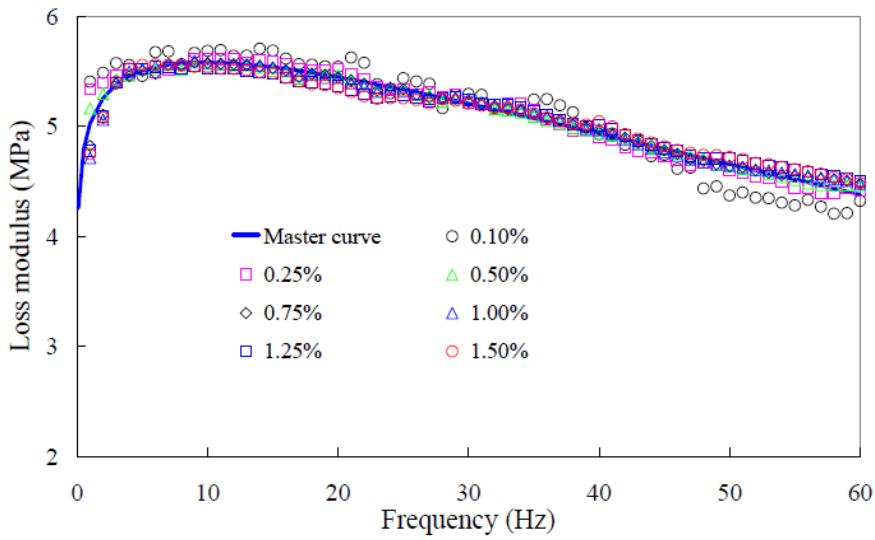


(b)

Figure 5. 27 Predicted results by using the Kraus model for strain amplitude dependent: (a) storage modulus, and (b) loss modulus of the MRE sample under uniaxial compression with 3% pre-strain in non-magnetic field and room temperature.

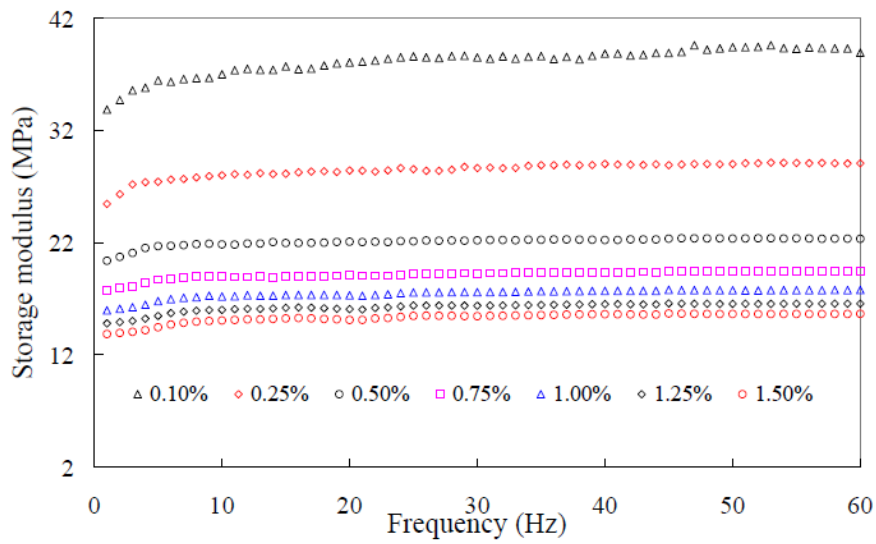


(a)

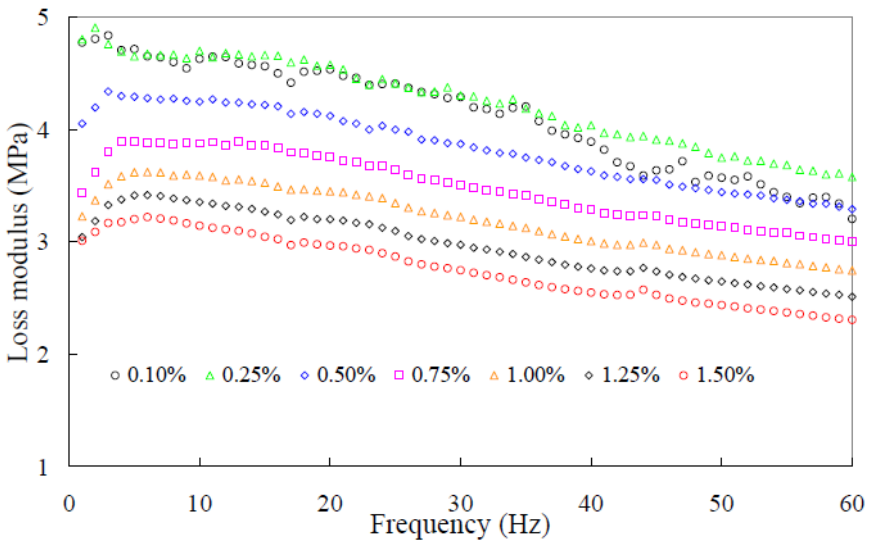


(b)

Figure 5. 28 Measured data of strain amplitude dependent: (a) storage modulus, and (b) loss modulus of the MRE sample under uniaxial compression with 3% pre-strain in magnetic field of 300 mT and temperature of 40 °C.

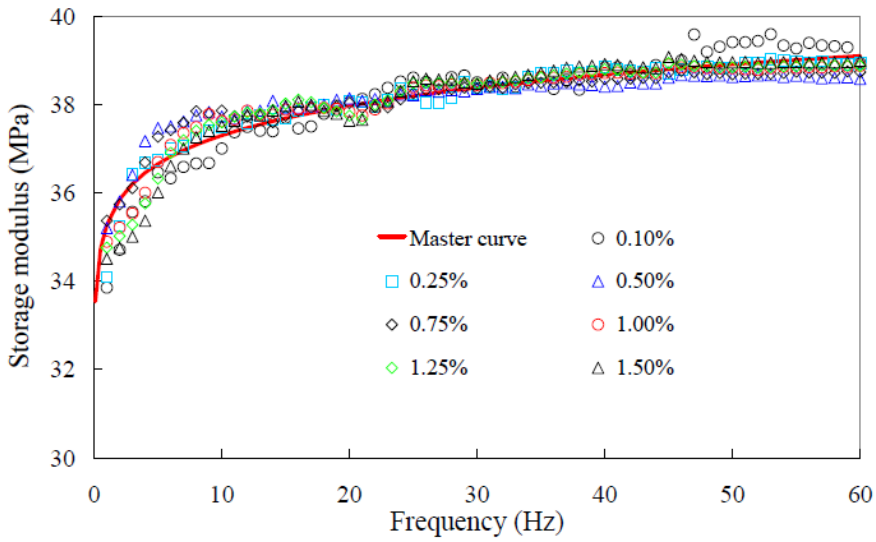


(a)

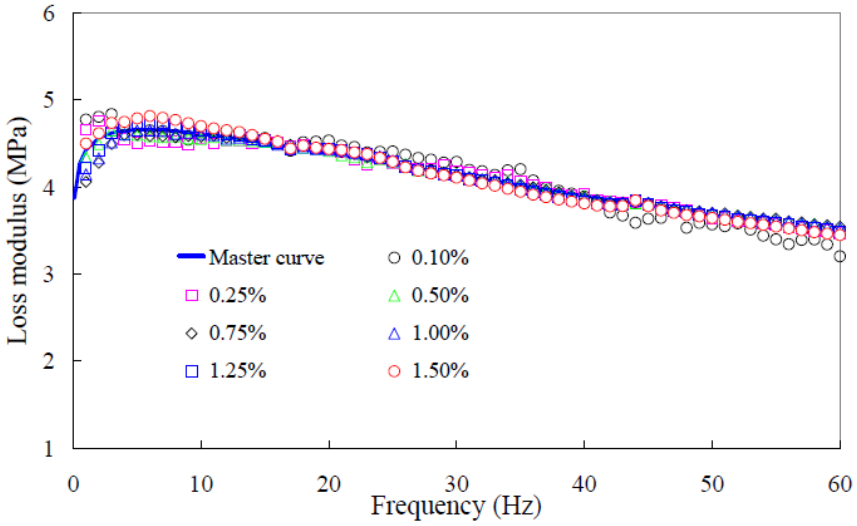


(b)

Figure 5. 29 Predicted results by using the Kraus model for strain amplitude dependent: (a) storage modulus, and (b) loss modulus of the MRE sample under uniaxial compression with 3% pre-strain in magnetic field of 300 mT and temperature of 40 °C

## 5.6 Generalized mathematical model for dynamic properties of MREs

### 5.6.1 State of the art

MRE based devices are often operated in the wide range of load frequency and amplitude, magnetic field, and temperature. With respect to design and practical application, it is essential to investigate and model the dependent dynamic properties of MREs under various loading conditions. The characterization and modelling of MREs have attracted a great deal of attentions from researchers and engineers. There were several existing models so far for describing the dynamic properties of MREs under the combination of magnetic and mechanical load conditions. Among these models, the parametric model has the advantage of efficient and rapid simulation of the dynamic behaviours of MRE based devices under various loading conditions. The magnetic field induced stiffness of MREs was described by using a nonlinear spring element connected in parallel with a linear viscoelastic model [Li et al. (2010), Zhu et al. (2012), Guo et al. (2014)].

In order to take the effects of the interfacial friction in high frequency range into account, a spring-Coulomb friction slider and smooth frictional elements were used in a nonlinear constitutive model [Chen and Jerrams (2011), Blom and Kari (2011)]. The nonlinear hysteresis behaviour of MREs in large amplitude excitation was modelled by the Ramberg-Osgood model, the Bouc-Wen model, and the Prager model respectively in parallel with the classic viscoelastic

model [Eem et al. (2012), Behrooz et al. (2014), Kaleta and Lewandowski (2007)].

Recently, a new viscoelastic model was developed by dividing the dynamic shear modulus of MREs into mechanical and magnetic parts [Xin et al. (2016)]. The influence of strain amplitude and magnetic field on the shear modulus was calculated by the Kraus model and the MR effect respectively. A modified Kelvin-Voigt model was proposed to describe the nonlinear relationships between the shear stress and shear strain of MREs under external magnetic field [Norouzi et al. (2016)]. In this model, the stiffness of spring and the damping of dashpot were dependent on the magnetic flux, strain amplitude and frequency. The storage and loss moduli were modelled by using power function of strain amplitude and frequency while the magnetic field dependent parameters were expressed by polynomial functions.

Wang et al. (2018) developed a mechanical model for a multi-layered MRE isolator based on the combination of the dynamic equations, constitutive models, and electromagnetic analysis. In each layer, the relationship of shear stress and shear strain was modelled by using the Kelvin-Voigt model and the Bouc-Wen model in parallel. The model parameters were identified based on the electromagnetic analysis results. Olabide et al. (2018) employed the fractional Zener model to describe the frequency dependent dynamic properties of anisotropic MREs under external magnetic field. The magnetic field induced dynamic shear modulus was predicted by the dipole model. Nadzharyan et al. (2018) examined the capability of various fractional viscoelastic models for the magnetoactive elastomer in a wide range of magnetic fields. The results showed that the viscoelastic model with one fractional element can adequately describe the rheological behaviour of the magnetoactive elastomer under low and for some cases high magnetic fields.

The elastic and rheological properties of MREs in addition to the external magnetic field are also dependent on the thermal-mechanical load conditions. The temperature changes in MREs and MRE based devices may be caused by the environmental temperature variations or/and internal temperature rise due to energy dissipation. The internal temperature of the MRE isolator was generated by the electromagnetic coil and had a remarkable effect on the stiffness and damping of the MRE isolator [Yu et al. (2016)]. MRE exhibits a temperature dependent softening and stiffening ability at low and high temperature respectively, which can have an adverse effect on material properties of MREs and the performance of MRE based devices [Zhang et al. (2011)]. However, there are a limited number of published studies on the parametric modelling of the temperature-dependent viscoelastic properties of MREs. The

dynamic modulus master curve of an isotropic magnetosensitive elastomer in the absence of magnetic field and the magnitude of complex modulus master curve of MRFs under magnetic field were constructed by Chool and Oyadiji (2005) and Olabide and Elejabarrieta (2016) respectively. There is a research gap in the development of the mathematical model for the dynamic properties of MREs taking into account the influence of magnetic field, temperature, strain amplitude and vibration frequency.

### 5.6.2 Description of the model

The dynamic properties of MREs are influenced by many factors such as magnetic field, temperature, strain amplitude, and excitation frequency. The dependence of these factors on the dynamic properties of MREs has been discussed respectively in the previous sections of this chapter. The objective of this section is to present a generalized mathematical model for dynamic properties of MREs taking into account the influence of magnetic field, temperature, strain amplitude and vibration frequency.

According to the DMA experiment results and the achievements of the previous sections, the influence of magnetic field, temperature, strain amplitude, and excitation frequency can be separated in small strain range. The first step is to take into account the effect of magnetic field. It leads to,

$$E'(\varepsilon_0,\omega,T,B) = b'_M E'(\varepsilon_0,\omega,T) \tag{5.36a}$$

$$E''(\varepsilon_0,\omega,T,B) = b''_M E''(\varepsilon_0,\omega,T) \tag{5.36b}$$

$$b'_M = 1 + c'_{MR} = 1 + \frac{c_1 B^m}{1 + d_1 B^m} \tag{5.36c}$$

$$b''_M = 1 + c''_{MR} = 1 + \frac{c_2 B^n}{1 + d_2 B^{2n}} \tag{5.36d}$$

in which $c_1$, $c_2$, $d_1$, $d_2$, $m$, and $n$ are model parameters, $b'_M$ and $b''_M$ are the generalized vertical shift factor for magnetic field dependent storage modulus and loss modulus respectively.

The next step is to take into account the influence of strain amplitude,

$$E'(\varepsilon_0,\omega,T,B) = b'_M\{E'_\infty + b'_k[E'(\omega,T) - E'_\infty]\} \tag{5.37a}$$

$$E''(\varepsilon_0,\omega,T,B) = b''_M\{E''_\infty + b''_k[E''_m(\omega,T) - E''_\infty]\} \tag{5.37b}$$

$$b'_K = \frac{1}{1 + \left({\varepsilon_0}/{\varepsilon_c}\right)^{2k}} \tag{5.37c}$$

$$b_K'' = \frac{2\left(\varepsilon_0/\varepsilon_c\right)^k}{1+\left(\varepsilon_0/\varepsilon_c\right)^{2k}} \tag{5.37d}$$

where $E'_\infty$, $E''_\infty$, $\varepsilon_c$, and k are model parameters, $b'_K$ and $b''_K$ are the generalized vertical shift factor for strain amplitude dependent storage modulus and loss modulus respectively.
The last step is to take into account the temperature effect,

$$E'(\varepsilon_0,\omega,T,B) = b'_M\left[(1-b'_k)E'_\infty + \frac{b'_k}{b_T}E'(\omega_r,T_r)\right] \tag{5.38a}$$

$$E''(\varepsilon_0,\omega,T,B) = b''_M\left[(1-b''_k)E''_\infty + \frac{b''_k}{b_T}E''_m(\omega_r,T_r)\right] \tag{5.38b}$$

in which $T_r$ denotes reference temperature, $\omega_r$ and $b_T$ are reduced frequency and vertical shift factor. They are determined by Eq. (5.15c) and Eq. (5.19) respectively. The generalized master curves for the storage modulus and loss modulus of MREs in reference temperature, selected strain amplitude, and non-magnetic field can be described by using the proposed model (please see Eq. (5.11)).

### 5.6.3 Parameter identification

There are twenty-two model parameters in the predictive model, including six parameters for the magnetic field effect, six parameters for influence of strain amplitude, four parameters for temperature effect, and six parameters for linear viscoelastic properties of MREs under uniaxial harmonic compression. The simple and direct way to identify these model parameters simultaneously by minimizing the sum of square of error (SSE) between the predicted and measured data. In this section, the parameter identification is performed in the sequential way with two steps. Firstly, the viscoelastic model parameters for dynamic modulus master curve and the numerical shift factors for isothermal dynamic modulus at different temperatures, magnetic fields, and strain amplitudes are identified by using a least square method and optimization algorithm such as the genetic algorithm (GA). Then the shift factor equation is selected based on the graphic display of numerical shift factors and the model parameters of shift factor equations are identified respectively. The model parameter identification is performed in the sequential way with two steps because it has an advantage when choosing a better shift factor equation.

Figure 5.30 presents the dynamic modulus master curve that takes into account for the influence

of magnetic field, strain amplitude and excitation frequency. The twenty-seven curves of the storage modulus and loss modulus of MREs under various magnetic fields, strain amplitudes, temperatures, and frequencies are merged into a single curve of the storage modulus and loss modulus of MREs in the absence of magnetic field. The reference temperature is 22°C and the strain amplitude is selected to be 1%.

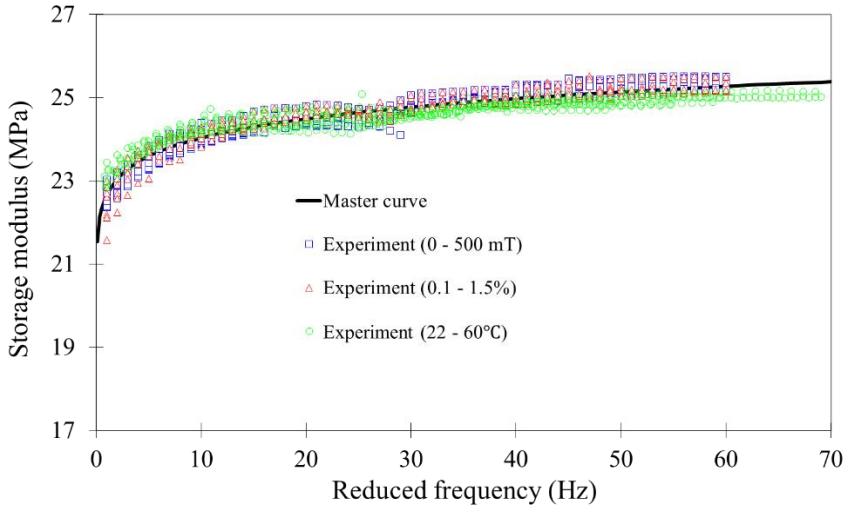


(a)

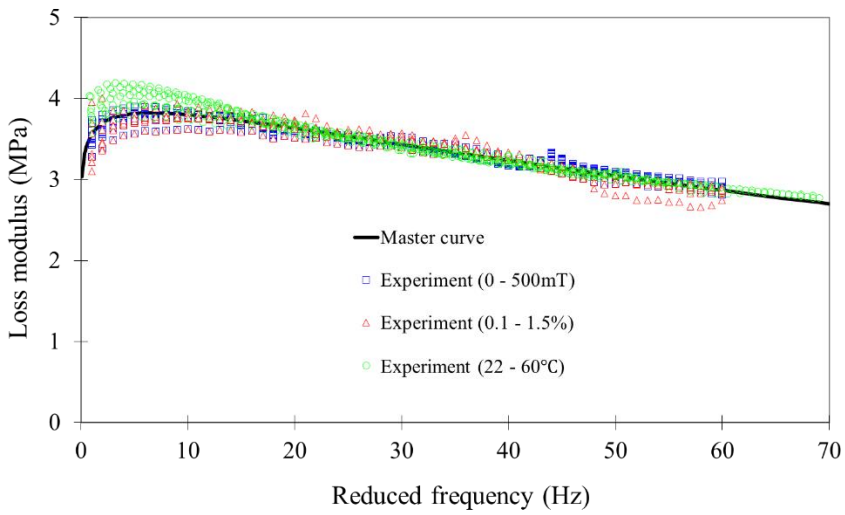


(b)

Figure 5. 30 Comparison of predicted results and measured data of strain amplitude dependent: (a) storage modulus, and (b) loss modulus of the MRE sample under uniaxial compression with 3% pre-strain, in magnetic field of 0 to 500 mT, strain amplitude of 0.1% to 1,5%, and temperature of 22 °C to 60 °C.

The statistical analysis of goodness-of-fit results (as listed in Table 5.13) show that the generalized mathematical model provides very good fitting results of the generalized master curve and can be used to describe the dynamic modulus of MREs under various magnetic fields,

strain amplitudes, temperatures, frequencies. Compared with the master curve considering only one of the influencing factors, the generalized master curve taking into account all these factors have a little larger discrepancy from experimental data. The maximum discrepancy occurs in the lower frequency range.

Table 5. 12 Goodness-of-fit statistical analysis of different storage modulus master curves

| | $S_e/S_y$ | $R^2$ | MGD | AGD |
|---|---|---|---|---|
| Temperature | 0.090 | 0.992 | 2.37% | 0.52% |
| Strain amplitude | 0.023 | 0.999 | 4.00% | 0.59% |
| Magnetic field | 0.329 | 0.894 | 3.80% | 0.62% |
| Magnetic field, temperature, and strain amplitude | 0.035 | 0.999 | 5.10% | 0.66% |

Table 5. 13 Goodness-of-fit statistical analysis of different loss modulus master curves

| | $S_e/S_y$ | $R^2$ | MGD | AGD |
|---|---|---|---|---|
| Temperature | 0.147 | 0.979 | 5.86% | 1.31% |
| Strain amplitude | 0.110 | 0.988 | 7.98% | 1.39% |
| Magnetic field | 0.276 | 0.926 | 7.09% | 1.80% |
| Magnetic field, temperature, and strain amplitude | 0.122 | 0.986 | 14.93% | 1.53% |

## 5.7 Summary

In this chapter, the influence of magnetic field, temperature, strain amplitude and frequency on the dynamic properties of MREs is investigated. A new mathematical model is developed to describe these influence factors. The generalized dynamic modulus master curve of MREs under various magnetic fields, temperatures, strain amplitudes and frequencies is constructed for the first time by the horizontal and vertical shift factors. The good correlations between the measured and predicted data are confirmed by performing statistical analysis for the goodness of fit. The constructed master curve and shift factors can be used to predict the viscoelastic properties of the MREs beyond the DMA experiment range of temperatures and frequencies.

The general achievements in this chapter can be summarized as follows:

(1) Inspired by the dynamic mechanical analysis (DMA) experiment results, a new approach is proposed to model the viscoelastic behaviour of MREs based on the modified Kelvin-Voigt model in which both the stiffness of spring and viscosity of dashpot are dependent on the excitation frequency and have a clear physical interpretation. Comparative analysis results show that the proposed model presents better fitting results of DMA experimental

data than the fractional Zener model and the CAM model.

(2) The time-temperature superposition (TTS) principle is extended to construct the dynamic modulus master curve of the MREs by using the horizontal shift factor and the vertical shift factor. The WLF empirical equation and the Arrhenius equation work well for the horizontal shift factor before the transition temperature. While the quadratic polynomial function presents the excellent fitting results of the vertical shift factor and the good fitting results of the horizontal shift factor respectively within the DMA test temperature range.

(3) The new fractional functions are proposed to fit the MR effect on the storage modulus and loss modulus of MREs. The statistical analysis results of goodness-of-fit show the proposed functions provide the better fitting results than the existing polynomial functions.

(4) A generalized mathematical model is proposed to describe the magnetic field, temperature, strain amplitude and frequency dependent dynamic moduli of MREs under uniaxial harmonic compression. A generalized dynamic modulus master curve of MREs is constructed, which can take into account the influence of magnetic field, temperature, strain amplitude, and excitation frequency. The good correlations between DMA experiment data and predicted results of the loss modulus and the storage modulus are evaluated respectively by the goodness-of-fit statistical analysis.

(5) The linear viscoelastic limit is discussed in detail. The Kraus model is adopted to predict the influence of strain amplitude on dynamic moduli of MREs. The obtained results indicate that the influence of magnetic field, strain amplitude, temperature, and frequency on the dynamic properties of MREs under uniaxial harmonic compression is separable in small strain range.

# 6 Characterization of MRE based mount

## 6.1 Introduction

Vibration and noise onboard have a major negative impact on ships, ship systems, the crew and the environment. The vibrations not only cause fatigue damage of ship, affect the health of crew onboard, but also more importantly raise a great environment concern. This has led to an increasing demand in shipbuilding industry for low vibration, low noise products to satisfy performance standards and to reduce environmental noise pollution.

Unwanted vibration onboard may come from many sources: machinery, propeller, and sea waves [LR (2015), ABS (2017), Carlton and Vlasic (2005)]. Three main vibration control methods, such as passive, active, and semi-active, have been proposed to control the level of vibrations in ship and offshore industry. Due to the complexity of ship structures, the coupling of different wave types and multiple wave propagation paths, active control is usually difficult to implement and very expensive. Passive control is only effective in a narrow bandwidth nearby the target frequency range and has only partial and limited uses in the varying environment of ships. Semi-active control based on smart materials takes the advantages of passive and active control systems [Kandasamy et al. (2016)]. It can adapt to the changes of external excitations without high-energy consumption as compared to active control system and provide more effective performance in a wide range of frequencies than passive control system.

Magnetorheological (MR) material is a class of smart materials whose dynamic mechanical properties can be changed continuously, rapidly and reversibly by the application of the external magnetic field. These unique properties have attracted increasing attentions and broad potential applications to vibration control in various engineering fields. For a low-frequency and high-amplitude vibration, the controllable stiffness of MR elastomers (MREs) should be much more effective than the controllable damping of MR fluids (MRFs) because the damping force depends on the speed and damping factor while the elastic force depends on the amplitude and stiffness [Du et al. (2011)].

In this chapter, a prototype of MRE based mount system is designed, manufactured and tested. The force transmissibility of the designed system under different test conditions is evaluated by experiment and dynamic modelling simulation. Three different case studies of the designed MRE device along with its control strategy according to the specific application requirement

are performed. This chapter is organized as follows. Section 6.2 designs and assembles the MRE based mount system. The force transmissibility and frequency shift of the MRE mount are evaluated by experiments in Section 6.3 and the dynamic modelling simulation is performed in Section 6.4. Section 6.5 presents the experimental case studies on the performance of the MRE mount with semi-active control. Finally, conclusions are presented in Section 6.6.

## 6.2 Design of semi-active MRE mount

### 6.2.1 Design and assembly of MRE mount

The designed MRE based mount consists of signal processing and control subsystem, MRE material, electrical magnets and power supply. The control circuit diagram of the designed system is shown as Figure 6.1. The power supply provides DC current to the electrical magnets. The signal processing and control subsystem controls the magnetic flux intensity by adjusting the magnitude of the current.

The signal processing and control subsystem includes sensors, signal processor, and signal controller. The accelerate meter is placed at the top of the upper electrical magnet and will start to record the movement data of the system once experiences the vibration. The digital signal collected by the accelerate meter will be sent to the fast Fourier transform (FFT) component to translate from the time domain signals to the frequency domain signals. The main vibration frequency of the system is identified in this signal processing and control subsystem.

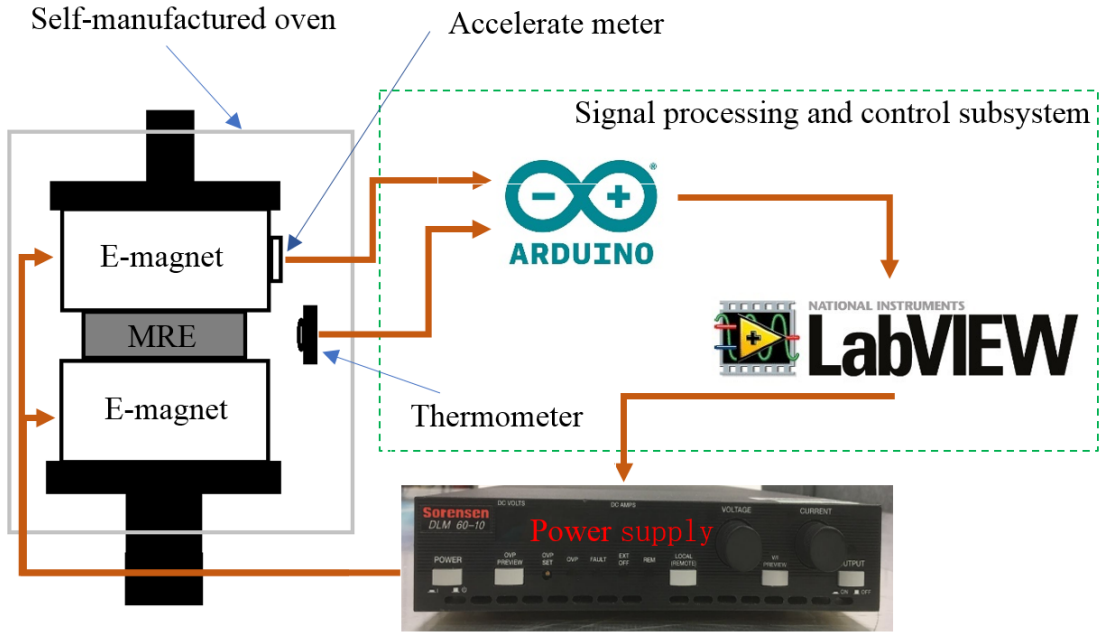


Figure 6. 1 The control circuit diagram of the designed MRE mount system

According to the designed control strategy, a signal will be sent to the power supply to turn it on when the vibration frequency of the system approaching the resonance frequency. A pair of electromagnets are activated to provide a stable external magnetic field to the MRE core to change its elastic and rheological properties. Then the resonance frequency of the system is changed with the applied current as well. If the vibration frequency of the system keeps increasing to approach the new resonance frequency, the signal processing and control subsystem will cut off the power supply. The elastic and rheological properties of the MRE core will return to its original values when removing the external magnetic field, all this happens in less than 0.1s. The natural frequency of the system also drops with the MRE material properties to the original value to avoid the resonance happens in the high frequency.

Figure 6.2 shows the Sorensen DLM 60-10 power supply. It can provide continuously variable output voltage and current for a broad range of applications. The near linear ripple of the device is as low as 2.5 mV rms and the noise is below 1.5 mV p-p. The output range of the power supply are 0-60 VDC of voltage and 0-10 ADC of current. Zero Voltage Switching (ZVS) technology is used in this power supply made it able to achieve exceptionally low, near-linear ripple and noise rivalling larger and more expensive linear power supplies. In addition, the high efficiency and fast load transient response assure that the DLM is ideal for even the most demanding applications.

This power supply DLM600 can also be controlled through the 16-bit programming LXI - compliant Ethernet LAN / RS-232C (M130), or 12-bit programming IEEE-488.2 / RS-232C (Option M9G), and standard analog programming 0-5 V, 0-10 V, or 0-5 kU. In this project, the device is controlled by LabVIEW software.

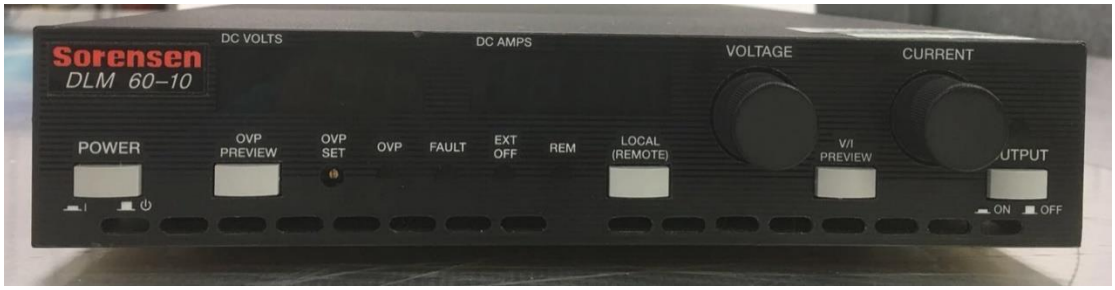


Figure 6. 2 Sorensen DLM 60-10 Power Supply

In general, there are two ways to produce the external magnetic field. One way is to use a pair of electromagnets directly. The other way is to use the power off self - maintaining

electromagnet system, which consists of a pair of electromagnets and permanent magnets. This system can produce a stable magnetic field when power off which means the system has high natural frequency at zero applied external magnetic field. Switch the power on during the normal machine working state, the external magnetic field generated by the electromagnets can counteract the magnetic field caused by the permanent magnets. However, this system may result in waste of energy and generate extra heat during the electromagnets working. That is the reason we choose a pair of electromagnets to generate the external magnetic field in this chapter.

Two electromagnets manufactured by XDA company (China) are used to provide the stable external magnetic field for the MRE core (as shown in Figure 6.3). The size of the electromagnet is 65 mm in diameter and 30 mm in height. The weight of the electromagnet is 210 g. A pair of electromagnets can provide 800 N force pull in maximum. Table 6.1 presents the detail of the magnetic flux intensity produced by a pair of electromagnets with Sorensen DLM 60-10 power supply.

Table 6. 1 Magnetic field generated by the power supply

| Magnetic field (mT) | 0 | 10 | 20 | 30 | 40 | 50 | 60 | 70 |
|---|---|---|---|---|---|---|---|---|
| Voltage (V) | 0 | 1.1 | 2.7 | 4.2 | 5.7 | 7.3 | 8.8 | 10.4 |
| Current (A) | 0 | 0.03 | 0.07 | 0.12 | 0.16 | 0.21 | 0.25 | 0.30 |

| Magnetic field (mT) | 80 | 90 | 100 | 110 | 120 | 130 | 140 | 150 |
|---|---|---|---|---|---|---|---|---|
| Voltage (V) | 12.0 | 13.6 | 15.3 | 16.9 | 18.6 | 20.3 | 22.2 | 24.1 |
| Current (A) | 0.35 | 0.39 | 0.44 | 0.48 | 0.53 | 0.58 | 0.63 | 0.67 |

| Magnetic field (mT) | 160 | 170 | 180 | 190 | 200 | 210 | 220 | 230 |
|---|---|---|---|---|---|---|---|---|
| Voltage (V) | 26 | 28.1 | 30.1 | 32.3 | 34.9 | 37.2 | 39.7 | 42.0 |
| Current (A) | 0.73 | 0.77 | 0.82 | 0.87 | 0.92 | 0.98 | 1.03 | 1.09 |

By the regression analysis of the data as shown in Table 6.1, the magnetic flux intensity can be approximately expressed as a linear function of the input current as follow.

$$B = 210.69I + 5.9663 \text{ with } R^2 = 0.999 \tag{6.1}$$

Figure 6. 3 Electromagnet

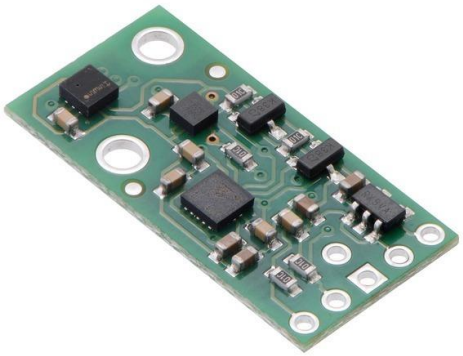

Figure 6. 4 AltIMU-10 v5 Gyro

Figure 6.4 shows the accelerate sensor AltIMU-10 v5 Gyro used to detect the isolator's movement was purchased from Robotshop (UK). This is a compact (25 mm × 13 mm) board that combines ST's LSM6DS33 3-axis gyroscope and 3-axis accelerometer, LIS3MDL 3-axis magnetometer, and LPS25H digital barometer to form an inertial measurement unit (IMU) and altimeter. In this study, the accelerometer function of this board is used to monitor the device up deck movement. It operates at voltages below 3.6 V, which can make interfacing difficult for microcontrollers operating at 5 V, for this reason, Arduino board is chosen to provide running environment.

SparkFun IR Thermometer Evaluation Board - MLX90614 purchased from SparkFun Electronics (USA) is applied to show the real-time surface temperature of the MRE core (as shown in Figure 6.5). The MLX9061 sensor is a high precision, small size, single zone IR thermometer with an optional SMBus (two-wire) or PWM interface. The sensor is connected to an ATmega328 running at 3.3 V with a STK500 (Arduino) 8 MHz bootloader.

Figure 6. 5 Thermometer Evaluation Board - MLX90614

Figure 6. 6 Arduino uno rev3

Arduino uno rev3 purchased from RS Components Ltd (UK) is applied to read the data collected by the accelerometer and Thermometer (as shown in Figure 6.6). Arduino is an open-source electronics platform consisting of hardware and software. The data can be linked and processed through LabVIEW software by using the VISA component.

### 6.2.2 Manufacture and test of the MRE core

The MRE core used in this chapter is the anisotropic MRE material fabricated with the silicone rubber and iron particles. The details of the material composition and synthesis process are the same as the preparation of the MRE samples in Chapter 4. The synthesis of the MRE material consists of three steps: Firstly, Elastosil A and Elastosil B (Wacker Chemie AG, Germany) are dispensed in a volume fraction of 10:1 and then the micron-sized iron powders (Sigma-Aldrich, US) in a volume fraction of 30% are added. Secondly, the mixture is well blended and placed in a vacuum chamber for 20 min to reduce the air bubbles trapped inside the material during mixing progress. Finally, the mixture is put into the aluminium moulds and cured for 20 h under room temperature with an external magnetic field of about 300 mT produced by a pair of the cylindrical grade N42 neodymium permanent magnets (E-magnets, UK).

The operation mode of MRE can be classified into several different groups, which are compression mode, shear mode and their combination. The MR effect for MRE operated in shear mode is relatively higher when comparing with that under compression mode. However, the MRE device based on compression mode may have much higher load capacity. In this research, the designed system is focus on solving the vibration problems onboard ship. The main vibration source onboard is main engine or electricity generator which require enough capacity to support the device. Due to this reason, the compression mode is chosen for the MRE based mount.

The MRE core is placed between two electric magnets. The direction of the magnetic field generated by the E-magnets is exactly parallel to the direction of the iron particles chain line inside of the MRE as shown in Figure 6.7. Each MRE based mount is able to take 1000 N compressive load in maximum which is almost three times the capacity of the MRE device works in shear mode. Although the MR effect of the device is decreased, but makes it more suitable and reliable for real industrial application. This MRE based vibration control device is designed to have the capability of replacing the traditional elastomer mount (as shown in Figure 6.8). For example, the following Figure 6.9 show both compression and shear mode of

traditional rubber mount operates in real application of vibration control in modern marine industry.

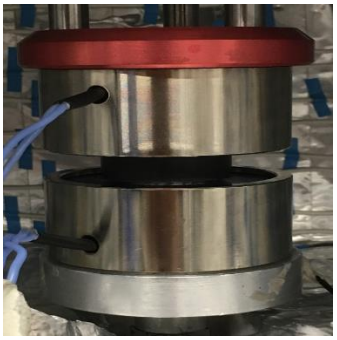

Figure 6. 7 MRE based mount

Figure 6. 8 Rubber naval mount

Figure 6. 9 Vibration control system

For the MRE core shape design, there are two different design plans at the beginning of design. The first plan is used a large cylinder MRE with the diameter of 33 mm and height of 11 mm as shown in Figure 6.10. The second plan is replaced the large core with three smaller size MRE cylinders with the diameter of 19 mm and height of 11 mm as shown in Figure 6.11 to ensure the MRE core of the designed device have the same cross section area and height. The MRE mount with one large core occupies smaller space and the MRE mount with three separate mini cores appears to have better heat dissipating capacity. Both of these two characteristics are important and need to be taken into consideration for the real industrial applications design.

Figure 6. 10 One large cylinder MRE

Figure 6. 11 Three-cylinder MRE

The comparative DMA experiments between these two different MRE mount are carried out with the 300 N preload and 200 N dynamic load amplitude in the room temperature (about 20 °C). The dynamic mechanical response of two different working states of the MRE mount are measured respectively in the external magnetic field of 0 mT and 210 mT. The force

transmissibility of the designed MRE mounts via the vibration frequency range from 1 Hz to 60 Hz are presented in Figure 6.12. The frequency shift is clearly observed in Figure 6.12 when the external magnetic field is increased from 0 mT to 210 mT.

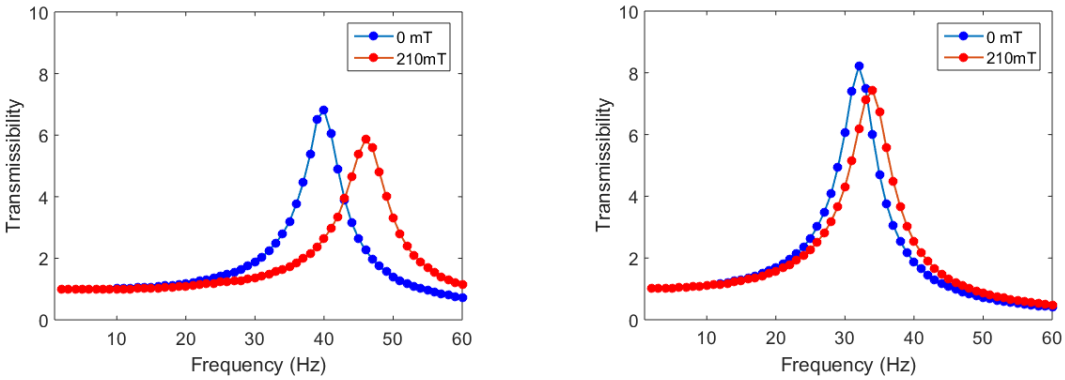


(a) (b)

Figure 6. 12 Transmissibility of (a) one large cylinder, and (b) three-cylinder MRE device under vibration frequency

According to the experiment results, the MRE mount with single large MRE core has lower force transmissibility value under both 0 mT and 210 mT external magnetic fields than the MRE mount with three separate cylinder core. However, the resonant frequency and the natural frequency shift capability of these two devices are also different. For single core MRE mount, the natural frequency of the total system is shifted by 6 Hz from 40 Hz to 46 Hz while the external magnetic field is increased from zero to 210 mT which is much higher than the three core MRE mount. The natural frequency of the three core MRE mount is only shifted by 2 Hz when the external magnetic field is applied. The MRE mount with single core shows a good performance in frequency shift ability and low vibration displacement. The final choice of the MRE core with single large cylinder is made based on the experimental results.

## 6.3 Experiment on efficiency of the MRE mount

### 6.3.1 Transmissibility and frequency shift of the MRE mount

The experiment is performed to investigate the force transmissibility of a single degree of freedom (DOF) designed MRE mount subjected to dynamic sinusoidal load. The excitation force is generated by the Instron machine E1000 plus. It simulates the device works at different vibration frequency such as a ship operates at the cruising speed when the machine works at the stable situation. In normal application, the natural frequency system is carefully designed according to the ship structures and usually has a fixed frequency. The purpose of this

experiment is to evaluate the frequency shift capability of the designed MRE mount system. The pre-strain of this experiment is set as 5% and the whole test is carried under the displacement amplitude control, the dynamic amplitude is 1%.

The natural frequency and the transmissibility of the designed MRE mount system are measured under different external magnetic field at room temperature condition. According to Figure 6.13, the colour bar indicates the force transmissibility of the device. The MRE mount has higher natural frequency under the higher external magnetic field. The natural frequency of this device at zero field is 40 Hz which is inside the 20 Hz to 50 Hz safe area for marine isolators.

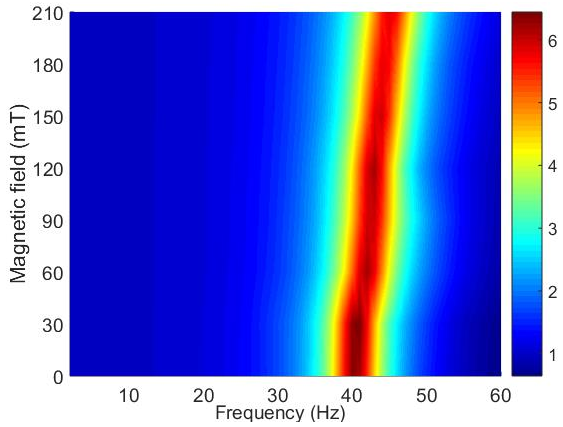


Figure 6. 13 force transmissibility of MRE mount under different magnetic field and vibration frequency

The force transmissibility remains at a stable value which is around 1 when the excitation frequency is range from 1 Hz to 30 Hz. As the excitation frequency approaches to the system resonant frequency, the response of the isolator increases. For example, the force transmissibility at zero magnetic field remains around 1 between 1 Hz and 30 Hz. After that, the force transmissibility value increases rapidly from 1 to 7 and reaches its maximum value at 40 Hz. When the excitation frequency passes the system's resonant frequency, the force transmissibility value drops to around 1 again at 50Hz and starts to remain at the stable value again. Through varying the external field, the stiffness of the designed MRE mount has changed. The natural frequency of the device is shifted by 6 Hz from 40 Hz at zero magnetic field to 46 Hz at 210 mT external magnetic field. This is due to the stiffness of the MRE core is increased with the external magnetic field.

The Figure 6.14 shows the force transmissibility of the MRE mount under different magnetic fields and environment temperatures. It can be found that the resonant frequency of the

designed MRE mount is reduced with the environment temperature. In zero external magnetic field test condition, the resonant frequency of the system is decreased by 4 Hz when the environment temperature is increased from 20 °C to 50 °C. This change trend becomes more obvious when the MRE mount is operated under 210 mT external magnetic field, the decrement of the resonant frequency is doubled and become 8 Hz. This type of reduction behaviour is mainly caused by the change of the stiffness of the MRE core. Meanwhile, the frequency shift ability of the designed MRE mount with the input current is reduced with the environment temperature. After applying a 210 mT magnetic field to the MRE core by the input current, the resonant frequency of the system is shifted by 6 Hz, 5 Hz, 4 Hz, 2 Hz at test temperature of 20 °C, 30 °C, 40 °C, 50 °C, respectively. This indicates that the control strategy of the designed MRE mount system needs to consider the temperature compensation according to the actual environment temperature of the device onboard.

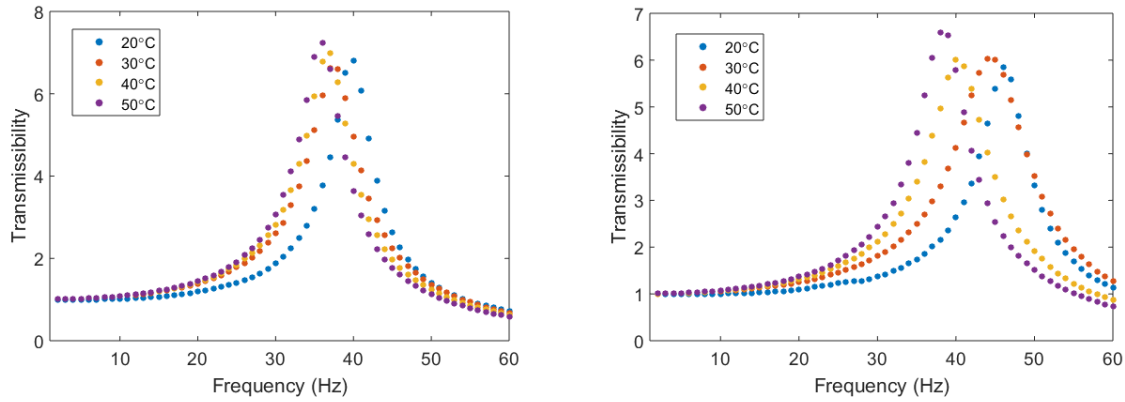


(a) (b)

Figure 6. 14 Transmissibility of MRE mount under different working state (a) 0 mT, and (b) 210 mT external magnetic field

The transmissibility is an important factor for design of vibration control system. High transmissibility means the system vibration resonance happened. In order to control the vibration impact on marine structures, the vibration control device based on MREs can be used to decrease the transmitted vibrations during the ship working periods that occurs when the machine vibration approaching the system natural frequency, and reduce the vibration and the noise of the system. The magnetic field can be applied on during these time periods to increase the natural frequency of the system, while the machine passes through the amplification period then switched off. This device can also be used to shift the natural frequency of system to a value according to the specific application design by the input current.

### 6.3.2 Dynamic properties of the designed MRE mount

The DMA test is performed to investigate dynamic mechanical properties of the MRE based mount under uniaxial harmonic compression. The influence of load amplitude, excitation frequency, external magnetic field, and environment temperature are investigated. The test frequency is range from 1 Hz to 60 Hz to simulate the mount working state frequency range for the electric generator. The pre-strain is set as 5% and the load amplitude is 0.5%. These DMA experiments are carried out at different reference temperatures varying from 20 °C to 50 °C with the interval of 10 °C. The dynamic properties of the MRE mount under different working states are measured respectively at 0 mT and 210 mT magnetic fields. The preload of these test is set at a constant value to represent the equilibrium position caused by the weight of the device above the MRE mount, in this case is 200 N.

The Figure 6.15 and Figure 6.16 show the dynamic mechanical properties of the MRE mount under different magnetic fields and environment temperatures. It can be observed that the storage modulus and the loss modulus of the MRE mount as shown in Figure 6.15 and Figure 6.16 are similar to the DMA experimental results obtained in the Chapter 5. The storage modulus increases with the vibration frequency and decreases with the environment temperature under both working states. The loss modulus also decreases with the vibration frequency and environment temperature according to the Figure 6.16.

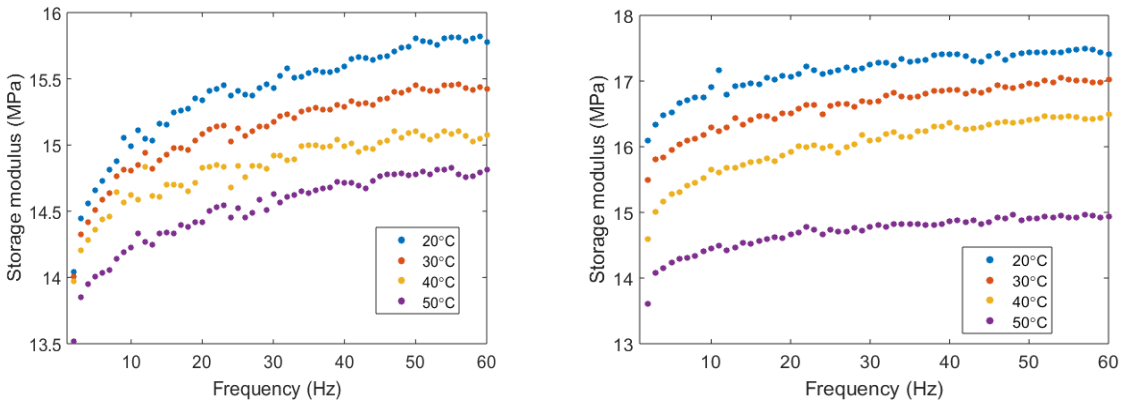


(a) (b)

Figure 6. 15 Storage modulus of MRE mount under different working states: (a) 0 mT, and (b) 210 mT external magnetic field

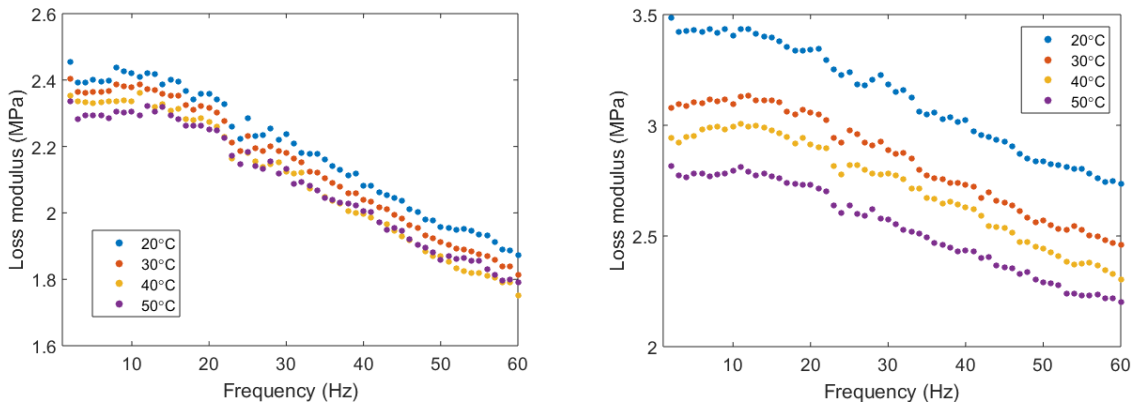


(a) (b)

Figure 6. 16 Loss modulus of MRE mount under different working states: (a) 0 mT, and (b) 210 mT external magnetic field

It can be noticed that loss modulus changes under external magnetic field of 210 mT is much more obvious than those under zero magnetic field when temperature varies from the room temperature (about 20 °C) to 50 °C. The loss modulus drops 21% under 210 mT external magnetic field and drops 5% under zero magnetic field respectively, when the environment temperature is increased from room temperature to 50 °C. It is necessary to take into account the coupling effect of external magnetic field and environment temperature in the design application of the MRE based mount.

## 6.4 Modelling and simulation of MRE mount

### 6.4.1 Dynamic modelling of the MRE mount

According to general theory, an unconstrained rigid body has six degrees of freedom (DOFs). In orthogonal OXYZ reference system where the origin O is the centre of gravity, these directions are lateral horizontal parallel to axes OX, longitudinal horizontal parallel to axes OZ, axial vertical parallel to axes OY and three rotations about these axes called here roll, pitch and yaw respectively. In such arrangement, a general mass-isolator system of the machine is considered as a rigid body supported by an isolator that has six modes of vibration, also and six natural frequencies. However, there are some basic assumptions when considering the vibration of ship or vehicle engine systems. The rotation behaviours of the mount are usually ignored. In this research, the shear behaviour caused by the excitation source is negligible when comparing with the vertical vibration behaviour of the system.

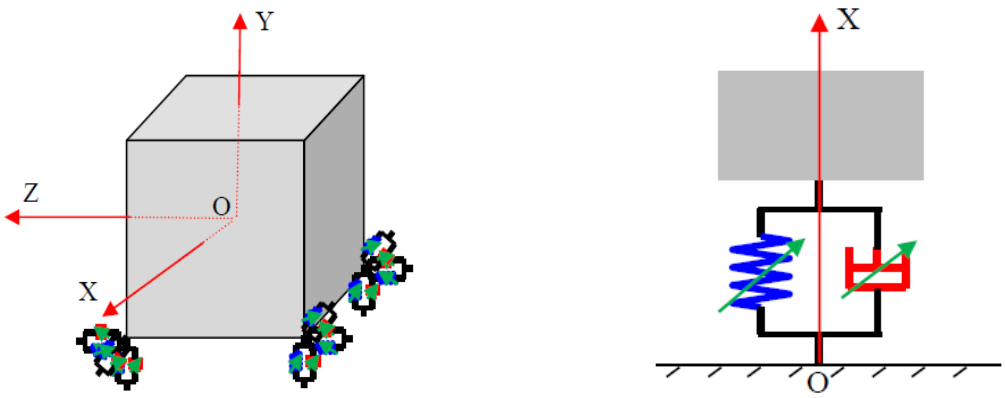


(a) (b)

Figure 6. 17 The dynamic model of: (a) a six-DOF system, and (b) a single-DOF system

The vibration control system based on single designed MRE mount is considered as a single DOF system. This dynamic system contains a mass and a MRE mount which can be described by using viscoelastic model. The stiffness and the damping properties of the MRE mount are dependent on the excitation frequency, strain amplitude, external magnetic field and the temperature. The equation of motion is given as follow:

$$M\ddot{X} + F_{MR}(\dot{X}, X) = F_{ex} \tag{6.2}$$

where M is the mass of the isolated object and the electromagnet, X is the dynamic displacement of the system, $F_{ex}$ is the excitation force, and $F_{MR}(\dot{X}, X)$ denotes the restore force of MRE which is dependent on the velocity and displacement. The dot means the derivate to time, in which $\dot{X}$ is the velocity and $\ddot{X}$ is the acceleration of the isolated object.

When the MRE mount system is subjected to harmonic excitation force, the resulting motion of the MRE mount system is also harmonic:

$$X(t) = X_a e^{i\omega t} \tag{6.3}$$

The strain of the MRE can be calculated by:

$$\varepsilon(t) = \varepsilon_a e^{i\omega t} \tag{6.4}$$

in which $\varepsilon_a = \frac{X_a}{L}$, and L is the thickness of the MRE mount.

The relationship between stress and strain of the MRE mount can be modelled by using viscoelastic model such as our proposed model and fractional Zener model.

$$\sigma(t) = (E' + iE'')\varepsilon(t) = (E' + iE'')\varepsilon_a e^{i\omega t} \tag{6.5}$$

where $E'$ and $E''$ are storage and loss modulus of the MRE mount which are dependent on the external magnetic field, environment temperature, load amplitude and excitation frequency.

The support force from MRE mount can be expressed as:

$$F_{MR}(\dot{X}, X) = A\sigma(t) = (K + iD)X_a e^{i\omega t} \tag{6.6}$$

where $A$ denotes the section area of the MRE mount, $K = \frac{AE'}{L}$ and $D = \frac{AE''}{L}$ are the stiffness and damping of the MRE mount respectively, $E'$ and $E''$ are storage modulus and loss modulus of the MRE core, which can be modelled by the viscoelastic models.

The excitation force can be calculated by using Eq. (6.2).

$$F_{ex} = (-M\omega^2 + K + iD)X_a e^{i\omega t} \tag{6.7}$$

The force transmissibility equation is obtained.

$$TR = \left|\frac{K + iD}{-M\omega^2 + K + iD}\right| \tag{6.8}$$

It leads to

$$TR = \frac{\sqrt{K^2 + D^2}}{\sqrt{(K - M\omega^2)^2 + D^2}} \tag{6.9}$$

The natural frequency of the MRE mount can be predicted by

$$\omega_0 = \sqrt{\frac{K}{M}} \tag{6.10}$$

According to the generalized mathematical model proposed in the Chapter 5, the stiffness of the MRE mount can be expressed as follow:

$$K = \frac{Ab'_M(B)}{L}\left\{[1 - b'_k(\varepsilon_a)]E'_\infty + \frac{b'_k(\varepsilon_a)}{b_T(T, T_r)}E'(\omega_r, T_r)\right\} \tag{6.11a}$$

$$\omega_r = a_T(T, T_r) \tag{6.11b}$$

where $b'_M(B)$ is the coefficients of the magnetic field induced storage modulus, $b'_k(\varepsilon_a)$ is the strain amplitude influence on the storage modulus, $a_T(T, T_r)$ and $b_T(T, T_r)$ are the horizontal and vertical shift factors respectively. They have been discussed in the Chapter 5.

The storage modulus master curve $E'(\omega_r, T_r)$ is constructed in the given strain amplitude, reference temperature, and non-magnetic field. For a given strain amplitude, the effect of strain amplitude on the storage modulus can be included in the model parameters of the master curve. Therefore, Eq. (6.11a) can be simplified as

$$K = \frac{A}{L}\frac{b'_M(B)}{b_T(T, T_r)}E'(\omega_r, T_r) \tag{6.12}$$

The natural frequency of the MRE mount in reference temperature and zero magnetic field is obtained by solving the nonlinear equation based on Eq. (6.10) and Eq. (6.12).

$$\omega_0^2 - \frac{A}{LM}\frac{b'_M(B)}{b_T(T, T_r)}E'(\omega_0, T_r) = 0 \tag{6.13}$$

### 6.4.2 Results and discussion

Figure 6.18 presents the variation of the force transmissibility of the MRE mount with different external magnetic fields in room temperature. It can be seen that numerical results agree well with experimental results of the force transmissibility of the MRE mount in room temperature and various magnetic fields. The resonance frequencies of the MRE mount under magnetic field of 0 mT, 120 mT, and 210 mT are 39.29 Hz, 41.62 Hz, and 43.94 Hz respectively. The resonance frequency increases with the increasing of external magnetic field. The frequency shift occurs when the MRE mount in an applied magnetic field, e.g. the fractional change in resonant frequency is 11.83% and the force transmissibility drops by 38.24% when the external magnetic field is increased from 0 mT to 210 mT.

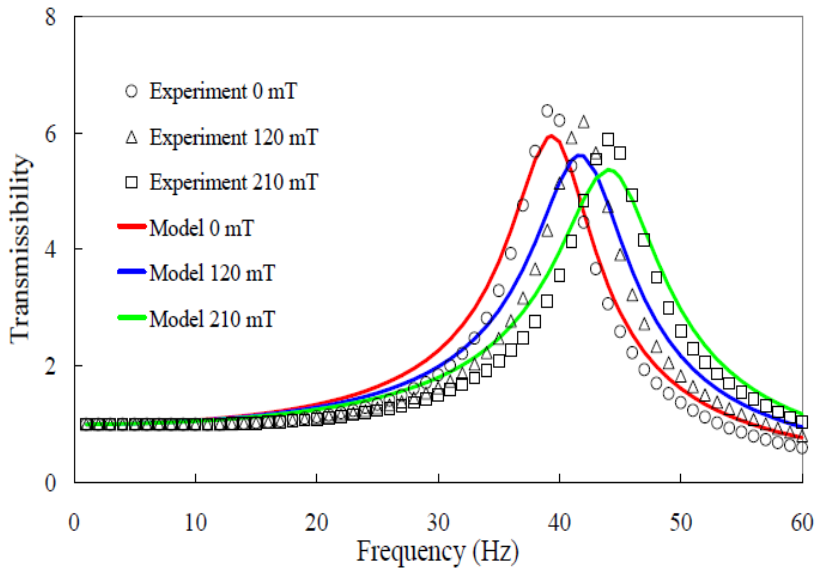

Figure 6. 18 The comparison of the experiment data and numerical results of the force transmissibility of the MRE mount under various magnetic fields in room temperature.

Figure 6.19 and Figure 6.20 show the variation of the force transmissibility of the MRE mount with different temperatures in magnetic field of 0 mT and 210 mT respectively. The agreements are found between the experiment data and numerical results of the force transmissibility of the MRE mount in different temperatures and external magnetic fields. The resonance frequency of the MRE mount varies with the temperature and external magnetic field. It is clearly observed that the resonance frequency of the MRE mount decreases with the increasing of temperature. This trend of variation is opposite to that of magnetic field. The frequency shift occurs when the temperature changes. The temperature effect on the frequency shift of the MRE mount in external magnetic field is larger than that in absence of magnetic field.

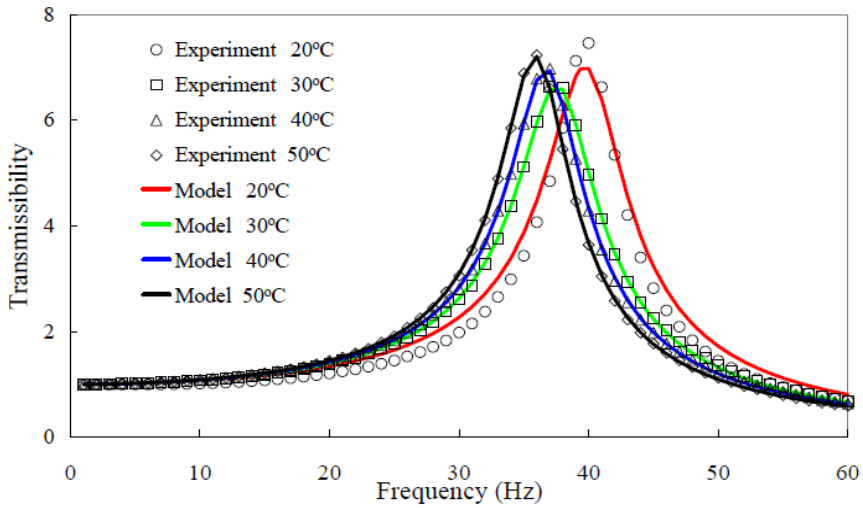


Figure 6. 19 The comparison of the experiment data and numerical results of the force transmissibility of the MRE mount under various temperatures in absence of external magnetic field.

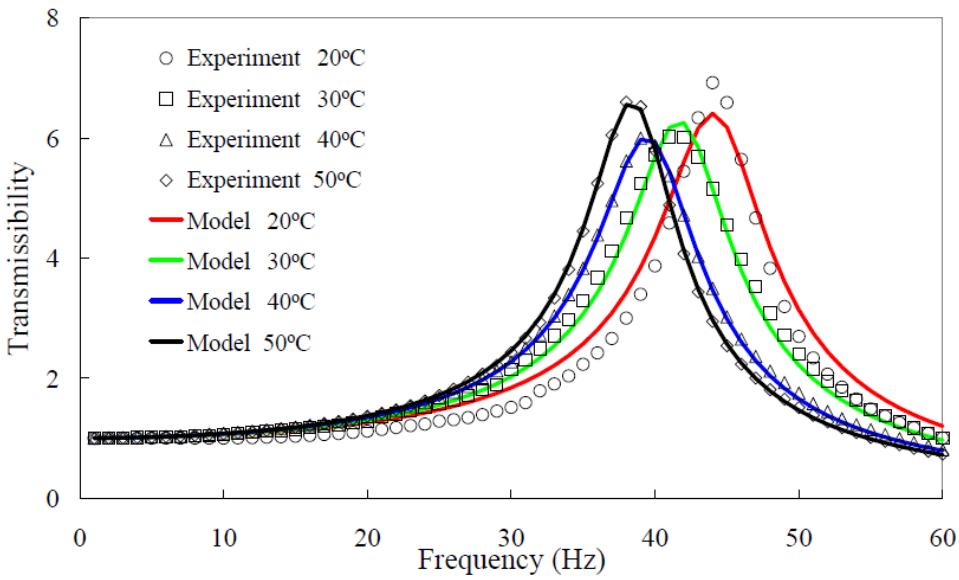


Figure 6. 20 The comparison of the experiment data and numerical results of the force transmissibility of the MRE mount under various temperatures in magnetic field of 210 mT.

Table 6.2 lists the variation of the resonance frequency of the MRE mount with temperature and external magnetic field. The resonant frequency of the MRE mount in absence of magnetic field reduces 4.01 Hz (about 10.15%) when temperature is increased from 20 °C to 50 °C. It indicates that MRE material can be significantly influenced by the temperature. According to our test in chapter 5, the inside part of MRE need more than 10 min to reach as its surface temperature. However, the total test period is less than 2.5 min, so the temperature effect caused by the electromagnets is neglected. While the resonant frequency of the MRE mount under external magnetic field of 210 mT reduces 5.9 Hz (about 13.43%) when temperature is increased from 20 °C to 50 °C. This means the external magnetic field increases the influence of temperature on the frequency shift of the MRE mount. The coupling effect of external magnetic field and environment temperature on the frequency shift of the MRE mount should be taken into consideration in design and application of the MRE mount.

Table 6. 2 The resonance frequency of the MRE mount in different temperatures and external magnetic fields.

| | 20°C | 30°C | 40°C | 50°C |
|---|---|---|---|---|
| 0 mT | 39.48 | 37.45 | 36.43 | 35.47 |
| 210 mT | 43.92 | 41.58 | 39.49 | 38.02 |

## 6.5 Experimental case studies on the MRE mount

### 6.5.1 On-off control of single mount at system resonance frequency

The excitation force is generated by the Instron machine E1000 plus. It simulates the MRE device works at a fix vibration frequency such as the marine operates at the cruising speed when the machine works at the stable situation. In normal application, the natural frequency of the system is carefully designed according to the ship structures and usually has a fixed frequency. The performance of designed system operates at the room temperature is performed by the experimental study.

The Figure 6.21 and Figure 6.22 illustrate the displacement and load relationship of the designed MRE mount, the changes of vibration amplitude and the force transmissibility are also recorded. In this experiment, the excitation force is generated by the Instron machine E1000 plus with the pre-load as 250 N and 50 N dynamic load amplitudes. At this state, the resonance frequency of the designed vibration control system is achieved as 30 Hz based on the previous experiments under this load state. The main purpose of this test is to evaluate the vibration control performance at the system resonance frequency.

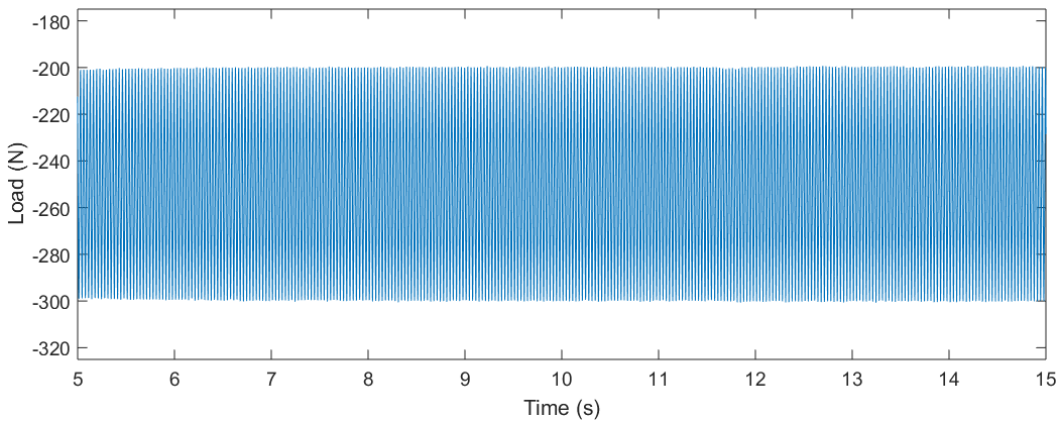


(a)

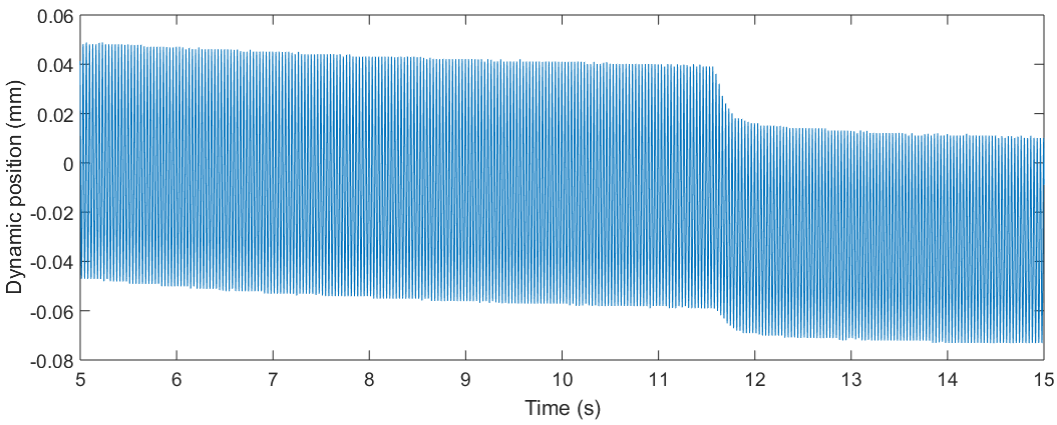

(b)

Figure 6. 21 (a)Load and (b)dynamic position time sequences of MRE mount under 250 pre-load and 50 N dynamic load with 30 Hz excitation frequency.

The dynamic load in this test is a sinusoidal harmonic load and the excitation frequency is fixed at 30 Hz as shown in Figure 6.21(a). According to the load channel record, the dynamic load remains at 200 N ± 50 N, and does not change too much while the external magnetic field is applied. It can be noticed from the Figure 6.21(b) above that the vibration behaviour of the total system is immediately changed once the external magnetic field is applied. The origin position of the vibration centre of the designed system under the pre-load is also changed instantly, it shifts from zero point to -0.03 mm. According to the experiment result figures, the effect of the applying the power supply to create a magnetic field for the designed MRE mount can instantly change the system operating state in less than 0.2 s which is quite fast for semi-active vibration control system.

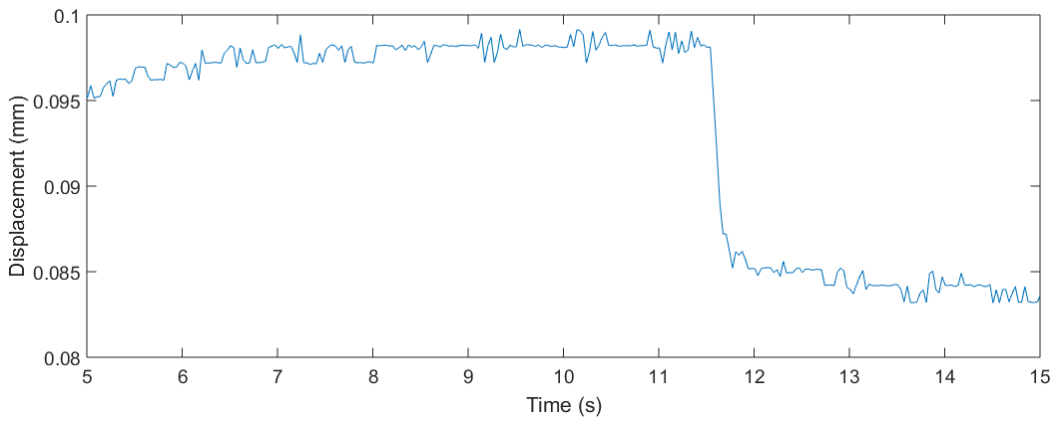


(a)

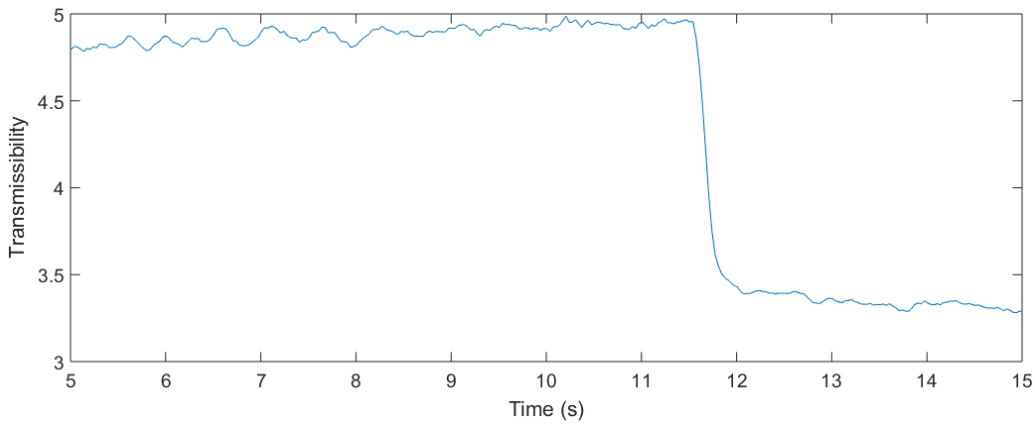


(b)

Figure 6. 22 (a) Vibration displacement and (b) force transmissibility time sequences of MRE

mount under 50 N dynamic load and 30 Hz frequency.

In Figure 6.22(a), the dynamic strain amplitude caused by the excited vibration is also reduced as 10%, and the absolute value of the displacement is dropped from 0.10 mm to 0.085 mm. The application of the external magnetic on the MRE based mount can effectively and significantly reduce structure vibration. The last Figure 6.22(b) illustrates the force transmissibility calculated based on the experiment data. The force transmissibility drops rapidly during the time period between 11.55 s and 11.80 s. The force transmissibility decreases about 1.5 in 0.25 s once the external magnetic field is applied. This is due to the natural frequency of the system is also shifted by the change of the stiffness of MRE to avoid the system resonance behaviour. This phenomenon of the designed MRE mount can be used for reducing the harmful vibration caused by the vibration source and the hull structure.

### 6.6.2 Real-time control of single mount with varying frequency

Dynamic mechanical test on designed MRE mount is carried out in this chapter to evaluate the performance of the vibration control system. In these case studies, the dynamic load is applied by Instron machine with 300 N pre-load and ±200 N dynamic load, or 250 N pre-load with ±50 N dynamic load. The Instron machine is used as the vibration excitation source and force and displacement recorder. The excitation frequency is increased from 1 Hz to 60 Hz which is similar as the marine engine and electric generator start-up phase. The experiments are carried out with two different temperature conditions: room temperature (20 °C) and machinery operation temperature (50 °C). Based on the previous DMA experiment data in this chapter, the force transmissibility curves of the different excitation frequency under both zero magnetic field and 210 mT external magnetic field are achieved. The control strategy of the MRE mount is designed based on these frequency nodes. The accelerate meter is attached on the upper electric magnet to record and measure the movement of the excitation source. The thermometer is place on the lower electric magnet and the monitor is approximately touched with the surface of the MRE core to detect the real-time temperature of the device in order to decide the suitable control strategy. The installation diagram of the designed MRE mount along with the sensors and vibration control system are shown in the following Figure 6.23.

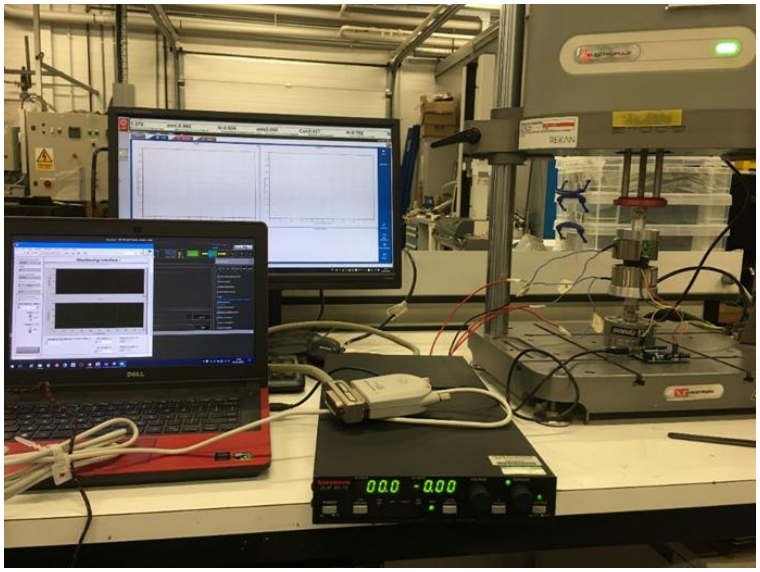

Figure 6. 23 Experiment setup of the semi-active MRE mount test.

Both the data of the real-time position of the upper deck of the mount and the surface temperature of the MRE core are transmitted to the Arduino board and processed. After this, the processed signal is delivered to the Labview software and do the fast Fourier transform (FFT) based on the real-time position data to achieve the real-time system vibration frequency. The surface temperature state helps the Labview software to decide the operation mode of the system. Based on the vibration frequency and the surface temperature, the control system sends the signal to the power supply of the electric magnets according to the predetermined policy of the control strategy. Both the front panel and the block diagram of the designed Labview VI are shown in the following Figures 6.24.

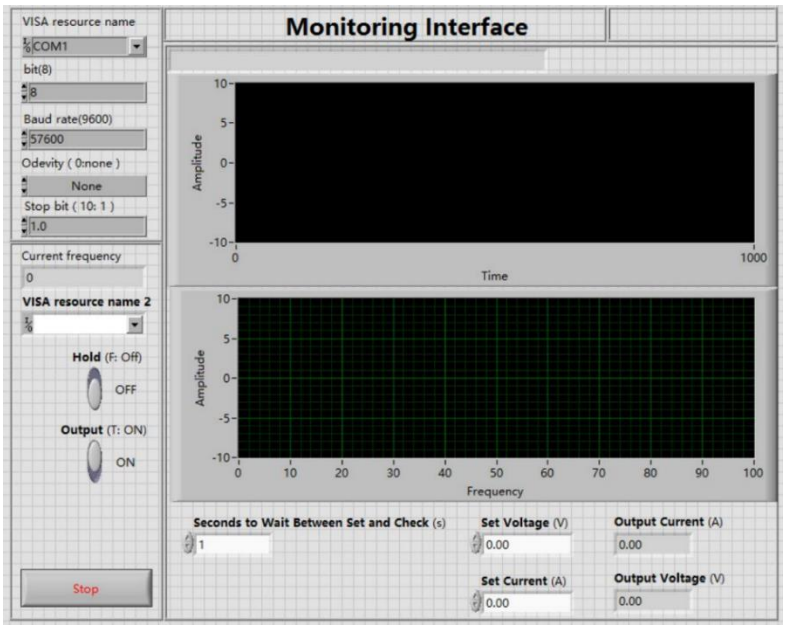


(a)

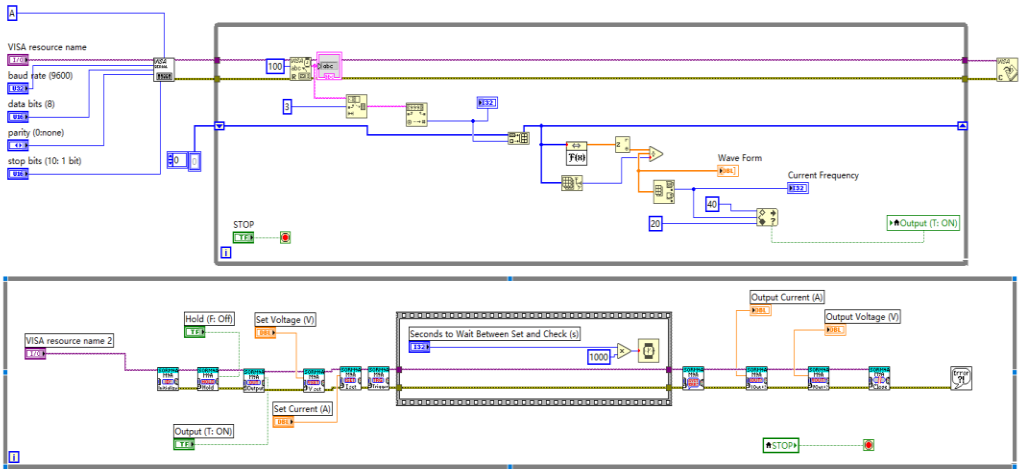


(b)

Figure 6. 24 Labview VI: (a) front panel, and (b) block diagram for self-control MRE mount.

This Labview VI is mainly consisting of three parts: signal read and process package, operation mode switch package, and the power supply control package. In the operation switch package, the frequency points of both the applying and disconnecting of the external power supply are pre-set based on the previous experiments data in the pre-design of the system in this chapter. The power supply control package decides the output mode switch between the current mode and voltage mode, and determines the value as well.

The comparison results between the system offline state and the vibration control system online sate with four case studies are shown in Figure 6.25 to Figure 6.32.

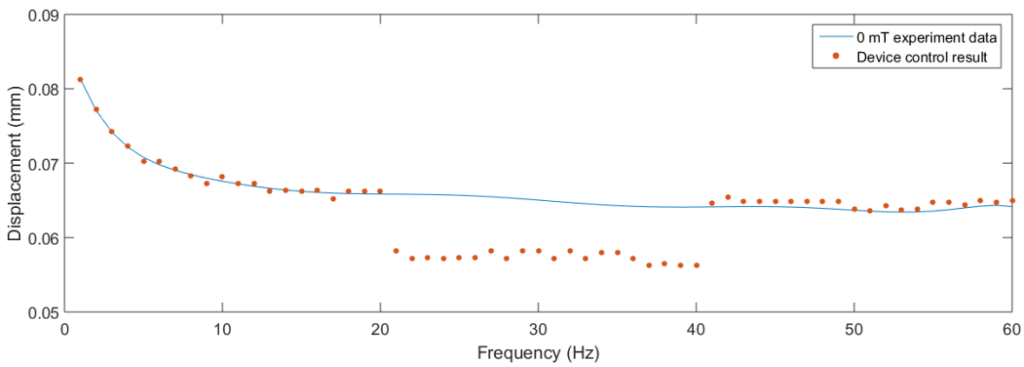


Figure 6. 25 Comparison of the displacement of MRE mount upper deck under different working states at room temperature (20 °C).

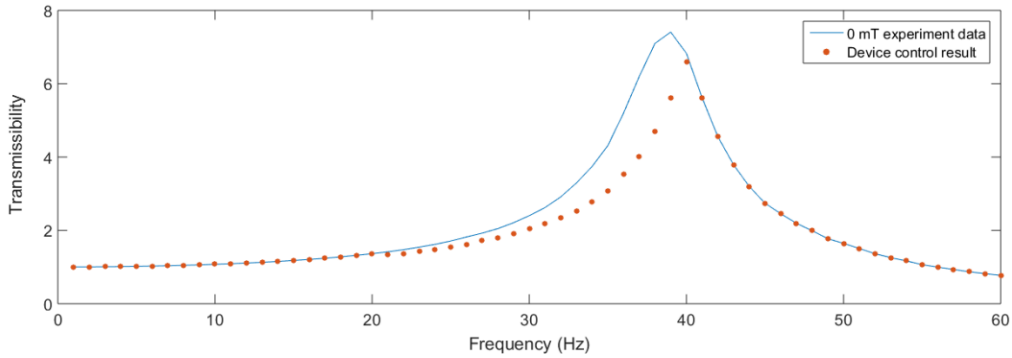


Figure 6. 26 Comparison of the force transmissibility of MRE mount upper deck under different working states at room temperature (20 °C).

In this case study, the mechanical test is carried out with 250 N pre-load which represents the equilibrium position caused by the weight of the mass, and ±50 N dynamic load with leaner increasing excitation frequency at room temperature condition. Figure 6.25 presents the comparison of the displacement of the MRE mount upper deck under different working states. The blue curve represents the original data achieved in the DMA test when the control system is not activated, and the red dotes are the experiment data achieved when the semi-active control system is activated. At the beginning state, the excitation frequency is increased from zero to 20 Hz, during this period the power of the electric magnets are cut off. The movement of the MRE mount is exactly the same as the mount with zero external magnetic field. When the vibration frequency of the system reaches 20 Hz, the device starts its second phase, the power supply is on to shift the force transmissibility peak from 37 Hz to 40 Hz. In the last state, the excitation frequency keeps increasing which is over 40 Hz, the power supply is cut off to make the system return to its original state. It can be noticed the force transmissibility of the system is reduced during the 20 Hz to 40 Hz period because of the designed MRE mount. The displacement of the upper deck of the MRE mount is also decreased with more than 15% when the control system is activated.

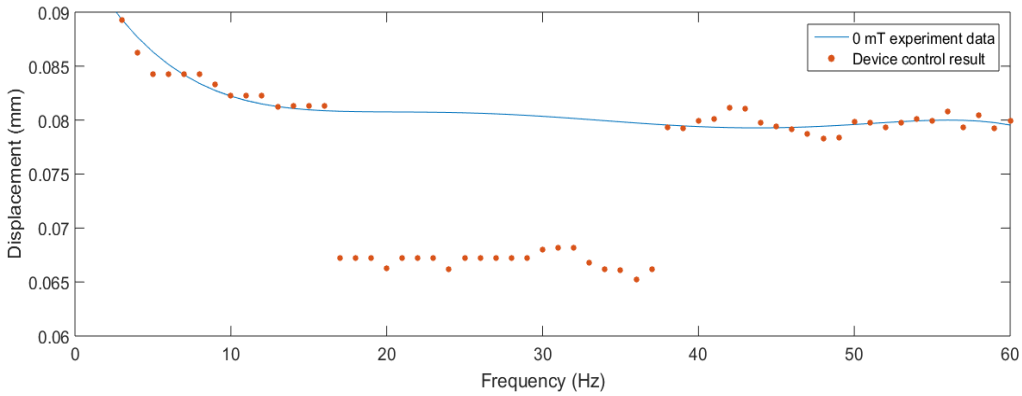

Figure 6. 27 Comparison of the displacement of MRE mount upper deck under different working states at 50 °C.

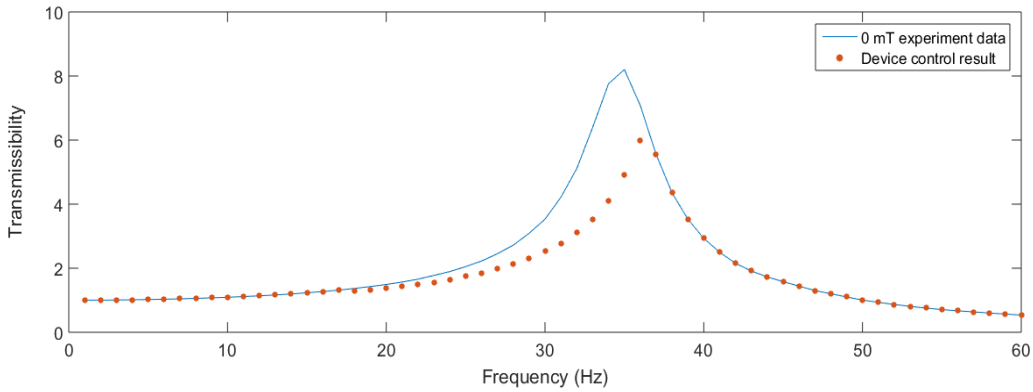


Figure 6. 28 Comparison of the force transmissibility of MRE mount upper deck under different working states at 50 °C.

Figure 6.27 and Figure 6.28 show the mechanical test is carried out with the same load condition at 50 °C environment temperature condition. In this work condition, the resonance frequency of system is shifted due to the high environment temperature, the activate frequency of the designed system is also changed. The power supply for the MRE mount is turned on at 17 Hz and switched off at 37 Hz to process the semi-active vibration control for the system. During this period, the force transmissibility of the system is reduced, especially at the original resonance frequency at 35 Hz, the force transmissibility is reduced by more than 50%. This reduction of the force transmissibility is much more significant than that in the low temperature which is about 25%. According to the experiment result, it can be noticed the MRE mount has better performance in the high temperature condition.

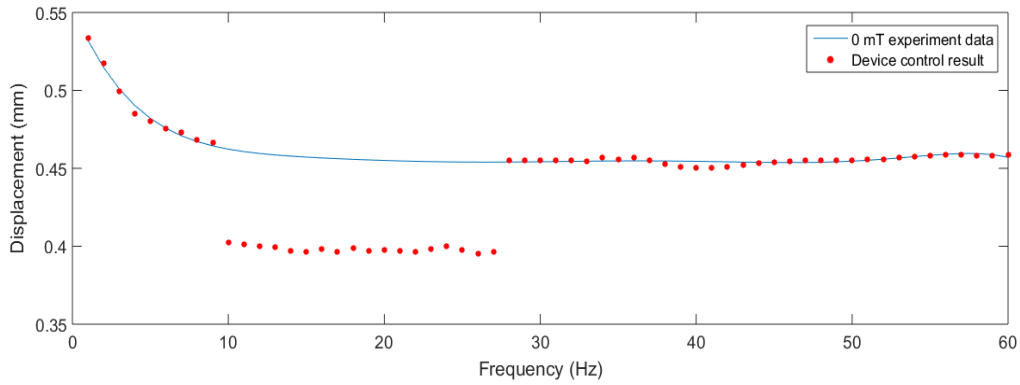


Figure 6. 29 Comparison of the displacement of MRE mount upper deck with large deformation at 20 °C

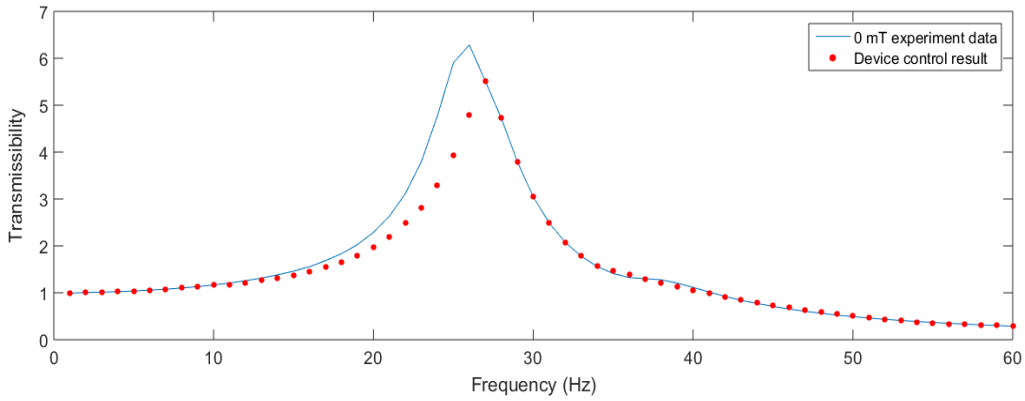


Figure 6. 30 Comparison of the force transmissibility of MRE mount upper deck with large deformation at 20 ℃

Figure 6.29 and Figure 6.30 illustrate the maximum displacement and the force transmissibility of the MRE mount under 300 N pre-load and ±200 N dynamic load. The experiments are carried at 20 ℃. In this case, the power supply is only activated when the excitation frequency is between 10 Hz and 27 Hz. During this period, both the displacement of the vibration and the force transmissibility are decreased significantly. The maximum displacement is reduced by 12% when the device is activated which is less than the small deformation condition. The reduction of the force transmissibility of the designed MRE mount is lower than other cases. The peak of the force transmissibility is slightly reduced by 10% and shifted by 1 Hz from 26 Hz to 27 Hz.

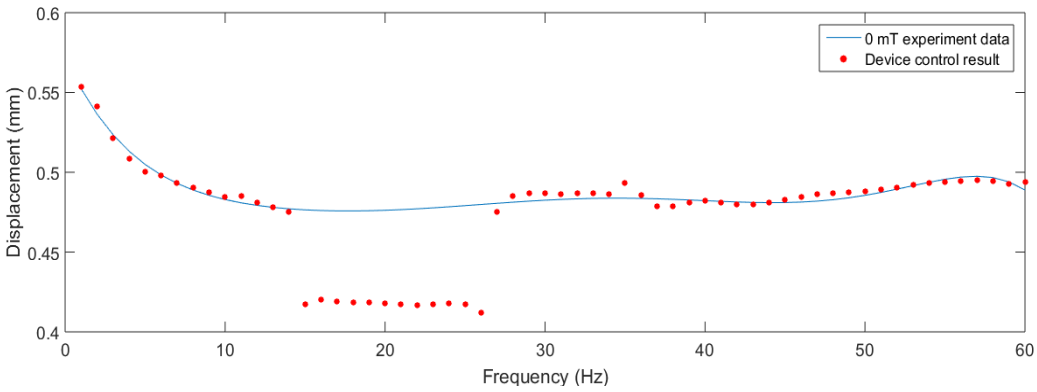


Figure 6. 31 Comparison of the displacement of MRE mount upper deck with large deformation at 50 ℃

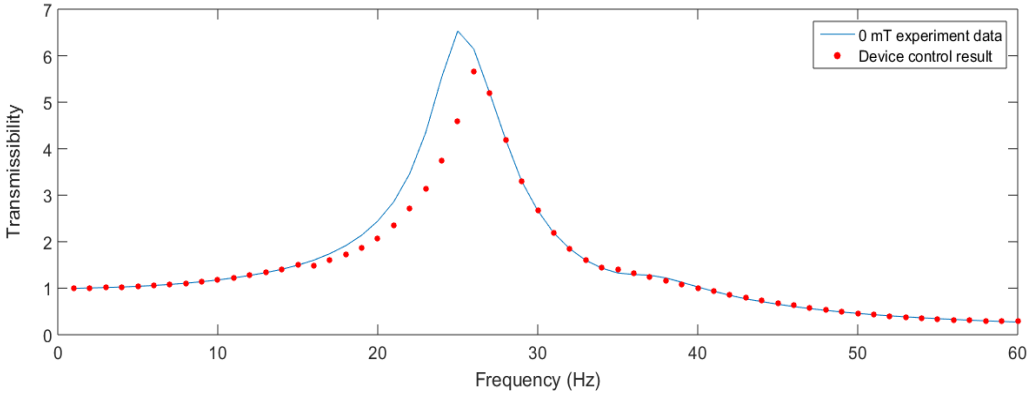


Figure 6. 32 Comparison of the force transmissibility of MRE mount upper deck with large deformation at 50 ℃

Figure 6.31 and Figure 6.32 illustrate the experiment results of the MRE mount with large deformation and ±200 N dynamic load, environment temperature is 50 ℃. The power supply is activated at 15 Hz to start to control the vibration and cut off when the excitation keeps increasing to 26 Hz. From the experiment data above, it can be noticed that the ability of the device to reduce the force transmissibility does not change too much with the environment temperature in the large deformation condition. In this case, the force transmissibility drops more than 30% at the original peak point. The maximum transmissibility is also decreased with 13% with the vibration control system is applied. The position of the maximum transmissibility is raised by 1 Hz when comparing with the zero external magnetic field data which is equal to the MRE inactivated situation.

The present experiment results indicate the MRE mount has better performance with low pre-strain rather than large deformation condition. In practical industry application design, springs and dampers can be installed along with the MRE mount in order to adjust the balances state of the vibration control system to the low pre-strain system. Besides, the MRE mount has stronger frequency shift ability in the high environment temperature. This is mainly caused by the matrix material of the MRE has lower stiffness under the thermal load. Super soft matrix material can be selected in the feature fabrication of MRE material to achieve the ideal performance.

## 6.6 Summary

In this chapter, a prototype of MRE based mount system is designed, manufactured and tested. The natural frequency shift ability and the performance of the force transmissibility of the

designed system under different test conditions are evaluated by DMA experiments and mathematical modelling simulation. A serial of case studies are carried out to perform the designed device under the different external magnetic field conditions and environment temperatures. It can be found that the vibration transmitted by the MRE mount decreases when the external magnetic field increases. According to the MRE mount performance testing results, the magnetic field can be activated on while the machine passes through the amplification period and resonance frequency, after that switched off where the two transmissibility curves meet. Under this logic, the self-control system is applied for the MRE mount to process the real time semi-active control of the system under the specific application requirement. The results show an obvious reduction in the vibration response and transmissibility can be obtained by applying a magnetic field to the MRE mount in a proper range of excitation frequency. Form the experiments above, the MRE mount illustrates outstanding frequency shift ability in the low deformation conditions, and it also has good performance under the large deformation. These experiment data and conclusions can be used in the further design of the vibration control device based on the MRE materials.

# 7 Conclusion

## 7.1 Contribution of the work

This thesis has investigated the nonlinear dynamic behaviour of MREs under the combined magnetic-thermal-mechanical load and developed a prototype of MRE based semi-active vibration control device. A state of the art review is performed on the fabrication method of MREs, especially the selection of the magnetic particles and the matrix materials. The main experimental and numerical studies on MRE material along with its applications are reviewed. The research gaps are found in the characterization and modelling of the temperature effect on the dynamic properties of MREs under various magnetic fields, strain amplitudes and frequencies.

DMA test, quasi-static test and DSC test on MRE materials have been carried out in this research. The influence of magnetic field, environment temperature, strain amplitude, excitation frequency, and pre-strain on the dynamic properties of the MREs under uniaxial harmonic compression is obtained and discussed. Moreover, the coupling effect of the environment temperature and the other impact factors on dynamic moduli of the MREs are first time well investigated. The temperature has an important influence on the dynamic modulus of the MREs made from silicone rubber embedded with iron particles subjected to uniaxial harmonic compression. A transition behaviour of the MRE samples is observed at about 50 °C for dynamic modulus. The variation of the dynamic modulus with temperature can be mainly divided into two stages. The storage modulus initially decreases with the increasing of temperature up to transition temperature and then increases or maintains a stable value when temperature increases until to 60 °C. The loss modulus decreases with the increasing of temperature below the transition temperature and then approximately remains constant with increasing temperature until 60 °C.

The influence of magnetic field, temperature, strain amplitude and frequency on the dynamic properties of MREs under uniaxial harmonic compression is investigated respectively by mathematical modelling. Inspired by the DMA experiment results, a new approach is proposed to model the viscoelastic behaviour of MREs based on the modified Kelvin-Voigt model in which both the stiffness of spring and viscosity of dashpot are dependent on the excitation frequency and have a clear physical interpretation. The time-temperature superposition (TTS) principle is extended to construct the dynamic modulus master curve of the MREs for the first

time by using the horizontal shift factor and the vertical shift factor. The new fractional functions are proposed to fit the MR effect on the storage modulus and loss modulus of MREs and the Kraus model is adopted to predict the influence of strain amplitude on dynamic moduli of MREs. A generalized mathematical model is developed to describe the magnetic field, temperature, strain amplitude and frequency dependent dynamic moduli of MREs under uniaxial harmonic compression. The good correlation between DMA experiment data and predicted results of dynamic moduli are evaluated respectively by the goodness-of-fit statistical analysis. The proposed mathematical model can be used to predict the dynamic moduli of MREs beyond the DMA experiment range of magnetic field, temperature, strain amplitude and frequency.

A prototype of MRE based mount along with its control system is designed, manufactured and tested. The designed vibration control system presents an outstanding operation performance with the total system response time less than 0.2 s. The natural frequency shift ability and the performance of the force transmissibility reduction of the designed system are evaluated. Based on our generalized mathematical model, the dynamic properties of MRE mount is modelled and simulated. The comparison between the experiment data and simulation reveals a satisfactory result. Furthermore, a serial of case studies is carried out to perform the designed device under different external magnetic fields and environment temperatures. Obvious frequency shift and the force transmissibility are monitored in all cases which indicate the designed vibration control can provide an outstanding improvement in marine vibration control. This proved MRE material based device is capable of solving vibration control problems in marine engineering.

## 7.2 Recommendations for future work

1. Investigation of the temperature effect on MRE materials fabricated with other materials. For industry application, it can choose natural rubber as the matrix to reduce the cost or use new ultra-soft material to improve the frequency shift ability. The fill particles of the MRE may also vary with the specific applications. It is necessary to take the environment temperature impact into consideration when investigating the mechanical properties of these material. In most cases, the thermal effect may play an important role on this type of material. The change tendency of the MREs' dynamic mechanical properties according to the temperature may be totally different from each

other. For specific MRE material, it needs to carry out the new DMA tests, or at least the DMA experiments on the pure matrix material samples. It is necessary to investigate the temperature effect on MRE with different volume ratio of the filler, although the 30% of filler is typical ideal ratio for MRE. However, the existing experiment data for MRE are normally achieved in the room temperature condition. According to author's research, the environment temperature may largely affect the performance of MRE material. It is worth to carry out the experiment studies on the coupling effect while combine the different volume ratio of the fill particles and the environment temperature.

2. The further DMA test can be carried out to evaluate the dynamic mechanical properties of MRE material beyond our test conditions such as the environment temperature range to verify the predicted data of the generalized master curve.

3. For the practical application of MRE material, the creep behaviour of the material needs to be take into consideration. In previous researches, the factors which affect the creep and stress relaxation of MREs are well discussed in the room temperature conditions. The creep behaviour of MREs in different temperatures may become more complicate. The experiment studies of temperature effect on the creep behaviour of MRE material should be carry out.

4. The proposed mathematical model can be extended to describe the dynamic properties of the MRE materials fabricated with other components in small strain regime once the model parameters are identified by DMA experimental data of these MRE materials. The method of constructing the generalized master curve can be applied to other inhomogeneous and anisotropic particle reinforced composite materials within small strain regime. It is also necessary to develop a generalized MRE model to predict its dynamic properties of MREs under large deformation.

# Reference


[1]. ABS 2017, Guidance notes on noise and vibration control for inhabited spaces

[2]. Aguib S, Nour A, Benkoussas B, Tawfiq I, Djedid T, Chikh N. (2016). Numerical simulation of the nonlinear static behavior of composite sandwich beams with a magnetorheological elastomer core, Composite Structures, 139, 111-119

[3]. Aguib S, Nour A, Djedid T, Bossis G, Chikh N. (2016). Forced transverse vibration of composite sandwich beam with magnetorheological elastomer core, Journal of Mechanical Science & Technology, 30(1), 15-24

[4]. An JS, Kwon SH, Choi HJ, Jung JH, Kim YG. (2017). Modified silane-coated carbonyl iron/natural rubber composite elastomer and its magnetorheological performance, Composite Structures, 160, 1020-1026

[5]. Aziz SAA, Mazlan SA, Ismail NIN, Choi SB, Ubaidillah, Yunus NAB. (2017). An enhancement of mechanical and rheological properties of magnetorheological elastomer with multiwall carbon nanotubes, Journal of Intelligent Material Systems and Structures, 28(20), 3127-3138

[6]. Aziz SAA, Mazlan SA, Ismail NIN, Ubaidillah, Choi SB, Nordin NA, Mohamad N. (2018). A comparative assessment of different dispersing aids in enhancing magnetorheological elastomer properties, Smart Materials and Structures, 27(11), 117002

[7]. Bagley RL and Torvik PJ. (1983). Fractional calculus ─A different approach to the analysis of viscoelastically damped structures, AIAA Journal, 21(5), 741-748

[8]. Bagley RL and Torvik PJ. (1986). On the Fractional Calculus Model of Viscoelastic Behavior, Journal of Rheology, 30, 133-155

[9]. Baranwal D and Deshmukh TS. (2012). MR-fluid technology and its application- a review, International Journal of Emerging Technology and Advanced Engineering, 2(12), 563-569.

[10]. Bastola AK, Hoang VT, Li L. (2017). A novel hybrid magnetorheological elastomer developed by 3D printing, Materials & Design, 114, 391-397.

[11]. Bayane BM, Yang EH, Qiu YJ. (2017). Dynamic modulus master curve construction using Christensen-Anderson-Marasteanu (CAM) model, International Journal of Engineering Research and Application, 7(1), 53-63

[12]. Behrooz M, Wang XJ, Gordaninejad F. (2014). Modeling of a new semi-active/passive magnetorheological elastomer isolator, Smart Materials and Structures, 23(4), 045013

[13]. Behrooz M, Wang XJ, Gordaninejad F. (2014). Performance of a new magnetorheological elastomer isolation system, Smart Materials and Structures, 23(4), 045014

[14]. Blom P and Kari L. (2011). A nonlinear constitutive audio frequency magneto-sensitive rubber model including amplitude, frequency and magnetic field dependence, Journal of Sound and Vibration, 330, 947-954

[15]. Boczkowska A and Awietjan SF. (2011). Effect of the elastomer stiffness and coupling agents on rheological properties of magnetorheological elastomers, WIT Transactions on Engineering Sciences, 72, 263-274

[16]. Boczkowska A, Awietjan SF, Pietrzko S, Kurzydłowski KJ. (2012). Mechanical properties of magnetorheological elastomers under shear deformation, Composites Part B: Engineering, 43, 636-640

[17]. Booij HC and Thoone GPJM. (1982). Generalization of Kramers-Kronig transforms and some approximations of relations between viscoelastic quantities, Rheologica Acta, 21, 15-24

[18]. Borcea L and Bruno O. (2001). On the magneto-elastic properties of elastomer–ferromagnet composites, Journal of the Mechanics and Physics of Solids, 49(12), 2877-2919

[19]. Bornassi S and Navazi HM. (2018). Torsional vibration analysis of a rotating tapered sandwich beam with magnetorheological elastomer core, Journal of Intelligent Material Systems and Structures, 29(11), 2406-2423

[20]. Böse H and Röder R. (2009). Magnetorheological elastomers with high variability of their mechanical properties, Journal of Physics: Conference Series, 149, 012090

[21]. Çakmak UD, Hiptmair F, Major Z. (2014). Applicability of elastomer time-dependent behavior in dynamic mechanical damping systems, Mech Time-Depend Mater, 18(1)139-151

[22]. Carlson JD and Jolly MR. (2000). MR fluid, foam and elastomer devices, Mechatronics, 10(4-5), 555-569

[23]. Carlton JS, Vlasic D, (2005). Ship vibration and noise: Some topical aspects, 1st International Ship Noise and Vibration Conference, London.

[24]. Cassagnau P amd Mélis F. (2003). Non-linear viscoelastic behaviour and modulus recovery in silica filled polymers, Polymer, 44, 6607-6615

[25]. Castañeda PP and Galipeau E. (2011). Homogenization-based constitutive models for magnetorheological elastomers at finite strain, Journal of the Mechanics and Physics of Solids, 59, 194-215

[26]. Chen L and Jerrams S. (2011). A rheological model of the dynamic behaviour of magnetorheological elastomers, Journal of Applied Physics, 110(1), 013513

[27]. Chen L, Gong XL, Jiang WQ, Yao JJ, Deng HX, Li WH. (2007). Investigation on magnetorheological elastomers based on natural rubber, Journal of Materials Science, 42(14), 5483-5489

[28]. Chen L, Gong XL, Li WH. (2007). Microstructures and viscoelastic properties of anisotropic magnetorheological elastomers, Smart Materials and Structures, 16, 1-6

[29]. Chen L, Gong XL, Li WH. (2008). Damping of magnetorheological elastomers, Chinese journal of Chemical Physics, 21(6), 581-585

[30]. Chen L, Gong XL, Li WH. (2008). Effect of carbon black on the mechanical performances of magnetorheological elastomers, Polymer Testing, 27(3), 340-345

[31]. Chen SW, Li R, Zhang Z, Wang XJ. (2016). Micromechanical analysis on tensile modulus of structured magneto-rheological elastomer, Smart Materials and Structures, 25(3), 035001

[32]. Choi WJ, Xiong YP, Shenoi RA. (2010). Vibration characteristics of sandwich beams

with steel skins and magnetorheological elastomer cores, Advances in Structural Engineering, 13(5), 837-847

[33]. Collette C, Kroll G, Saive G, Guillemier V, Avraam M, Preumont A. (2009). Isolation and damping properties of magnetorheologic elastomers, Journal of Physics: Conference Series, 149, 012091

[34]. Chool WW and Oyadiji SO. (2005). Characterizing effect temperature and magnetic field strengths on complex shear modulus properties of magnetorheological (MR) fluid, International Journal of Modern Physics B, 19(7-9), 1318-1324

[35]. Clément F, Bokobza L, Monnerie L. (2005). Investigation of the Payne effect and its temperature dependence on silica-filled polydimethylsiloxane networks, Rubber Chemistry and Technology, 78, 211-244

[36]. Christensen DW, Anderson DA, Rowe GM. (2017). Relaxation spectra of asphalt binders and the Christensen-Anderson rheological model, Road Materials and Pavement Design, 18, 382-403

[37]. Damiani R and Sun LZ. (2017). Microstructural characterization and effective viscoelastic behavior of magnetorheological elastomers with varying acetone contents, International Journal of Damage Mechanics, 26(1), 104-118

[38]. Daniel L, Hubert O, Buiron N, Billardon R. (2008). Reversible magneto-elastic behaviour: a multiscale approach, Journal of the Mechanics and Physics of Solids, 56(3), 1018-1042

[39]. Daniel L, Rekik M, Hubert O. (2014). A multiscale model for magneto-elastic behaviour including hysteresis effects, Archive of Applied Mechanics, 84(9-11), 1307-1323

[40]. Dargahi A, Sedaghati R, Rakheja S. (2019). On the properties of magnetorheological elastomers in shear mode: Design, fabrication and characterization. Composites Part B: Engineering, 159, 269-283

[41]. Davis LC. (1999). Model of magnetorheological elastomers, Journal of Applied Physics, 85(6), 3348-3351

[42]. Dealy J and Plazek D. (2009). Time-temperature superposition -A user guide, Rheology Bulletin, 78(2), 16-31

[43]. Deng HX and Gong XL. (2008). Application of magnetorheological elastomer to vibration absorber, Communications in Nonlinear Science and Numerical Simulation, 13, 1938-1947

[44]. Deng HX, Gong XL. (2007). Adaptive tuned vibration absorber based on magnetorheological elastomer, Journal of Intelligent Material Systems and Structures, 18(12), 1205-1210

[45]. Deng HX, Gong XL, Wang LH. (2006). Development of an adaptive tuned vibration absorber with magnetorheological elastomer, Smart Materials and Structures, 15(5), N111

[46]. Diani J, Fayolle B, Gilormini P. (2009). A review on the Mullins effect, European Polymer Journal, 45(3), 601-612

[47]. Dinzart F and Lipiński P. (2009). Improved five-parameter fractional derivative model for elastomers, Archives of Mechanics, 61(6), 459-474

[48]. Dong XF, Ma N, Qi M, Li JH, Chen R, Ou JP. (2012). The pressure-dependent MR effect of magnetorheological elastomers, Smart Materials and Structures, 21, 075014

[49]. Du HP, Li WH, Zhang N. (2011). Semiactive variable stiffness vibration control of vehicle seat suspension using MRE isolator, Smart Materials and Structures, 20, 105003

[50]. Eem SH, Jung HJ, Koo JH. (2012). Modeling of magneto-rheological elastomers for harmonic shear deformation, IEEE Transactions on magnetics, 48(11), 3080-3083

[51]. Ewoldt RH, Hosoi A, McKinley GH, 2008. New measures for characterizing nonlinear viscoelasticity in large amplitude oscillatory shear, Journal of Rheology, 52, 1427-1458

[52]. Fan L, Wang G, Wang W, Lu H, Yang F, & Rui X. (2019). Size effect of carbon black on the structure and mechanical properties of magnetorheological elastomers. Journal of Materials Science, 54(2), 1326-1340

[53]. Fan YC, Gong XL, Jiang WQ, Zhang W, Wei B, Li WH. (2010). Effect of maleic anhydride on the damping property of magnetorheological elastomers, Smart Materials and Structures, 19(5), 055015

[54]. Fan YC, Gong XL, Xuan S, Qin L, Li X. (2012). Effect of cross-link density of the matrix on the damping properties of magnetorheological elastomers, Industrial & Engineering Chemistry Research, 52(2), 771-778

[55]. Fu J, Yu M, Dong XM, Zhu LX. (2013). Magnetorheological elastomer and its application on impact buffer, Journal of Physics: Conference Series, 412, 242-251

[56]. Fu J, Li P, Liao G, Lai J, Yu M. (2017). Development and dynamic characterization of a mixed mode magnetorheological elastomer isolator, IEEE Transactions on Magnetics, 53(1), 1-4

[57]. Gao W and Wang X. (2016). Steady shear characteristic and behavior of magneto-thermo-elasticity of isotropic MR elastomers, Smart Materials and Structures, 25(2), 025026

[58]. Gavrilovici AM, Anitas EM, Chirigiu L, Bica I, & Negrutiu ML. (2019). Magnetodielectric effects in magnetorheological elastomers based on polymer fabric, silicone rubber, and magnetorheological suspension, Advances in Polymer Technology, 2019, 1983547

[59]. Ge L, Gong X, Fan Y, Xuan S. (2013). Preparation and mechanical properties of the magnetorheological elastomer based on natural rubber/rosin glycerin hybrid matrix, Smart Materials and Structures, 22(11), 115029

[60]. Ginder JM, Nichols ME, Elie LD, Tardiff JL. (1999). Magnetorheological elastomers: properties and applications, Proceedings of SPIE ─The International Society for Optics and Photonics, 3657, 131-138

[61]. Gong XL, Xu YG, Xuan SH, Guo CY, Luhang Zong LH. (2012). The investigation on the nonlinearity of plasticine-like magnetorheological material under oscillatory shear rheometry, Journal of Rheology, 56(6), 1375-1391

[62]. Gong XL, Zhang XZ, Zhang PQ. (2005). Fabrication and characterization of isotropic magnetorheological elastomers, Polymer Testing, 24(5), 669-676

[63]. Guedes RM. (2011). A viscoelastic model for a biomedical ultra-high molecular weight polyethylene using the time–temperature superposition principle, Polymer Testing, 30,

294-302

[64]. Guo F, Cheng-bin Du CB, Li RP. (2014). Viscoelastic parameter model of magnetorheological elastomers based on Abel dashpot, Advances in Mechanical Engineering, 2014, 629386

[65]. Gu X, Yu Y, Li Y, Li J, Askari M, Samali B. (2019). Experimental study of semi-active magnetorheological elastomer base isolation system using optimal neuro fuzzy logic control, Mechanical Systems and Signal Processing, 119, 380-398

[66]. Heinrich G and Klüppel M. (2002). Recent advances in theory of filler networking in elastomers, Advances in Polymer Science, 160, 1-44

[67]. Huber DL, Martin JE, Anderson RA, Read DH, Frankamp BL, Gulley GL. (2005). Magnetostriction of field structured magnetoelastomers, Sandia National Laboratories Report, Physical Review E 74, 051507, 2006

[68]. Hyun K and Kim W. (2011). A new non-linear parameter Q from FT-Rheology under nonlinear dynamic oscillatory shear for polymer melts system, Korea-Australia Rheology Journal, 23(4), 227-235

[69]. IMO Resolution MSC.337 (91). (2012). Adoption of the code on noise levels on board ships, Report of the Maritime Safety Committee (MSC) on its ninety-first session, Annex 1.

[70]. Ivaneyko D, Toshchevikov VP, Saphiannikova M, Heinrich G. (2011). Magneto-sensitive elastomers in a homogeneous magnetic field: a regular rectangular lattice model, Macromolecular Theory and Simulations, 20(6), 411-424

[71]. Ivaneyko D, Toshchevikov VP, Saphiannikova M, Heinrich G. (2012). Effects of particle distribution on mechanical properties of magneto-sensitive elastomers in a homogeneous magnetic field, Condensed Matter Physics, 15(3), 33601, 1-12

[72]. Jang DI, Yun GE, Park JE, Kim YK. (2018). Designing an attachable and power-efficient all-in-one module of a tunable vibration absorber based on magnetorheological elastomer, Smart Materials and Structures, 27, 085009

[73]. Jolly MR, Carlson JD, Muñoz BC. (1996). A model of the behaviour of magnetorheological materials, Smart Materials and Structures, 5, 607-614

[74]. Jóźwiak B, Orczykowska M, Dziubiński M. (2015). Fractional generalizations of Maxwell and Kelvin-Voigt models for biopolymer Characterization, PLOS One, 0143090

[75]. Jung HJ, Lee SJ, Jang DD, Kim IH, Koo JH, Khan F. (2009). Dynamic characterization of magneto-rheological elastomers in shear mode, IEEE Transactions on Magnetics, 45(10), 3930-3933

[76]. Jung HJ, Spencer Jr BF, Lee IW. (2003). Control of seismically excited cable-stayed bridge employing magnetorheological fluid dampers, Journal of Structural Engineering, 129(7), 873-883

[77]. Kaleta J, Królewicz M, Lewandowski D. (2011). Magnetomechanical properties of anisotropic and isotropic magnetorheological composites with thermoplastic elastomer matrices, Smart Materials and Structures, 20, 085006

[78]. Kaleta J, Królewicz M, Lewandowski D, Przybylski M, Zając P. (2012). Selected

magnetomechanical properties of magnetorheological elastomers with thermoplastic matrices, Composites Theory and Practice, 12(3), 210-215

[79]. Kaleta J and Lewandowski D. (2007). Inelastic properties of magnetorheological composites: II. Model, identification of parameters, Smart Materials and Structures, 16, 1954-1960

[80]. Kandasamy K, Cui FS, Townsend N, Foo CC, Guo JY, Shenoi RA, Xiong YP, 2016, A review of vibration control methods for marine offshore structures, Ocean Engineering, 127, 279-297

[81]. Kawasetsu T, Horii T, Ishihara H, & Asada M. (2018). Mexican-hat-like response in a flexible tactile sensor using a magnetorheological elastomer, Sensors, 18(2), 587

[82]. Keinänen J, Lindroos T, Kallio M, Aalto S, Juntunen M, Vessonen I. (2007). Dynamic properties of magnetorheologic elastomer, Journal of Structural Mechanics, 40(1), 39-47

[83]. Keip MA and Rambausek M. (2016). A multiscale approach to the computational characterization of magnetorheological elastomers, International Journal for Numerical Methods in Engineering, 107(4), 338-360

[84]. Khimi SR and Pickering KL. (2015). Comparison of dynamic properties of magnetorheological elastomers with existing antivibration rubbers, Composites Part B: Engineering, 83, 175-183

[85]. Khimi SR and Pickering KL. (2016). The effect of silane coupling agent on the dynamic mechanical properties of iron sand/ natural rubber magnetorheological elastomers, Composites Part B: Engineering, 90, 115-125

[86]. Kim M, Mohammad LN, Elseifi MA. (2015). Effects of various extrapolation technique for abbreviated dynamic modulus test data on MEPDG rutting predictions, Journal of Marine Science and Technology, 23(3), 353-363

[87]. Komatsuzaki T, Inoue T, Iwata Y. (2016). Experimental investigation of an adaptively tuned dynamic absorber incorporating magnetorheological elastomer with self-sensing property, Experimental Mechanics, 56(5), 871-880

[88]. Koo JH, Khan F, Jang DD, Jung HJ. (2010). Dynamic characterization and modeling of magneto-rheological elastomers under compressive loadings, Smart Materials and Structures, 19(11), 117002.

[89]. Kontou E and Katsourinis S. (2016). Application of a fractional model for simulation of the viscoelastic functions of polymers, Journal of Applied Polymer Science, 133(23), 43505

[90]. Królewicz M, Kaleta J, Lewandowski D, Przybylski M. (2013). Cyclic tests of thermoplastic magnetorheological elastomers, 6th ECCOMAS Thematic Conference on Smart Structures and Materials, SMART 2013, 24-26

[91]. Królewicz M, Przybylski M, Lewandowski D, Kaleta J. (2012). Manufacture and testing of anisotropic magnetorheological elastomers, Proceeding of 11th Youth Symposium on Experimental Solid Mechanics, Brasov, Romania

[92]. Kumbhar SR, Maji S, Kumar B. (2013). Development and Characterization of Isotropic Magnetorheological Elastomer. Universal Journal of Mechanical Engineering, 1(1), 18-21

[93]. Ladipo IL, Fadly JD, Faris WF. (2016). Characterization of magnetorheological elastomer (MRE) engine mounts, Materials Today: Proceedings, 3(2), 411-418

[94]. Leong SAN, Mazlan SA, Mohamad N, Aziz SAA, Ubaidillah. (2016). An overview of nanoparticles utilization in magnetorheological materials, AIP Conference Proceedings, 1710, 020002

[95]. Li R and Sun LZ. (2011). Dynamic mechanical behaviour of magnetorheological nanocomposites filled with carbon nanotubes, Applied Physics Letter, 99, 131912

[96]. Li W and Zhang X. (2008). Research and applications of MR elastomers, Recent Patents on Mechanical Engineering, 1(3), 161-166

[97]. Li R, Zhang Z, Chen SW, Wang XJ. (2015). Micromechanical analysis on anisotropy of structured magneto-rheological elastomer, IOP Conference Series: Materials Science and Engineering, 87, 012068

[98]. Li SB, Mi YL, Wang XR. (2017). Superposed nonlinear rheological behavior in filled elastomers, Journal of Rheology 61, 409-425

[99]. Li WH and Zhang XZ. (2010). A study of the magnetorheological effect of bimodal particle based magnetorheological elastomers, Smart Materials and Structures, 19(3), 035002

[100]. Li YC, Li JC, Weihua Li WH, Du HP. (2014). A state-of-the-art review on magnetorheological elastomer devices, Smart Materials and Structures, 23, 123001

[101]. Li WH, Wang XY, Zhang XZ, Zhou Y. (2009). Development and analysis of a variable stiffness damper using an MR bladder, Smart Materials and Structures, 18(7), 074007

[102]. Li WH, Zhou Y, Tian TF. (2010). Viscoelastic properties of MR elastomers under harmonic loading, Rheologica Acta, 49, 733-740

[103]. Li Y and Li J. (2015). A Highly Adjustable base isolator utilizing magnetorheological elastomer: experimental testing and modeling, Journal of Vibration and Acoustics, 137(1), 011009

[104]. Liao GJ, Gong XL, Kang CJ, Xuan SH. (2011). The design of an active–adaptive tuned vibration absorber based on magnetorheological elastomer and its vibration attenuation performance, Smart Materials and Structures, 20, 075015

[105]. Liao GJ, Gong XL, Xuan SH. (2014). Phase based stiffness tuning algorithm for a magnetorheological elastomer dynamic vibration absorber, Smart Materials and Structures, 23, 015016

[106]. Lin CR and Lee YD. (1996). Strain-dependent dynamic properties of filled rubber network systems, Macromolecular Theory and Simulations, 5, 1075-1104

[107]. Lion A. (1996). A constitutive model for carbon black filled rubber: experimental investigations and mathematical representation, Continuum Mechanics and Thermodynamics, 8(3), 153-169

[108]. Lion A, Kardelky C, Haupt P. (2003). On frequency and amplitude dependence of the Payne effect: theroy and experiments, Rubber Chemistry and Technology, 76(2), 533-547

[109]. Lokander M and Stenberg B. (2003). Improving the magnetorheological effect in isotropic magnetorheological rubber materials, Polymer Testing, 22, 677–680

[110]. Lokander M and Stenberg B. (2003). Performance of isotropic magnetorheological rubber materials, Polymer Testing, 22, 245-251

[111]. Lokander M, Reitberger T, Stenberg B. (2004). Oxidation of natural rubber-based magnetorheological elastomers, Polymer Degradation and Stability, 86(3), 467-471

[112]. LR 2015, Guidance notes: General overview of ship structural vibration problems.

[113]. Luo WB, Hu XL, Wang CH, Li QF. (2010). Frequency- and strain-amplitude-dependent dynamical mechanical properties and hysteresis loss of CB-filled vulcanized natural rubber, International Journal of Mechanical Sciences, 52, 168-174

[114]. Lu XS, Li M, Yang K, Xie HE, Yin Q, Wang D. (2010). SEBS based magnetorheological elastomer: preparation and property, 7th OAPS Working Paper Series, 2010-011

[115]. Madigosky WM, Lee GF, Niemiec JM. (2006). A method for modeling polymer viscoelastic data and the temperature shift function, The Journal of the Acoustical Society of America, 119(6), 376-3765

[116]. Mai TT, Morishita Y, Urayama K. (2017). Novel features of the Mullins effect in filled elastomers revealed by stretching measurements in various geometries, Soft Matter, 13(10), 1966-1977

[117]. Mainardi F and Spada G. (2011). Creep, relaxation and viscosity properties for basic fractional models in rheology, The European Physical Journal, Special issue, 193,133-160

[118]. Markou, AA and Manolis GD. (2016). A fractional derivative Zener model for the numerical simulation of base isolated structures, Bulletin of Earthquake Engineering, 14(1), 283-295

[119]. Melenev P, Raikher Y, Stepanov G, Rusakov V, Polygalova L. (2011). Modeling of the field-induced plasticity of soft magnetic elastomers, Journal of Intelligent Material Systems and Structures, 22, 513-538

[120]. Merckel Y, Brieu M, Diani J, Caillard J. (2012). A Mullins softening criterion for general loading conditions, Journal of the Mechanics and Physics of Solids, 60, 1257-1264

[121]. Merger D and Wilhelm M. (2014). Intrinsic nonlinearity from LAOStrain ─ experiments on various strain- and stress-controlled rheometers: a quantitative comparison, Rheologica Acta, 53(8), 621-634

[122]. Metzler R, Schick W, Kilian HG, Nonnenmacher TF. (1995). Relaxation in filled polymers: A fractional calculus approach, The Journal of Chemical Physics, 103 (16), 7180-7186

[123]. Miedzińska D, Lazowski J, Boczkowska A. (2010). Introduction to n-body simulation of magnetorheological elastomer (MRE) microstructure forming process, Journal of KONES Powertrain and Transport, 17(1), 249-253

[124]. Mikhailov VP and Bazinenkov AM. (2016). Active vibration isolation platform on base of magnetorheological elastomers, Journal of Magnetism and Magnetic Materials, 431, 266-268

[125]. Moreira RAS, Real JDC, Rodrigues D. (2010). A generalized frequency-temperature viscoelastic model, Shock and Vibration, 17, 407-418

[126]. Nadzharyan TA, Kostrov SA, Stepanov GV, Kramarenko EY. (2018). Fractional rheological models of dynamic mechanical behavior of magnetoactive elastomers in magnetic fields, Polymer, 142, 316-329

[127]. Nakano T. (2013). Applicability condition of time–temperature superposition principle (TTSP) to a multi-phase system, Mech Time-Depend Mater, 17(3), 439-447

[128]. Nanpo J, Nagashima K, Umehara Y, Kawai M, Mitsumata T. (2016). Mgnetic-field sensitivity of storage modulus for bimodal magnetic elastomers, The Journal of Physical Chemistry B, 120 (50), 12993–13000

[129]. Nayak B, Dwivedy SK, Murthy KSRK. (2012). Multi-frequency excitation of magnetorheological elastomer-based sandwich beam with conductive skins, International Journal of Non-Linear Mechanics, 47, 448–460

[130]. Ni YQ, Ying ZG, Chen ZH. (2010). Magneto-rheological elastomer (MRE) based composite structures for micro-vibration control, Earthquake Engineering and Engineering Vibration, 9(3), 345-356

[131]. Nie ZJ, Yu W, Zhou CX. (2016). Nonlinear rheological behavior of multiblock copolymers under large amplitude oscillatory shear, Journal of Rheology, 60, 1161-1179

[132]. Norouzi M, Alehashem SMS, Vatandoost H, Ni YQ, Shahmardan MM. (2016). A new approach for modeling of magnetorheological elastomers, Journal of Intelligent Material Systems and Structures, 27(8), 1121-1135

[133]. Ogden RW and Roxburgh DG. (1999). A pseudo–elastic model for the Mullins effect in filled rubber, Proceedings of the Royal Society of London A: Mathematical, Physical and Engineering Sciences, 455, 2861-2877

[134]. Olabide IA and Elejabarrieta MJ. (2016). Maximum attenuation variability of isotropic magnetosensitive elastomers, Polymer Testing, 54, 104-113

[135]. Olabide IA and Elejabarrieta MJ. (2017). Effect of synthesis variables on viscoelastic properties of elastomers filled with carbonyl iron powder, Journal of Polymer Research, 24, 139-148

[136]. Olabide IA and Elejabarrieta MJ. (2018). A new magneto-dynamic compression technique for magnetorheological elastomers at high frequencies, Polymer Testing, 66, 114-121

[137]. Olabide IA, Berasategui J, Elejabarrieta MJ, Ali MMB. (2014). Characterization of the linear viscoelastic region of magnetorheological elastomers, Journal of Intelligent Material Systems and Structures, 25(16), 2074-2081

[138]. Olabide IA, Kuzhir P, Elejabarrieta MJ. (2018). Linear magneto-viscoelastic model based on magnetic permeabilitycomponents for anisotropic magnetorheological elastomers, Journal of Magnetism and Magnetic Materials, 446, 155-161

[139]. Pan YH and Zhong Z. (2017). A viscoelastic constitutive modeling of rubber-like materials with the Payne effect, Applied Mathematical Modelling, 50, 621-632

[140]. Park JH, Cho MW, Lee ES, Lee CH, Kim CH, Cho WO, Kim NK. (2011). A study of vibration characteristics for siloxane based MR elastomers, 18th International Congress on Sound and Vibration, Rio de Janeiro, Brazil

[141]. Poojary UR and Gangadharan KV. (2017). Magnetic field and frequency dependent LVE limit characterization of magnetorheological elastomer, Journal of the Brazilian Society of Mechanical Sciences and Engineering, 39(4), 1365-373

[142]. Popp KM, Kröger M, Li HW, Zhang XZ, Kosasih PB. (2010). MRE properties under shear and squeeze modes and applications, Journal of Intelligent Material Systems and Structures, 21(15), 1471-1477

[143]. Poulos AS, Renou F, Jacob AR, Koumakis N, Petekidis G. (2015). Large amplitude oscillatory shear (LAOS) in model colloidal suspensions and glasses: frequency dependence, Rheologica Acta, 54(8), 715-724

[144]. Qi S, Guo H, Chen J, Fu J, Hu C, Yu M, & Wang ZL. (2018). Magnetorheological elastomers enabled high-sensitive self-powered tribo-sensor for magnetic field detection. Nanoscale, 10(10), 4745-4752

[145]. Qi S, Yu M, Fu J, Zhu M, Xie YP, Li W. (2018). An EPDM/MVQ polymer blend based magnetorheological elastomer with good thermostability and mechanical performance, Soft Matter, 14, 8521-8528

[146]. Qiao XY, Lu XS, Gong XL, Yang T, Sun K, Chen XD. (2015). Effect of carbonyl iron concentration and processing conditions on the structure and properties of the thermoplastic magnetorheological elastomer composites based on poly(styrene-b-ethylene-co-butyleneb-styrene) (SEBS), Polymer Testing, 47, 51-58

[147]. Robertson CG, Lin CJ, Rackaitis M, Roland CM. (2008). Influence of particle size and polymer-filler coupling on viscoelastic glass transition of particle-reinforced polymers, Macromolecules, 41, 2727-2731

[148]. Rendek M and Lion A. (2010). Amplitude dependence of filler-reinforced rubber: Experiments, constitutive modelling and FEM — Implementation, International Journal of Solids and Structures, 47, 2918-2936

[149]. Rouleau L, Pirk R, Pluymers B, Desmet W. (2015). Characterization and modeling of the viscoelastic behavior of a self-adhesive rubber using dynamic mechanical analysis tests, Journal of Aerospace Technology and Management, 7(2), 200-208

[150]. Rowe GM and Sharrock MJ. (2011). Alternate shift factor relationship for describing temperature dependency of viscoelastic behavior of asphalt materials, Transportation Research Record: Journal of the Transportation Research Board, 2207, 125-135

[151]. Ruddy C, Ahearne E, Byrne G. (2007). A review of magnetorheological elastomers: properties and applications, Proceedings of the International Manufacturing Conference (IMC) 24, Waterford Institute of Technology, Waterford, Ireland, 999-1005

[152]. Sapouna K, Xiong YP, Shenoi RA. (2017). Dynamic mechanical properties of isotropic/anisotropic silicon magnetorheological elastomer composites, Smart Materials and Structures, 26, 115010

[153]. Sariman MZ, Harun MH, Yamin AKM, Ahmad F, Yunos MR. (2015). Magnetorheological fluid engine mounts: a review on structure design of semi-active engine mounting, Internal Journal of Materials, 2, 6-16

[154]. Sasso m, Palmieri G, Amodio D. (2011). Application of fractional derivative models in linear viscoelastic problems, Mech Time-Depend Mater, 15, 367-387

[155]. Schubert G and Harrison P. (2015). Large-strain behaviour of Magneto-Rheological Elastomers tested under uniaxial compression and tension, and pure shear deformations, Polymer Testing, 42, 122-134

[156]. Shan LY, Yiqiu Tan YQ, Zhang H, Xu YA. (2016). Analysis of linear viscoelastic response function model for asphalt binders, Journal of Materials in Civil Engineering, 28(6), 04016010

[157]. Shariff MHBM and Bustamante R. (2016). 2016 An anisotropic model for the Mullins effect in magnetoactive rubber-like materials, Journal of Mechanics of Materials and Structures, 11(5), 559-582

[158]. Shen YF, Golnaraghi MF, Heppler GR. (2004). Experimental research and modeling of magnetorheological elastomers, Journal of Intelligent Material Systems and Structures, 15(1), 27-35

[159]. Singh PK, Soulages JM, Ewoldt RH. (2018). Frequency-sweep medium-amplitude oscillatory shear (MAOS), Journal of Rheology, 62, 277-293

[160]. Skalski P and Kalita K. (2017). Role of magnetorheological fluids and elastomers in today's world, Acta Mechanica et Automatica, 11(4), 267-274

[161]. Song HY, Nnyigide OS, Salehiyan R, Hyun K. (2016). Investigation of nonlinear rheological behavior of linear and 3-arm star 1,4-cis-polyisoprene (PI) under medium amplitude oscillatory shear (MAOS) flow via FT-rheology, Polymer, 104, 268-278

[162]. Sorokin VV, Ecker E, Stepanov GV, Shamonin M, Monkman GJ, Kramarenko EY, Khokhlov AR (2014). Experimental study of the magnetic field enhanced Payne effect in magnetorheological elastomers, Soft Matter, 10(43), 8765-8776

[163]. Sorokin VV, Stepanov GV, Shamonin M, Monkman GJ, Kramarenko EY. (2017). Magnetorheological behavior of magnetoactive elastomers filled with bimodal iron and magnetite particles, Smart Materials and Structures, 26, 035019

[164]. Starkova O and Aniskevich A. (2007). Limits of linear viscoelastic behavior of polymers, Mech Time-Depend Mater, 11, 111-126

[165]. Sławiński G, Miedzińska D, Niezgoda T, Boczkowska A. (2011). Experimental researches of magnetoreological elestomers stiffness changes under external magnetic field, CMM-2011 – Computer Methods in Mechanics, Warsaw, Poland

[166]. Sun S, Yang J, Du H, & Li W. (2018). Overcoming the conflict requirement between high-speed stability and curving trafficability of the train using an innovative magnetorheological elastomer rubber joint., Journal of Intelligent Material Systems and Structures, 29(2), 214-222

[167]. Sun SL, Deng HX, Yang J, Li WH, Du HP, Alici G, Nakano M. (2015). An adaptive tuned vibration absorber based on multilayered MR elastomers, Smart Materials and Structures, 24(4), 045045

[168]. Sun SS, Yang J, Li WH, Du H, Alici G, Yan TH, Nakano M. (2017). Development of an isolator working with magnetorheological elastomers and fluids, Mechanical Systems and Signal Processing, 83, 371-384

[169]. Suo S, Xu ZD, Li WH, Gan YX. (2018). Improved mathematical model for analysis of the Payne effect of magnetorheological elastomers, Journal of Aerospace Engineering,

31(5), 04018046

[170]. Tang SY, Zhang X, Sun S, Yuan D, Zhao Q, Yan S, Deng L, Yun G, Zhang S & Li W. (2018). Versatile microfluidic platforms enabled by novel magnetorheological elastomer microactuators, Advanced Functional Materials, 28(8), 1705484

[171]. Tian TF, Zhang XZ, Li WH, Alici G, Ding J. (2013). Study of PDMS based magnetorheological elastomers, Journal of Physics, 412, 1-8

[172]. Tschoegl NW, Knauss WG, Emri I. (2002). The effect of temperature and pressure on the mechanical properties of thermo- and/or piezorheologically simple polymeric materials in thermodynamic equilibrium – A critical review, Mechanics of Time-Dependent Materials, 6, 53-99

[173]. Ubaidillah S, Sutrisno J, Purwanto A, Mazlan SA. (2015). Recent progress on magnetorheological solids: materials, fabrication, testing, and applications, Advanced Engineering Materials, 17(5), 563-597

[174]. Usman M, Sung SH, Jang DD, Jung HJ, Koo JH. (2009). Numerical investigation of smart base isolation system employing MR elastomer, Journal of Physics: Conference Series, 149, 425-428

[175]. Varga Z, Filipcsei G, Zrínyi M. (2005). Smart composites with controlled anisotropy, Polymer, 46(18), 7779-7787

[176]. Vicente JD, Klingenberg DJ, Alvarez RH. (2011). Magnetorheological fluids: a review, Soft Matter, 7, 3701-3710

[177]. Wahab NAA, Mazlan SA, Kamaruddin S, Ismail NIN, Choi SB, Sharif AHR. (2016). Fabrication and investigation on field-dependent properties of natural rubber based magneto-rheological elastomer isolator, Smart Materials and Structures, 25(10), 107002

[178]. Wang Q, Dong XF, Li LY, Ou JP. (2018). Mechanical modeling for magnetorheological elastomer isolators based on constitutive equations and electromagnetic analysis, Smart Materials and Structures, 27, 065017

[179]. Wang Y, Hu Y, Chen L, Gong X, Jiang W, Zhang P, Chen Z. (2006). Effects of rubber/magnetic particle interactions on the performance of magnetorheological elastomers, Polymer Testing, 25(2), 262-267

[180]. Watanabe M, Ikeda J, Takeda Y, Kawai M, Mitsumata T. (2018). Effect of sonication time on magnetorheological effect for monomodal magnetic elastomers, Gels, 4, 49

[181]. Wu J, Gong X, Fan Y, Xia H. (2012). Improving the magnetorheological properties of polyurethane magnetorheological elastomer through plasticization, Journal of Applied Polymer Science, 123(4), 2476-2484

[182]. Xin FL, Bai XX, Qian LJ. (2016). Modeling and experimental verification of frequency-, amplitude-, and magnetodependent viscoelasticity of magnetorheological elastomers, Smart Materials and Structures, 25, 105002

[183]. Xu QW and Engquist B. (2018). A mathematical model for fitting and predicting relaxation modulus and simulating viscoelastic responses, Proceedings of The Royal Society A: Mathematical Physical and Engineering Sciences 474 (2213)

[184]. Xu Y, Gong XL, Xuan S. (2013). Soft magnetorheological polymer gels with controllable

rheological properties, Smart Materials and Structures, 22(7), 075029

[185]. Yalcintas M and Dai H. (2004). Vibration suppression capabilities of magnetorheological materials based adaptive structures, Smart Materials and Structures, 13(1), 1-11

[186]. Yang J, Du H, Li W, Li Y, Li J, Sun S, Deng HX. (2013). Experimental study and modeling of a novel magnetorheological elastomer isolator, Smart Materials and Structures, 22(11), 117001

[187]. Yang J, Gong XL, Zong L, Peng C, Xuan S. (2013). Silicon carbide-strengthened magnetorheological elastomer: preparation and mechanical property, Polymer Engineering & Science, 53(12), 2615-2623

[188]. Yang J, Sun S, Tian T, Li W, Du H, Alici G, Nakano M (2016). Development of a novel multi-layer MRE isolator for suppression of building vibrations under seismic events, Mechanical Systems and Signal Processing, 70, 811-820

[189]. Ying ZG and Ni YQ. (2017). Advances in structural vibration control application of magneto-rheological visco-elastomer, Theoretical & Applied Mechanics Letters, 7, 61-66

[190]. Yin BY, Hu XL, Luo WB, Song K. (2017). Application of fractional calculus methods to asymmetric dynamical response of CB-filled rubber, Polymer Testing, 61, 416-420

[191]. Yu M, Qi S, Fu J, Yang PA, Zhu M. (2015). Preparation and characterization of a novel magnetorheological elastomer based on polyurethane/epoxy resin IPNs matrix, Smart Materials and Structures, 24(4), 045009

[192]. Yu M, Zhao LJ, Fu J, Zhu M. (2016). Thermal effects on the laminated magnetorheological elastomer isolator, Smart Materials and Structures, 25, 115039

[193]. Yu Y, Li Y, Li J, Gu X. (2016). A hysteresis model for dynamic behaviour of magnetorheological elastomer base isolator, Smart Materials and Structures, 25(5), 055029

[194]. Yu Y, Li Y, Li J. (2014). A new hysteretic model for magnetorheological elastomer base isolator and parameter identification based on modified artificial fish swarm algorithm, International Symposium on Automation and Robotics in Construction and Mining, Sydney, Australia, ISARC 2014, 176-183

[195]. Yunus NA, Mazlan SA, Ubaidillah, Choi SB, Imaduddin F, Aziz SAA, Khairi MHA. (2016). Rheological properties of isotropic magnetorheological elastomers featuring an epoxidized natural rubber, Smart Materials and Structures, 25, 107001

[196]. Yusoff NIM, Chailleux E, Airey GD. (2011). A comparative study of the influence of shift factor equations on master curve construction, International Journal of Pavement Research and Technology, 4(6):324-336

[197]. Zhang W, Gong XL, Xuan SH, Jiang WQ. (2011). Temperature-dependent mechanical properties and model of magnetorheological elastomers, Industrial & Engineering Chemistry Research, 50, 6704-6712

[198]. Zhang W, Gong XL, Sun TL, Fan YC, Jiang WQ. (2010). Effect of cyclic deformation on magnetorheological elastomers, Chinese Journal of Chemical Physics, 23(2), 226-230

[199]. Zhang XZ, Li WH, Gong XL. (2008). An effective permeability model to predict field-dependent modulus of magnetorheological elastomers, Communications in Nonlinear

Science and Numerical Simulation, 13, 1910-1916

[200]. Zhang XZ, Peng SL, Wen WJ, Li WH. (2008). Analysis and fabrication of patterned magnetorheological elastomers, Smart Materials and Structures, 17, 045001.

[201]. Zhu JT, Xu ZD, Guo YQ. (2013). Experimental and modeling study on magnetorheological elastomers with different matrices, Journal of Materials in Civil Engineering, 25(11), 1762-1771

[202]. Zhu JT, Xu ZD, Guo YQ. (2012). Magnetoviscoelasticity parametric model of an MR elastomer vibration mitigation device, Smart Materials and Structures, 21, 075034

[203]. Zhu YS, Gong XL, Dang H, Zhang XZ, Zhang PQ. (2006). Numerical analysis on magnetic-induced shear modulus of magnetorheological elastomers based on multi-chain model, Chinese Journal of Chemical Physics, 19(2), 126-130.

# Appendix A List of publication

1. **Title: Temperature Dependent Dynamic Mechanical Properties of Magnetorheological Elastomers: Experiment and Modelling**

   Authors: Yanxiang Wan, Yeping Xiong, Shengming Zhang

   Journal: Composite Structures, Volume 202 (2018), pp. 768-773

   DOI: https://doi.org/10.1016/j.compstruct.2018.04.010

Composite Structures 202 (2018) 768–773

Contents lists available at ScienceDirect

Composite Structures

journal homepage: www.elsevier.com/locate/compstruct

Temperature dependent dynamic mechanical properties of Magnetorheological elastomers: Experiment and modeling

Yanxiang Wan[a,*], Yeping Xiong[a], Shengming Zhang[b]

[a] University of Southampton, UK
[b] Lloyd's Register, UK

ARTICLE INFO

*Keywords:*
Magnetorheological elastomer
Temperature effect
Dynamic mechanical analysis test
Viscoelasic modeling
Master curve

ABSTRACT

Magnetorheological elastomers (MREs) are a group of smart composite materials which are composed of magnetic particles dispersed in an elastomeric matrix. The controllable dynamic properties of these materials rely on many factors, in which temperature is a significant influencing factor requiring further investigations. In this paper, the dynamic mechanical analysis (DMA) tests have been performed to determine the viscoelastic properties of MREs with different test conditions. Based on the experiment results, the dynamic properties of MREs is modelled respectively by fractional Maxwell model (FMM) and generalized Maxwell model (GMM), and then the master curve of complex modulus is constructed using the time–temperature superposition (TTS) principle. The results show that the transition behavior of the silicon rubber based MRE samples under uniaxial compression occurs at about 50 °C. The storage modulus exhibits two different trends with the temperature variation: It first decreases rapidly and then increases slightly or maintains a stable value with increasing temperature.

2. **Title: Temperature Effect on Viscoelastic Properties of Anisotropic Magnetorheological Elastomers under Compression**

Authors: Yanxiang Wan, Yeping Xiong, Shengming Zhang

Journal: Smart Materials and Structures, Volume 28 (2019): 015005

DOI: https://doi.org/10.1088/1361-665X/aaeaf8

IOP Publishing Smart Materials and Structures

Smart Mater. Struct. **28** (2019) 015005 (13pp) https://doi.org/10.1088/1361-665X/aaeaf8

# Temperature effect on viscoelastic properties of anisotropic magnetorheological elastomers under compression

**Yanxiang Wan[1,3], Yeping Xiong[1] and Shengming Zhang[2]**

[1] University of Southampton, United Kingdom
[2] Lloyd's Register, United Kingdom

E-mail: yw8g12@soton.ac.uk, Y.Xiong@soton.ac.uk and Shengming.Zhang@lr.org

Received 4 September 2018, revised 19 October 2018
Accepted for publication 24 October 2018
Published 20 November 2018

**Abstract**

Magnetorheological elastomers (MREs) are a class of smart materials composed of an elastomer and micron-sized magnetic particles. Besides the loading amplitude and frequency, the elastic and rheological properties of MREs are also dependent on the external magnetic field and temperature. Previous studies focused on the influences of external magnetic field, strain amplitude and frequency on the dynamic properties, however, the temperature effect was rarely reported. In this paper, dynamic mechanical analysis (DMA) tests were carried out to investigate the viscoelastic properties of the anisotropic MRE samples under various temperatures and magnetic fields. A transition behavior of the anisotropic MRE samples was observed at about 50 °C for the dynamic modulus. The storage modulus initially decreased with the increasing of the temperature up to 50 °C and then increased or maintained a stable value when the temperature increased up to 60 °C. The time-temperature superposition (TTS) principle was extended to construct the dynamic modulus master curve of the MREs by using the horizontal shift factor and the vertical shift factor. The good correlations between the measured and predicted data were confirmed by performing statistical analysis for the goodness of fit. The constructed master curve and shift factors can be used to predict the viscoelastic properties of the MREs beyond the DMA experiment's range of temperatures and frequencies.

Keywords: magnetorheological elastomers, dynamic mechanical analysis, viscoelastic properties, temperature effect, time-temperature superposition

3. **Title: Numerical analysis of residual stress in butt-welded high tensile strength steel structures.**

   Authors: Yanxiang Wan, Yeping Xiong, Shengming Zhang

   Conference: Analysis and Design of Marine Structures: Proceedings of the 5th International Conference on Marine Structures (MARSTRUCT 2015), Taylor and Francis, pp. 597-608

4. **Title: Numerical analysis of residual stress in butt-welded high tensile strength steel structures.**

   Authors: Yanxiang Wan, Yeping Xiong, Shengming Zhang

   Conference: 3rd Annual International Conference on Advanced Material Engineering (AME2017). vol. 110, Atlantis Press, pp. 415-420

5. **Title: Temperature dependent dynamic mechanical properties of magnetorheological elastomers: experiment and modelling**

   Authors: Yanxiang Wan, Yeping Xiong, Shengming Zhang

   Conference: 20th International Conference on Composite Structures, Paris, France

# Appendix B Additional DMA experiment results

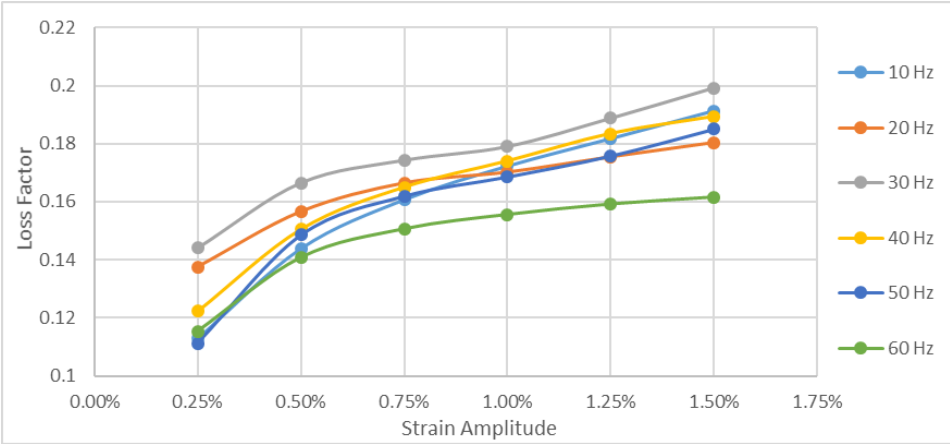


Figure B. 1 Dependence of loss factor on strain amplitude at room temperature, pre-strain of 5%, magnetic field of 0 mT, and vibration frequency from 10 Hz to 60 Hz

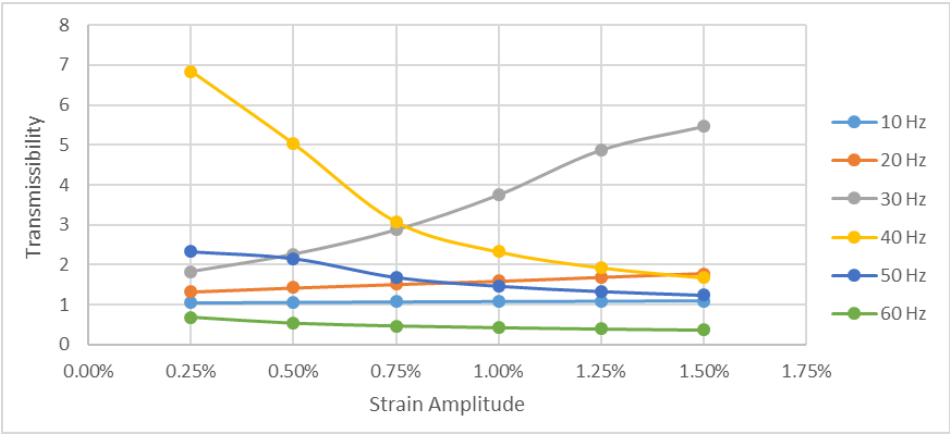


Figure B. 2 Dependence of transmissibility on strain amplitude at room temperature, pre-strain of 5%, magnetic field of 0 mT, and vibration frequency from 10 Hz to 60 Hz

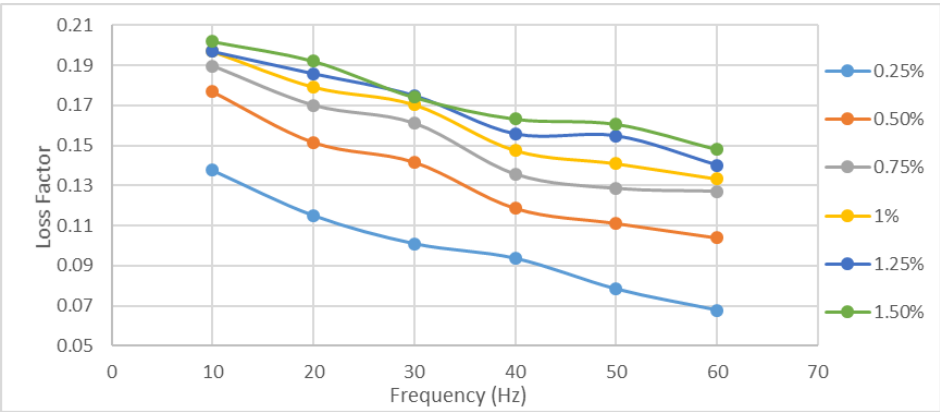


Figure B. 3 Dependence of loss factor on frequency at room temperature, pre-strain of 5%, magnetic field of 300 mT, and strain amplitudes from 0.25% to 1.5%

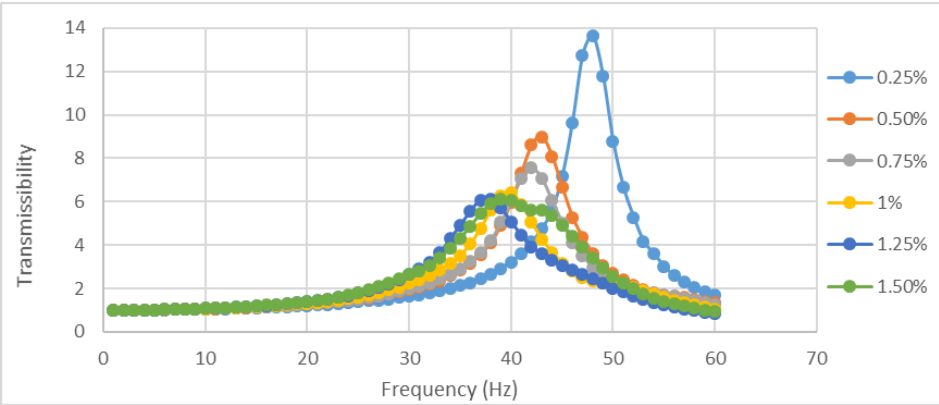


Figure B. 4 Dependence of transmissibility on frequency at room temperature, pre-strain of 5%, magnetic field of 300 mT, and strain amplitudes from 0.25% to 1.5%

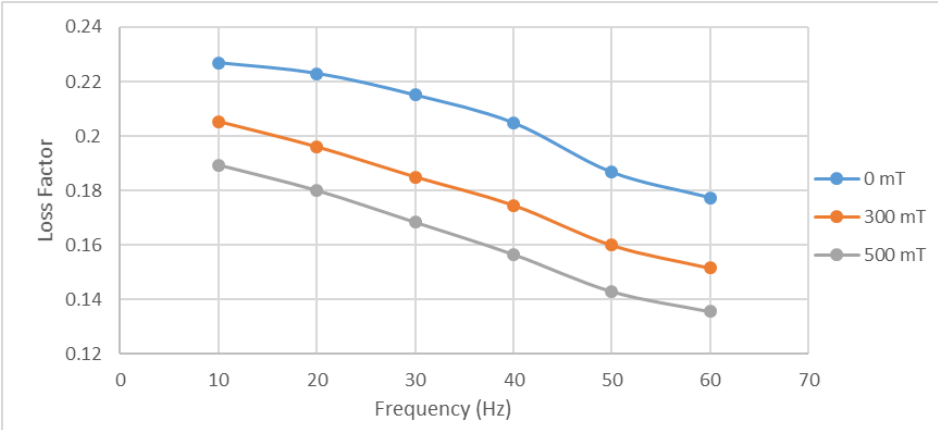


Figure B. 5 Dependence of loss factor on external magnetic field and frequency at room temperature, pre-strain of 5%, and strain amplitude of 1.5%

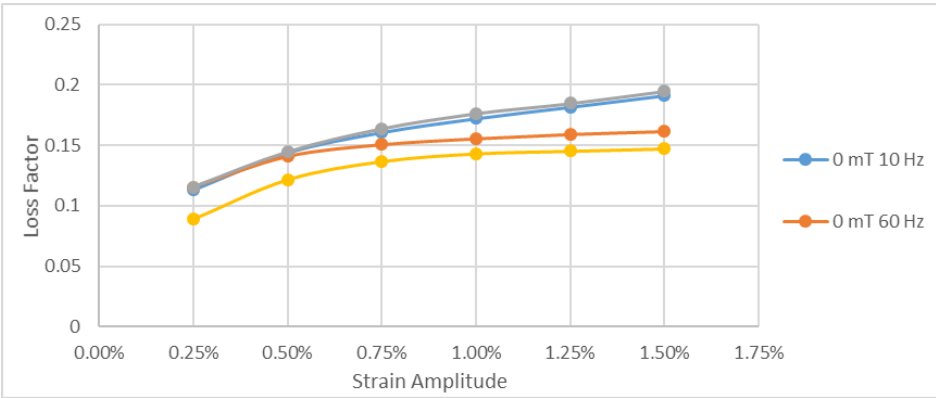


Figure B. 6 Dependence of loss factor on external magnetic field and strain amplitude at room temperature, pre-strain of 5%, and the test frequency is 10 Hz and 60 Hz

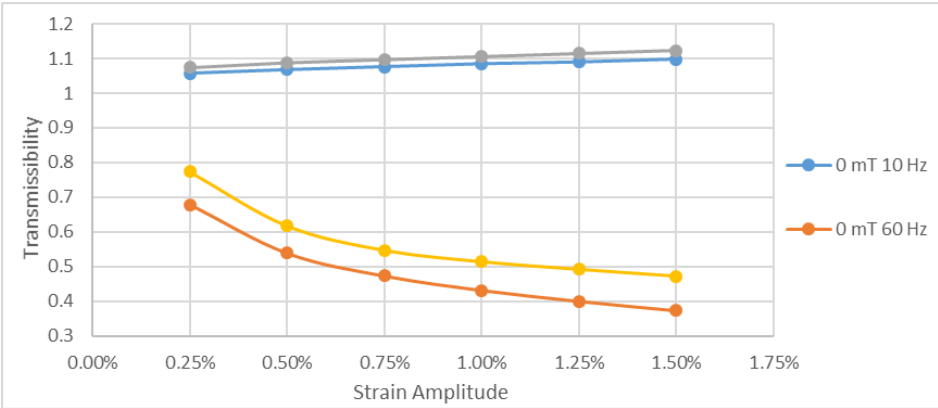


Figure B. 7 Dependence of transmissibility on external magnetic field and strain amplitude at room temperature, pre-strain of 5%, and the test frequency is 10 Hz and 60 Hz

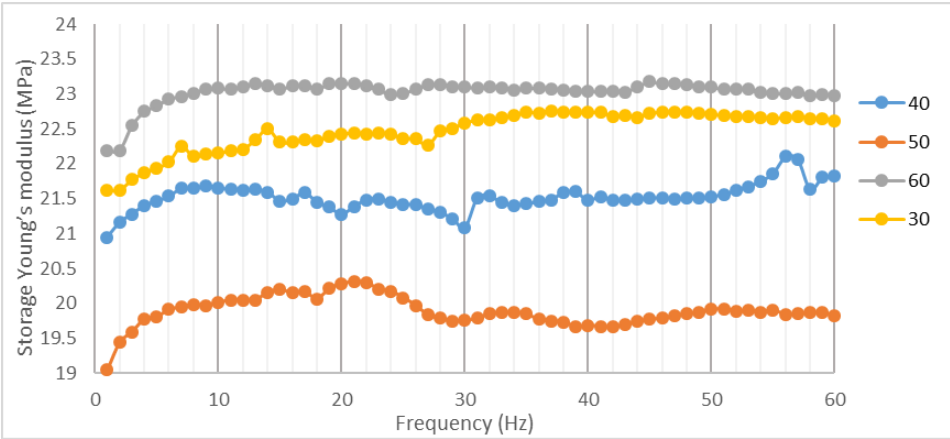


Figure B. 8 Dependence of storage modulus on temperature and frequency at pre-strain of 5%, strain amplitude of 1%, and non-magnetic field

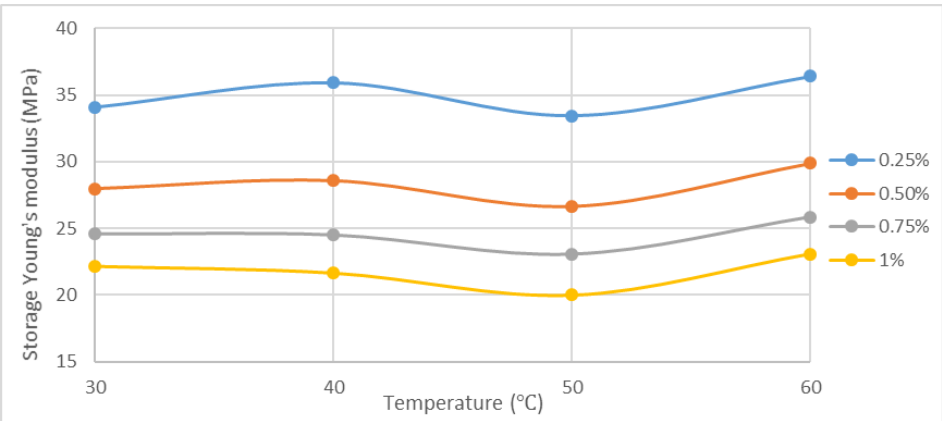


Figure B. 9 Dependence of storage modulus on temperature and strain amplitude at pre-strain of 5%, vibration frequency of 10 Hz, and non-magnetic field

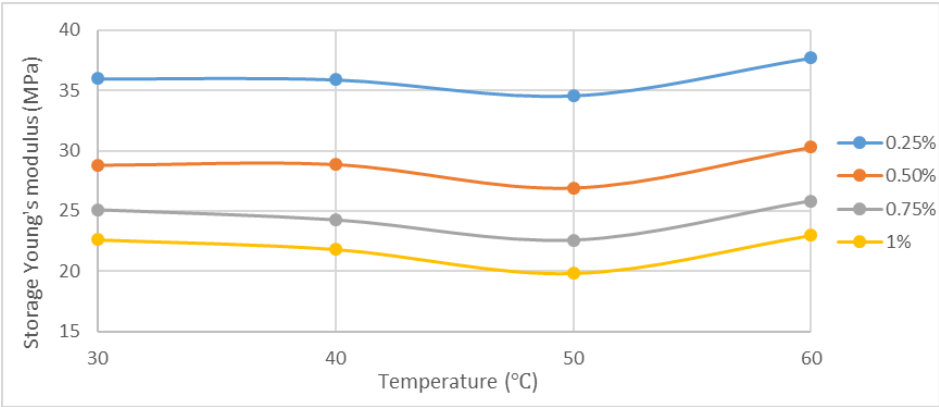


Figure B. 10 Dependence of storage modulus on temperature and strain amplitude at pre-strain of 5%, vibration frequency of 60 Hz and non-magnetic field

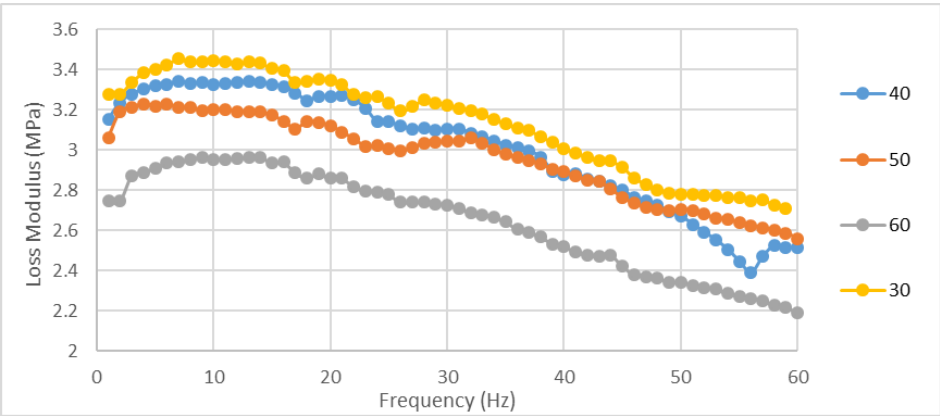


Figure B. 11 Dependence of loss modulus on temperature and frequency at pre-strain of 5%, strain amplitude of 1%, and non-magnetic field

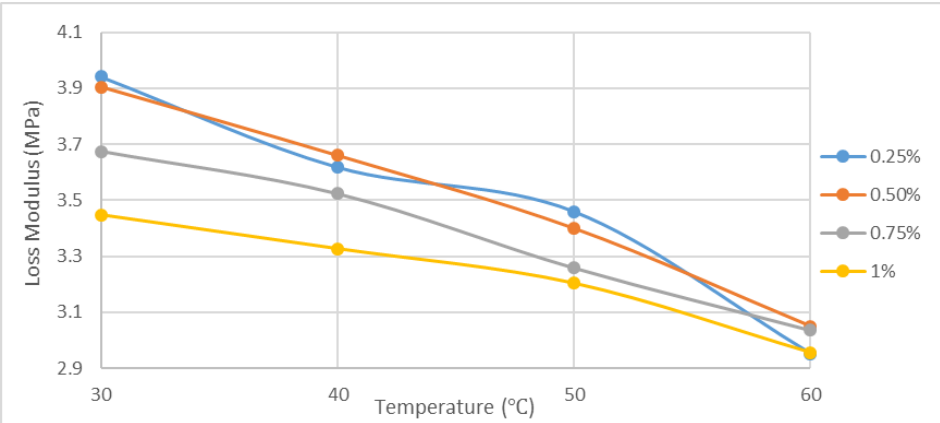


Figure B. 12 Dependence of loss modulus on temperature and strain amplitude at pre-strain of 5%, vibration frequency of 10 Hz, and non-magnetic field

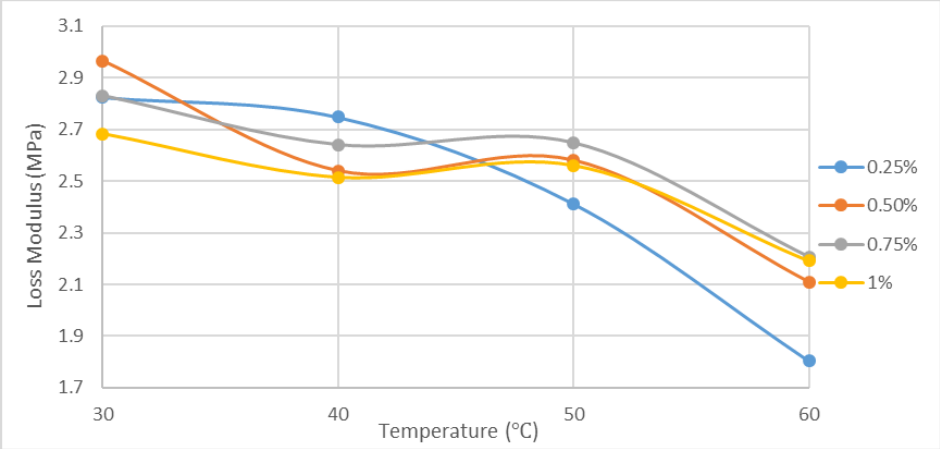


Figure B. 13 Dependence of loss modulus on temperature and strain amplitude at pre-strain of 5%, vibration frequency of 60 Hz, and non-magnetic field

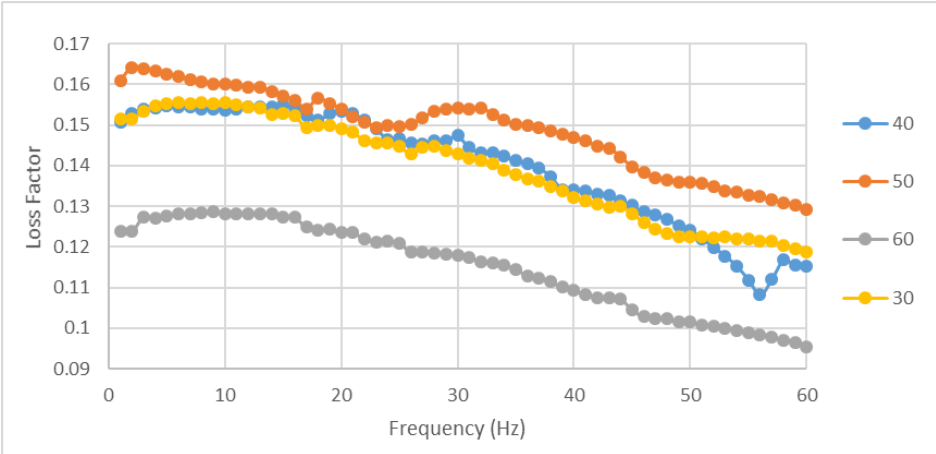


Figure B. 14 Dependence of loss factor on temperature and frequency at pre-strain of 5%, strain amplitude of 1%, and non-magnetic field

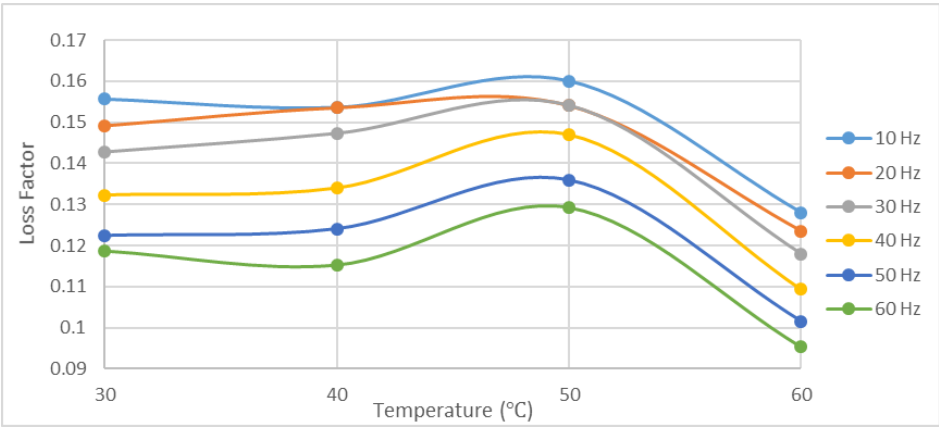


Figure B. 15 Dependence of loss factor on temperature and frequency at pre-strain of 5%, strain amplitude of 1%, and non-magnetic field

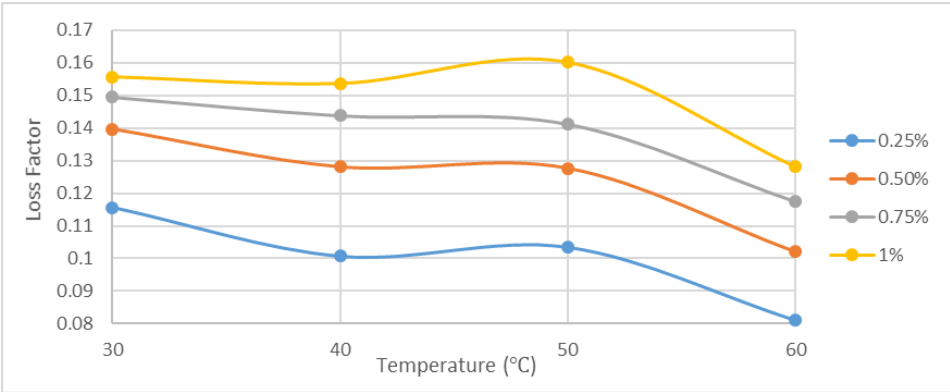


Figure B. 16 Dependence of loss factor on temperature and strain amplitude at pre-strain of 5%, vibration frequency of 10 Hz, and non-magnetic field

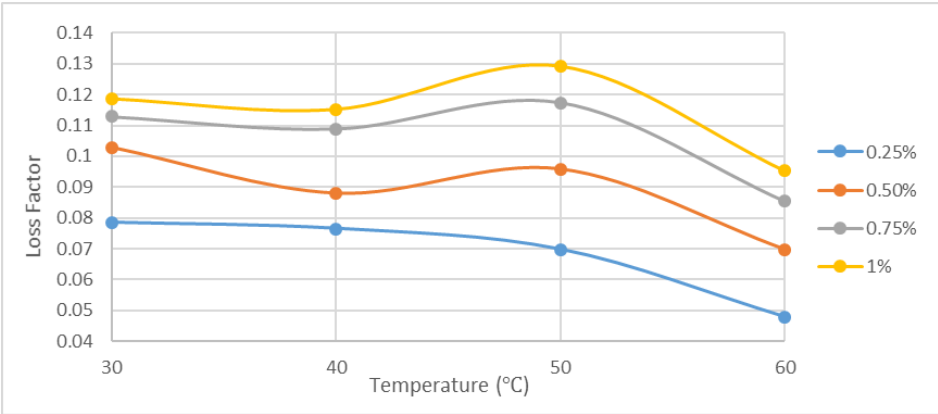


Figure B. 17 Dependence of loss factor on temperature and strain amplitude at pre-strain of 5%, vibration frequency of 60 Hz and non-magnetic field

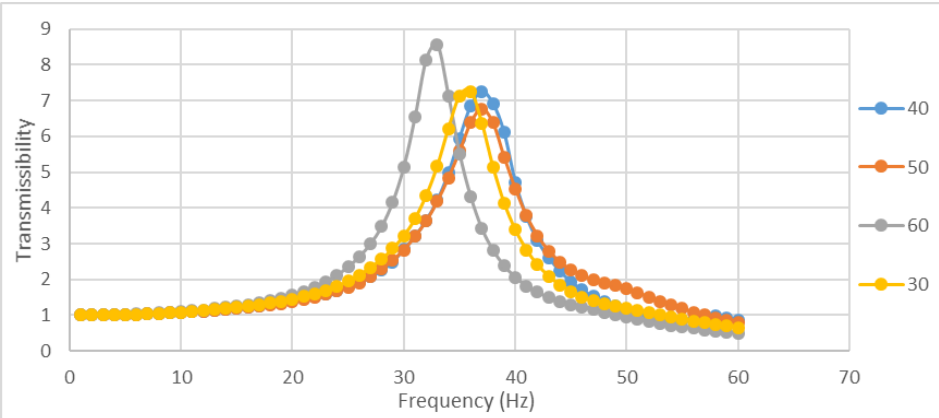


Figure B. 18 Dependence of transmissibility on temperature and frequency at pre-strain of 5%, strain amplitude of 1%, and non-magnetic field

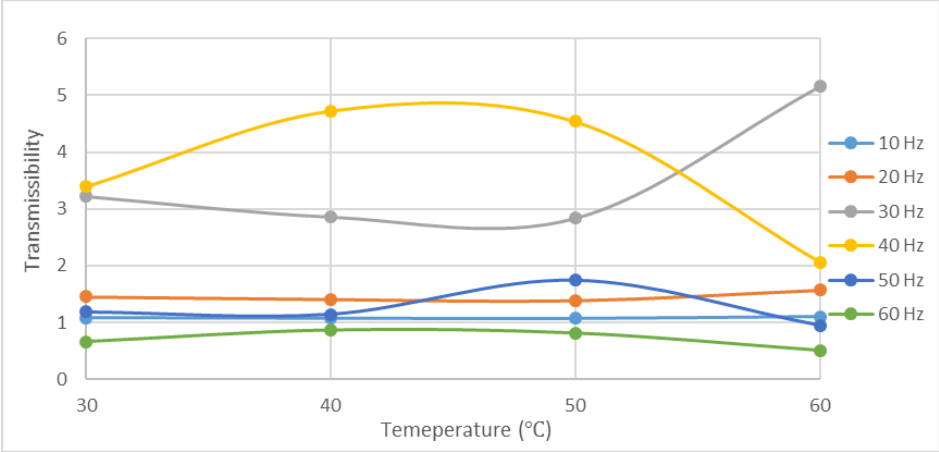


Figure B. 19 Dependence of transmissibility on temperature and frequency at pre-strain of 5%, strain amplitude of 1%, and non-magnetic field

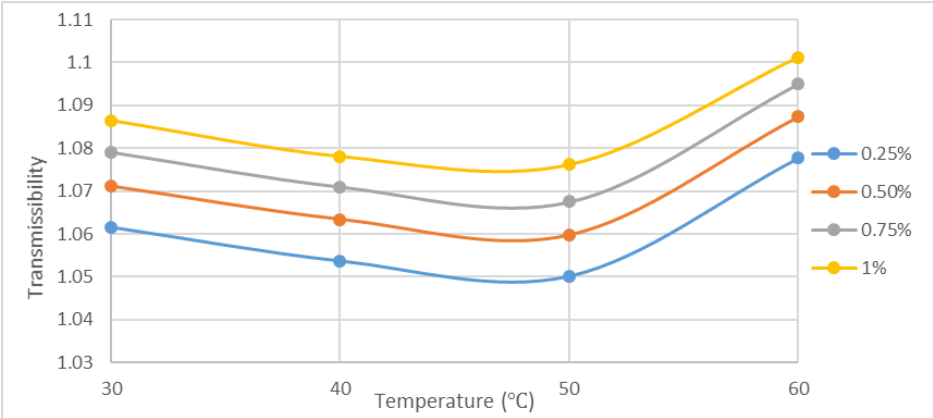


Figure B. 20 Dependence of transmissibility on temperature and strain amplitude at pre-strain of 5%, vibration frequency of 10 Hz, and non-magnetic field

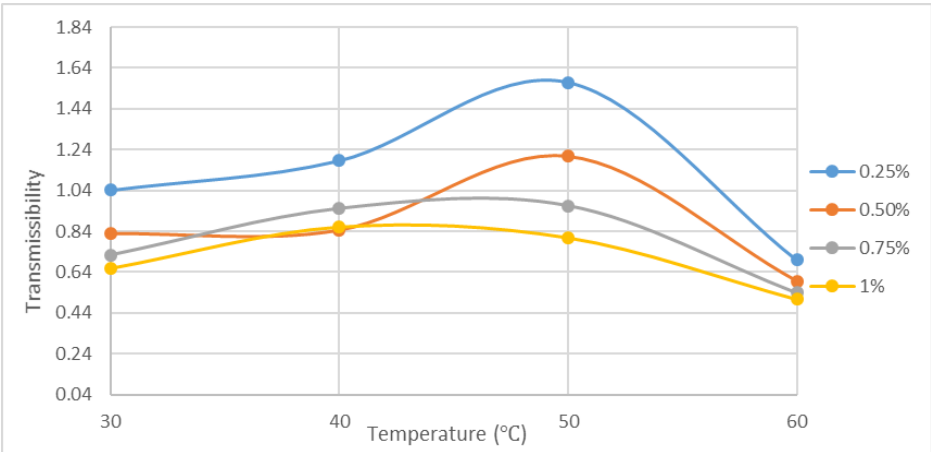


Figure B. 21 Dependence of transmissibility on temperature and strain amplitude at pre-strain of 5%, vibration frequency of 60 Hz and non-magnetic field

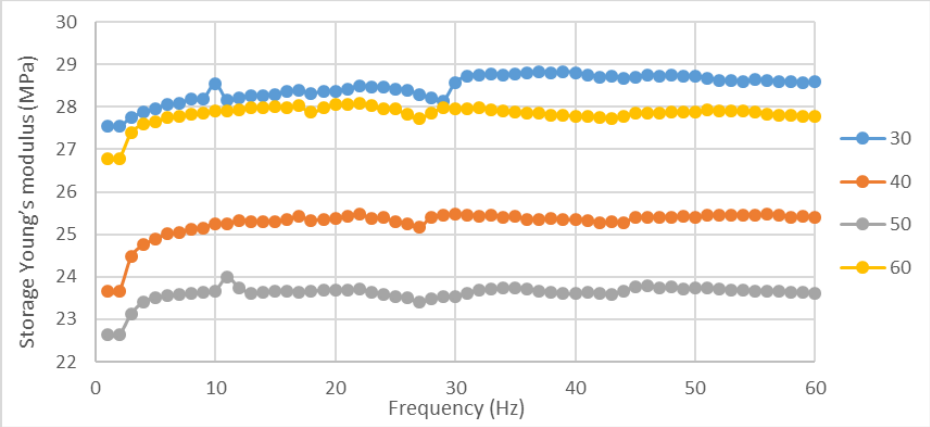


Figure B. 22 Dependence of storage modulus on temperature and frequency at pre-strain of 5%, strain amplitude of 1%, and magnetic field of 300 mT

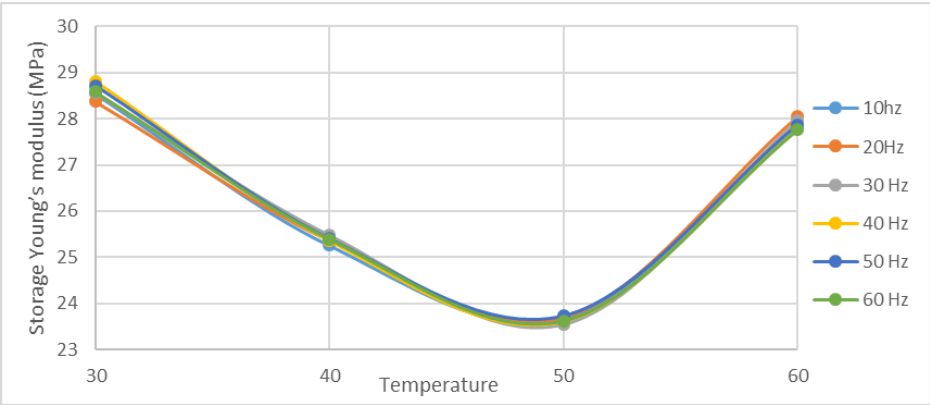


Figure B. 23 Dependence of storage modulus on temperature and frequency at pre-strain of 5%, strain amplitude of 1%, and magnetic field of 300 mT

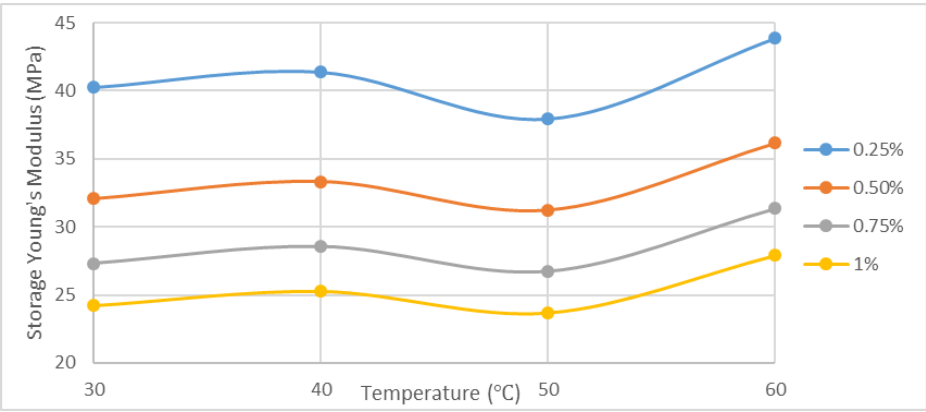


Figure B. 24 Dependence of storage modulus on temperature and strain amplitude at pre-strain of 5%, vibration frequency of 10 Hz, and magnetic field of 300 mT

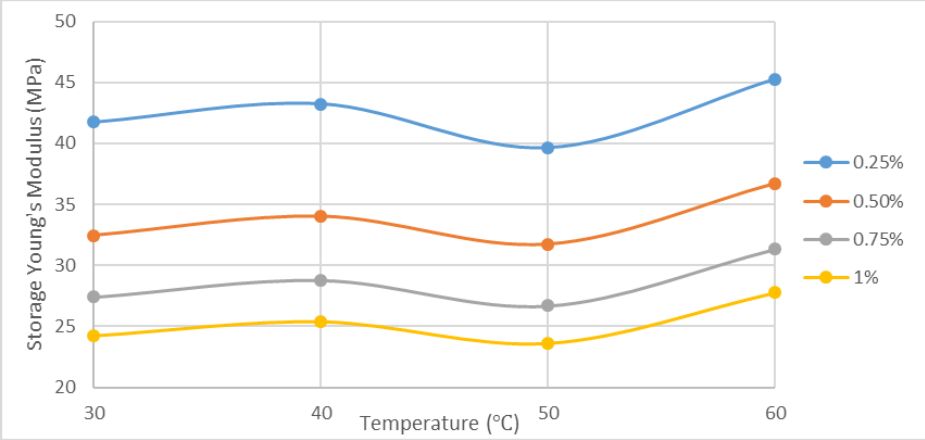


Figure B. 25 Dependence of storage modulus on temperature and strain amplitude at pre-strain of 5%, vibration frequency of 60 Hz, and magnetic field of 300 mT

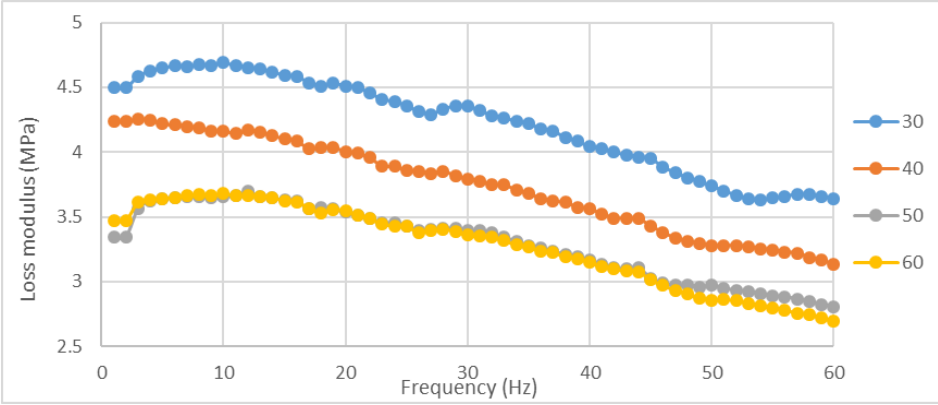


Figure B. 26 Dependence of loss modulus on temperature and frequency at pre-strain of 5%, strain amplitude of 1%, and magnetic field of 300 mT

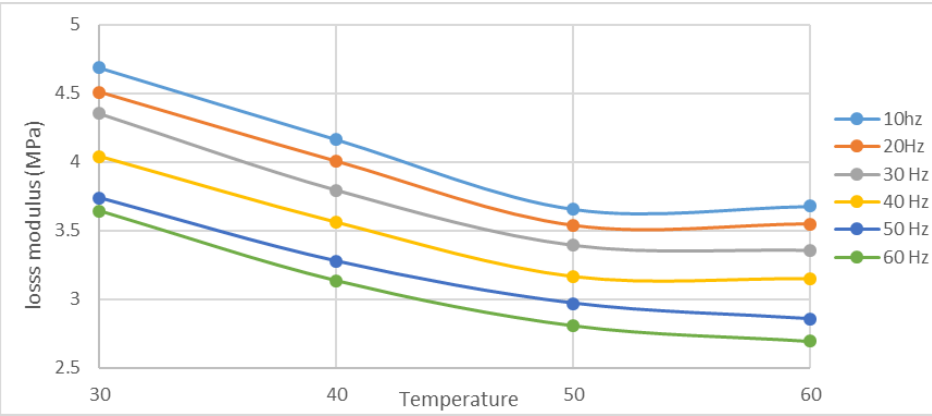


Figure B. 27 Dependence of loss modulus on temperature and frequency at pre-strain of 5%, strain amplitude of 1%, and magnetic field of 300 mT

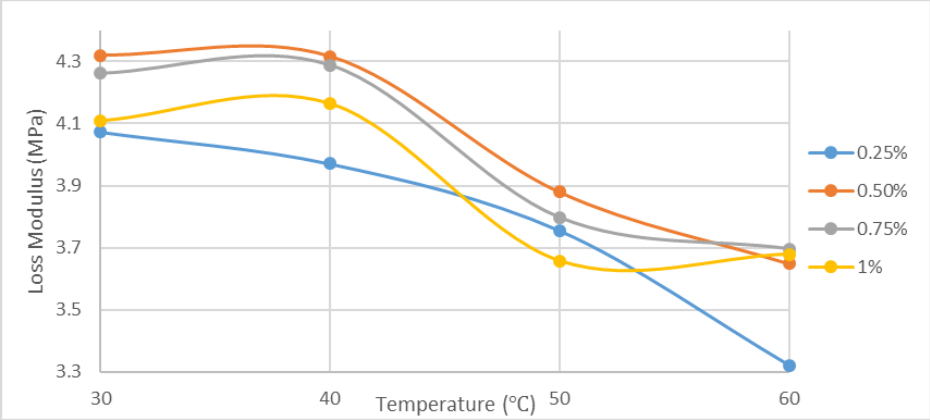


Figure B. 28 Dependence of loss modulus on temperature and strain amplitude at pre-strain of 5%, vibration frequency of 10 Hz, and magnetic field of 300 mT

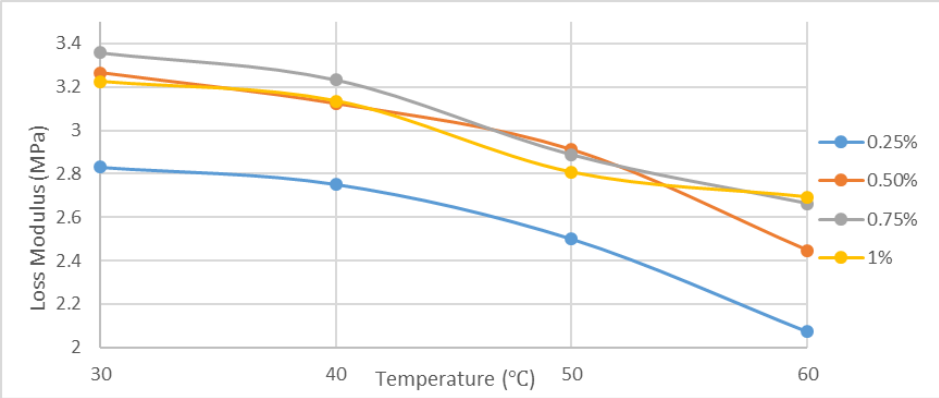


Figure B. 29 Dependence of loss modulus on temperature and strain amplitude at pre-strain of 5%, vibration frequency of 60 Hz, and magnetic field of 300 mT

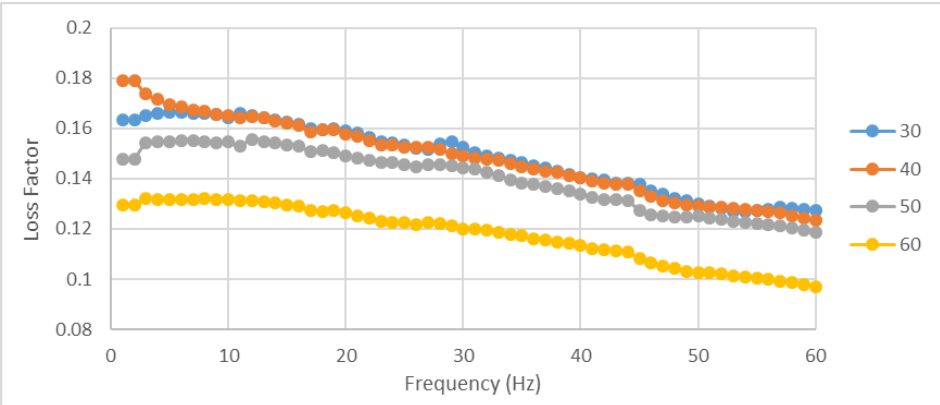


Figure B. 30 Dependence of loss factor on temperature and frequency at pre-strain of 5%, strain amplitude of 1%, and magnetic field of 300 mT

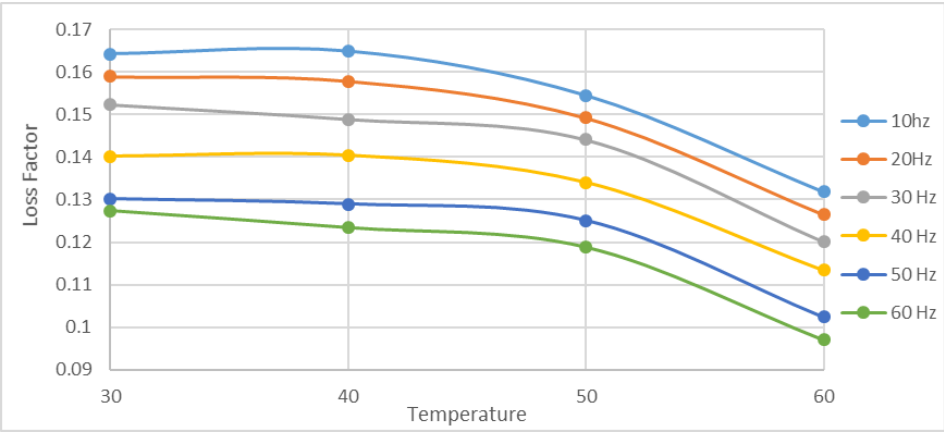


Figure B. 31 Dependence of loss factor on temperature and frequency at pre-strain of 5%, strain amplitude of 1%, and magnetic field of 300 mT

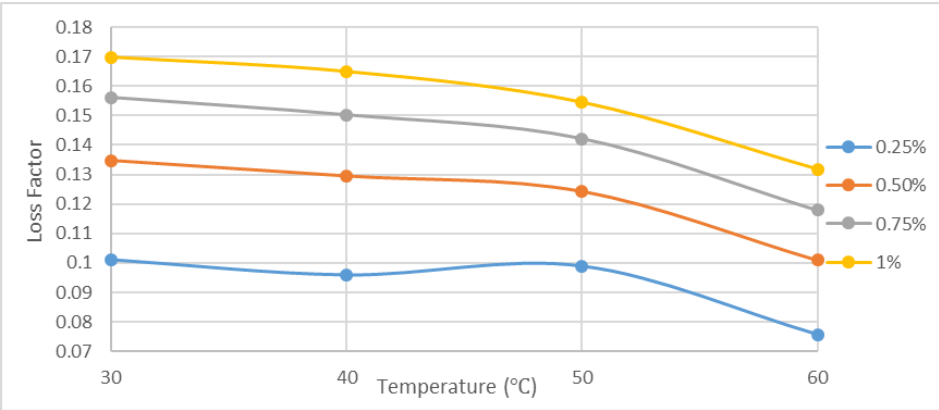


Figure B. 32 Dependence of loss factor on temperature and strain amplitude at pre-strain of 5%, vibration frequency of 10 Hz, and 300 mT

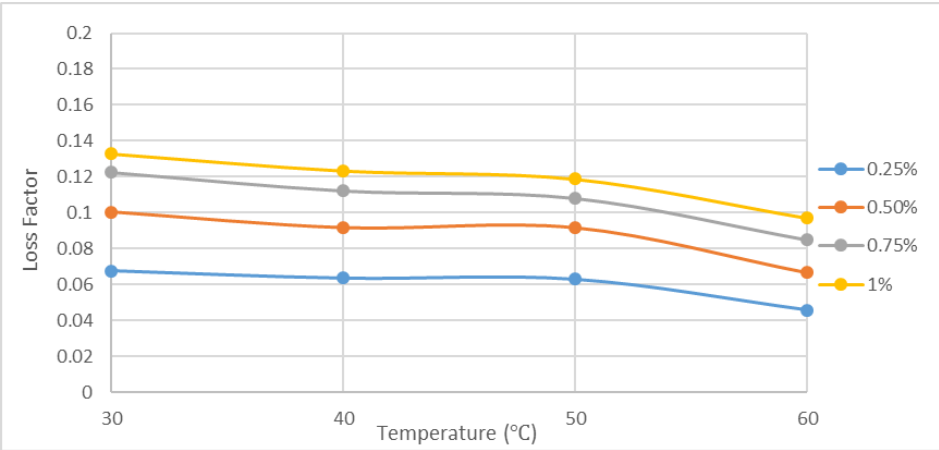


Figure B. 33 Dependence of loss factor on temperature and strain amplitude at pre-strain of 5%, vibration frequency of 60 Hz, and magnetic field of 300 mT

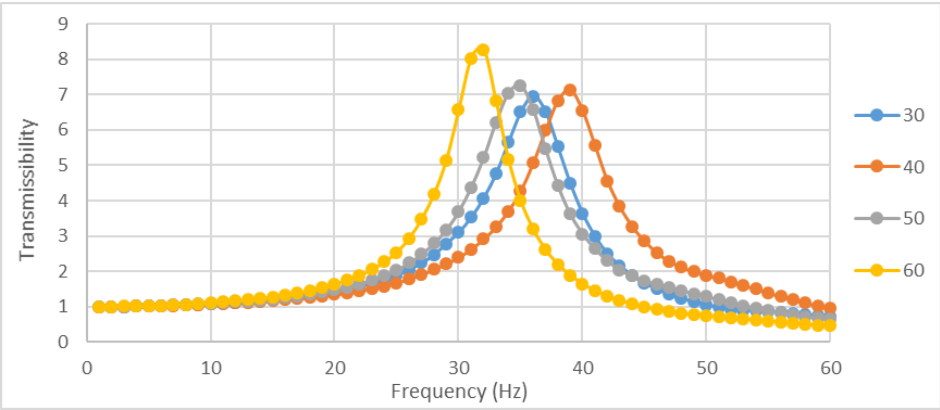


Figure B. 34 Dependence of transmissibility on temperature and frequency at pre-strain of 5%, strain amplitude of 1%, and magnetic field of 300 mT

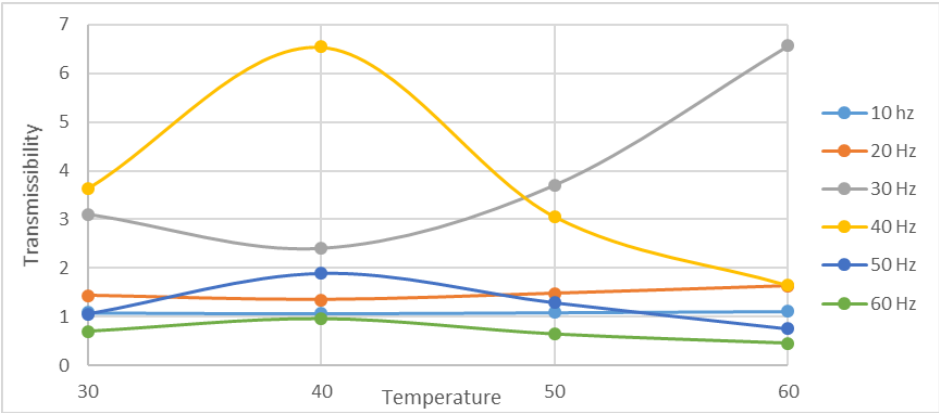


Figure B. 35 Dependence of transmissibility on temperature and frequency at pre-strain of 5%, strain amplitude of 1%, and magnetic field of 300 mT

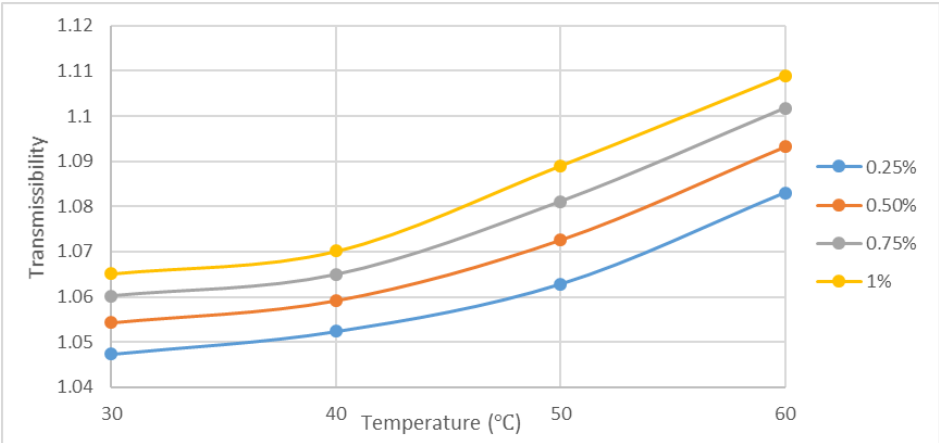


Figure B. 36 Dependence of transmissibility on temperature and strain amplitude at pre-strain of 5%, vibration frequency of 10 Hz, and 300 mT

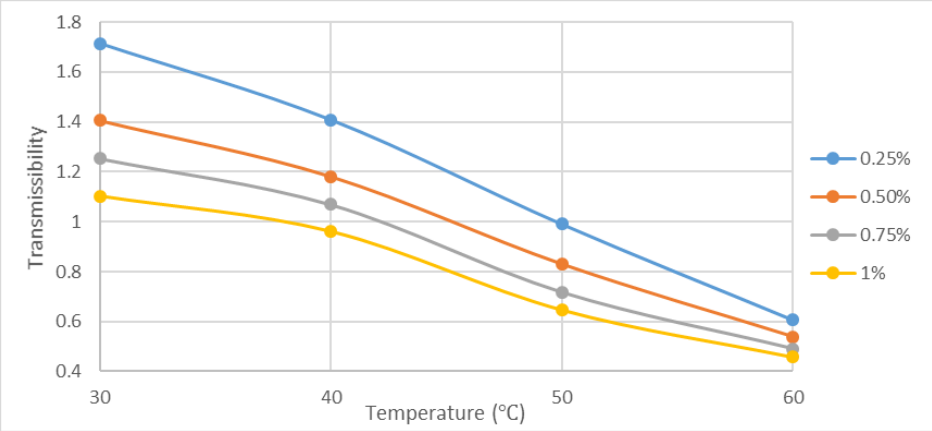


Figure B. 37 Dependence of transmissibility on temperature and strain amplitude at pre-strain of 5%, vibration frequency of 60 Hz, and 300 mT

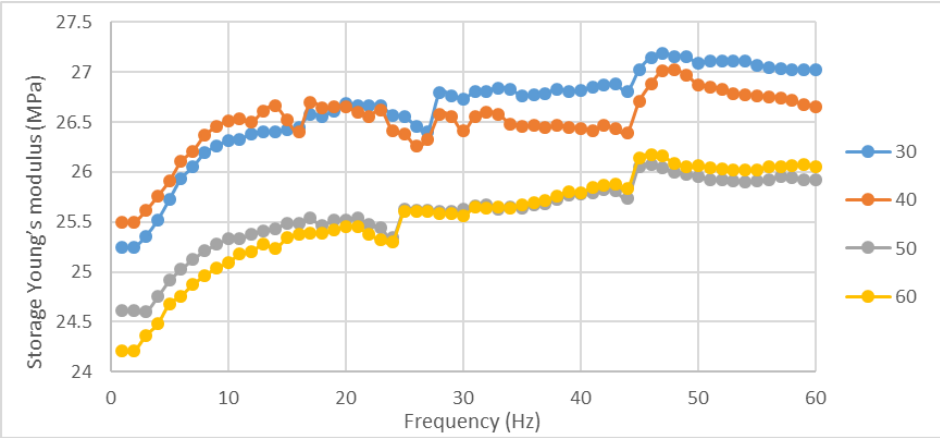


Figure B. 38 Dependence of storage modulus on temperature and frequency at pre-strain of 5%, strain amplitude of 1%, and magnetic field of 500 mT

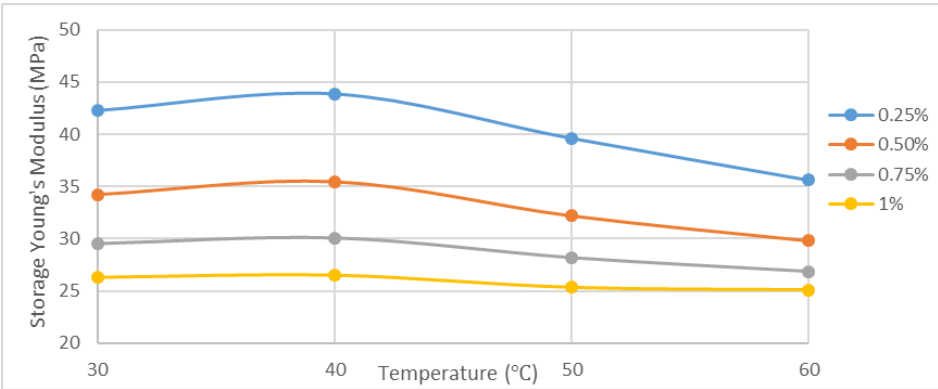


Figure B. 39 Dependence of storage modulus on temperature and strain amplitude at pre-strain of 5%, vibration frequency of 10 Hz, and magnetic field of 500 mT

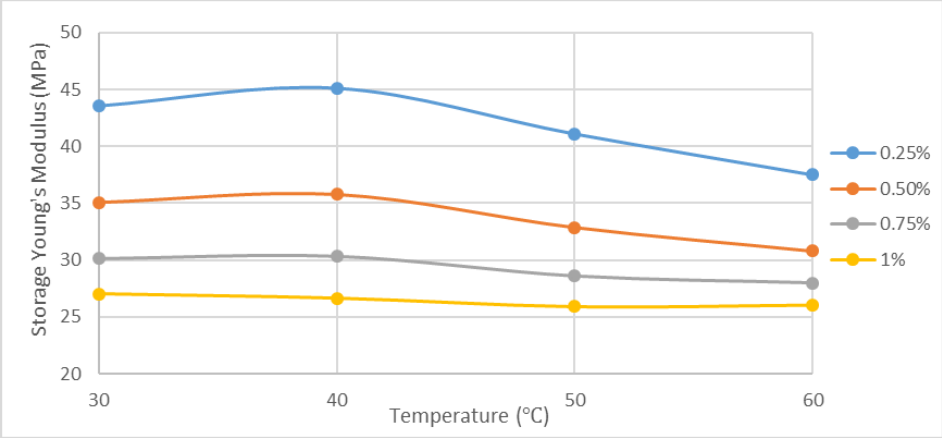


Figure B. 40 Dependence of storage modulus on temperature and strain amplitude at pre-strain of 5%, vibration frequency of 60 Hz, and magnetic field of 500 mT

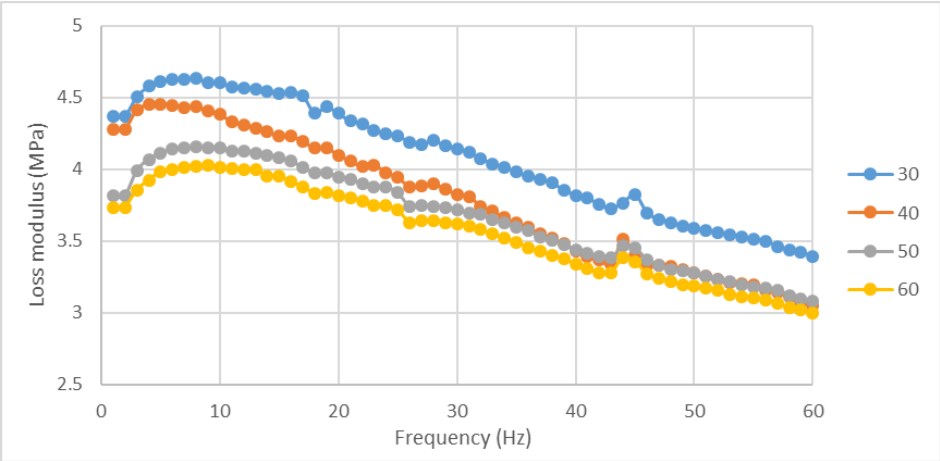


Figure B. 41 Dependence of loss modulus on temperature and frequency at pre-strain of 5%, strain amplitude of 1%, and magnetic field of 500 mT

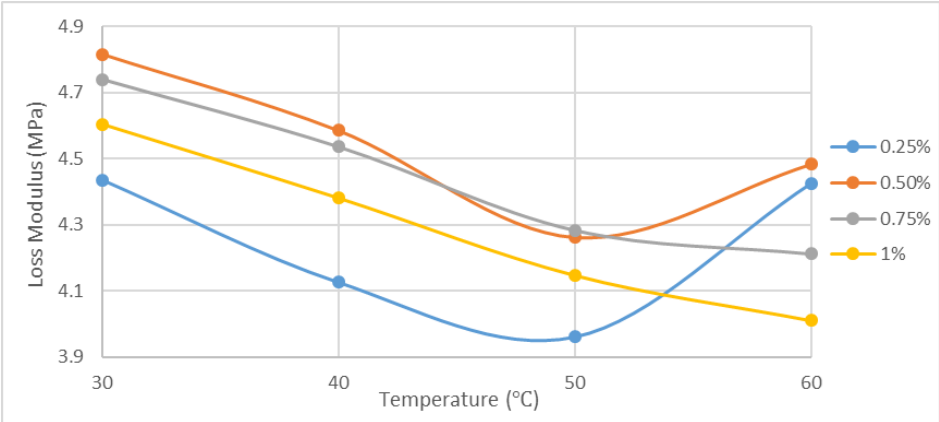


Figure B. 42 Dependence of loss modulus on temperature and strain amplitude at pre-strain of 5%, vibration frequency of 10 Hz, and magnetic field of 500 mT

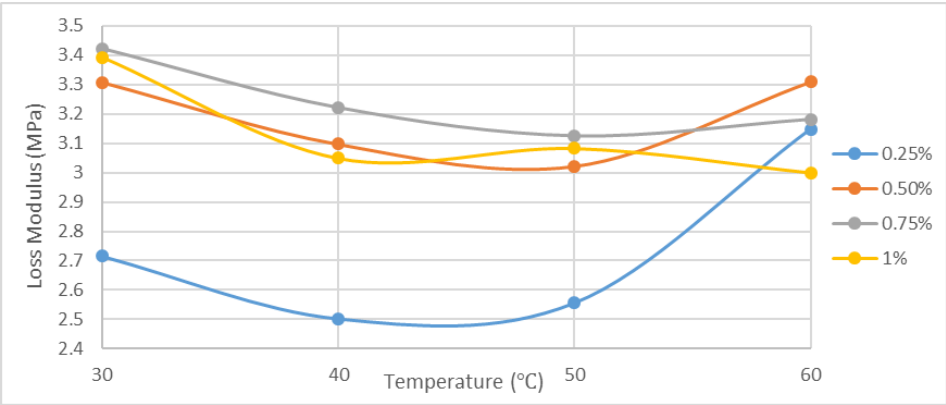


Figure B. 43 Dependence of loss modulus on temperature and strain amplitude at pre-strain of 5%, vibration frequency of 60 Hz, and magnetic field of 500 mT

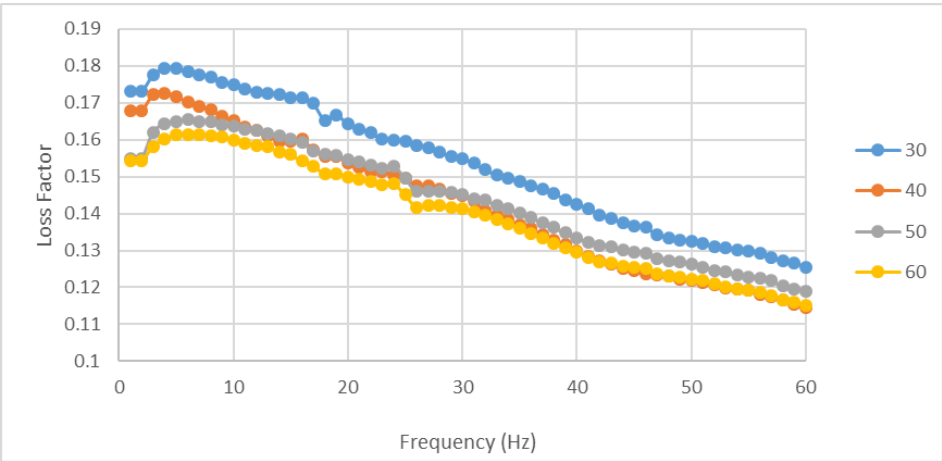


Figure B. 44 Dependence of loss factor on temperature and frequency at pre-strain of 5%, strain amplitude of 1%, and magnetic field of 500 mT

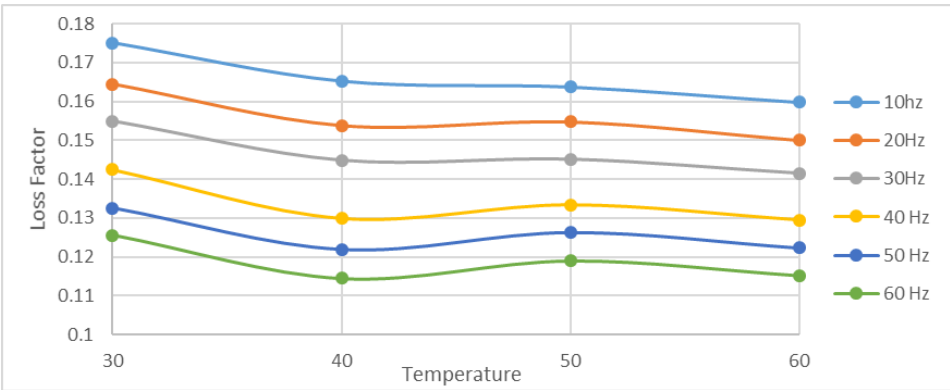


Figure B. 45 Dependence of loss factor on temperature and frequency at pre-strain of 5%, strain amplitude of 1%, and magnetic field of 500 mT

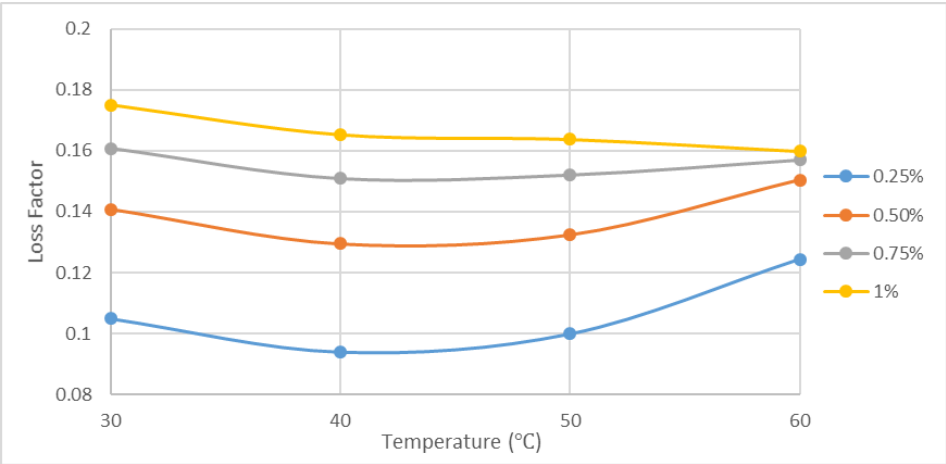


Figure B. 46 Dependence of loss factor on temperature and strain amplitude at pre-strain of 5%, vibration frequency of 10 Hz, and magnetic field of 500 mT

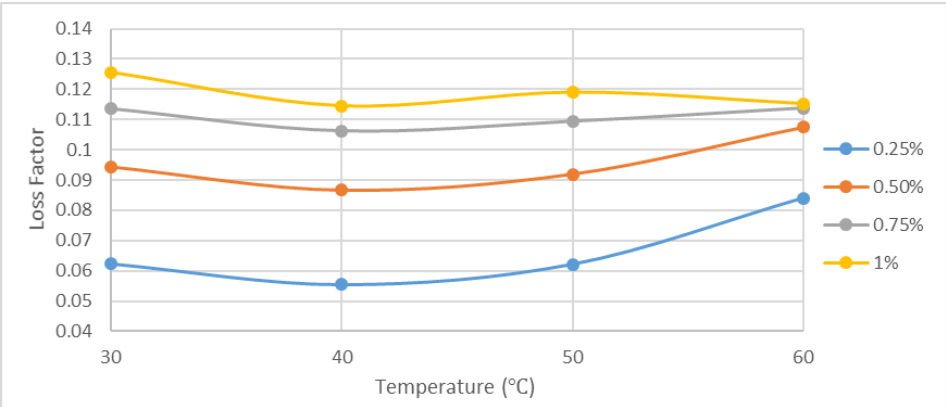


Figure B. 47 Dependence of loss factor on temperature and strain amplitude at pre-strain of 5%, vibration frequency of 60 Hz, and magnetic field of 500 mT

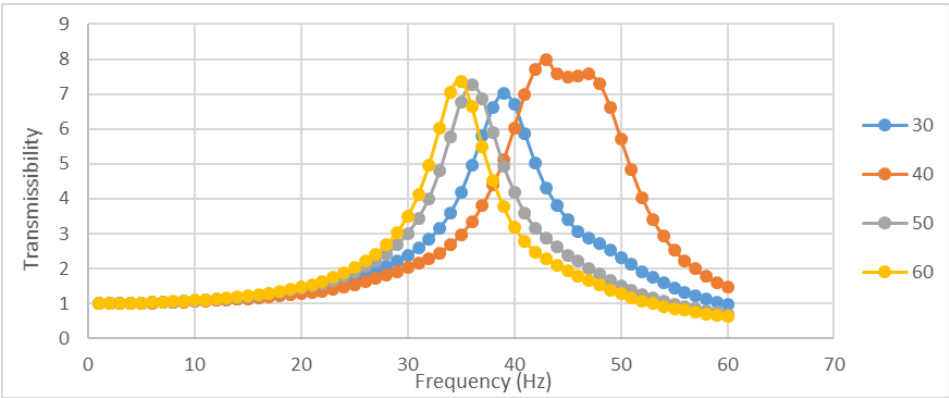


Figure B. 48 Dependence of transmissibility on temperature and frequency at pre-strain of 5%, strain amplitude of 1%, and magnetic field of 500 mT

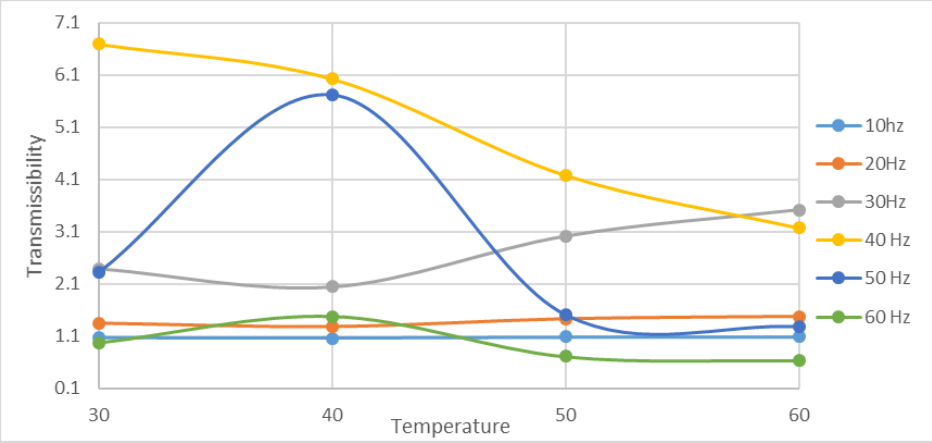


Figure B. 49 Dependence of transmissibility on temperature and frequency at pre-strain of 5%, strain amplitude of 1%, and magnetic field of 500 mT

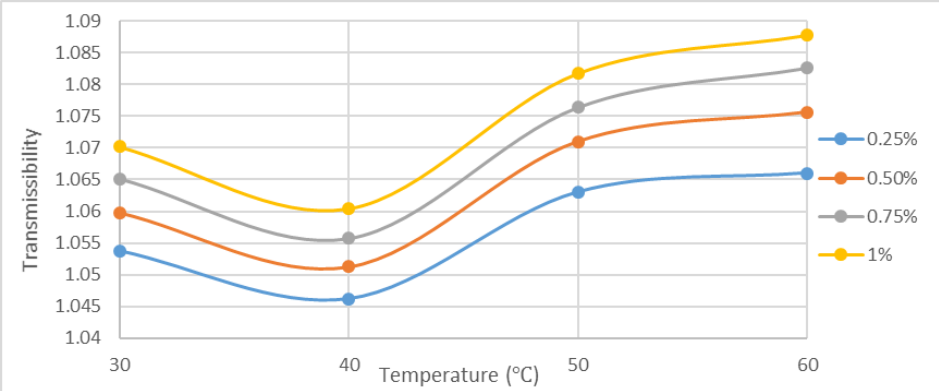


Figure B. 50 Dependence of transmissibility on temperature and strain amplitude at pre-strain of 5%, vibration frequency of 10 Hz, and magnetic field of 500 mT

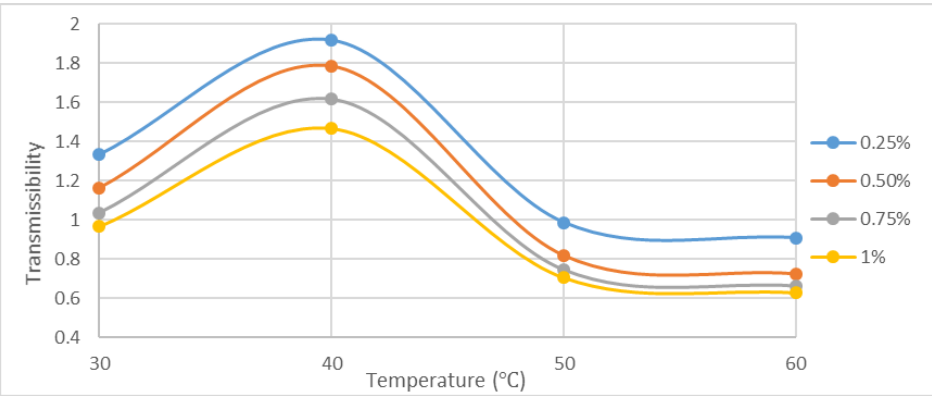


Figure B. 51 Dependence of transmissibility on temperature and strain amplitude at pre-strain of 5%, vibration frequency of 60 Hz, and magnetic field of 500 mT

# Appendix C Design calculation of oven

## C.1 Introduction

The oven is made of aluminum alloy sheet and its shape is a cubic box with same length, width, and height as 250 mm. The thickness of aluminum alloy sheet is 10mm. The top and bottom of the oven are designed as perforated plates for the Instron testing machine to apply mechanical loads on MRE smpecimen. The diameter of the opening on the upper and lower bottom plates is 100mm. In order to guarantee the test temperature stays around the target temperature, an insulation layer of aluminum silicate is placed on the inner wall of the oven, and the heating wire and the aluminium foil are well arranged on the inner surface of the insulating layer on the side of the oven. The length of the heating wire is 18 m and its thermal power is 100 W. The small observation window on one side of the oven is also made of special glass. During the dynamic mechanical analysis (DMA) experiment, a special cotton seal is used to seal the gap between the loading arm of the Instron test machine and top and bottom plates of the oven. The insulation layer on the inner wall of the oven is an aluminum silicate with thickness of 20mm. In this appendix, the heat transfer of the oven is assessed and the effect of aluminum shell, the gap, and the small window on the heat transfer of the oven is small neglected for the sake of simple calculation.

## C.2 Heat transfer

Heat loss of the oven during DMA experiment is mainly through heat conduction and heat radiation, therefore the rate of heat transfer of the oven can be expressed as,

$$\dot{Q} = \dot{Q}_c + \dot{Q}_r \tag{C.1}$$

where $\dot{Q}_c$ and $\dot{Q}_r$ are the rate of the conduction heat transfer and the radiation heat transfer respectively.

The rate of the conduction heat transfer can be calculated by using Fourier's Law.

$$\dot{Q}_c = kA\frac{\mathrm{T}-T_0}{\Delta X} \tag{C.2}$$

where A and T0 are the surface area and temperature respectively, Δx is the thickness of the material, k is the thermal conductivity of the material.

The rate of the radiation heat transfer can be calculated by using Stefan-Boltzmann law.

$$\dot{Q}_r = \varepsilon\sigma A(T^4 - T_0^4) \quad \text{(C.3)}$$

in which A and T0 are the surface area and temperature respectively, $\sigma = 5.67 \times 10^{-8}$ W/m$^2$K$^4$ is the Stefan-Boltzmann constant, ε is the emissivity coefficient, which varies between 0 and 1, indicating the radiation of heat from a body according the Stefan-Boltzmann Law. The emissivity coefficient is equal to 1 for an ideal black body.

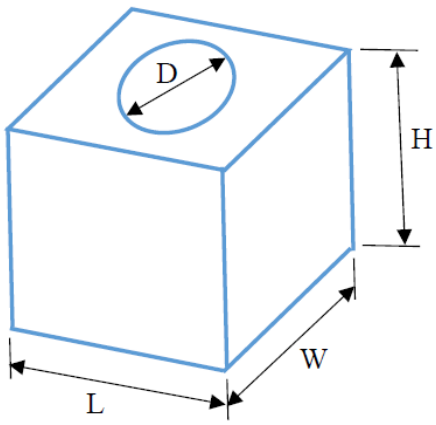


Figure C. 1 The diagram of cubic box

As shown in Figure C.1, W = L = H = 250 mm. Therefore, the surface area of the oven is obtained.

$$A = 2(W * H + H * L + L * W) = 0.375 \text{ m}^2 \quad \text{(C.4)}$$

Aluminum silicate is one of ideal thermal insulation, fire-proof, and sound-absorbing materials. Its thermal conductivity is about 0.09 W/mK. The thickness of the insulation layer on the inner wall of the oven is 20 mm according to the design of the oven. The rate of conduction heat transfer is obtained by substituting the thermal conductivity, thickness of the insulation layer, and surface area into Eq. (C.2).

$$\dot{Q}_c = 0.09 * 0.375 \frac{T - T_0}{0.02} = 1.69(T - T_0) \quad \text{(C.5)}$$

The emissivity coefficient of aluminum alloy sheet is in the range of 0.09 to 0.11. Substituting emissivity coefficient, surface area into Eq. (C.3), Tthe rate of radiation heat transfer is obtained.

$$\dot{Q}_r = 0.11 * 5.67 * 10^{-8} * 0.375(T^4 - T_0^4) = 2.34 \times 10^{-9}(T^4 - T_0^4) \quad \text{(C.6)}$$

Substituting Eq. (C.5) and Eq. (C.6), the heat loss of the oven during DMA experiment is obtained.

$$\dot{Q} = 1.69(T - T_0) + 2.34 \times 10^{-9}(T^4 - T_0^4) \quad \text{(C.7)}$$

Figure C.2 presents the rate of heat loss as function of test temperature when the room temperature is 20 oC. It can be seen that the rate of heat loss varies linearly with test temperature indicating the rate of heat loss is mainly due to the heat transfer by conduction.

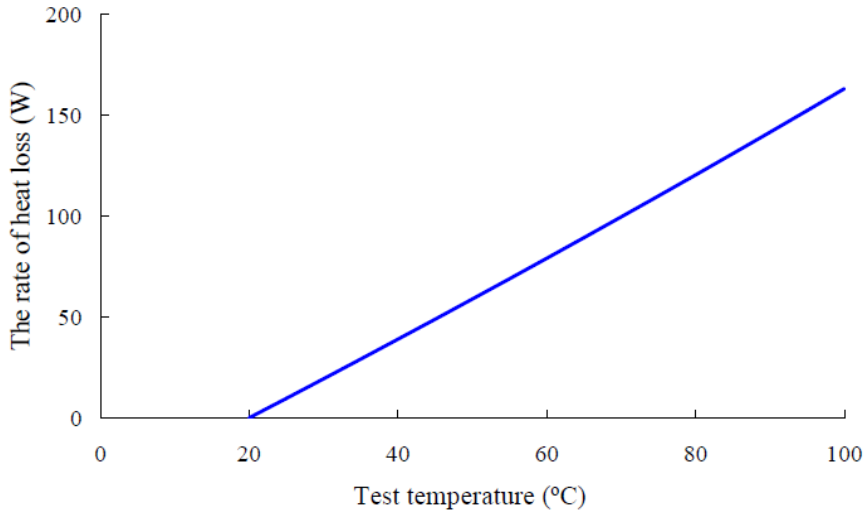


Figure C. 2 The rate of heat loss vary with test temperature when the room temperature is 20 °C

When room temperature is 20 °C and maximum test temperature is 70 °C, the maximum rate of heat loss is about 99.5 W. It is less that the thermal power of the heating wire used in the oven which is 100 W.

## C.3 Summary

The heat transfer of the designed oven is assessed by using Fourier's Law and Stefan-Boltzmann law. The results show that the heat loss of the oven is mainly caused by the conduction heat transfer. When room temperature is 20 °C, the designed oven can be used for DMA experiment of MRE sample under test temperature of 70 °C.

# Appendix D Numerical results of particle filled elastomer

## D.1 Introduction

Rubbers or rubber like materials are widely used for the matrix of magnetorheological elastomers (MREs) because of their excellent damping and energy absorption properties. They can deform largely and nonlinearly under load and fully recover to the initial configuration after the load removal. Their loading and unloading stress-strain curves are not the same depending on different influence factors such as time, frequency, temperature and loading history. These nonlinearities have an important effect on the performance of rubber based MREs. This appendix is to calculate the mechanical properties of micron-sized particle filled rubber by using commercial finite element analysis (FEA) software. Comparative analysis is performed between FEA results and predicted results by using theoretical models.

## D.2 FEA of hyper-elastic behaviour

Hyper-elastic models are broadly classified into two categories: the phenomenological models (e.g. the Mooney-Rivlin model and the Ogden model) and the micromechanical models based on both physics of polymer chains network and statistical methods (e.g. the Neo-Hookean model and the Arruda-Boyce model).

It is important for a hyper-elastic model to take an adequate form of the deformation energy density providing good fit with a number of experiment data sets. The stress tensors are determined as the derivative of the deformation energy density with respect to the strain tensors. When hyper-elastic materials are assumed to be homogeneous and isotropic, the deformation energy density can be expressed in phenomenological models as a function of strain tensor invariants (e.g. the Mooney-Rivlin model), or principal stretch ratios (e.g. the Ogden model). These hyper-elastic models are available and easy to implement in commercial FEA software. The model parameters are identified and calibrated based on experimental results of samples. The number of model parameters required to describe a hyper-elastic material is usually dependent on the deformation characteristics of samples under load. There are many modes required to determine the material constants that characterize the hyper-elastic behavior in quasi-static load conditions. The fitting capability and accuracy of different hyper-elastic models have been evaluated for rubber or rubber-like materials under uniaxial tension/compression, biaxial (usually equibiaxial) tension/compression, and pure shear (i.e. planar tension and planar compression).

Since the standard test of samples has not been conducted to determine the material constants of elastomer matrix in this project, the input data in ANSYS are calculated by calibrating the well-known Treloar's (1958) experimental data of vulcanized rubber with 8% Sulphur (PP) (Shahzad et al. 2015). The Mooney-Rivlin model with two parameters presented by Marckmann and Verron (2006) fitting PP rubber under uniaxial tension and the Ogden model with one order by Steinmann et al. (2012) calibrating PP rubber under uniaxial tension, equibiaxial tension and pure shear are used respectively in finite element model. In this Appendix, ANSYS Solid185 is employed to calculate hyper-elastic behavior of Treloar's PP rubbery samples under uniaxial tension, equibiaxial tension and pure shear considering the compatibility between hyper-elastic and magnetic calculation.

Figure D.1 and Figure D.2 show the comparison of Treloar's experimental data, the fitting curve of the experimental data and FEA of representative volume element (RVE) of Treloar's PP tubbery samples. It can be found that both the Ogden model with one order and the Mooney-Rivlin model with two parameters are capable of characterizing hyper-elastic behaviour of Treloar's PP rubbery samples although there are some discrepancies when the PP rubbery samples are subjected to equibiaxial tension or pure shear.

FEA results based on Ogden model with one order are in very good agreement with Steinmann's fitting curve of the experimental data. FEA results based on Mooney-Rivlin model with two parameters are found in very good agreement with Treloar's experimental data under equibiaxial tension and to Marckmann's fitting curve of the experimental data under pure shear. The constitutive model and its material constants calibrated by the experimental data of samples play an important role in FEA of the hyper-elastic response of the PP rubbery samples.

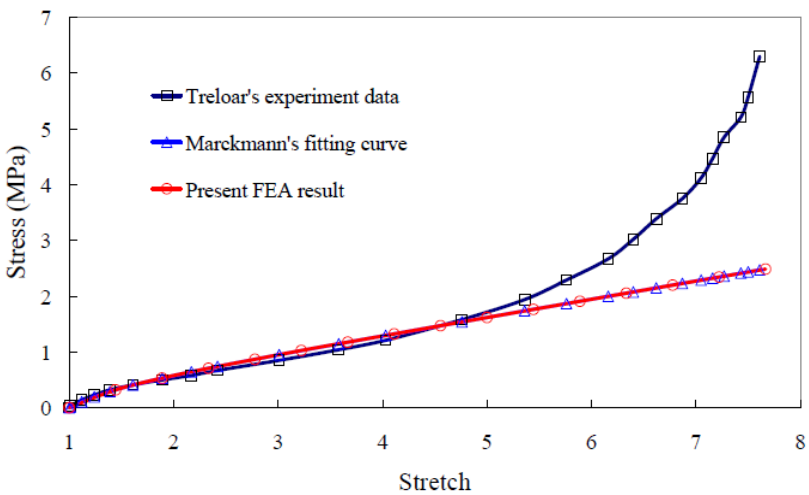


(a)

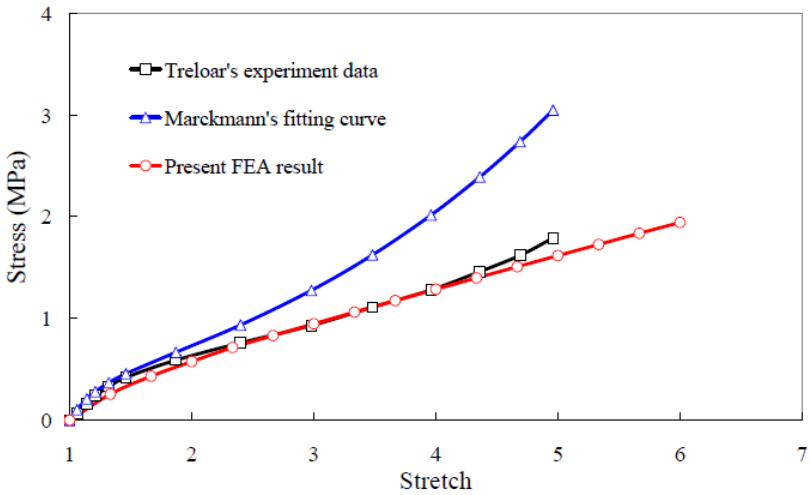


(b)

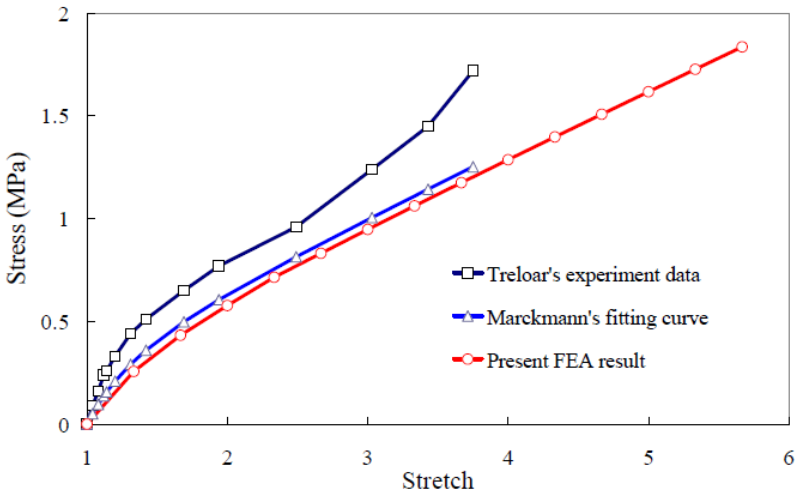


(c)

Figure D. 1 Hyper-elastic behaviour of PP rubber under: (a) uniaxial tension, (b) equibiaxial tension, and (c) pure shear based on the Mooney-Rivlin

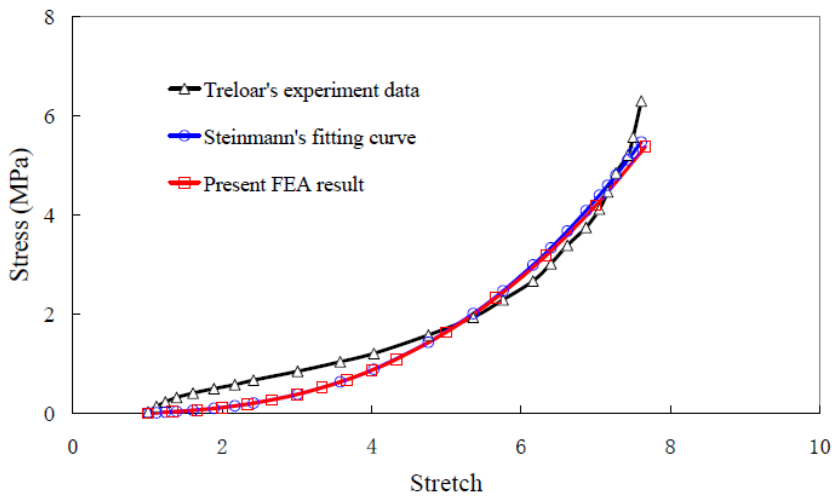


(a)

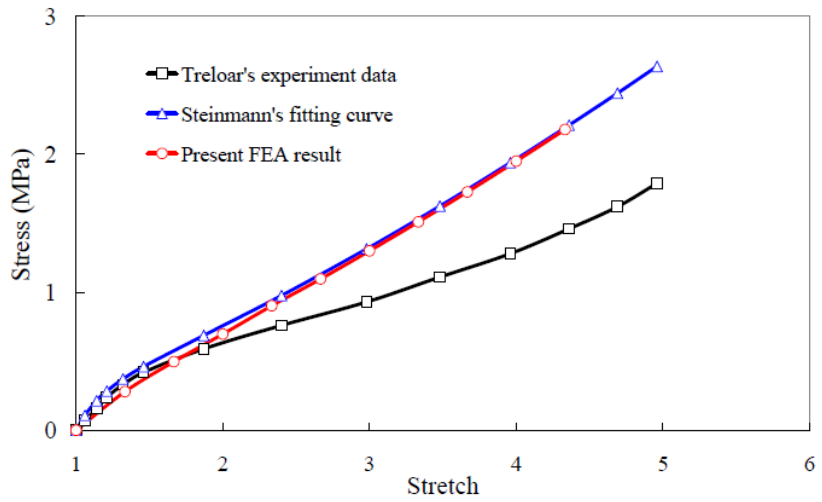


(b)

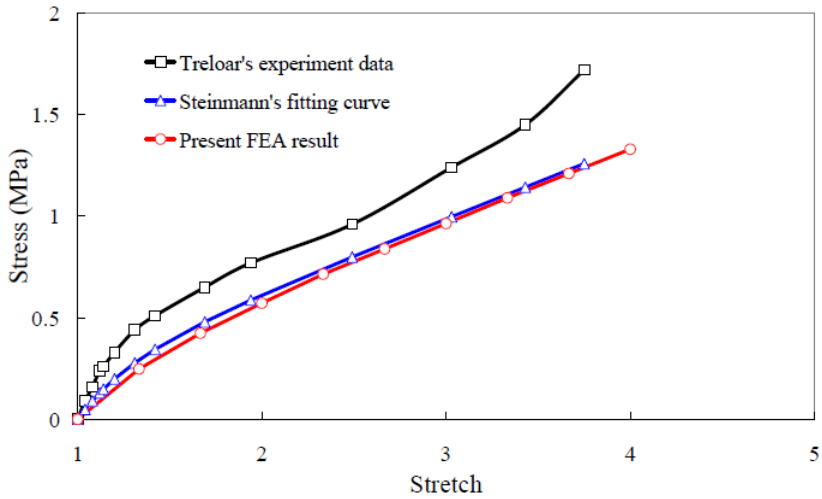


(c)

Figure D. 2 Hyper-elastic behaviour of PP rubber under: (a) uniaxial tension, (b) equibiaxial tension, and (c) pure shear based on the Ogden model

## D.3 FEA of MRE in the absence of an external magnetic field

Various empirical equations have been proposed to evaluate the stiffening effects of micron-sized particles on the mechanical properties of polymer composites. However, most of them neglected the influence of particle properties and considered the special case of rigid particles in an incompressible matrix. The stiffening effect of particles on polymer matrix is a function of particle volume fraction independent of particle size.

- Guths equation (1945):

$$\frac{E}{E_m} = 1 + 2.5V_f + 1.44V_f^2 \text{ and } \frac{E}{E_m} = 1 + 0.67f_sV_f + 1.62f_s^2V_f^2 \qquad \text{(D.1)}$$

- Brinkman equation (1952):

$$\frac{E}{E_m} = \left(1 - V_f\right)^{-5/2} \tag{D.2}$$

- Budiansky equation (1965):

$$\frac{E}{E_m} = \frac{1}{\left(1-2.5V_f\right)} \tag{D.3}$$

- Castaneda equation (1989):

$$\frac{E}{E_m} = \frac{1}{\left(1-3V_f\right)} \tag{D.4}$$

- Govindjee and Simo equation (1991):

$$\frac{E}{E_m} = \frac{1-0.5V_f}{1-V_f} \tag{D.5}$$

Where, $E$ and $E_m$ are elastic modulus of composite and matrix respectively, $V_f$ is filler volume fraction, $f_s$ is a shape factor determined mainly by the ratio of asymmetric particles length to their diameter.

In order to consider the impact of filler properties on overall composite properties, Mori and Tanaka (1973) proposed a model to predict the effective elastic modulus of polymer composite dispersed spherical particles.

$$K = K_m + \frac{V_f\left(K_f - K_m\right)}{\frac{3\left(1-V_f\right)\left(K_f-K_m\right)}{3K_m+4G_m}+1} \tag{D.6}$$

$$G = G_m + \frac{V_f\left(G_f - G_m\right)}{\frac{6\left(1-V_f\right)\left(K_m+2G_m\right)}{5\left(3K_m+4G_m\right)}\left(\frac{G_f}{G_m}-1\right)+1} \tag{D.7}$$

$$E = \frac{9KG_m}{3K+G_m} \tag{D.8}$$

Where, $V_f$ is volume fraction of filler, $K$, $G$, and $E$ are bulk modulus, shear modulus and elastic modulus respectively, subscripts $c$, $m$, and $f$ represented the composite, matrix, and filler respectively.

Hashin and Shtrikman (1963) and Hashin (1983) presented the upper bound and lower bound of the predictions as follow.

- Upper bound:

$$K^u = K_f + \frac{1-V_f}{\frac{1}{K_m-K_f}+\frac{3V_f}{3K_f+4G_f}} \quad (D.9)$$

$$G^u = G_f + \frac{1-V_f}{\frac{1}{G_m-G_f}+\frac{6V_f(K_f+2G_f)}{5G_f(3K_f+4G_f)}} \quad (D.10)$$

$$E^u = \frac{9K^u G^u}{3K^u+G^u} \quad (D.11)$$

- Lower bound:

$$K^l = K_m + \frac{V_f}{\frac{1}{K_f-K_m}+\frac{3(1-V_f)}{3K_m+4G_m}} \quad (D.12)$$

$$G^l = G_m + \frac{V_f}{\frac{1}{G_f-G_m}+\frac{6(1-V_f)(K_m+2G_m)}{5G_m(3K_m+4G_m)}} \quad (D.13)$$

$$E^l = \frac{9K^l G^l}{3K^l+G^l} \quad (D.14)$$

Recently Saadat (2015) proposed a method to predict the effective elastic modulus of composites with multiple types of anisotropic ellipsoidal inclusions. The physically consistent results and good predictive accuracy were obtained by employing effectiveness rather than average strains within phases to ensure that the energy stored within phases was summed to that stored in the composite.

FEA of a RVE containing one particle is an efficient and simple method for simulating nonlinear stress-strain behavior of MREs and calculating the effective modulus. The 3D geometrical model of RVE consists of a 30 μm brick imbedded with a sphere. The diameter of the sphere in finite element model varies from 6.856μm to 14.771μm and the particle volume fraction in correspondence is from 0.05 to 0.5. The number of elements and nodes are dependent on the predefined value of element size and the particle volume fraction. For example, the element size is set to 0.00125 μm and ANSYS creates 114529 elements consisting of 21017 nodes for the particle volume fraction of 0.4. The effective elastic modulus can be predicted by assuming the behavior of the MRE is linear elastic at infinitesimal strains.

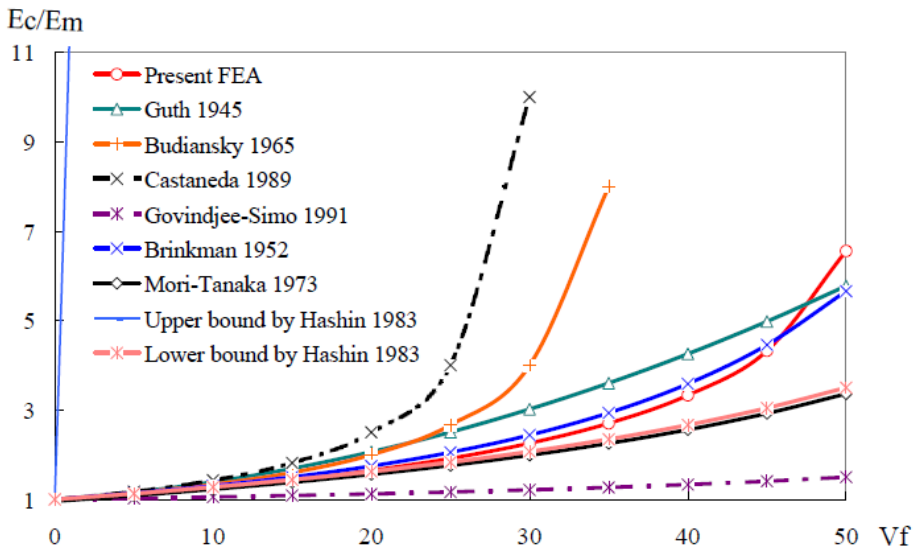


Figure D. 3 Comparison of FEA and various theoretical models for predicting the effect of iron particles embedded in PP rubbery matrix on the elastic modulus of MREs

It can be observed in Figure D.3 that the normalized elastic modulus increases as the increasing of iron particle volume fraction within rubbery matrix. All of obtained results fall in agreement when the particle volume fraction is smaller than 10% and the discrepancy is progressively increasing as the increasing of iron particle volume fraction. FEA results are in very good agreement with those predicted by the Brinkman model (1952) and exhibits some differences to the predicted results by the Mori-Tanaka model (1973) and the Hashin's lower bound (1983) when the iron particle volume fraction is more than 30%. The Hashin's upper bound (1983) fails in the predictions may be due to the big difference of the elastic modulus between iron particles and PP rubbery matrix despite it is necessary to be verified.

The nonlinear stress-strain behavior can be simulated by using hyper-elastic model based on the Ogden model with one order and linear elastic model respectively for PP rubbery matrix filled with iron particles. However, the incremental iterative calculation is terminated by ANSYS because some elements are seriously distorted at large strains and the finer finite element mesh is needed. It is too time consuming to perform the simulation by using personal computer. In our preliminary study, 2D geometrical model of RVE is used to simulate the nonlinear stress-strain behavior of PP rubbery matrix filled with iron particles under uniaxial tension, equibiaxial tension and pure shear. The obtained results of stress-stretch relationship are shown in Figure D.4 to Figure D.6.

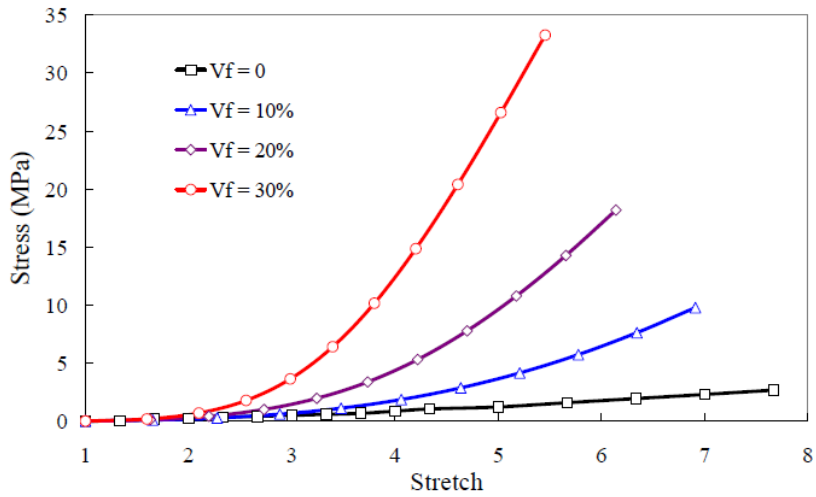


Figure D. 4 The uniaxial tension stress-stretch behaviour of PP rubber filled with different volume fractions of iron particles.

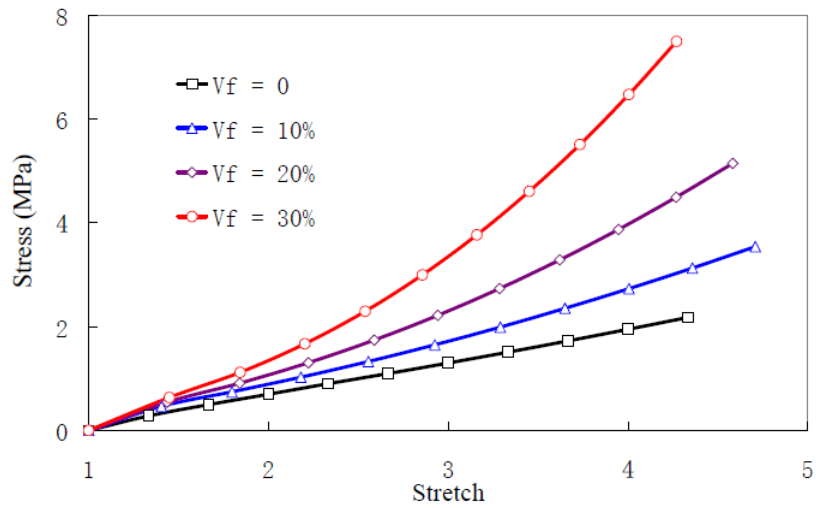


Figure D. 5 The equibiaxial tension stress-stretch behaviour of PP rubber filled with different volume fractions of iron particles.

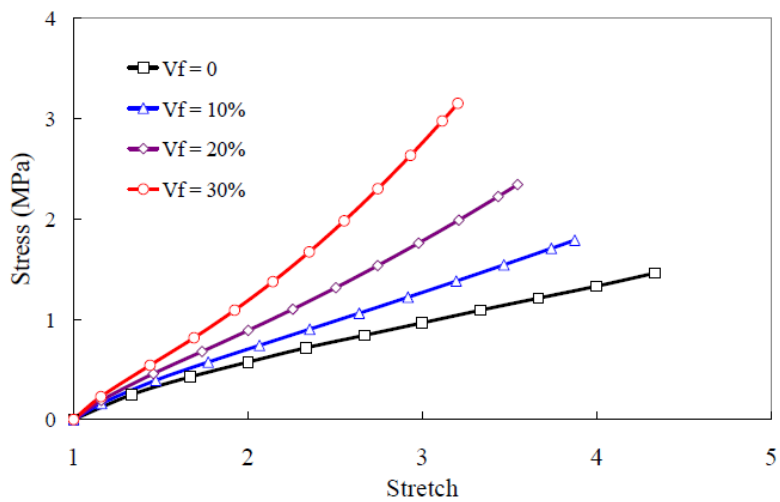


Figure D. 6 The pure shear stress-stretch behaviour of PP rubber filled with different volume fractions of iron particles.

## D.4 Summary

Numerical analyses have been performed by using ANSYS for the hyper-elastic properties of rubbery matrix and mechanical properties of the MRE under uniaxial tension, equibiaxial tension, and pure shear. The main results are presented as follows:

(1) FEA results are in very good agreement with the fitting curve of Treloar's experimental data although there are some discrepancies when the PP rubbery samples are subjected to equibiaxial tension. The constitutive model and its material constants calibrated by the experimental data of samples play an important role in FEA of the hyper-elastic response of the rubbery materials.

(2) The Ogden model with one order provides better reproduction of the rubbery samples under uniaxial tension and more orders are needed to describe the hyper-elastic behaviour of rubbery sample under biaxial tension and pure shear. The Mooney-Rivlin model with two parameters are not enough to describe the hyper-elastic behaviour of rubbery sample.

(3) The nonlinear stress-strain behavior of PP rubbery matrix filled with iron particles is strongly dependent on iron particle volume fraction. The elastic modulus increases as the increasing of iron particle volume fraction within rubbery matrix. FEA results are in very good agreement with those predicted by the Brinkman model (1952) and exhibit some differences comparing to the prediction results by the Mori-Tanaka model (1973) and the Hashin's lower bound (1983) when the iron particle volume fraction is more than 30%.